Interfacing quantum gases with femtosecond laser pulses: from strong-field ionization to ultracold plasma

Dissertation zur Erlangung des Doktorgrades
an der Fakultät für Mathematik, Informatik und Naturwissenschaften
Fachbereich Physik der Universität Hamburg

vorgelegt von
Tobias Kroker

Hamburg
2021

Gutachter/innen der Dissertation:	Prof. Dr. Markus Drescher Prof. Dr. Klaus Sengstock
Zusammensetzung der Prüfungskommission:	Prof. Dr. Markus Drescher Prof. Dr. Klaus Sengstock Prof. Dr. Roman Schnabel Prof. Dr. Henning Moritz Prof. Dr. Peter Schmelcher
Vorsitzende/r der Prüfungskommission:	Prof. Dr. Roman Schnabel
Datum der Disputation:	26.11.2021
Vorsitzender Fach-Promotionsausschusses PHYSIK:	Prof. Dr. Wolfgang Hansen
Leiter des Fachbereichs PHYSIK:	Prof. Dr. Günter H. W. Sigl
Dekan der Fakultät MIN:	Prof. Dr. Heinrich Graener

Abstract

The strong and coherent light fields of ultrashort laser pulses provide a versatile tool to manipulate and probe quantum gases on femtosecond timescales. For instance, they allow to locally ionize an ultracold atomic cloud and thus pave the way towards the creation of hybrid atom-ion quantum systems.

In this work, a new experimental setup combining state of the art techniques from ultracold quantum gases and ultrafast physics is presented. The setup enables absorption imaging of the neutral atoms as well as direct detection of the created electrons and ions with spatial and temporal resolution. Thus, it allows studying fundamental questions regarding the coherence transfer onto the ionization fragments during photoionization as well as the realization of hybrid atom-ion quantum systems and ultracold electron ensembles.

The dynamics of such systems critically depends on the nature of the photoionization processes during creation. Therefore, we have investigated strong-field ionization of ^{87}Rb in the intriguing regime where the Keldysh parameter is close to unity. Absorption imaging of the ultracold atomic gas after photoionization allows extracting the absolute atomic losses in a spatially resolved manner, thus overcoming the focal averaging. The absolute ionization probabilities obtained experimentally are compared to the predicted losses for different ionization models without any free parameter and shows a good agreement with ionization probabilities determined by ab-initio solving the time-dependent Schrödinger equation.

In addition, the strong light field of femtosecond laser pulses leads to an enormous acceleration of a Bose-Einstein condensate (BEC) submitted to large intensity gradients. Depending on the detuning of the fs laser pulse, strong repulsive or attractive dipole forces up to $2 \times 10^{10}\ g$ can be reached. An ultracold matter wave halo with a longitudinal beam temperature of $T_{\mathrm{beam}} = 20(5)$ nK at a tunable beam velocity up to $v_0 = 20$ mm/s has been realized. Even for high intensities, a description of the acceleration by transient optical dipolar forces is found to be accurate when including dissipation by photoionization.

As a central result, the creation of ultracold plasma in a BEC is studied. The large density combined with the low temperature of the BEC give rise to an initially strongly coupled plasma with an initial ionic coupling parameter of $\Gamma_{\mathrm{i}} = 4800$. This new regime leads to an ultrafast cooling of the plasma electrons trapped in the space charge potential of the dense ionic core. The experimental setup grants direct access to the electron temperature that relaxes from 5250 K to below 10 K in less than 500 ns. In addition, plasma dynamics simulations unravel the ultrafast exchange of energy between electrons and ions which yield a cooling rate of 400 K/ps.

Zusammenfassung

Die starken und kohärenten Lichtfelder ultrakurzer Laserpulse sind ein vielseitiges Werkzeug um Quantengase auf der Zeitskala von Femtosekunden zu manipulieren und untersuchen. Sie ermöglichen zum Beispiel die lokale Ionisation ultrakalter Atomwolken und ebnen somit den Weg zur Erzeugung hybrider Atom-Ionen-Quantensysteme.

In dieser Arbeit wird ein neues Experiment präsentiert, das modernste Techniken aus den ultrakalten Gasen und der Ultrakurzzeitphysik verbindet. Der Aufbau ermöglicht Absorptionsabbildung der neutralen Atome sowie einen direkten Nachweis der erzeugten Elektronen und Ionen mit räumlicher und zeitlicher Auflösung. Somit können fundamentale Fragen zum Kohärenztransfer auf die Ionisationsfragmente während der Photoionisation erforscht und hybride Atom-Ionen-Quantensysteme sowie ultrakalte Elektronenensembles realisiert und untersucht werden.

Die Dynamik dieser Systeme hängt empfindlich von der Natur der Photoionizationsprozesse während der Erzeugung ab. Aus diesem Grund wird die Starkfeldionisation von ^{87}Rb in dem komplexen Regime mit einem Keldysh-Parameter nahe eins untersucht. Die Absorptionsabbildung des ultrakalten Gases nach der Photoionisation erlaubt ortsaufgelösten Zugriff auf die absoluten Atomverluste ohne Mittelung über die Fokalebene. Die experimentell erhaltenen absoluten Ionisationswahrscheinlichkeiten werden mit erwarteten Verlusten verschiedener Ionisationsmodelle verglichen und sind in guter Übereinstimmung mit Ionisationswahrscheinlichkeiten, die durch ab-initio-Lösen der zeitabhängigen Schrödingergleichung bestimmt werden.

Darüberhinaus kann das starke Lichtfeld von Femtosekunden-Laserpulsen durch hohe Intensitätsgradienten zu enormen Beschleunigungen eines Bose-Einstein Kondensats (BEC) führen. In Abhängigkeit der Verstimmung des fs Laserpulses, können starke repulsive und attraktive Wechselwirkungen bis zu 2×10^{10} g erreicht werden. Dies ermöglicht die Erzeugung eines Materiewellenhalos mit einer longitudinalen Strahltemperatur von $T_{\mathrm{beam}} = 20(5)$ nK bei einer einstellbaren Strahlgeschwindigkeit von bis zu $v_0 = 20$ mm/s. Es zeigt sich, dass die Beschreibung der Beschleunigung durch optische Dipolkräfte auch für hohe Intensitäten akkurat ist, wenn der Atomverlust durch Photoionisation einbezogen wird.

Als ein zentrales Ergebnis wird die Erzeugung von ultrakaltem Plasma in einem BEC untersucht. Die Kombination aus hoher Dichte und geringer Temperatur der Atome im BEC führt zu einem initial stark gekoppelten Plasma mit einem Kopplungsparameter der Ionen von $\Gamma_{\mathrm{i}} = 4800$. In diesem neuartigen Regime werden die Elektronen im Raumladungspotential des dichten Ionenkerns gefangen und erfahren eine ultraschnelle Kühlung. Der experimentelle Aufbau ermöglicht direkten Zugriff auf die Elektronentemperatur, die in weniger als 500 ns von 5250 K auf 10 K fällt. Zusätzlich geben Simulationen der Plasmadynamik Einblick in den ultraschnellen Energieaustausch zwischen Elektronen und Ionen, der eine Kühlrate von 400 K/ps hervorbringt.

Publications

The following research articles have been published in the course of this thesis.

[1] P. Wessels, B. Ruff, T. Kroker, A. K. Kazansky, N. M. Kabachnik, K. Sengstock, M. Drescher, and J. Simonet, "Absolute strong-field ionization probabilities of ultracold rubidium atoms", *Commun. Phys.*, **1**, 32 (2018).

[2] T. Kroker, M. Großmann, K. Sengstock, M. Drescher, P. Wessels-Staarmann, and J. Simonet, "Ultrafast electron cooling in an expanding ultracold plasma", *Nat. Commun.*, **12**, 596 (2021).

Contents

1. Introduction **1**

1.1. Ultracold atoms in the field of ultrashort laser pulses 1

1.2. Structure of the thesis 4

2. Experimental setup for investigation of hybrid atom-ion quantum systems **7**

2.1. Preparation of ^{87}Rb quantum gases 8

2.1.1. Vacuum system 9

2.1.2. Laser cooling of ^{87}Rb 11

2.1.3. Evaporative cooling in a hybrid trap 14

2.1.4. Optical transport 17

2.1.5. Evaporative cooling in a crossed optical dipole trap 22

2.1.6. Absorption images and data acquisition 23

2.2. Charged particle detection 25

2.2.1. Spatially-resolved electron/ion detection 26

2.2.2. Time-resolved electron detection 29

2.2.3. Electromagnetic stray field control 30

2.3. Femtosecond laser pulses 34

2.3.1. Femtosecond laser system 34

2.3.2. Active beam stabilization 35

2.3.3. Diffraction limited micrometer focus 36

2.3.4. Intensity calibration 37

2.4. Conclusion 39

3. Ultracold atoms in ultrashort laser pulses **41**

3.1. Absolute strong-field ionization probabilities of ultracold ^{87}Rb atoms 41

3.1.1. Basics of strong-field ionization 42

3.1.2. Preparation of ultracold atomic targets 48

3.1.3. Measuring absolute local losses 48

3.1.4. Calculation of photoionized fraction 49

3.1.5. Non-resonant two-photon ionization at 511 nm 52

3.1.6. Resonant multiphoton ionization at 1022 nm 55

3.1.7. Conclusion 58

3.2. Strong-field acceleration of ultracold atoms 59

3.2.1. Gradient forces in strong light fields 59

3.2.2. Femtosecond acceleration of a BEC 61

3.2.3. Femtosecond compression of a BEC 67

3.2.4. Conclusion 70

4. Ultracold plasma triggered by femtosecond laser pulses in a BEC **73**
4.1. Ultracold plasma . . . 74
4.1.1. Plasma regimes and coupling parameter . . . 74
4.1.2. Ultracold microplasma in a BEC . . . 77
4.1.3. Dynamical timescales . . . 78
4.2. Charged particle tracing simulations . . . 81
4.2.1. Initial charge distributions . . . 81
4.2.2. FEM simulation of experimental environment . . . 82
4.2.3. CPT trajectory simulations . . . 83
4.2.4. CPT plasma simulations . . . 84
4.3. Ultrafast electron cooling in an expanding ultracold plasma . . . 87
4.3.1. Direct observation of electron temperatures . . . 87
4.3.2. Formation of ultracold plasma . . . 90
4.3.3. Ultrafast plasma dynamics . . . 92
4.3.4. Plasma lifetime . . . 100
4.4. Ultracold electron sources . . . 106
4.5. Conclusion . . . 110

5. Outlook **111**
5.1. Strongly-coupled ultracold plasma . . . 111
5.2. Hybrid atom-ion systems . . . 113
5.3. Further experimental outlook . . . 114

A. Appendix **I**
A.1. Further contributions to the experimental setup . . . I
A.2. Bake-out of the vacuum chambers . . . II
A.3. Pin configuration of alkali metal dispensers . . . IV
A.4. Radio-Frequency Antenna . . . V
A.5. Magnetic field compensation currents . . . VI
A.6. Fit results focus measurements . . . VII

1. Introduction

1.1. Ultracold atoms in the field of ultrashort laser pulses

Controlled systems of ultracold trapped particles arise great interest as the quantum nature of ultracold particles predominates in the ultralow temperature limit. Quantum degenerate many-body systems are of particular interest as their collective behavior is dominated by the fundamental laws of quantum mechanics.

Based on the work of Satyendra Nath Bose on quantum statistics [3], Albert Einstein predicted in 1924-1925 the macroscopic occupation of the ground state by the atoms of an ideal gas in an external trapping potential at sufficiently low temperatures which leads to the formation of a Bose-Einstein condensate (BEC) [4]. The experimental realization of the first BECs in dilute gases of alkali atoms [5–7] required several technical innovations such as the cooling and trapping with laser light [8–12] as well as magnetic traps for neutral atoms and radiofrequency (RF) forced evaporative cooling [13–16]. The high degree of experimental control over neutral quantum gases includes tuning the interparticle interactions by Feshbach resonances [17] or transitions into Rydberg states with enhanced dipole interactions [18]. In addition, the translational degree of freedom is controllable by light fields of optical lattices produced by interfering laser beams [19, 20] or arrays of optical microtraps [21, 22]. Quantum gases trapped in such tunable potentials can serve as a quantum simulator for interacting many-body systems [23] providing insight to complex systems, which are not tractable by classical calculations, and giving access to unexplored physical parameter regimes [24–26].

The emergence of pulsed laser sources, which provide ultrashort pulses of coherent radiation, paves the way to investigate ultrafast dynamics in microscopic systems and light-matter interaction in high-intensity laser fields [27]. The first pulsed laser sources have been realized by Q-switching of a ruby laser [28]. The development of mode-locked laser sources with femtosecond pulse generation [27] enables pump-probe spectroscopy on the timescale of chemical reactions opening the field of femtochemistry [29, 30]. Further decrease of the pulse duration to the attosecond domain [31] allows for time-resolved studies of electron dynamics in atomic systems [32, 33]. The advent of chirped pulse amplification [34] enabled focal intensities beyond 10^{18} W/cm^2 allowing studies of light-matter interaction in strong laser fields [33, 35–37].

Combining the world of ultracold quantum systems with the toolbox of ultrashort laser pulses allows to exploit the advantages of both worlds (see Fig. 1.1). The coherent light fields allow to initiate and probe dynamics in macroscopic quantum systems on ultrashort timescales by strong-field ionization (see Fig. 1.1a) and non-linear gradient forces in the focal intensity distribution of a pulse (see Fig. 1.1b). Moreover, ultracold clouds provide a versatile ground to study these interactions quantitatively as they benefit from negligible thermal atomic motion, high target control and are accessible by absorption imaging [1]. These studies can provide the basis for a controlled preparation of ultracold matter waves and hybrid atom-ion systems, where the subsequent dynamics sensitively depends on the nature of these interactions.

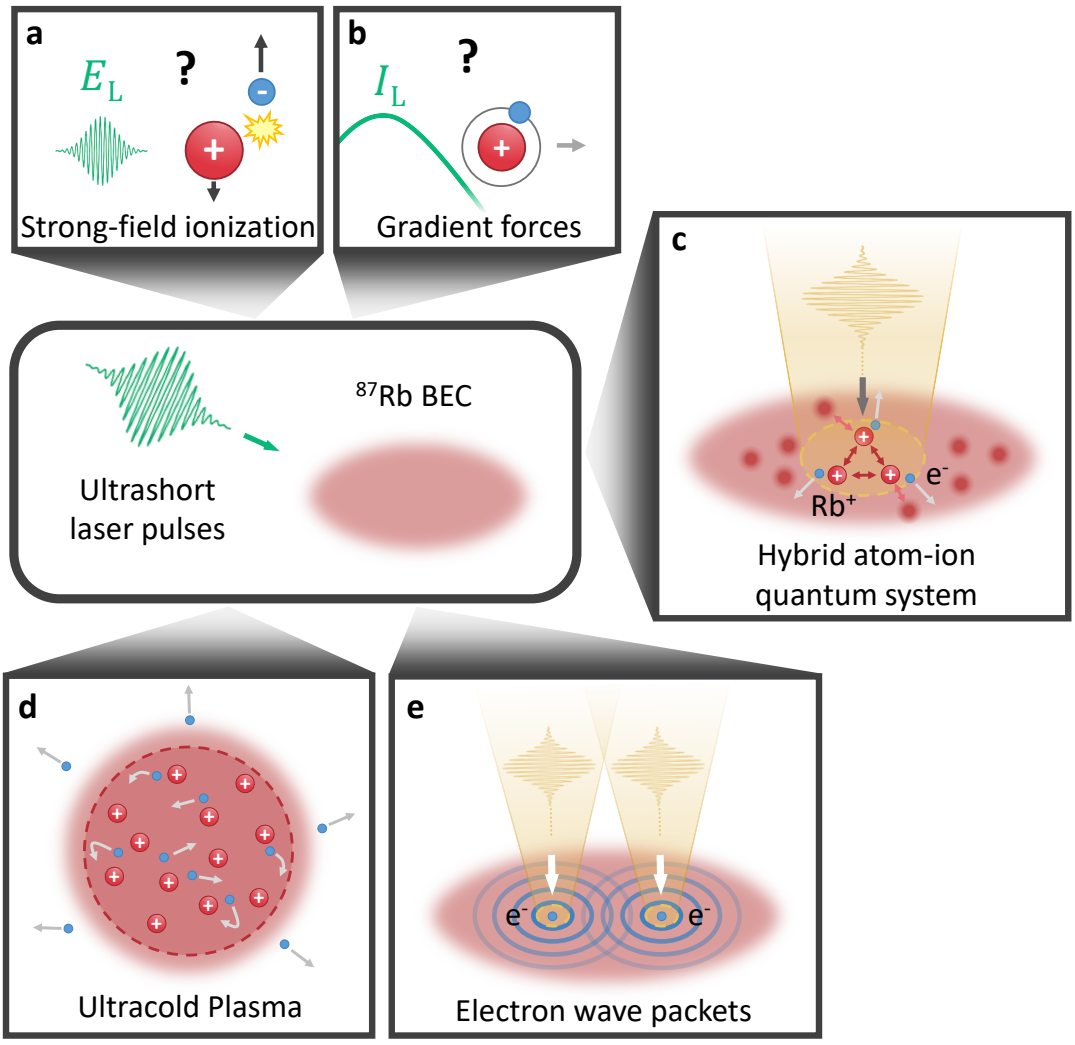

Figure 1.1: Ultracold atoms in strong light fields of ultrashort laser pulses. The local interaction of atoms in a BEC with femtosecond laser pulses enables fundamental studies linking several areas of modern physics. The experimental setup presented in this thesis combines absorption imaging of the neutral atoms with position- and time-sensitive detection of charged particles. **a.-b.** Ultracold atoms provide a well-controlled ground to quantitatively investigate strong-field ionization and non-linear gradient forces on alkali atoms. **c.** Local ionization of a BEC allows to instantaneously create hybrid quantum systems of few ions immersed in a BEC. **d.** Many ionized atoms form an ultracold plasma at BEC densities. **e.** Two ultracold electron wave packets are created by two ultrashort laser pulses in adjacent focii in a BEC. The interference patterns of the expanding matter waves on the charged particle detectors probe spatial coherence. A time delay between the pulses gives access to temporal coherence properties.

Historically, trapping of single ions was experimentally realized even before the neutral atoms [38, 39]. Ion traps are typically formed by a combination of static electric and magnetic fields in Penning traps [40] or radiofrequency electric quadrupole fields in a Paul trap [41]. The combination with laser cooling [42, 43] enables creation of ionic quantum systems with long-range Coulomb interactions [44] and high degree of control over the external and internal degrees of freedom. Such systems serve as optical frequency standards [45], quantum simulators for many-body systems [46, 47] and give rise to quantum information processing platforms [48–50].

When few cold ions are immersed in an ensemble of ultracold atoms, hybrid atom-ion quantum systems are created [51–53], which allow studying cold atom-ion collisions [54–56], impurity physics leading to the emergence of mesoscopic polaron and molecular states [57–61] as well as cold chemistry [62]. Moreover, such systems constitute a model platform for quantum information processing [63, 64]. The experimental realization is typically achieved by spatially overlapping cold ions trapped in a linear Paul trap with optically [65] or magnetically trapped ultracold atomic clouds [66]. However, the minimum ion-atom collision energy is limited to the millikelvin regime by the micromotion of the ion in the RF electric field of the Paul trap [67], ruling out reaching the quantum regime of atom-ion scattering. Recent work approaches the quantum regime by additional buffer gas cooling of ytterbium ions in an ultracold cloud of lithium atoms [68] and atom-ion Feshbach resonances were observed between single barium ions and ultracold lithium atoms [69]. Another approach is given by optical trapping of ions in high power dipole traps has been demonstrated [70–72] or exciting to Rydberg states with high principal quantum number where the electron orbit is mainly located outside the atomic cloud and the ionic core remains as impurity at submicrokelvin temperatures [73]. Furthermore, photoionization of long-range Rydberg molecules can serve as a trigger for ultracold atom-ion scattering [55] or field ionization of Rydberg atoms [60]. This enables transport studies of ion impurities in a BEC, which can be sensed by the ion-induced Rydberg blockade on a second, highly excited Rydberg atom [74].

In this work, a quantum gas experiment is set up targeting quantum system consisting of atoms, ions and electrons by accessing the position and momentum of the neutral atoms as well as the kinetic energy and arrival time of the charged ions and electrons on opposite detectors. Local photoionization of a ^{87}Rb BEC with single ultrashort pulses allows to create a tunable number of ions on instantaneous timescales compared to the atomic and charged particle motion.

By tuning the photon energy, the temperature of the created ions can be controlled down to the millikelvin limit, comparable to typical temperatures achieved in Paul traps. This may provide an alternative route towards the creation of a hybrid quantum system (Fig. 1.1c). Whereas the RF ion traps inherently involve a continuous energy input to the hybrid system, here, the ion is immersed in the quantum gas without any driving external electromagnetic fields facilitating buffer gas cooling in the ultracold atomic cloud. The experimental setup allows to study transport properties of the ionic impurities as well as polaron and molecule formation.

In addition, photoionization of a BEC with femtosecond laser pulses allows for the investigation of strongly coupled many-body systems of charged particles. When a critical number of atoms is ionized, ultracold plasma can be created [75] (see Fig. 1.1d). Ultracold neutral plasma created from atomic clouds trapped in magneto-optical traps have been intensively studied [76–78] and approaches the regime of strong coupling, where the interparticle Coulomb interaction prevails the thermal energy of the charge carriers. As well-controlled model systems, they provide insight in extreme plasma conditions as given in inertial confinement fusion [79] and astronomical plasmas as the core of Jovian planets and white dwarfs [80]. Recent works access

the strong coupling regime by laser cooling of the ions [81] and vastly increase the evolution times by magnetic confinement [82].

Creation of ultracold plasma from a BEC enables orders of magnitude higher plasma densities, which implicates higher initial coupling parameters and ultrafast dynamics in the plasma. In addition, the BEC densities allow for creation of micrometer-sized plasma with only hundreds to thousands of charge carriers facilitating theoretical description with a full molecular dynamics approach. These small systems bridge ultracold plasmas with the field of ionized nanoclusters [83–85], which give rise to the formation of nanoplasmas [86–88]. Creating ultracold plasma by photoionization of a BEC loaded into an optical lattice enables tunable initial spatial correlation and allows to circumvent disorder-induced heating, which limits the achievable coupling strengths in laboratory plasma realizations [77, 89]. Utilizing broadband ultrashort laser pulses close to the ionization threshold enables ultrafast creation of Rydberg gases [90], which convert into ultracold plasma and vice versa due to avalanche ionization and three-body recombination, respectively [91–93].

Finally, the experiment is also designed to investigate coherence transfer from the bosonic neutral atoms to its fermionic constituents during photoionization. For this purpose, two atoms shall be ionized in adjacent focii creating two cold electron wave-packets (see Fig. 1.1e). The matter-wave interference pattern is measured with spatial and temporal resolution by the charged particle detectors giving access to the coherence properties. A tunable time-delay between the ionizing pulses allows to address the speed limits of information transfer in quantum systems [94, 95].

In conclusion, the novel experimental setup presented in this work enables ultrafast manipulation and probing of macroscopic quantum systems providing access to so far inaccessible observables. Thus, it allows addressing a variety of intriguing questions at the intersection of ultracold quantum gases and ultrafast physics.

1.2. Structure of the thesis

This work is partitioned in three main chapters. The first chapter (Chap. 2) introduces the novel quantum gas machine, which was built in the course of this thesis and enables photoionization of ultracold ^{87}Rb atoms as well as direct detection of the created charged particles. The second part (Chap. 3) presents the experimental results of the investigation of strong-field ionization and gradient forces in the light field of ultrashort laser pulses. In the last part (Chap. 4) ultracold plasma creation in a ^{87}Rb BEC is presented and studied. The subsequent outlook (Chap. 5) describes the accessible future directions of this experiment.

Chapter 2

Within this chapter, the experimental setup is presented, which was built during this thesis.

First, the quantum gas machine is introduced, which enables the creation of ^{87}Rb BEC held in a crossed optical dipole trap. Here, the employed cooling mechanisms and the optical transport are explained. Second, the charged particle detection setup is described, which enables electron/ion detection with spatial and temporal resolution. Last, the femtosecond laser setup is addressed, which provides ultrashort laser pulses with variable wavelength focused to a micrometer sized volume within the atomic cloud.

Chapter 3

This chapter presents the experimental investigation of the response of ultracold atoms exposed to femtosecond laser pulses. In the first part, strong-field photoionization of ^{87}Rb atoms is studied. After an introduction of the basic concepts of photoionization in strong laser fields, the experimental method is explained, which enables accurate extraction of absolute ionization probabilities by absorption imaging of the ultracold atomic target. Subsequently, the obtained results for non-resonant and resonance-enhanced photoionization are presented and compared to theoretically predicted ionization rates. In the second part, the gradient forces exerted by the inhomogeneous light field of the laser pulses are investigated. Here, the ultrafast momentum transfer by repulsive and attractive pulses focused into a BEC is shown and the suitability for ultracold atom sources and pulsed dipole traps is discussed.

Chapter 4

In this chapter, the creation of ultracold microplasma in a BEC by photoionization with femtosecond laser pulses is presented. A short introduction of the defining parameters of plasma is followed by the experimental creation of ultracold plasma in a BEC. Second, the charged particle tracing simulations are described, which allow to access the microplasma dynamics on a single particle level. In the third part, the experimental and simulation results are presented, which disclose efficient electron cooling occurring on ultrafast timescales. Finally, the suitability of ultracold microplasma as a source for ultracold electrons is discussed.

Chapter 5

This chapter gives an outlook on the future investigations, which were made accessible with the built experimental setup. Here, the route towards creation of strongly-coupled ultracold plasma is discussed as well as future experiments with hybrid atom-ion quantum systems created by photoionization.

2. Experimental setup for investigation of hybrid atom-ion quantum systems

Photoionization of ultracold quantum gases with ultrashort laser pulses provides a pathway to the instantaneous creation of hybrid systems of ultracold atoms and ions and allows to trigger plasma formation with ultralow initial temperatures. Tailored experiments enabling detection of electrons and ions as well as the neutral atomic cloud provide direct access to the dynamics of such hybrid systems. In this chapter the experimental apparatus is presented, which allows for local photoionization of a ^{87}Rb BEC with femtosecond laser pulses and provides a spatially resolved charged particle detection as well as absorption imaging of the neutral atoms. In Section 2.1 the basic concepts of cooling and trapping of neutral atoms are examined and the quantum gas machine as well as its mode of operation is presented. Section 2.2 focuses on the charged particle detection setup, which allows for electron/ion detection with spatial resolution. In addition, a gated electron detection scheme is presented, which enables time-resolved electron detection. The chapter concludes with Section 2.3, which describes the femtosecond laser pulse generation within the dedicated laser system as well as the beam transport to the experiment and the realization of a local ionization region within the BEC.

The described experiment has been set up during this PhD thesis. Previous descriptions of the design of the experiment can be found in the PhD thesis of Bernhard Ruff [95] and at an early stage of the experiment within the master thesis of Jakob Butlewski [96]. The experimental setup has been designed and setup by Juliette Simonet, Philipp Wessels-Staarmann, Bernhard Ruff and the author. In addition, central elements have been designed and setup in the frame of several diploma theses [97–99], master theses [96, 100–102] and bachelor theses [103–109]. A more detailed list can be found in Sec. A.1.

The data analysis infrastructure used for the absorption images was originally developed by Sören Dörscher and adapted for this experiment by Bernhard Ruff, Philipp Wessels-Staarmann, Mario Großmann and the author. The analysis framework for the charged particle detection data was developed by Mario Großmann and the author.

2.1. Preparation of ^{87}Rb quantum gases

In an ideal gas, the mean kinetic energy of the atoms is directly related to the temperature T_a via $\left\langle p_a^2 \right\rangle / 2m_a = \frac{3}{2} k_B T_a$. Whereas hot and dilute gases can be described classically, a quantum mechanical description is imperative when the de Broglie wavelength of the atoms $\lambda_{dB,a} = h/p_a$ exceeds the mean interparticle distance and the matter wave packets start to overlap. When the phase-space density determined by the atomic density ρ_a and the de Broglie wavelength exceeds a critical value of $\rho_{PSD,a} = \rho_a \times \lambda_{dB,a}^3 \geq 2.612$, Bose-Einstein condensation occurs. In order to reach this phase of matter experimentally, dilute atomic ensembles need to be cooled to the nanokelvin domain.

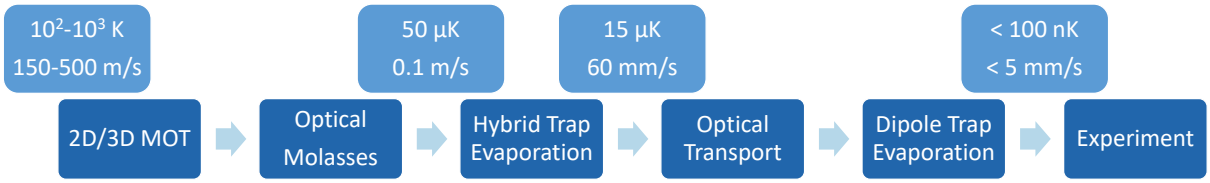

Figure 2.1: Quantum Gas Preparation Cycle. Cooling stages to produce a Bose-Einstein condensate of ^{87}Rb in the experimental setup. The corresponding atomic temperature and thermal velocities at different stages determined by the mean kinetic energy are given.

In this experiment, the preparation of ultracold ^{87}Rb quantum gases involves several cooling stages, which is schematically illustrated in Fig. 2.1 and discussed in the following section. To avoid collisions with the background gas leading to atomic losses, the different cooling stages are executed under ultra high vacuum conditions (see Sec. 2.1.1). In the first vacuum chamber the atoms are laser cooled from a few hundred Kelvin to 50 µK in a magneto-optical trap during 10 s and in a bright optical molasses during 450 ms (see Sec. 2.1.2). Subsequently, the atoms are transferred into a hybrid trap constituted of a magnetic quadrupole trap and an optical dipole trap and further cooled by RF forced evaporation cooling down to 15 µK within 8 s (see Sec. 2.1.3). Afterwards, the atoms are transported into a second vacuum chamber in optical tweezers in 1.7 s (see Sec. 2.1.4), where the atoms are evaporatively cooled to quantum degeneracy in a crossed optical dipole trap within 3 s (see Sec. 2.1.5). In total, the experimental cycle lasts 30 s. During this cycle, the thermal velocities of the atomic sample are gradually lowered from a few hundred meters per second to a few millimeters per second.

2.1.1. Vacuum system

Cooling an atomic ensemble to nanokelvin temperatures requires optimal isolation from the environment to prevent both heating and atomic losses. Whereas the atoms are basically transparent for heat radiation due to their narrow absorption spectrum, collisions with the background gas are the limiting factor for quantum gas lifetimes. Consequently, quantum gas experiments are typically carried out under ultra-high vacuum (UHV) conditions at pressures below 1×10^{-11} mbar. Figure 2.2 depicts a computer-aided design (CAD) model of the novel vacuum system, which was set up within this work.

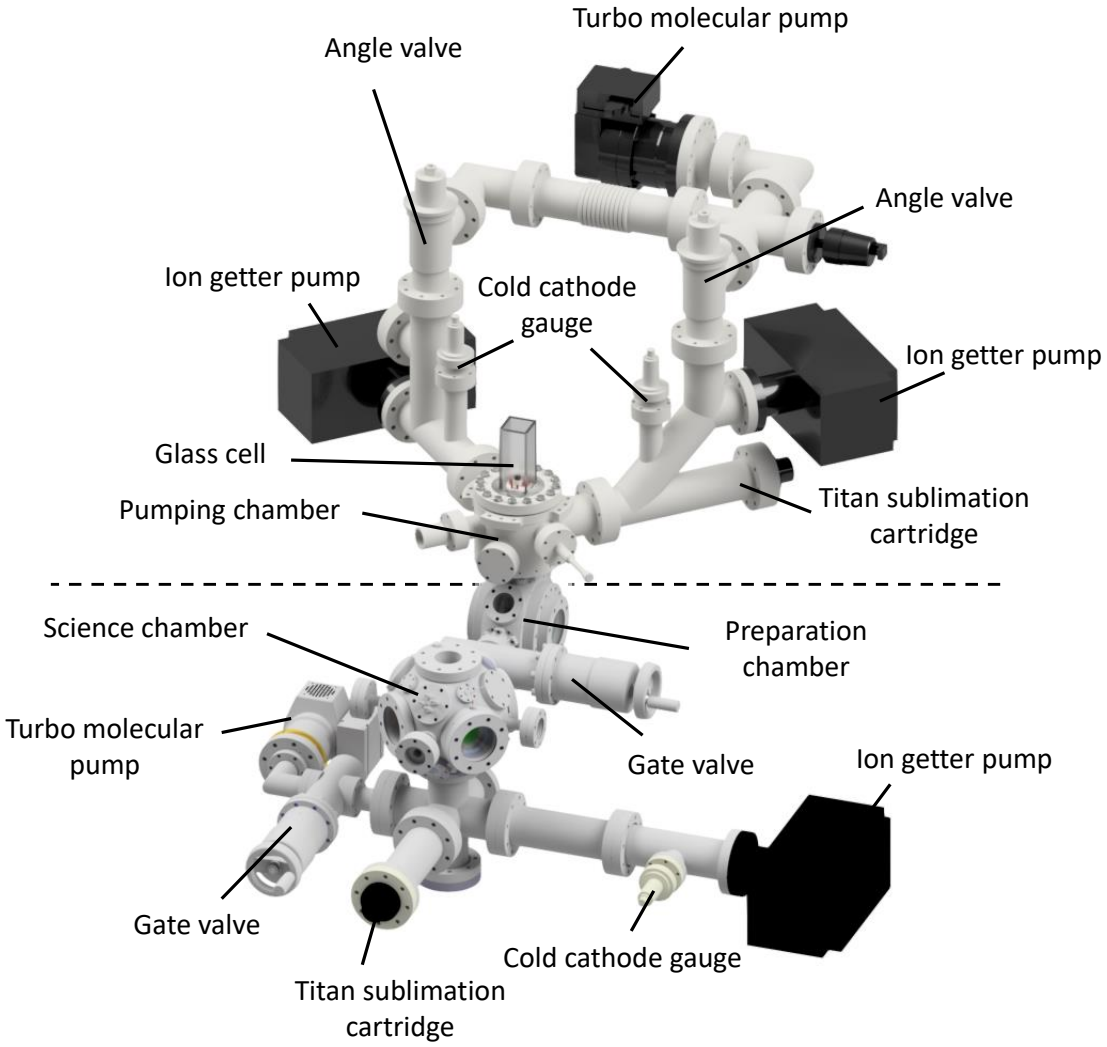

Figure 2.2: Vacuum System. CAD model of the vacuum system of the quantum gas experiment. A differential pumping stage connects the glass cell at a pressure of 10^{-9} mbar to the Preparation chamber and Science chamber at a base pressure below 10^{-11} mbar.

As the experiment is designed for investigation of atom-ion quantum systems and the creation of low energy photoelectrons, minimizing magnetic stray fields is essential. Accordingly, the vacuum system is composed of two main parts, the Preparation and the Science chamber, which

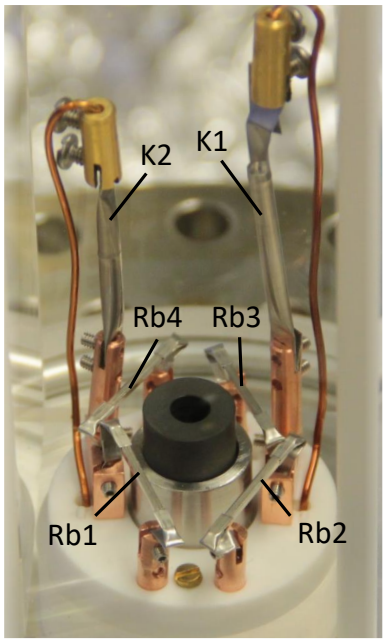

Figure 2.3: Dispenser Configuration. The 2D glass cell is equipped with four rubidium (Rb 1-4) and two potassium (K 1-2) dispensers mounted around the differential pumping tube. A MACOR glass ceramic mounting isolates the different electrodes.

are connected by a gate valve enabling independent evacuation. This allows to spatially separate the cooling techniques and vacuum devices which are based on strong magnetic fields from the ionization region. In addition, the vacuum system is built from stainless steel components with low magnetic susceptibility.

The Preparation chamber, where the 3D-MOT and hybrid trap are located, is attached to the pumping chamber, which connects it with the 2D-MOT glass cell over a differential pumping stage, a thin tube of graphite which enables a difference in the pressure of three orders of magnitude. Furthermore, the pumping chamber connects both the glass cell and the Preparation chamber to a pumping stage equipped with an ion getter pump (IGP) and a turbo molecular pump (TMP), which is connected over a valve. For the Preparation chamber, the pump stage is additionally supported by a titanium sublimation cartridge.

The second vacuum part consists of the Science chamber, which is connected to a pumping stage containing a turbo molecular pump connected by a gate valve, an ion getter pump as well as a titanium sublimation cartridge. Cold cathode gauges in front of each ion getter pump allow to simultaneously measure the pressure in the glass cell, the Preparation chamber as well as the Science chamber. For reaching a base pressure below 1×10^{-11} mbar in the Preparation and Science chamber, both parts of the vacuum system were baked-out separately. The procedure, which has taken two to three weeks per chamber, is described in Section A.2. After the successful evacuation of both chambers the valve gate was opened.

The alkali atoms used in this experiment are evaporated from alkali metal dispensers. These dispensers consist of small metal boats containing the alkaline atoms bound as an alkali-metal chromate with a reducing agent. The mildly exothermic reduction reaction leading to alkali metal evaporation is thermally activated and can therefore be controlled by the electric current supply though the metal tubes and thus the resistive heating. The actual setup in principle features experiments with two alkali species as the vacuum system is equipped with four rubid-

ium dispensers[1] as well as two potassium dispensers enriched with fermionic ^{40}K[23]. Whereas the rubidium dispensers are horizontally arranged around the graphite tube of the differential pumping stage, the potassium dispensers are mounted in upright position (see Fig. 2.3). The different electrical potentials are isolated by a MACOR glass ceramic mounting, which ensures separation of the connecting wires from the electrical vacuum feed-throughs (see Sec. A.3 for the pin assignment).

2.1.2. Laser cooling of ^{87}Rb

Laser cooling relies on the absorption and re-emission of near-resonant photons. Whereas the atomic internal degrees of freedom can absorb both the energy $\hbar\omega_\mathrm{L}$ and the angular momentum of the photon, the linear momentum $\vec{p}_\mathrm{L} = \hbar\vec{k}_\mathrm{L}$ causes a change in the center of mass motion of the atom [110]. As the subsequent re-emission occurs isotropically and hence averages out over a multitude of absorption-emission cycles, a laser beam of directed photons can exert a force $\vec{F} = d\vec{p}/dt = \hbar\vec{k}\gamma_\mathrm{p}$, the so-called spontaneous force, onto an atom. The force is proportional to the scattering rate

$$\gamma_\mathrm{p} = \frac{s_0\gamma/2}{1 + s_0 + \left[2\left(\delta + \omega_\mathrm{D}\right)/\gamma\right]^2}, \tag{2.1}$$

where $s_0 = I/I_\mathrm{s}$ denotes the ratio between the laser intensity I and the saturation intensity I_s [110], which is 1.67 mW for the D^2 line in ^{87}Rb from the electronic ground state $5^2S_{1/2}$ to the first excited state $5^2P_{3/2}$ with a decay rate of $\gamma = 2\pi \times 6.065$ MHz [111].

The rate of excitations and thus the force on the atoms depends on the detuning of the laser $\delta = \omega_\mathrm{L} - \omega_\mathrm{A}$ relative to the atomic resonance with frequency ω_A. Due to the Doppler shift $\omega_\mathrm{D} = -\vec{k}_\mathrm{L} \cdot \vec{v}_\mathrm{A}$, the resonance condition and consequently the force is dependent on the velocity $\vec{v}_\mathrm{A}$ relative to the laser propagation direction. For Doppler cooling, a red-detuned light field ($\delta < 0$) is used, which is shifted towards resonance, when atoms are moving towards the laser beam and the light field selectively decelerates the atoms. By using a pair of counter-propagating red-detuned laser beams for each dimension, an atomic ensemble experiences a viscous damping force in all directions and thus is cooled in a so-called optical molasses.

For the laser cooling, the D_2 transition of ^{87}Rb between the electronic ground state $5^2S_{1/2}$ and the first excited state $5^2P_{3/2}$ is employed. Figure 2.4 depicts the hyperfine structure of the involved levels. The cooling laser drives the transition from the $|5^2S_{1/2}, F = 2\rangle$ substate to the $|5^2P_{3/2}, F' = 3\rangle$ state. As a small fraction of atoms undergoes a transition to the $|5^2S_{1/2}, F = 1\rangle$ ground state, which is not resonant for the cooling laser, a second laser frequency is used to repump the atoms back into the cooling cycle via the $|5^2P_{3/2}, F' = 2\rangle$ hyperfine state.

The achievable kinetic energies are limited by the randomness of the absorption and re-emission process to the energy corresponding to the natural linewidth of the cooling transi-

[1] SAES Getters - Rb/NF/4.8/17/FT 10 + 10
[2] AlfaVakuo - AS-K40(5%)-10-3F
[3] Alvasource - AS-K40(8.4%)-15-3S

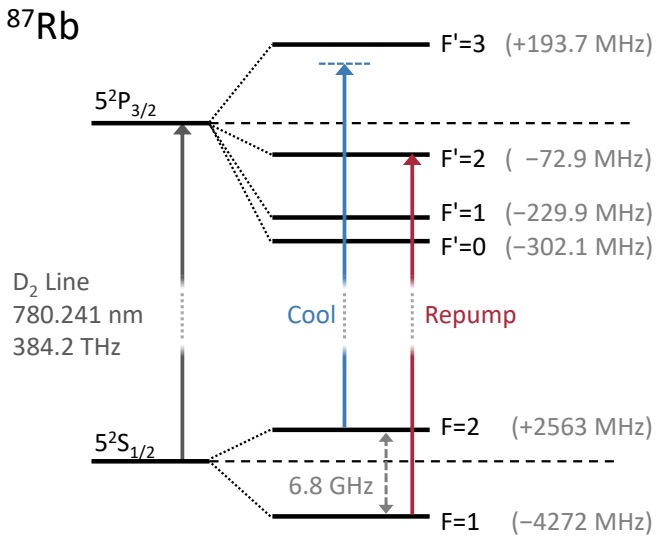

Figure 2.4: D_2 line of ^{87}Rb. Hyperfine structure of the D_2 transition of ^{87}Rb. The cooling laser is red-detuned with respect to the transition from the $F = 2$ to the $F' = 3$ hyperfine state and the repumping laser resonantly drives the transition from $F = 1$ to $F' = 2$. Data taken from [111].

tion [110, 112]. The associated Doppler limit is given by $k_B T_D = \frac{\hbar\Gamma}{2}$ with a Doppler temperature of $T_D = 141.5\,\mu K$ for the D_2 line in ^{87}Rb. However, already in 1988 it was reported, that optical molasses allows cooling beyond the Doppler limit [11], which can be explained by Sisyphus cooling in the polarization gradient formed by the counter-propagating beams [12, 113]. Laser cooling with absorption and re-emission of photons exhibits a fundamental lower limit, as the atomic momentum can only be changed in units of the photon recoil. The recoil limit given by $k_B T_{rec} = \frac{\hbar^2 k^2}{m_a}$ determines the lowest temperature for processes based on resonant absorption [110]. For the D_2 transition in ^{87}Rb the recoil temperature is given by $T_{rec} = 362$ nK [111].

Laser System

The cooling laser system was built by Marlene Fricke [97] and rebuilt during the authors master thesis [101]. A scheme of the setup is given in Fig. 2.5. It consists of two commercial diode lasers[4], which are frequency stabilized using saturated absorption spectroscopy [97], resonant with the cooling and repumping transition respectively. The cooling laser light is split into two paths supplying the 2D- and 3D-MOT and subsequently amplified by two tapered amplifiers (TA) providing an output power of 1.5 W. For both the cooling and the repumping light, deflection by acousto-optic modulators (AOM) allows to control the laser intensity as well as detuning of the frequency relative to the atomic transitions. Finally, the laser light is distributed onto different optical fibers, which transfer the laser light for the 2D-MOT, 3D-MOT and pushing beam as well as absorption imaging in both vacuum chambers to the experimental setup. Whereas the cooling and repumping beams used in the 2D-MOT are already superimposed on the optical table and are coupled into the same optical fiber, the 3D-MOT beams are superimposed in a fiber

[4] TOPTICA, DL Pro 100

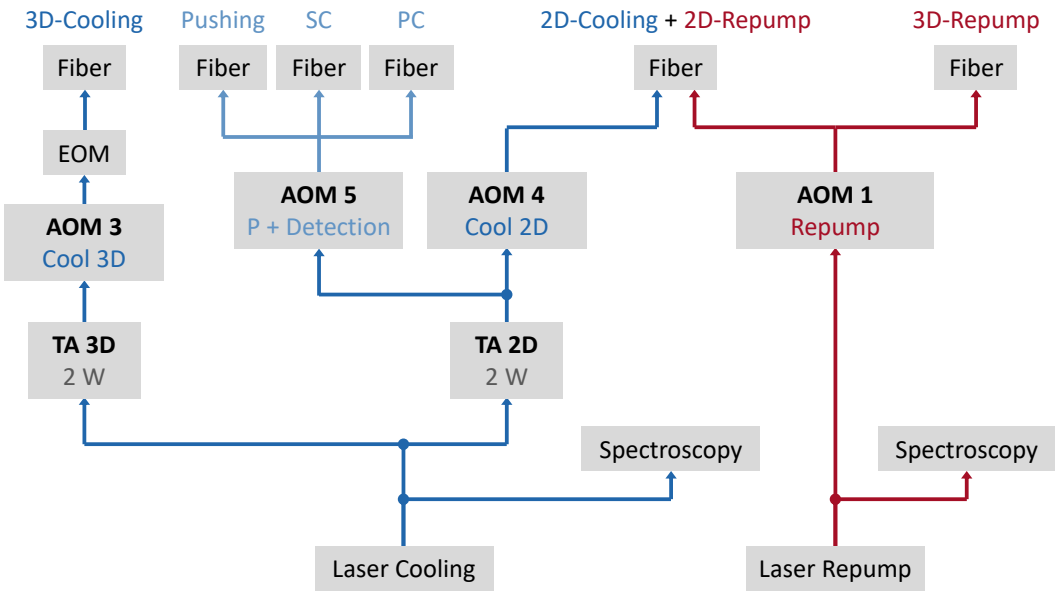

Figure 2.5: Cooling Laser System. Schematic view of the laser system used for laser cooling of ^{87}Rb. Two laser diodes are frequency-stabilized using saturated absorption spectroscopy. Tapered amplifiers (TA) are used for amplification. The laser frequency and intensity is dynamically controlled by acousto-optic modulators (AOM) and an electro-optic modulator (EOM). The laser light is transported to the experimental setup with optical fibers.

port cluster[5], which distributes both the cooling and repumping light equally to all six MOT beams. In addition, an electro-optic modulator (EOM) is used to precisely control the 3D-MOT cooling intensity during the optical molasses.

2D-3D-MOT Setup

In order to additionally trap the laser-cooled neutral atoms, a magnetic quadrupole field is employed, which causes a position-dependent Zeemann shift (see Eq. 2.3) of the atomic magnetic levels. This results in a position-dependent spontaneous force, as the opposed laser becomes resonant when atoms drift away from the trap center. This enables simultaneous trapping and cooling of the atomic sample in a magneto-optical trap (MOT) [9].

Two different MOT setups are implemented for the first stage of atom cooling. A 2D-MOT serves as high-flux atom source [114] for efficient loading of the 3D-MOT. Figure 2.6a shows the side view on the 2D-3D-MOT loading beam path. The 2D-MOT is formed by two perpendicular pairs of counter-propagating elongated elliptical beams. The resonant pushing beam transfers the trapped atoms into the 3D-MOT, which consists of three perpendicular pairs of counter-propagating beams. The expanded beams are provided by fiber telescopes. The Helmholtz coils provide the 3D magnetic gradient field used for the MOT as well as the hybrid trap (see Sec. 2.1.3).

Figure 2.6b shows a CAD model of the optical setup at the Preparation chamber. The MOT

[5] Schäfter+Kirchhoff GmbH.

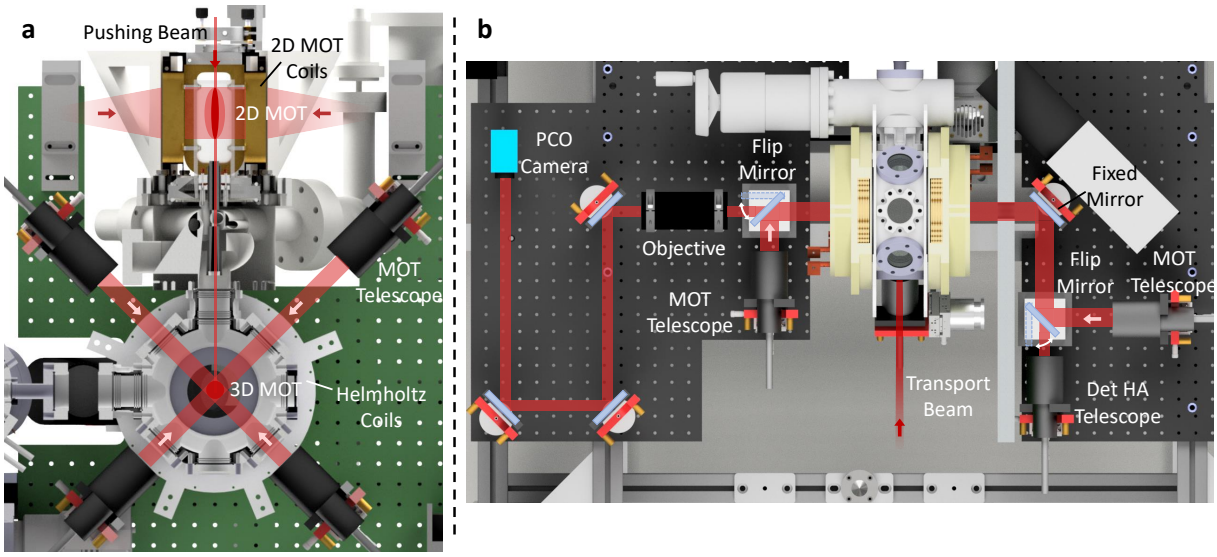

Figure 2.6: CAD model of the Preparation chamber optics setup. a. Side view. The 2D-MOT traps and cools atoms from the ^{87}Rb background gas, which are transferred to the 3D-MOT in the Preparation Chamber by a resonant pushing beam. **b.** Top view. The horizontal MOT beams are superimposed with the beam for absorption imaging by two flip mirrors.

beams on the magnetic coils symmetry axis are provided by two fiber telescopes and superimposed with the detection beam by two mirrors mounted on motorized flip mirror holders[6]. This enables absorption imaging of the atoms in the hybrid trap. The imaging objective was designed within the bachelor thesis of Jette Heyer and provides a magnification of $M = 2.73(6)$ and a spatial resolution of 5.5 µm [108].

After ten seconds of MOT loading, the magnetic field is switched off and the atoms are further cooled while expanding in a bright optical molasses for 450 ms. After the molasses phase we obtain $N_\mathrm{a} = 1.6(4) \times 10^9$ atoms at a temperature of $T_\mathrm{a} = 47(1)$ µK, which corresponds to a phase-space density of $\rho_{\mathrm{PSD,a}} = 1.3(3) \times 10^{-6}$ [115].

2.1.3. Evaporative cooling in a hybrid trap

Magnetic quadrupole trap

After bright molasses cooling, the atomic cloud can be transferred into the magnetic trap, which is formed by a magnetic quadrupole field $\vec{B}(\vec{r})$. The potential energy of the neutral atoms in the magnetic field is given by the Zeemann energy

$$U_\mathrm{mag}(\vec{r}) = -\vec{\mu} \cdot \vec{B}(\vec{r}), \tag{2.2}$$

where $\vec{\mu} = g_\mathrm{F}\mu_\mathrm{B}\vec{F}/\hbar$ denotes the magnetic dipole moment of the atom with the Bohr magneton μ_B and the Landé factor $g_\mathrm{F} = 1/2$. The magnetic moment is determined by the total angular momentum $\vec{F} = \vec{S} + \vec{L} + \vec{I}$ composed of the electron spin $|\vec{S}| = 1/2$, the orbital angular momen-

[6] OWIS, Motorized Flip Mirror Holders KSHM 90

tum $|\vec{L}| = 0$ and the nuclear spin $|\vec{S}| = 3/2$. As the atoms are prepared in the $F = 2$ ground state, the Zeemann energy is given by

$$U_{\mathrm{mag}}(\vec{r}) = -\mu_{\mathrm{B}} g_{\mathrm{F}} m_{\mathrm{F}} B(\vec{r}), \tag{2.3}$$

with the magnetic quantum number $m_{\mathrm{F}} \in \{0; \pm 1; \pm 2\}$ assigning the projection of the total angular momentum onto the magnetic field. In the $F = 2$ hyperfine manifold, atoms with $m_{\mathrm{F}} > 0$ can be trapped in the Zeemann potential, atoms with $m_{\mathrm{F}} \leq 0$ experience either zero or even a repulsive potential and hence are not trapped.

The coils producing the magnetic quadrupole field have been designed during the master thesis of Harry Krüger [100] and characterized within the master thesis of Jakob Butlewski [96]. The coils provide a magnetic gradient of 1.516(8) G/(A cm) along their symmetry axis as well as a radial gradient of 0.79(2) G/(A cm). The magnetic trap is operated with a current of 115 A provided by two power supplies[7] connected in series yielding an axial/radial magnetic gradient of 174.3(2) G/cm and 91(2) G/cm. To ensure a maximal transfer efficiency, this current is rapidly switched on by insulated-gate bipolar transistors (IGBT)[8], which allow for a switching time of 240 µs [96].

Hybrid trap

Trapping in magnetic fields relies on the magnetic moment of the atom adiabatically following the magnetic field direction on the atoms trajectory through the trap, i.e. if the magnetic field direction changes slowly compared to the Larmor frequency of the magnetic moment precessing around the magnetic field $\omega_{\mathrm{Larmor}} = g_{\mathrm{F}} m_{\mathrm{F}} \mu_{\mathrm{B}} B/\hbar$ [116]. The magnetic quadrupole field vanishes the center. As a result, the magnetic quantum number can flip in the absence of a magnetic field and the quadrupole trap suffers from Majorana losses [117]. To circumvent this loss channel, in Ioffe-Pritchard magnetic traps [13] an uniform offset field is employed. In contrast, the hybrid trap utilizes an additional optical dipole trap beam, which shifts the trapping potential minimum away from the magnetic field zero [5, 118].

The electric field $\vec{E}_{\mathrm{L}}$ of an intense laser is able to induce an electric dipole moment $\vec{p} = \alpha \vec{E}_{\mathrm{L}}$ proportional to its magnitude and the polarizability α of the atomic internal state. The interaction of the induced dipole moment with the driving electric field of the laser yields a potential energy of $U_{\mathrm{dip}} = -\frac{1}{2}\vec{p} \cdot \vec{E}_{\mathrm{L}} = -\frac{1}{2\varepsilon_0 c} Re(\alpha) I$, which can be calculated for the electronic ground state of ^{87}Rb with respect to the atomic transitions ω_1 and ω_2 and natural widths Γ_1 and Γ_2 of the D_1 and D_2 lines [119]

[7] DELTA Electronica, SM45 - 140
[8] Mitsubishi Electric - CM200DX-24S

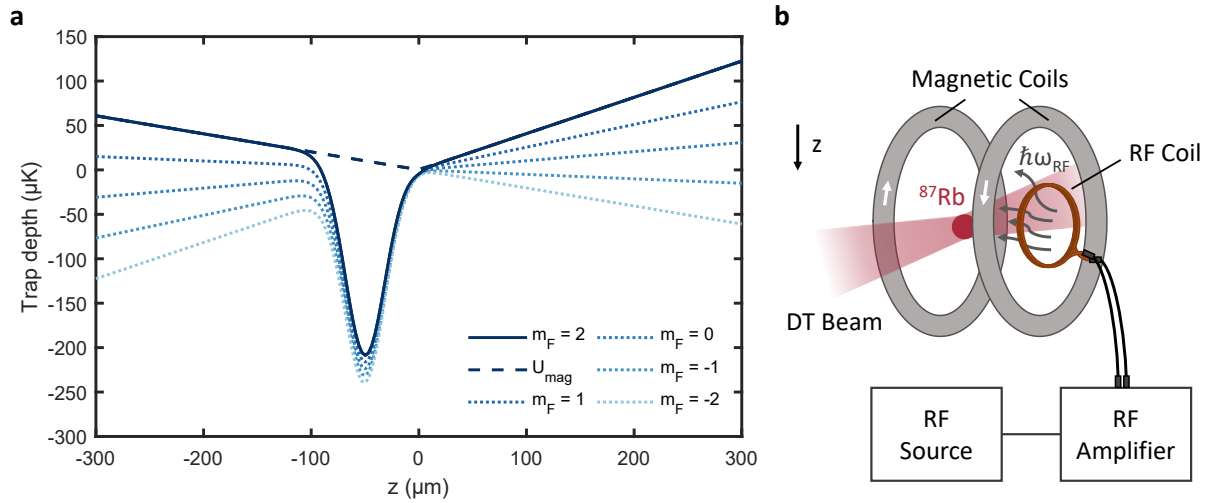

Figure 2.7: Forced radiofrequency evaporation in a hybrid trap. a. Potential energies of the m_F substates of the $|5^2S_{1/2}, F = 2\rangle$ ground state in dependency on their position relative to the trap center in the hybrid trap (solid/dotted blue lines) and for $m_F = 2$ in the magnetic trap (dashed blue line). The energies are calculated for a current of 115 A as well as a dipole trap beam waist of $w_1 = 37$ μm, 3.1 W beam power and 50 μm displacement. **b.** The ultracold atoms are trapped in the combination of a magnetic quadrupole trap and a dipole trap beam. A small copper coil serves as RF antenna. The RF signal is provided by a direct digital signal synthesizer (source) and amplified by a high power amplifier.

$$U_{\mathrm{dip}}(\vec{r}) = -\frac{\pi c^2}{2} \times \left[\frac{1}{\omega_1^3} \left(\frac{\Gamma_1}{\omega_1 - \omega_L} + \frac{\Gamma_1}{\omega_1 + \omega_L} \right) + \frac{1}{\omega_2^3} \left(\frac{\Gamma_2}{\omega_2 - \omega_L} + \frac{\Gamma_2}{\omega_2 + \omega_L} \right) \right] \times I(\vec{r}), \quad (2.4)$$

where ω_L denotes the angular frequency of the laser. In the rotating-wave approximation, which assumes $|\omega_{1/2} - \omega_L| \ll |\omega_{1/2} + \omega_L|$, the dipole potential is proportional to $I(\vec{r})/\delta$. A focused red-detuned laser beam thus produces a trapping potential for the atom yielding a restoring dipolar force $F_{\mathrm{dip}} \propto -\vec{\nabla} \cdot I(\vec{r})/\delta$. As the photon scattering rate is proportional to $I(\vec{r})/\delta^2$, optical dipole traps utilize far-detuned light at high intensities to reduce resonant excitations [119].

The DT beam is focused to a waist of $w_1 \approx 37$ μm perpendicular to the magnetic coil symmetry axis and aligned with a displacement of 50-100 μm with respect to the magnetic trap zero in z direction. The fiber telescope used for the hybrid trap dipole beam is described in Sec. 2.1.4. The relative alignment can be fine-adjusted by a dedicated periscope employing fine thread screws and differential micrometer screws (see 2.8) or by shifting the magnetic field zero with homogeneous offset fields generated by the compensation coils (see Sec. 2.2.3). The resulting potential energy for an atom displacement in z direction is depicted in Fig. 2.7a for 115 A current in the magnetic coils and a DT beam power of 3.1 W, which yields a trap depth of 210 μK as well as a radial/axial trap frequency of $f_{\mathrm{rad}} = 8$ Hz and $f_{\mathrm{ax}} = 1.2$ kHz.

The laser light used for the dipole trap beam is produced by a commercial master oscillator power amplifier (MOPA) laser system[9] with an output power of 18 W at a wavelength of

[9] Innolight, MEPHISTO MOPA 15 NE

$\lambda_{DT} = 1064$ nm. The power is distributed onto the transport beam (see Sec. 2.1.4) and a second dipole trap beam (see Sec. 2.1.5). Both beams are deflected by an AOM before being transported to the experiment, which allows for an active power control within a feedback loop. This laser system was build during the Diploma thesis of Markus Pfau [99] and a more recent description can be found in [95].

RF evaporation in the hybrid trap

The transition between different m_F substates can be driven by radiofrequency (RF) photons with a photon energy $\hbar\omega_{RF}$, which enables to selectively remove the highest energy atoms from the ensemble and evaporatively cool the atomic cloud. By subsequently decreasing the RF frequency on a timescale that allows continuous atomic re-thermalization via collisions, the atomic cloud is gradually cooled. This technique, called RF forced evaporation, was used for the first time in 1986 for spin-polarized atomic hydrogen [14] and nowadays constitutes a standard technique in quantum gas experiments.

The evaporation is performed by an exponential frequency sweep from 30 MHz to 2.8 MHz within eight seconds, which allows the atoms to continuously re-thermalize during the evaporation. As depicted in Fig. 2.7b, the RF photons are provided by a RF antenna, which is directly attached to the side vacuum window in the Preparation chamber. The antenna consists of a coil of three windings with a 50 mm diameter and is optimized for the frequency range between 2 and 35 MHz used for RF evaporation. The characterized frequency response is given in the appendix (see Sec. A.4). In addition, a direct digital signal synthesizer[10] is used as RF source, which enables RF generation with an output power up to 10 dBm from 0.3 MHz to 400 MHz. The signal is amplified by 43 dB by a 30 W high power amplifier[11].

During the experimental sequence, the laser is switched on for the last four seconds of RF forced evaporation at a constant power of 3.1 W. After evaporation, in order to achieve optimal transfer from the hybrid trap to the optical dipole trap, the magnetic gradient is reduced linearly in two steps, from 115 A to 30 A within 165 ms and to 3.4 A within 500 ms. Subsequently, the magnetic trap is switched off and the atoms are transported to the Science chamber (see Sec. 2.1.4).

2.1.4. Optical transport

As the quantum gas setup is designed to provide an experimental platform for hybrid systems consisting of ultracold atoms and charged particles, minimizing the influence of electromagnetic stray fields is essential. As a consequence, the cooling mechanisms relying on strong magnetic fields are spatially separated from the ionization region, located in an adjacent vacuum chamber

[10] Wieserlabs UG, WL-FlexDDS-NG-DUAL
[11] Mini-Circuits, LZY-22+

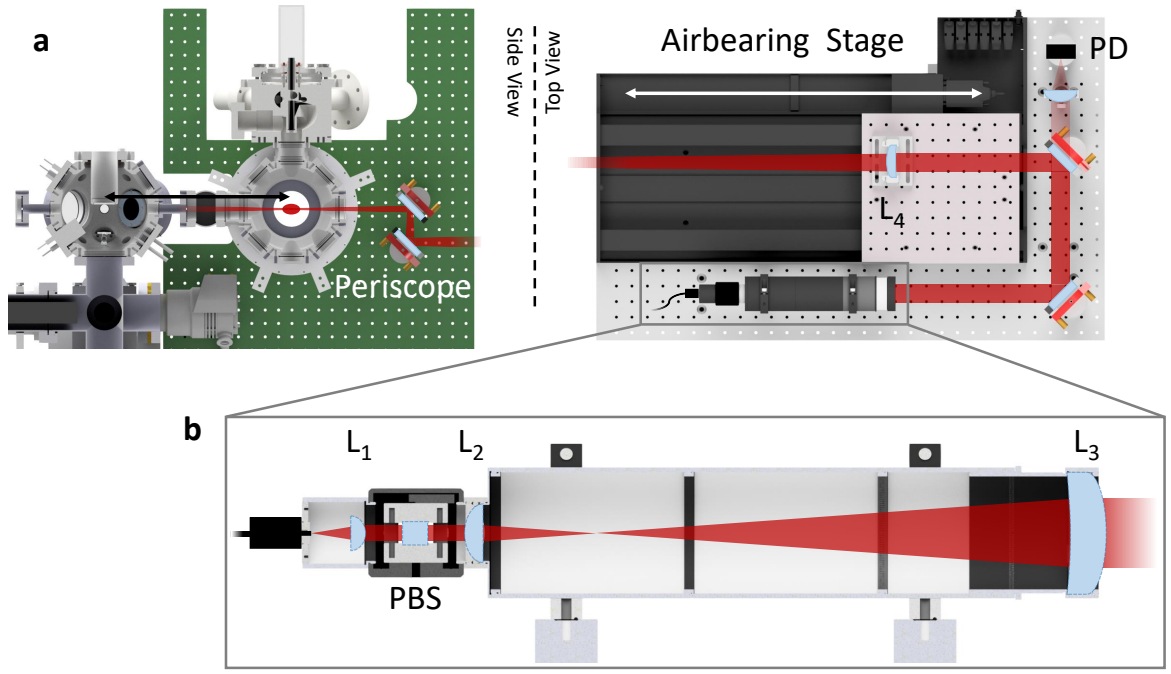

Figure 2.8: Optical setup for the transport beam. a. Side/Top view scheme of the optical setup. The atomic cloud is moved in the focus of the transport beam from the Preparation chamber to the Science chamber. A periscope is used to align the transport beam on the axis of the two vacuum chambers. The longitudinal movement is realized by a moving lens mounted on an airbearing stage, which focuses the collimated beam out of the fiber telescope. A photodiode (PD) measures the beam power leakage through a mirror. **b.** Fiber telescope providing an expanded collimated beam required for the diffraction-limited micrometer-sized focus. A first lens (L_1) collimates the beam out of the fiber, which is then expanded by a telescope (L_2 and L_3) after polarization cleaning by a polarizing beam splitter (PBS).

(Fig. 2.8). Such transport is typically realized by either moving the magnetic [120] or the optical [121] trapping potential.

Lens	L_1	L_2	L_3	L_4
Type	aspherical	achromat	achromat	achromat
Focal Length (mm)	25	45	200	750
Diameter (mm)	12.5	25.4	50.8	50.8

Table 2.1: Fiber telescope optics. Lens setup in the fiber telescope for the optical transport beam.

Here, the transport of the atomic sample is realized by moving the focus of the dipole trap beam used for the hybrid trap. The transport beam is focused into the hybrid trap by an achromatic lens (L_4[12]) mounted onto an airbearing stage[13] as illustrated in Fig. 2.8a. The transport beam is aligned onto the centers of both vacuum chambers separated by $d = 350$ mm, which is well within the travel range of the translation stage. The intensity of the transport beam is measured by the leakage through a high reflectivity mirror on a photodiode and actively controlled. In order to balance sufficient potential depths and large capture volume, a beam waist

[12] Thorlabs AC508-750-C
[13] Dover Motion, AG-400, controlled by: Aerotech, Soloist ML-10-40-IO

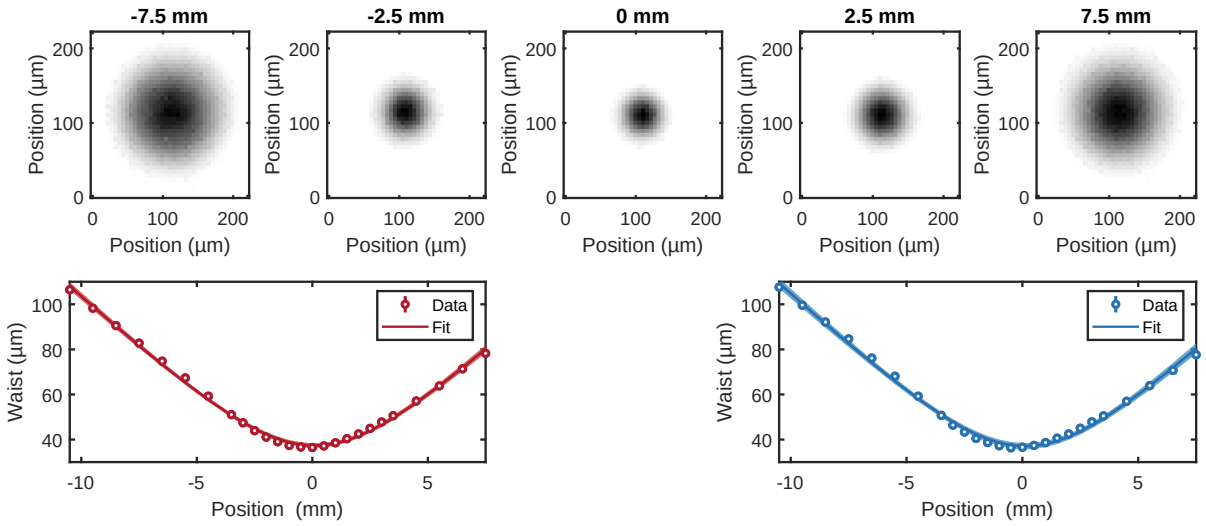

Figure 2.9: Waist of the transport beam. Measured 2D intensity profiles for different positions of the focusing lens. The resulting beam diameters are determined by Gaussian fits to the column/row sum profiles (red/blue data points). The solid lines are given by a hyperbolic fit to the obtained diameters according to Eq. 2.7. The shaded areas illustrate the 95% confidence interval of the fit.

of $w_0 = 35 - 40$ µm is required. Figure 2.8b depicts the fiber telescope which was built for this purpose. The diverging beam out of the optical fiber is collimated by an aspheric lens (L_1[14]) and subsequently expanded by two achromatic lenses (L_2[15] and L_3[16]) to reach the beam diameter of 8 mm required for a diffraction-limited focus. The utilized lens configuration of the telescope is given in Tab. 2.1. In order to avoid interference with the second crossing DT beam used for the DT evaporation (see Chapter 2.1.5) the polarization is selected by a polarizing beam splitter cube (PBS).

The beam profile has been measured in dependency of the longitudinal position of L_4 as depicted in Fig. 2.9. In addition, the beam diameter obtained by a Gaussian fit to the column sum (red data points) and row sum profiles (blue data points) of the distributions is shown. The focus size $w_{1,2}$ as well as the Rayleigh length $z_{\mathrm{R},1,2}$ are determined by fitting the hyperbolic function

$$w(z) = w_{1,2} \cdot \sqrt{1 + \left(\frac{z}{z_{\mathrm{R},1,2}}\right)^2} \tag{2.5}$$

to the measured beam diameters in dependency of the position z along the propagation axis of the beam. The fit yields a waist of $w_1 = 37.0(10)$ µm and $w_1 = 37.3(6)$ µm and a Rayleigh length of $z_{\mathrm{R}1} = 3.8(1)$ mm and $z_{\mathrm{R}2} = 3.9(1)$ mm. This corresponds to a beam quality factor $M^2_{1,2} = \theta_{1,2}\frac{\pi w_{1,2}}{\lambda_{\mathrm{L}}}$ of $M^2_1 = 1.06(9)$ and $M^2_2 = 1.05(6)$, where $\theta_{1,2}$ denotes the divergence half-angle of the beam.

As the hybrid trap allows for evaporative cooling down to quantum degeneracy as discussed

[14] Thorlabs AL1225H-B
[15] Thorlabs AC254-045-B
[16] Thorlabs AC508-300-C

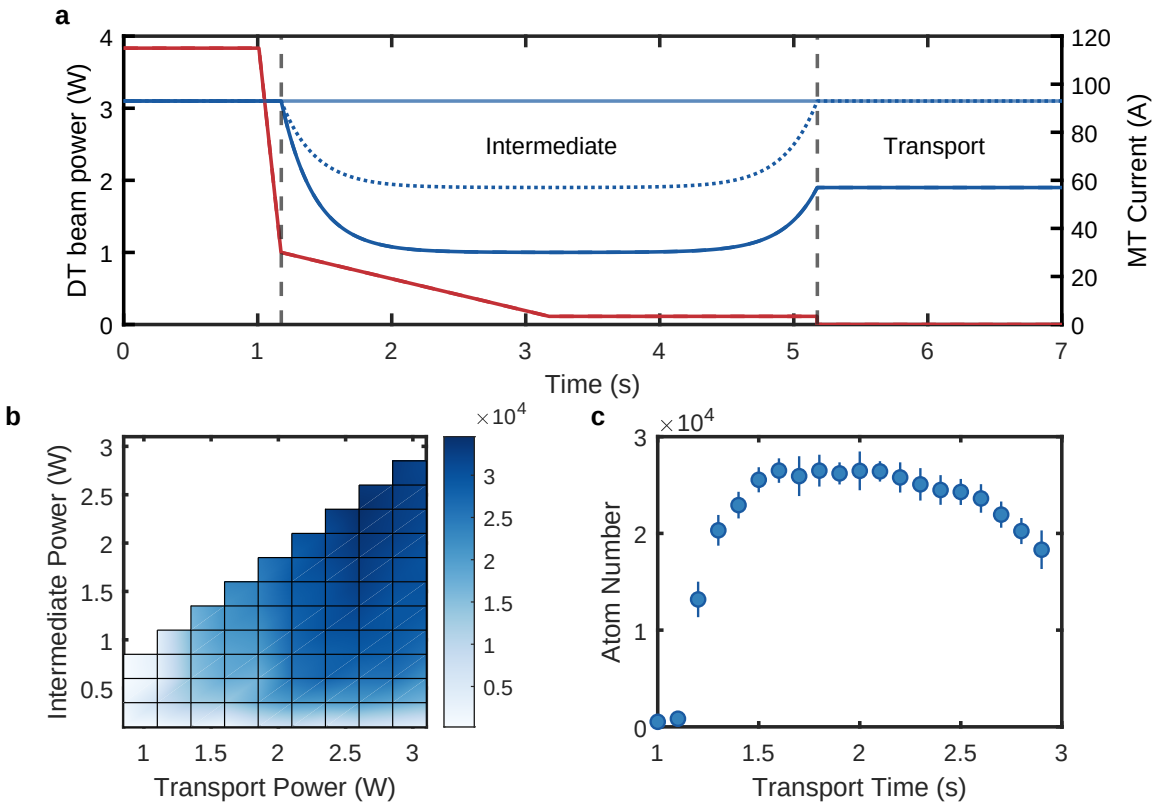

Figure 2.10: Optimization Optical Transport. a. DT beam power (blue lines) and MT current (red line) used for the characterization of the transport in dependency of the preceding hybrid trap evaporation. The DT beam power is exponentially decreased to an intermediate level, which sets the temperature of the transported sample. Subsequently, the power is re-increased exponentially to a larger or equal value than for the transport. **b.** Measured atom number in the BEC in dependency of the intermediate as well as the transport power of the transport beam for a transport duration of 1.7 s. **b.** Measured atom number in the BEC in dependency of the transport duration at a constant transport beam power of 3.1 W.

in Sec. 2.1.3, atomic ensembles can be prepared for optical transport in the temperature range between degeneracy and the trap depth of 210 µK at the maximum transport beam power of 3.1 W. For characterization of the optimal transport temperature, the atoms are held in the hybrid trap after forced RF evaporation and subsequently further evaporated by exponentially reducing the DT power down to different intermediate values within two seconds. The DT beam power and the MT current during this evaporation are displayed in Fig. 2.10a. In order to identify the optimum DT power for transport for each cloud temperature, the atoms are transported to the Science chamber either at the intermediate power or after exponentially increasing the DT power again adiabatically for two seconds to a higher transport power.

Figure 2.10b shows the measured BEC atom number after further evaporation in the Science chamber as a measure for the transport quality in dependency of these two DT powers. Here the intermediate and transport power have been varied from 0.1 W to 3.1 W, which yields trap depth span from 6 µK to 210 µK as well as a radial/axial trap frequency span from $f_{\mathrm{rad}} = 1.4$ Hz and $f_{\mathrm{ax}} = 220$ Hz to $f_{\mathrm{rad}} = 8$ Hz and $f_{\mathrm{ax}} = 1.2$ kHz. Apparently, for each intermediate laser power,

the transport efficiency increases monotonously with the transport power. This can be attributed to the increasing confinement due to the higher trap depth and frequency, which minimizes atom losses due to heating during the transport. In addition, employing atomic samples at higher temperature and atom numbers shows to be superior to further evaporated clouds and the efficiency saturates for intermediate powers above 2 W. As a consequence, optical transport is conducted at full laser power in the experimental cycle, as it further allows to avoid the four additional seconds of cycle duration for intermediate evaporation.

Optical transport involves two main sources of heating onto the transported atomic ensemble. First, parametric heating can result from mechanical vibrations inducing an oscillation of the waist position during motion. Hence, the air bearing stage, that decouples the lens motion from vibrations in the experimental setup is mounted onto a massive lapped granite measuring plate with a flatness below 2 µm avoiding mechanical stress. In addition, the transport itself introduces heating intrinsically, as it requires acceleration and subsequent deceleration in the dipole trap potential inducing center of mass oscillations after optical transport. The resulting amount of heating decisively depends on the applied velocity profile. Two approaches tackle this problem, which can be distinguished by comparing the transport time T_{trans} to the axial trapping potential period $T_{\mathrm{ax}} = f_{\mathrm{ax}}^{-1} \approx 0.13$ s determined by the axial trapping frequency $f_{\mathrm{ax}} = 8.0$ Hz. The adiabatic transport approach utilizes transport times $T_{\mathrm{trans}} \gg T_{\mathrm{ax}}$ to minimize center of mass displacement from the trapping center during transport. In contrast, non-adiabatic transport exploits a triangular velocity profile, where center of mass oscillations in the trapping potential can be suppressed by adapting the transport time to even multiples of the inverse trapping frequency [122]. As discussed in previous works, the translation setup only features travel times down to 0.8 s over the full transport distance [95, 103], rendering optimal transport impossible for lower multiples of T_{ax}.

Figure 2.10c shows the measured BEC atom numbers for a triangular velocity profile in dependency of the transport duration. Here, a transport laser power of 3.1 W is applied. As the BEC atom number reflects the phase-space density of the transported atomic sample, it gives a measure for the transport efficiency accounting for atom number efficiency and heating. The obtained data reveals a plateau of the transport efficiency between 1.3 s and 2.3 s duration, pointing towards the quasi-adiabatic regime. For lower transport times, the efficiency drops to almost zero, as heating effects are increased. At longer transport times, the transport efficiency is decreasing as well due losses caused by collisions with the background gas typically limiting atomic sample lifetimes in optical dipole traps. Transport times beyond 3 s are not feasible, since this implies an excessive transport beam power duty cycle causing thermal power instabilities. As a consequence, a transport duration of 1.7 s has been chosen, which is well within the plateau while preventing unnecessarily extended experimental cycle durations.

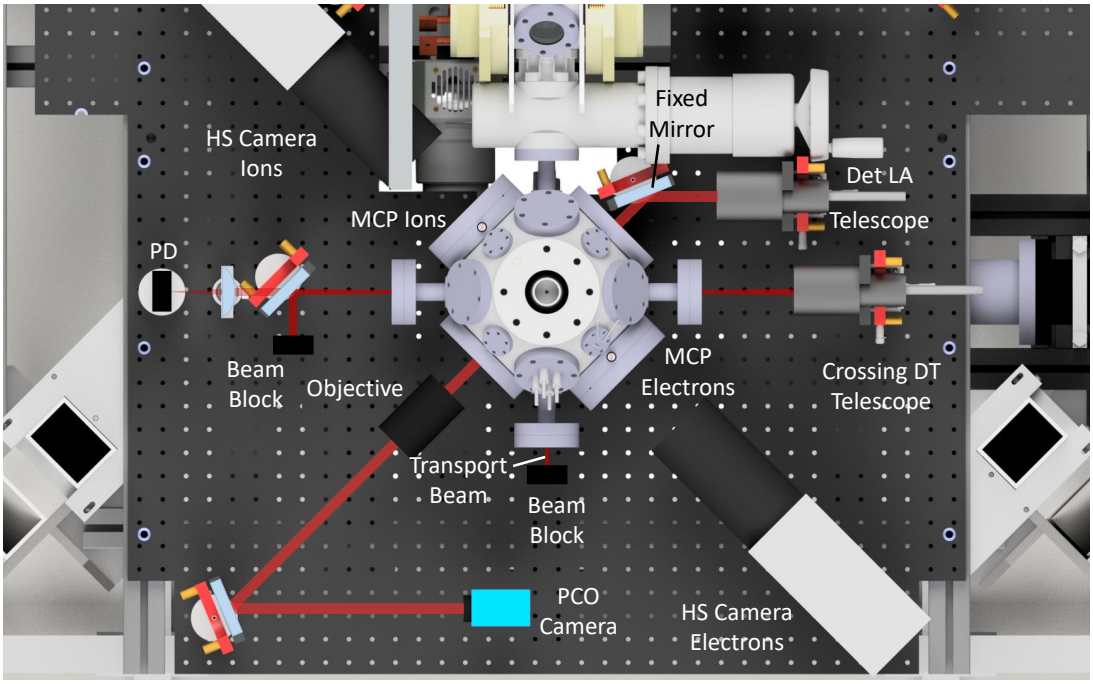

Figure 2.11: Optics Science Chamber. Top view on the realized beam paths in the Science chamber for the crossed dipole trap and absorption imaging.

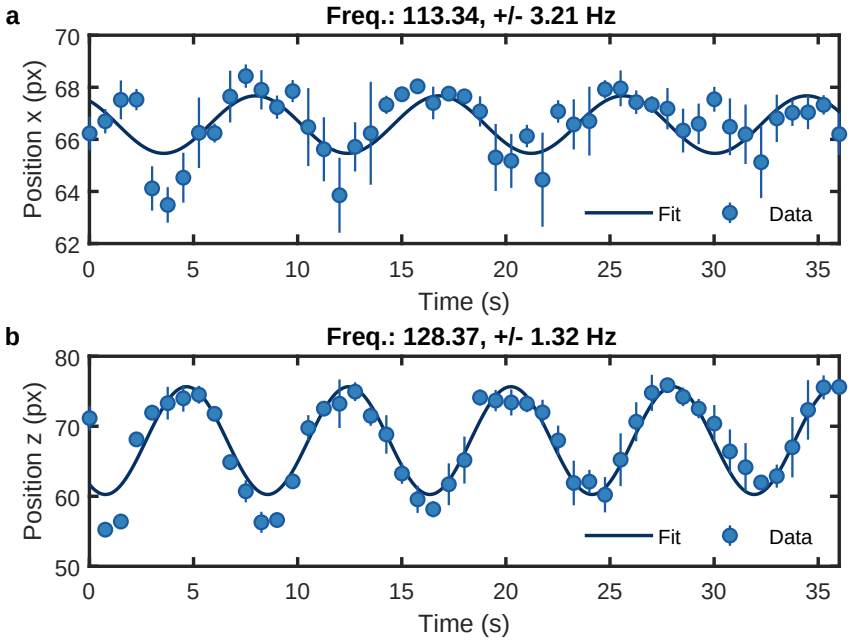

Figure 2.12: Trap Frequency Measurement. a.-b. Measured center of mass position of the ultracold cloud in x-/z-direction after 10 ms time-of-flight in dependency of the hold time after excitation (data points) and the corresponding sinusoidal fit function (solid line).

2.1.5. Evaporative cooling in a crossed optical dipole trap

After the successful transfer of the atomic ensemble into the Science chamber, a second evaporative cooling stage is employed in the crossed dipole trap. Evaporative cooling in the crossed DT is realized by successively decreasing the trapping potential controlled by the trapping laser

intensity and hence gradually removing the atoms with highest kinetic energy. For this purpose, a second perpendicular dipole trap beam is switched on and provides additional strong confinement in the longitudinal direction of the transport beam. An overview of the utilized beam paths in the Science chamber is given in Fig. 2.11. In order to minimize heating by the imposed second dipole potential, the laser power is exponentially ramped up to 3.1 W during the transport time. After a hold time of 1 ms, the laser powers are simultaneously reduced to 2 W and subsequently ramped down exponentially to 43 mW. As the evaporative cooling process requires successive atomic thermalization, the evaporation lasts three seconds. Within this evaporation, the atomic ensemble exceeds the critical phase space density and forms a Bose-Einstein condensate. Finally, the BEC is held in the crossed optical dipole trap and is prepared for studies using femtosecond laser pulses.

The BEC properties are determined by the atom number and the trap frequencies, which are given by the curvature of the superimposed dipolar potential U_{CDT} of the two trapping beams

$$\omega_{\mathrm{x}} = \sqrt{\frac{1}{m_{\mathrm{a}}} \frac{\partial^2 U_{\mathrm{CDT}}}{\partial x^2}}\Bigg|_{\min(U_{\mathrm{CDT}})} \tag{2.6}$$

and accordingly for y and z. In order to access the final trap frequencies determining the BEC properties, the crossing dipole trap beam power is abruptly increased to 150 mW for 5 ms reducing the gravitational sag and thus inducing a center of mass displacement of the atoms. Afterwards, the beam power is instantaneously restored to 43 mW and the atom displacement evokes oscillations in the crossed dipole trap with the trap frequencies. When the DT is switched off after a variable subsequent hold time, the corresponding momentum oscillations translate into spatial oscillations during the time-of-flight. Figure 2.12 shows the measured center of mass positions in x and z position in dependency of the hold time after a time-of-flight evolution of 10 ms. The sinusoidal fits to the obtained data yield trap frequencies of $\omega_{\mathrm{x}} = 2\pi \times 113(3)$ Hz and $\omega_{\mathrm{z}} = 2\pi \times 128(1)$ Hz.

2.1.6. Absorption images and data acquisition

Besides providing charged particle detection, the experimental setup allows for absorption imaging of the density distribution of neutral atoms. For this purpose, an expanded collimated probe laser pulse of 50 µs duration, resonant to the D_2 transition in ^{87}Rb, is imposed on the atomic ensemble. Figure 2.13 illustrates a scheme of this imaging technique. The attenuation of the laser intensity dI while passing an atomic ensemble can be described by Beer-Lambert law

$$dI = \rho \sigma I dy \tag{2.7}$$

and is proportional to the laser intensity I_0 as well as the local density ρ, the thickness dy and the absorption cross section σ. Accordingly, the laser intensity decreases exponentially while passing the atomic ensemble and the amount of transmitted light decreases with the illuminated

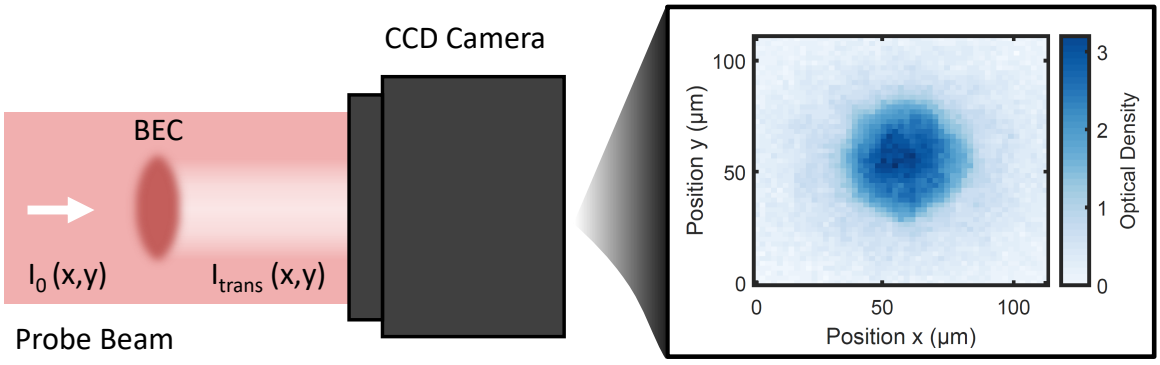

Figure 2.13: Absorption Imaging. The atomic cloud absorbs a fraction of the incident laser light of the resonant probe beam pulse. The transmitted intensity distribution is imaged onto a CCD camera. The absorption image shows the 2D optical density distribution of a BEC obtained after 10 ms time-of-flight.

local line density $\tilde{\rho}_\mathrm{a} = \int \rho_\mathrm{a}(x,y,z)\,dz$. By recording the transmitted 2D intensity distribution $I_\mathrm{trans}(x,y)$ on a charge-coupled device (CCD) camera as well as the incoming intensity profile $I_0(x,y)$ in a reference shot without atoms, the 2D projection of the atomic density distribution is accessible.

The optical density $OD(x,y)$ is given by the product of the local line density ρ_a and the resonant absorption cross section $\sigma_0 = 3\lambda^2/(2\pi)$ and can then be calculated as [95]:

$$OD(x,y) = -\left(1+\delta^2\right) \times \ln\left(\frac{I_0(x,y)}{I_\mathrm{trans}(x,y)}\right) + c_\mathrm{I} \times \left(\frac{I_0(x,y) - I_\mathrm{trans}(x,y)}{I_\mathrm{sat}}\right) \tag{2.8}$$

where the conversion factor c_I depends on properties of the imaging system as the magnification and the quantum efficiency of the camera. This representation accounts for the saturation of the D_2 transition for high detection intensities as well as the detuning of the detection pulse. A more detailed description of the utilized image processing can be found in [95]. As depicted in Fig. 2.11, for absorption imaging in the Science chamber a commercial imaging objective[17] is employed, which provides a spatial resolution of 3.5 µm at a magnification of 3.0 [101].

[17] LENS-Optics GmbH, N-BK7, 502.8 mm, 3.014x, AR 780 & 1064 nm

2.2. Charged particle detection

The central feature of the experimental setup is the charged particle detection, which enables direct detection of the created electrons and ions on spatially resolving detectors. Figure 2.14 shows a sectional view of the equipped Science chamber. The quantum gas target is held in the center of the vacuum chamber by the two dipole trap beams, which cross from an 45° angle to the detection axis into the drawing plane. The ionizing femtosecond laser pulse enters from above through a re-entrant viewport, which is required due to the small working distance of the high-resolution objective. The created charged particles are directed onto opposing position sensitive detectors by an external extraction field, which is created by two transparent mesh electrodes. Beneath the Science chamber, the vacuum pumping system is attached.

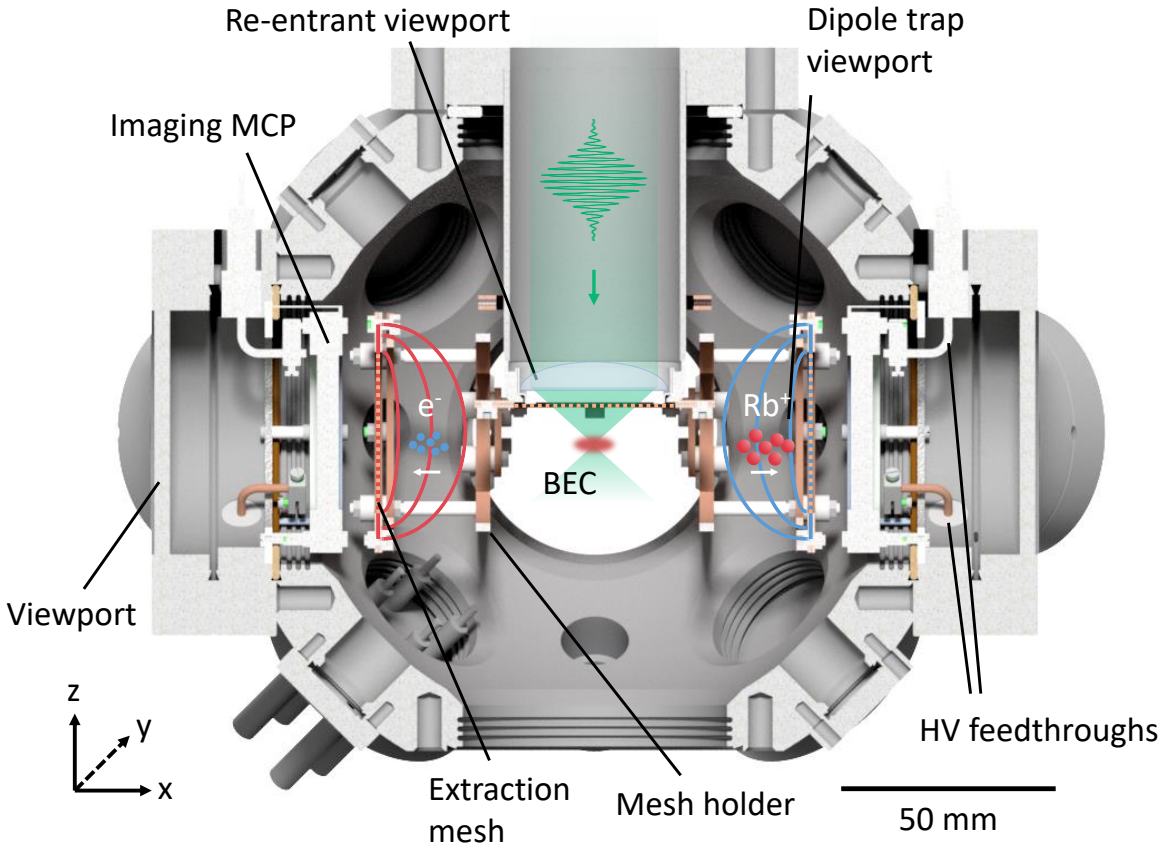

Figure 2.14: CAD image of a central cut through the Science chamber. Sectional view into the Science chamber equipped with two charged particle detection units for electron/ion detection. The red/blue lines illustrate the electric field created by the positively/negatively charged extraction mesh.

In the following, the mode of operation for the charged particle detection is described. Additionally, a gated detection scheme is introduced, which allows for electron detection with additional temporal resolution. Furthermore, the compensation setup for electromagnetic stray fields is presented, which is fundamental for reliable investigations of slow electrons.

2.2.1. Spatially-resolved electron/ion detection

As the centerpiece of the experiment, the charged particle detection on spatially resolved detectors gives information on the kinetic energy as well as the angular velocity distribution of the electron/ion ensembles. Figure 2.15 displays a sketch of the working principle of the detection units.

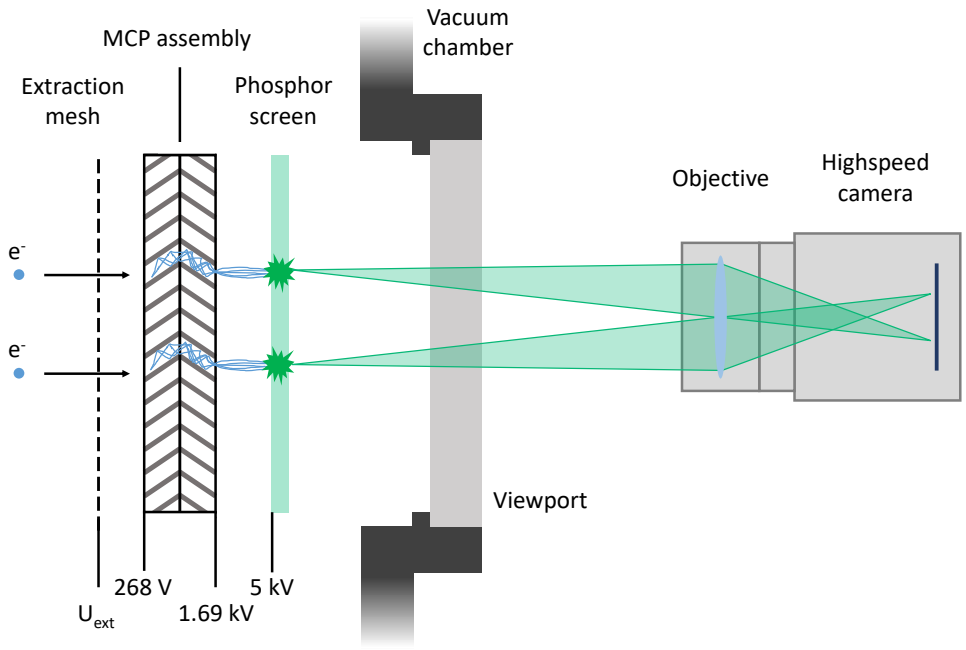

Figure 2.15: Electron detection scheme. The photoelectrons are drawn towards the detection unit by a positively charged extraction mesh electrode. After post-acceleration onto a MCP assembly, the electrons are multiplied into avalanches of secondary electrons within the micro-channels and cause flashes of light within a subsequent phosphor screen. The emitted light is imaged by an objective lens onto the chip of a highspeed camera enabling spatially-resolved detection of the electrons' points of incidence.

After photoionization, the electrons/ions are accelerated onto the position sensitive detection units. For this purpose, a static extraction field is created by two opposing mesh electrodes at variable potential $\pm U_{\text{ext}}$. These electrodes consist of etched copper meshes with a custom-made electrolytically applied gold coating [102, 107]. The grid size of 8 lines per millimeter in combination with the high permeability of 70-80% after coating ensure homogenous creation of an extraction field perpendicular to the mesh plane, while minimizing the charged particle losses in the mesh. After passing the meshes, the electrons are post-accelerated towards a microchannel plate (MCP) assembly consisting of two MCPs in Chevron configuration with a channel diameter of 12 µm and a channel pitch of 15 µm. Here, the incident electrons are multiplied resulting in an avalanche of hundreds of thousands to millions of secondary electrons[18], which are further accelerated towards the attached P46 ($Y_3Al_5O_{12}$:Ce) phosphor screen, which provides a quantum efficiency of 70 photons per incident electron at 5 kV kinetic energy [123].

[18] A total gain of $\geq 4 \times 10^6$ is specified for a voltage difference of 2 kV over the Chevron configuration.

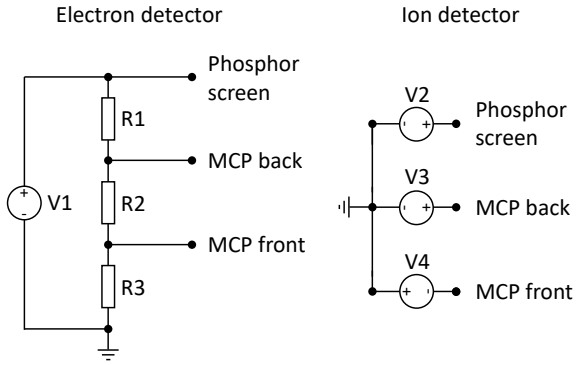

R1	139.5 MΩ
R2	139.5 MΩ
R3	23.3 MΩ
El. MCP	2x 62 MΩ
Ion MCP	2x 41 MΩ

Detector	Electron	Ion
Extr. Mesh	+ U_{ext}	- U_{ext}
MCP Front	268 V	- 1 kV
MCP Back	1.69 kV	600 V
P46	5.0 kV	2.8 kV

Figure 2.16: Voltage divider overview. A schematic overview on the used circuits to provide high-voltage supply for the electron/ion detection units is given. The tables contain the utilized resistivities and the resulting electric potentials.

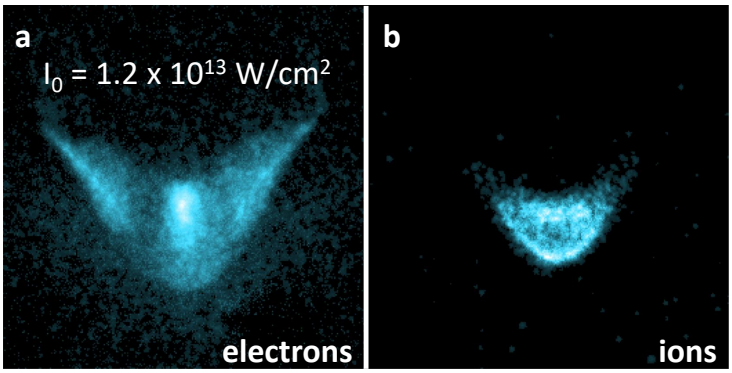

Figure 2.17: Direct detection of charged particles. a. False color image of the measured electron distributions at $U_{\text{ext}} = 300\ V$ for photoionization of a BEC with a single fs pulse at 511 nm wavelength and a peak intensity of $I_0 = 1.2 \times 10^{12}$ W/cm^2. **b.** False color image of the corresponding ion distribution. The images are averaged over more than 10 realizations.

The emitted light from the phosphor screen is imaged by an objective lens[19] onto a highspeed camera[20], which is operated at a frame rate of 1000 fps. Utilized at full resolution of the CMOS chip of 1280 x 800 pixels to image the phosphor screen with a diameter of 45 mm, a spatial resolution of 56 µm can be attained. In addition, the high-speed cameras support frame rates up to 120 kHz at a limited resolution of 128 x 128 pixels corresponding to a spatial resolution of 350 µm.

The detection efficiency for electrons $\eta_{\text{e}} \approx 0.4$ is given by the product of the transparency of the extraction meshes and the open area ratio as well as the quantum efficiency of the MCP. In order to ensure a constant, optimal quantum efficiency of approximately 80% [124] for all extraction voltages, the electrons are post-accelerated onto the same front potential $U_{\text{front,e}} =$ 268 V of the MCP. For the ions, the identical detection scheme is used with opposite polarity for the extraction and post-acceleration. The detection efficiency is limited to $\eta_{\text{i}} \approx 0.1$ due to

[19] Nikon, AF-S NIKKOR 50 mm 1:1.4 G
[20] Vision Research, Phantom Miro 310

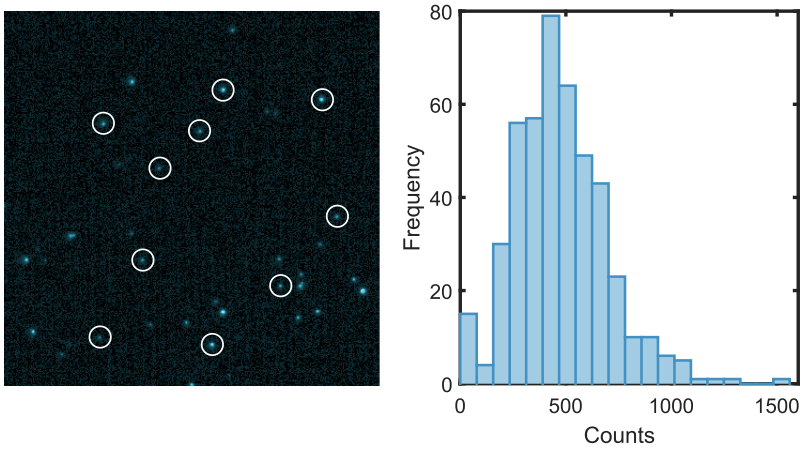

Figure 2.18: Absolute electron number extraction. Zoom into a single-shot electron distribution obtained at $U_{\text{ext}} = 5$ V. The number of counts is integrated in circular masks around distinct locations of electron incidence (white circles). Histogram of the measured counts on the camera for 455 electron impacts in total.

the lower quantum efficiency of the MCP material [125].

Figure 2.16 displays an overview on the voltage dividers and the voltages, which are applied on the different electrodes. In addition, both the electron and ion mesh holder (see Fig.2.14), which are used as mounting for the extraction mesh within the vacuum chamber, are independently accessible by voltage feedthroughs. Controlling the electric potential of these holders enables shaping of the electron/ion ensembles on the way to the detector analogously to the effect of electrostatic lenses. For all measurements presented here, the holders have been grounded. In Fig.2.17 shows the recorded distribution of electrons/ions at an extraction voltage of $U_{\text{ext}} = 300\ V$, which were created by photoionization of a BEC with a single fs pulse at 511 nm wavelength and a peak intensity of $I_0 = 1.2 \times 10^{12}$ W/cm^2.

In order to quantitatively access the number of created electrons for an ionization event, the electron detection unit has been characterized. First, the brightness per recorded electron impact is extracted. In order to enable separation of single electron impacts, few photoelectrons are created at a peak intensity of $I_0 = 2.7 \times 10^{12}$ W/cm^2 and extracted by a voltage of $U_{\text{ext}} = 5$ V. Figure 2.18a depicts a zoom into the electron distribution. The brightness per recorded electron is determined by the integrated counts in a circular area with a radius of 10 pixels around distinct electron impacts (white circles). Figure 2.18a shows the histogram of counts on the camera chip obtained for 455 electron impacts, yielding an average of $n_{\text{count}} \approx 430$ counts per detected electron. Accordingly, the expected number of counts per incident electron on the detector is then given by the product with the detection efficiency of the detector $n_{\text{cpe}} = n_{\text{count}} \times \eta_{\text{e}} \approx 172$.

However, deducing a reliable measure for the number of created electrons is challenging as both the probability to record an electron and the brightness per recorded electron for each velocity class of electrons strongly depend on the applied extraction field. Indeed, when decreasing the extraction voltage, the effective detection efficiency decreases as the field does not suffice to efficiently draw the electrons with high kinetic energies to the detectors. As CPT

trajectory simulations reveal (Chap. 4.2), significant numbers of electrons end up on different surfaces in the vacuum chamber at low extraction fields. Moreover, the high flux of plasma electrons on a small part of the MCP area as seen for $U_{\text{ext}} = 300$ V in Fig. 4.8c can lead to electron depletion in the microchannel material and thus a systematic underestimation of the number of incident electrons in this part of the detector. Furthermore, detection of low kinetic energy electrons is typically limited by residual electric and magnetic fields. Hence, it requires high experimental control over such stray fields (see Chap. 2.2.3).

2.2.2. Time-resolved electron detection

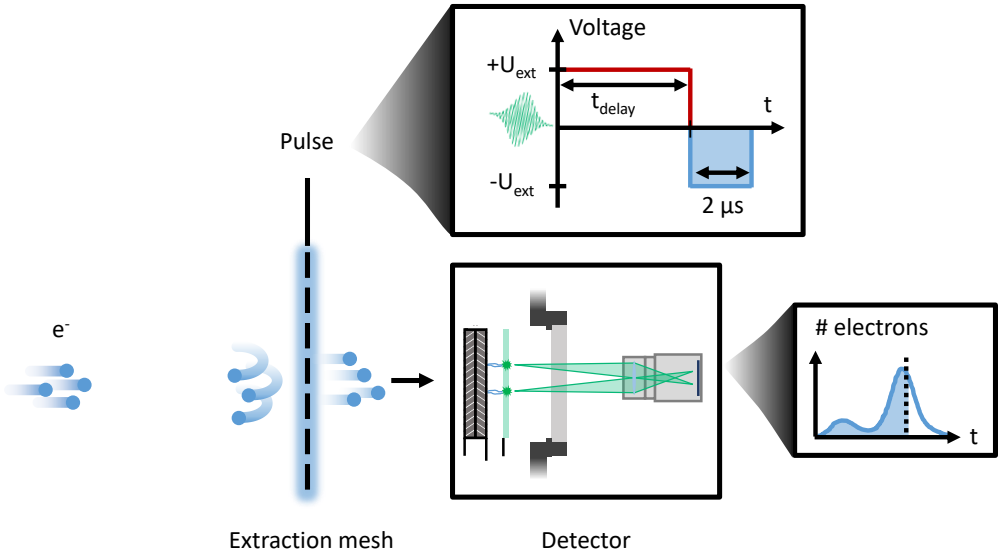

Figure 2.19: Time-resolved electron detection scheme. The electrons are accelerated onto the detector by the extraction field. After a variable delay t_{delay}, a HV pulse reverses the polarity of the extraction field and electrons still in front of the extraction mesh are repelled. Thus, the detector records the time-integrated signal of incident electrons up to t_{delay}. The spatial resolution is maintained in this mode. Figure is adapted from [2] and licensed under CC BY 4.0.

Whereas the detection scheme provides electron/ion detection with spatial resolution, it only gives limited access to the underlying temporal distribution of incident particles. As charged particle tracing simulations show (see Chapter 4.2), the detected electron ensembles for typical experimental parameters span over a time frame of less than 1 µs even for the lowest applicable extraction fields. With a maximum frame rate of 120 kHz, the imaging system does not support adequate time-resolution. Thus, a gated electron detection scheme is used in order to access the arrival time of the electrons being drawn to the detector. Fig. 2.19 shows the schematic working principle of this technique. The electron extraction is exerted by a static voltage $\pm U_{\text{ext}}$ on the meshes. After a variable delay t_{delay} with respect to the femtosecond laser pulse, a negative voltage pulse with a duration of 2 µs is applied onto the electron extraction mesh and rapidly reverses the potential. The resulting repulsive potential prevents electrons from passing

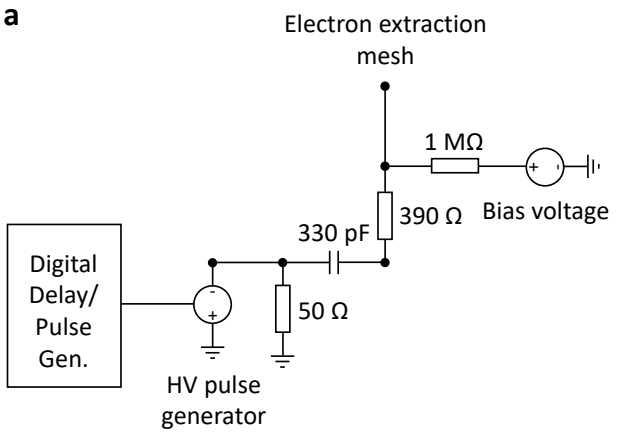

b

U_{ext}	Bias Voltage	HV Pulse
5 V	6.5 V	- 12 V
10 V	11 V	- 24 V
15 V	16.5 V	- 37 V
25 V	28 V	- 62 V
50 V	56 V	- 124 V
100 V	112 V	- 249 V
200 V	225 V	- 500 V
300 V	335 V	- 744 V

Figure 2.20: Capacitative Coupling of the repulsive HV pulse. a. Electric circuit utilized to reverse the bias voltage U_{ext} on the extraction meshes. **b.** Applied bias and pulse voltages for each extraction voltage.

the extraction mesh for time-of-flight durations $\tau_{\text{TOF}} > t_{\text{delay}}$ and consequently interrupts the electron flux onto the detector. Thus, the detection scheme enables measuring the accumulated electron signal up to t_{delay}, while maintaining the spatial resolution.

For this detection method, the temporal resolution is not limited by the charged particle detector itself but the attainable rise-time and temporal jitter of the applied voltage pulse. The experimental cycle is synchronized with the programmable output of the PHAROS Timing Electronics Module. Albeit, a temporal jitter of the pulses relative to the femtosecond laser pulses of 6 ns remains, which is on the order of the round trip time of the pulse in the oscillator cavity of $f_{\text{osc}}^{-1} = (83\ \text{MHz})^{-1} = 12$ ns. In order to optimize the profile of the HV pulses, a tailored circuit was used to switch the polarity of the extraction mesh, which is illustrated in Fig. 2.20a. Whereas the extraction voltage U_{ext} is applied as bias voltage, the HV pulse with a voltage of $U_{\text{pulse}} \approx -2U_{\text{ext}}$ is generated by a high-voltage pulse generator[21] which is triggered by a digital delay generator[22] and capacitatively coupled onto the meshes. The depicted circuit allows reverse voltages up to $U_{\text{ext}} = 300$ V with a 0% to 100% rise time below 30 ns. Figure 2.20b depicts the actual bias and pulse voltages employed in the circuit for each extraction voltage.

2.2.3. Electromagnetic stray field control

Since the experimental setup is designed for the investigation of hybrid atom-ion quantum systems as well as slow photoelectrons with meV kinetic energies, a high degree of control over electromagnetic stray fields is imperative. For the electric stray fields, the stainless steel vacuum chamber as well as the electrodes surrounding the ionization volume work as passive shield. In order to prevent accumulation of electric charges on the glass surface of the re-entrant viewport,

[21] DEI HV-1000-N
[22] Stanford Instruments, DG645 - digital delay/pulse generator

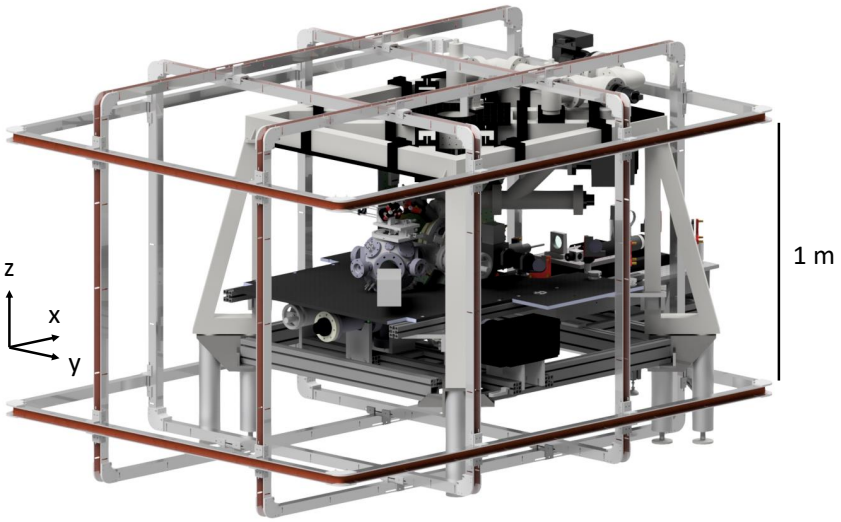

Figure 2.21: Compensation coil design. Overview on the compensation cage consisting of a pair of coils for the *x*-,*y*- and *z*-direction.

it is shielded by a high-transparency gold-coated copper mesh as used for the mesh electrodes. Comparison of CPT simulations using a FEM simulation of our experimental environment with measured data reveals a control over electric field gradients down to the V/m level (see Sec. 4.2).

Apart from electric fields the compensation of static magnetic stray fields is fundamental. Since passive magnetic field shielding schemes using for example mu-metal are not applicable due to the required extensive optical access to the ionization volume, a cage of three compensation coil pairs has been designed. This cage enables compensation of magnetic offset-, as well as gradient fields in Helmholtz or Anti-Helmholtz configuration, respectively. The demands for the coil design are determined by the required field homogeneity, the bandwidth for active magnetic field compensation, as well as geometrical constraints given by the remaining experimental setup.

The constraint for the field homogeneity, which limits the minimum residual magnetic stray field, is given by the displacement of the point of incidence of an electron with 50 meV kinetic energy in the detector plane. In order to keep this displacement below 175 µm, which is half the spatial resolution of the electron detector, a maximum field deviation of $B_{\mathrm{dev}} = 0.5$ mG is required over the full distance of 120 mm between both detection units. Thus, the cage consists of meter-sized pairs of coils surrounding the whole experimental setup and being centered around the ionization volume. Figure 2.21 shows the CAD model of the design. Each coil consists of four layers with 13 windings and two layers with 6 windings of insulated copper wire with a diameter of 2 mm wounded onto a rectangular frame of four aluminum profiles, which are connected by insulating polyoxymethylene (POM) brackets to prevent eddy currents. Table 2.2 lists the specifications and electrical ratings of each coil pair. Furthermore, the dependency of the

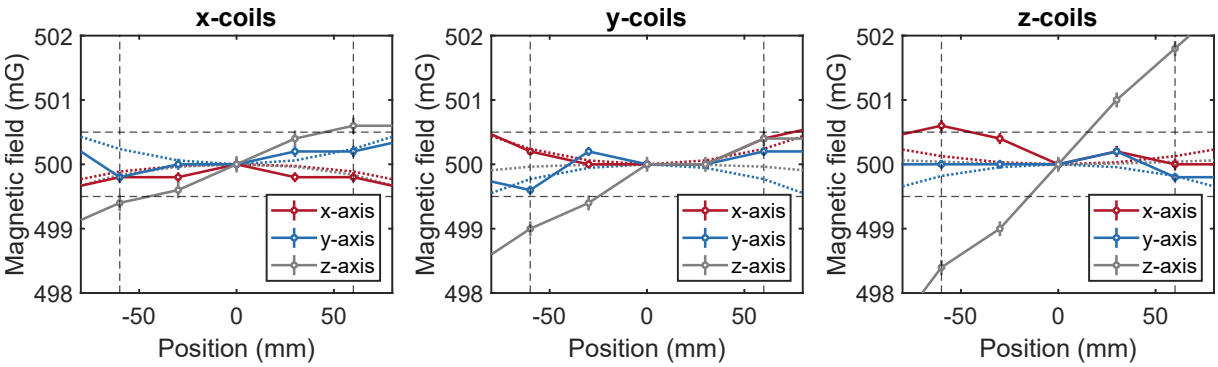

Figure 2.22: Magnetic compensation fields. Calculated magnetic field profile of the three compensation coil pairs obtained for a field amplitude of 500 mG (dashed lines). The datapoints and solid lines display the measured fields after installation on the optical table and are taken from [96].

field amplitude on the applied current is given. Controlling the current allows for compensating the magnetic fields with 10 mG accuracy for all three dimensions in space.

axis	layers	turns	size (cm)	distance (cm)	R (Ω)	L (mH)	B/I (mG/A)
x	4 / 2	13 / 6	162 x 132	74.5	0.6 / 0.3	2.7 / 0.8	150.0 / 68.6
y	4 / 2	13 / 6	212 x 140	81.5	0.6 / 0.3	4.0 / 1.2	134.3 / 61.8
z	4 / 2	13 / 6	220 x 170	100	0.6 / 0.3	4.7 / 1.4	117.4 / 53.9

Table 2.2: Dimensions and electrical properties of the compensation coil design for a pair of full/half layers in each direction.

The static magnetic compensation fields were characterized within the master thesis of Jakob Butlewski [96], Fig.2.22 compares the spatial profile of the measured magnetic fields on the optical table to the expected field obtained by numerically solving Biot-Savart's law. The homogeneity is tested for compensation of a static field of 0.5 G, which is on the order of the earth's magnetic field. The measured magnetic fields meet the requirements regarding the field homogeneity for displacements in the x- and y-direction from the ionization center. The magnetic field gradient in z-direction can be attributed to the magnetic susceptibility of the optical table beneath the compensation cage and can be compensated by an additional anti-Helmholtz field [96].

In addition, the compensation coil system allows to add arbitrary superpositions of offset and gradient fields for controlled deflection of charged particle beams. For the measurements reported in Chapter 4, the Helmholtz coils were utilized to create an additional magnetic offset field of 370 mG in xy-direction, i.e. perpendicular to the detection axis in the horizontal plane, in order to increase the energy resolution of the detector and re-center the electron signal on the detector.

Besides magnetic field compensation in the Science chamber, the coils are used to compensate stray fields in the Preparation chamber and during optical transport. For this purpose, the currents are switched during the experimental cycle. The corresponding currents are given in Sec. A.5.

Furthermore, the compensation coil design supports an active compensation of AC magnetic

stray fields using a magneto-resistive sensor[23], a bipolar power supply[24] as well as an adapted customized circuit for the feedback loop [95]. In the experiment, the main contribution to AC magnetic stray fields occurs at the power line frequency of 50 Hz and the corresponding harmonics. The active compensation system was tested for a smaller set of coils and reaches an attenuation of 30 dB at 50 Hz in one dimension as well as an suppression of the residual stray field below 0.5 mG [106]. By adapting the output capacitors of the power supply to $C = 1$ µF, similar attenuation should be accessible by use of the half layer compensation coils with reduced inductivity and a cutoff frequency $f_0 = \frac{1}{2\pi\sqrt{LC}}$ of 4-5 kHz.

[23]Honeywell, HMC1001
[24]HighFinesse, BCS 5A/10V

2.3. Femtosecond laser pulses

Femtosecond laser pulses constitute a versatile tool for instantaneous manipulation of quantum gases in high-intensity laser fields. In this section the available sources of high-intensity ultrashort laser pulses with variable frequencies are introduced. After a short presentation of the laser system, the creation of a micrometer-sized focus and the active stabilization of the laser beam path are discussed.

2.3.1. Femtosecond laser system

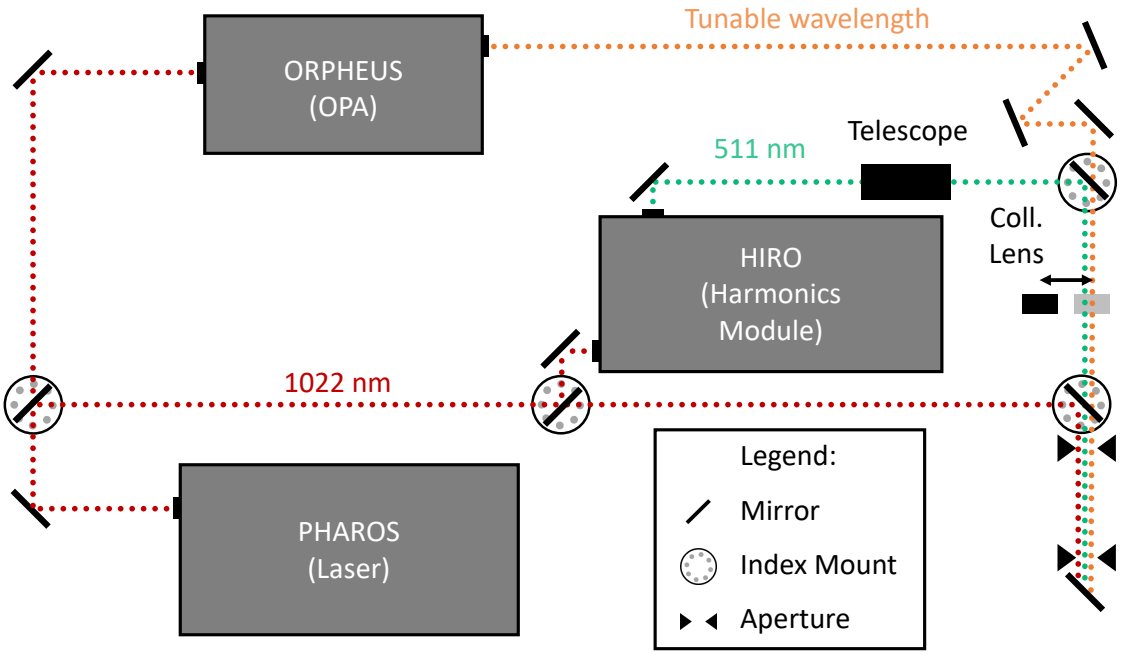

Figure 2.23: Femtosecond laser system. The femtosecond laser pulses are created at a wavelength of 1022 nm. The optional mirrors with index mounts enable direct usage of the fundamental wavelength or distribution to frequency conversion in the harmonics module as well as the OPA. The exiting light can be collimated by a telescope or collimation lens, respectively.

In this experiment, the femtosecond laser pulses are generated by a commercial Kerr-lens mode-locked chirped-pulse amplification (CPA) solid-state laser system[25]. Further descriptions of this system can be found in [95, 126]. This laser system is based on a ytterbium doped potassium-gadolinium tungstate (Yb:KGW) oscillator, which creates pulses at a central wavelength of $\lambda_F = 1022$ nm and a bandwidth of $\Delta\lambda_F = 4.36$ nm (FWHM) at a repetition rate of 83 MHz. The generated femtosecond pulses are amplified by CPA. In this technique, the pulses are stretched in time, amplified by a regenerative amplifier and compressed subsequently. The temporal stretching and re-compression is exerted by a transmission diffraction grating, which introduces and re-compensates a positive frequency chirp. After CPA the pulses exhibit a FWHM pulse duration of 300^{+30}_{-23} fs and the laser attains a maximum output power of 6 W and is oper-

[25] Light Conversion, PHAROS PH1-06

ated at a tunable repetition rate of $f_{\mathrm{rep}} = 100\,\mathrm{kHz}$, synchronized with the cycle of quantum gas generation.

Besides using the fundamental wavelength directly, the laser system offers two modules for frequency conversion. The harmonics module[26] allows for higher-harmonic generation within a Beta-Barium-Borate (BBO) crystal. As the conversion efficiency scales quadratically with the intensity and is limited to about 60% [101], the output power can be controlled with the regenerative amplifier up to a maximum of 3.6 W. Generation of the second harmonic results in a central wavelength of $\lambda_{\mathrm{SH}} = 511.4$ nm with a bandwidth of $\Delta\lambda_{\mathrm{SH}} = 1.75$ nm FWHM and a pulse duration of 215^{+20}_{-15} fs FWHM. The output spectrum is measured by use of a spectrometer and the durations are obtained in a scanning autocorrelator[27]. In addition, a second module[28] enables frequency conversion by optical parametric amplification. Exploiting different non-linear optical processes, the optical parametric amplifier (OPA) provides an output range spanning from 210 nm to 2900 nm, with a wavelength dependent output power ranging from 3 to 530 mW.

2.3.2. Active beam stabilization

The femtosecond laser system is located in a separate adjacent laboratory in order to be shared with other experimental setups and to accomplish laser safety in the quantum gases laboratory. Thus, the ultrashort pulses need to be transported over a distance of approximately 10 meters. Since beam transport in optical fibers is not an option due to pulse-broadening by dispersion and intensity issues when focusing the pulses into the narrow fiber core, the beam is transported through the air. In order to guarantee experimental reproducibility, an active beam stabilization is required to control pointing instabilities. To ensure laser safety and minimize air turbulence, the majority of the beam path is encased by aluminum pipes. Figure 2.24a displays an overview of the femtosecond laser pulse transport.

The beam position and angle are actively controlled with a commercial 4D beam stabilization system[29], which drives two piezo-actuated mirrors. Previous characterizations revealed superior performance with respect to both, attenuation and bandwidth if the distance between both piezo units is maximized [105], thus they are integrated into the beam path each in one of the laboratories. In a typical experimental sequence, pulses are only provided within a millisecond window after a quantum gas generation cycle of 30 seconds. Thus, a second collinear laser[30] beam is used as pilot for the beam stabilization. The superposition and separation is realized by two interference filters[31]. Subsequent additional spectral filters ensure negligible pilot laser power entering the ionization chamber.

The beam line including the active beam stabilization was designed, set up and characterized together with Donika Imeri in her bachelor work [109]. In this configuration, the beam sta-

[26] Light Conversion, HIRO Customizable Harmonic Generator for PHAROS
[27] Femtochrome, FR-103XL
[28] Light Conversion, ORPHEUS Collinear Optical Parametric Amplifier
[29] TEM Messtechnik, Aligna 4D
[30] Schäfter + Kirchhoff, 51nanoFCM-830-8-H19-P-5-2-28-0-150
[31] Semrock Inc., Laser beam splitter HC BS R785

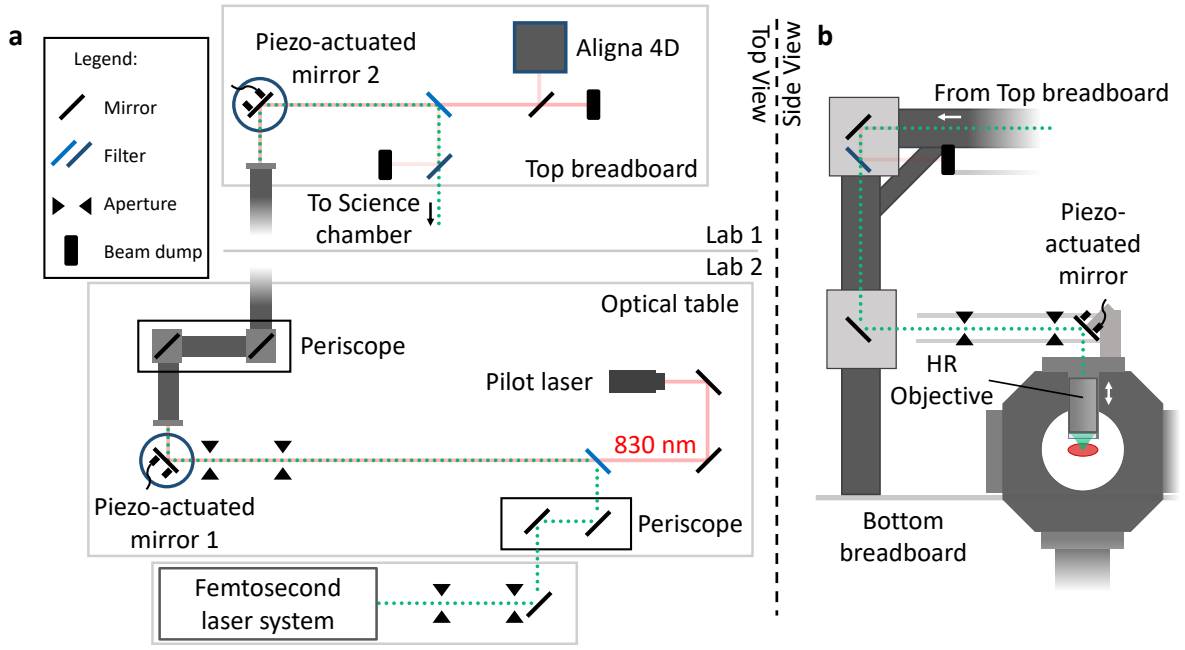

Figure 2.24: Active beam stabilization. a. The femtosecond laser is superimposed with a continuous wave pilot laser, which is used for the beam stabilization. The Aligna 4D system measures position and angle deviations and actively compensates them by controlling two piezo-actuated mirrors (blue circles). **b.** Beam path to the Science chamber. A periscope as well as a piezo-actuated mirror allow for coarse and fine alignment of the femtosecond laser beam onto the atomic cloud.

bilization system attains an attenuation of pointing fluctuations by 20 dB up to a bandwidth of 100 Hz, thus achieving a maximum fluctuation amplitude of 70 µm. Even though this amplitude significantly exceeds the waist of the dipole trap beams and thus the extent of the BECs, it only corresponds to a fluctuation of 70 µrad in the incidence angle of the femtosecond laser beam and translates to negligible displacement of the focus position of the high-resolution objective (see Chapter 2.3.3) ensuring reproducible experimental conditions over multiple days.

2.3.3. Diffraction limited micrometer focus

In order to allow local manipulation of a Bose-Einstein condensate, a micrometer-sized ionization volume within the atomic target is required. For this purpose, a commercially available apochromatic high-resolution objective[32] is used, which provides a numerical aperture NA = 0.5. The working distance of 13.89 mm is realized by the use of a re-entrant viewport. In this configuration the objective provides a theoretical minimal focus size of 600 nm when being compensated by a window with 3.5 mm thickness [95], which is done by adding microscope slides to the re-entrant window. Within this work, a total thickness of 3 mm was used, thus reducing the resolving power by a factor of 1.5.

Precise knowledge of the focal size of the laser is crucial since it determines the ionization probabilities within the atomic cloud. On that account, the laser focus for a central wavelength of 511 nm, which is used for the measurements in Chapter 4, was determined with a

[32] Mitutoyo, G Plan Apo 50x

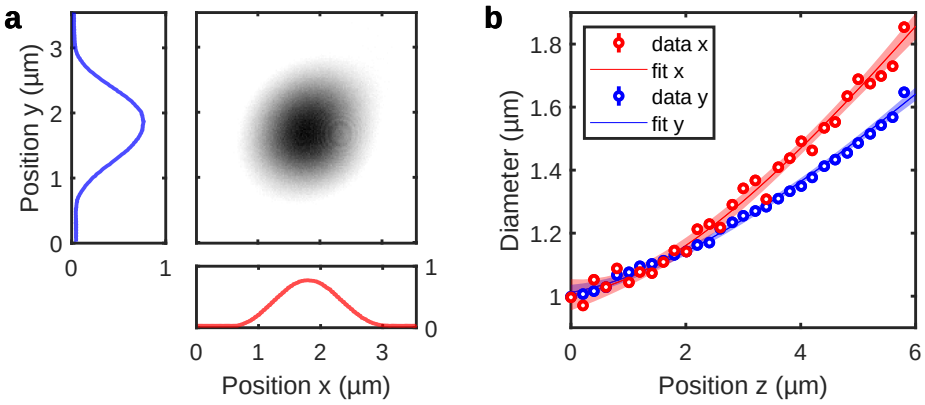

Figure 2.25: Femtosecond laser Focus measurement. **a.** False-color image of the focused femtosecond laser beam at 511 nm wavelength. The row sum and column sum profile of the focal intensity distribution are shown (blue/red line). **b.** Measured beam diameter in x- and y-direction as a function of the objective position. The solid lines correspond to the diameter profile fitted to the data points. The shaded areas indicate the 95 % confidence interval of the fit.

second, identical objective. The intensity distribution obtained in the focus plane is displayed in Fig. 2.25a. The distributions were imaged by a second objective [33] with a numerical aperture of $NA = 1.25$ and a magnification of 100 onto a camera. Figure 2.25b depicts the beam diameters in two dimensions for different objective positions in the beam propagation direction. These are obtained by fitting 2D Gaussian profiles to the intensity distributions. The focus characterization gives a beam waist of $w_1 = 0.99(3)$ µm and $w_2 = 1.00(5)$ µm and a Rayleigh length of $z_{\mathrm{R},1} = 5.3(2)$ µm and $z_{\mathrm{R},2} = 4.1(2)$ µm. Compared with the calculated Rayleigh length of $z_{\mathrm{R}} = \pi w_{1/2}^2/\lambda = 6.1$ µm this yields a beam quality factor of $M_1^2 = 1.14$ and $M_2^2 = 1.50$ attributable to the reduced amount of glass used behind the focusing objective.

Figure 2.24b shows the utilized beam path for the alignment onto the objective. A periscope provides the degrees of freedom to coarsely align the femtosecond laser beam onto the objective. The fine-adjustment is executed by use of a piezo-actuated mirror [34] directly in front of the objective. For focusing, the objective mounting enables translation with micrometer resolution in the beam propagation direction. In addition, the mount enables translation in both perpendicular directions to adjust the focus position relative to the crossed dipole trap.

2.3.4. Intensity calibration

For the prediction of ionization probabilities and generated charge carrier distributions not only the spatial and temporal intensity profile but also the actual value of the peak intensity I_0 is fundamental. The pulse energies $E_{\mathrm{P}} = P/f_{\mathrm{rep}}$ can be inferred from the averaged laser power P at a given pulse repetition rate f_{rep} and determine the applied peak power $P_0 = E_{\mathrm{P}}/\left(\sqrt{2\pi}\tau\right)$ including the rms pulse duration $\tau = \tau_{\mathrm{FWHM}}/\left(2\sqrt{2\ln(2)}\right)$. The applied peak intensities I_0 are

[33] Edmund Optics, 100X DIN Achromatic Commercial Grade Objective
[34] Newport Corporation, Picomotor Actuator 8301NF

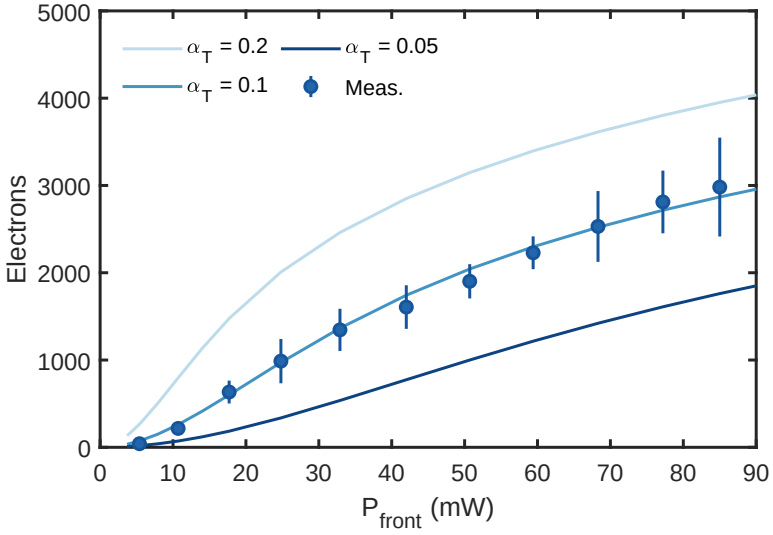

Figure 2.26: Intensity Calibration. Measured numbers of created electrons for different laser powers P_{front} at $U_{\text{ext}} = 200$ V (data points) as well as the calculated numbers of electrons assuming a transmittance of 0.2, 0.1 and 0.05 (solid lines). Figure is taken from [2] and licensed under CC BY 4.0.

then given by

$$I_0 = \frac{2P_0}{\pi w_1 w_2}. \tag{2.9}$$

The experimental setup only provides access to the femtosecond laser power before passing the high resolution microscope objective. As the transmittance α_T critically depends on collimation, pointing and angle of the incident laser beam, the actual peak intensities inside the vacuum chamber have to be calibrated. The averaged laser power used for the calculation of the applied peak intensity in the focus is given by $P = \alpha_T P_{\text{front}}$. Here, P_{front} denotes the power in front of the objective, which is measured through a circular aperture with the same diameter as the objective aperture (4 mm) at a pulse repetition rate of 100 kHz. Figure 2.26 shows the measured number of created photoelectrons in a BEC at an extraction voltage of $U_{\text{ext}} = 200$ V. The solid lines depict the expected numbers of electrons assuming a transmittance of 0.2, 0.1 and 0.05, which are calculated with the absolute ionization probabilities reported in Chapter 3.1 and in the publication [1]. The best agreement is obtained for $\alpha_T = 0.1$. As a result, the peak intensity can be tuned up to $I_0 = 6 \times 10^{13}$ W/cm^2.

2.4. Conclusion

In this chapter, the experimental setup was presented, which enables photoionization experiments with ultracold atomic samples of ^{87}Rb held in an optical dipole trap. First, the quantum gas machine is introduced, which provides generation of Bose-Einstein condensates with a typical cycle time of 30 s. During this cycle, the atoms are first laser cooled and then further cooled by RF forced evaporation in a hybrid trap. After optical transport into a second vacuum chamber, the atoms are evaporatively cooled to quantum degeneracy in a crossed optical dipole trap. The density distribution of the neutral atoms can be recorded by absorption imaging with a spatial resolution of 3.5 µm.

In the second part, the charged particle detection is presented, which allows for spatially resolved electron and ion detection by use of imaging MCPs. A gated detection scheme furthermore allows for electron detection with temporal resolution in the ten nanosecond domain. Disturbing stray electric fields are passively shielded and stray magnetic fields are compensated by a cage of compensation coils.

In the last part, the femtosecond laser system is described, which generates femtosecond laser pulses at the fundamental wavelength of 1022 nm, the second-harmonic wavelength of 511 nm and additionally between 210-2900 nm by optical parametric amplification. A beam line using active beam stabilization transports the femtosecond laser light to the high-resolution microscope, which focuses the light into the BEC with a waist of $w_1 = 0.99(3)$ µm and $w_2 = 1.00(5)$ µm. This enables local instantaneous photoionization at peak intensities up to $I_0 = 6 \times 10^{13}$ W/cm^2.

3. Ultracold atoms in ultrashort laser pulses

Clouds of ultracold atoms exhibit negligible thermal atomic motion and high experimental control over target size and density and enable accurate diagnostics by absorption imaging. Thus, they serve as an ideal atomic target for accurate investigations of the atomic response to the strong light field of ultrashort laser pulses. In the following chapter the two main mechanisms, photoionization and optical dipole forces, of this strong-field interaction are studied.

In section 3.1 the strong-field photoionization of ^{87}Rb atoms with femtosecond laser pulses is investigated. After a short summary on the basic mechanisms of strong-field ionization, the experimental method is introduced which employs absorption imaging of the local atomic losses allowing an accurate extraction absolute ionization probabilities. In addition, the measured ionization yields for non-resonant two-photon and resonance-enhanced four-photon ionization at central wavelengths of 511 nm and 1022 nm are presented and compared quantitatively to the ionization losses predicted by different strong-field ionization models. The data shown in this section is mainly taken from [1].

In section 3.2 the gradient forces exerted by the inhomogeneous focal intensity distribution of the femtosecond laser pulses onto a BEC are studied. For this purpose, the momentum transfer of repulsive femtosecond laser pulses is quantified in time-of-flight measurements. The resulting matter wave halos can be used as atomic beam sources with an ultracold longitudinal beam temperature of 20(5) nK. In addition, attractive laser pulses for ultrafast compression of a BEC and the suitability for a crossed pulsed dipole trap are investigated.

The acquisition and evaluation of the presented experimental data in the following chapter was performed in cooperation with Juliette Simonet, Philipp Wessels-Staarmann and Bernhard Ruff.

3.1. Absolute strong-field ionization probabilities of ultracold ^{87}Rb atoms

Extending the high experimental control established for ultracold atomic systems to the preparation of ultracold atom-ion and electron systems requires profound knowledge of the utilized strong-field ionization processes. The nature of these processes decisively affects the dynamics of the created charge carriers. In the transition from the multiphoton to the tunneling ionization regime a drastic modification of the photoelectron spectra has been observed in rare gas atoms [127]. For increasing ionizing intensities, a discrete periodical structure, which is evoked by atomic resonances induced by the AC Stark shift [128], dissolves into a continuous energy spectrum of photoelectrons.

In order to distinguish ionization processes, accurate quantitative tests for the validity of different models of strong-field ionization are inevitable. Such tests depend on reliable experiments accessing absolute ionization probabilities. The experimental challenge is given by the non-linear dependence on experimental properties as the atomic target density distribution, ex-

cited state fraction and detection efficiencies as well as photon-flux and geometrical alignment of the ionizing laser pulse. Precise measurements of ionization cross sections are performed with laser cooled atomic samples captured in magneto-optical traps [129, 130], where the increase of the trap loss rates is measured as an ionizing laser beam is switched on. The high sensitivity of this method enables measuring low ionization rates, but relies on the calibration of the significant excited state fraction caused by the resonant photon absorption and re-emission cycles utilized in laser cooling. The excited state contribution to the ionization rates can be avoided by switching the MOT and ionizing beams in an alternating mode [131–133].

Here, an alternative experimental methodology is presented, which exploits high experimental control over ultracold ^{87}Rb atomic targets trapped in an off-resonant optical dipole trap as well as the ionizing femtosecond laser pulses. Resonant absorption imaging of the atomic cloud before and after application of the pulse provides access to both, the target densities and the ionization losses. For this reason, absolute strong-field ionization probabilities for ^{87}Rb are determined experimentally and are compared to various ionization models.

3.1.1. Basics of strong-field ionization

The advance of high-intensity laser sources in the past decades has triggered a variety of investigations on the photoionization of single atoms subjected to strong-laser fields. Comprehensive overviews on this widespread topic can be found in various review papers [33, 35–37]. In the following, the basic qualitative concepts of the different ionization models are presented as well as their inherent quantitative predictions of ionization rates.

In order to distinguish different intuitive regimes of strong-field ionization, traditionally the Keldysh adiabacity parameter [134] γ is used, which relates the atomic ionization potential E_I to the ponderomotive potential U_P.

$$\gamma = \sqrt{\frac{E_\mathrm{I}}{U_\mathrm{P}}} \quad \text{with} \quad U_\mathrm{P} = \frac{e^2 I}{2c\varepsilon_0 m_e \omega^2} \tag{3.1}$$

The ponderomotive potential is given by the time-averaged kinetic energy of the quiver motion of a free electron in the presence of a driving laser field. Thus, it depends on the angular frequency ω and intensity I of the laser.

Figure 3.1 gives an overview on three main intuitive ionization models. In the case of small laser intensities ($\gamma \gg 1$), a perturbative ionization description within the multiphoton-ionization (MPI) model can be applied. Here, the ionization dynamics is described by transitions from unperturbed electronic states to the ionization continuum induced by photon absorption from the light field (see Fig. 3.1a). As the laser intensity increases ($\gamma \ll 1$), the potential gradient created by the strong light field significantly distorts the binding Coulomb potential and typically a field description of the ionization mechanisms is required. In the tunnel ionization (TI) regime the ionization process can be described by the tunneling of the valence electron through the Coulomb barrier (see Fig. 3.1b) created by the superposition of light and ionic Coulomb field.

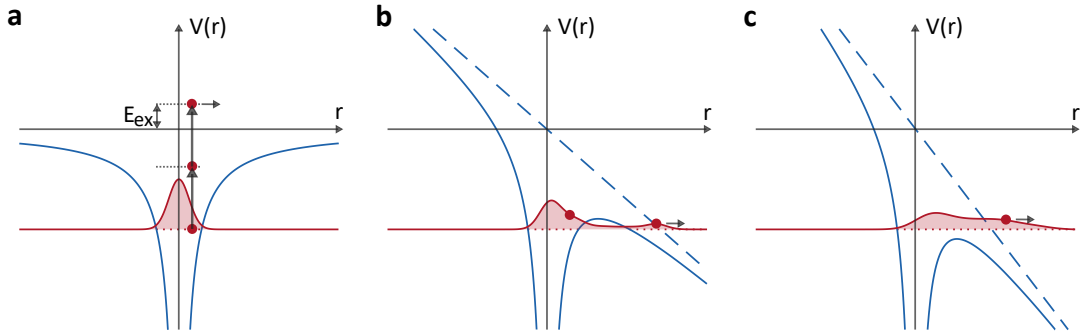

Figure 3.1: Regimes of strong-field ionization. a. The valence electron (red) is captured in the Coulomb potential of the ion (solid blue line). For low intensities ($\gamma \gg 1$) the electron is excited to the ionization continuum by photon absorption resulting in a kinetic energy given by the excess energy. **b.-c.** For increasing intensities ($\gamma \ll 1$), the potential gradient of the laser field (dashed blue line) deforms the Coulomb potential resulting in a potential barrier. The ionization process is then given by the quantum mechanical tunneling through the barrier (b) or classically by the electron being dragged over the barrier (c).

Further increase of the intensity leads to suppression of the Coulomb barrier to the point where the electronic ground state is not bound anymore. In this so-called over-the-barrier ionization (OBI) regime the atom is classically torn apart by the laser field (see Fig. 3.1c).

Multiphoton ionization

For low laser intensities ($\gamma \gg 1$) the photo-ionization process can be described within time-dependent perturbation theory, where the dipole interaction operator $\hat{D}$ is treated perturbatively and induces transitions between different eigenstates of the non-interacting hamiltonian of the atom. Assuming the atom is initially in the electronic ground state $|i\rangle = |g\rangle$, the transition rate $\Gamma_{e,f}$ to a different eigenstate $|f\rangle = |e\rangle \neq |g\rangle$ is given to the lowest order of the interaction operator by Fermi's Golden rule

$$\Gamma_{e,f} \propto |\langle f|\hat{D}|e\rangle|^2, \tag{3.2}$$

with the dipole operator $\hat{D} = e\vec{E}_\mathrm{L}\vec{r}$ and the electric field $\vec{E}_\mathrm{L}$ of the laser. This formula can be extended for multi-photon excitations into the continuum. For example, the two-photon transition or ionization rate is given by

$$\Gamma_{e,f} \propto |\sum_m \langle f|\hat{D}|m\rangle\langle m|\hat{D}|e\rangle|^2 \tag{3.3}$$

with the sum over all intermediate bound and continuum eigenstates $|m\rangle$ of the non-interacting Hamilton operator. For higher n-photon ionization processes, $n-1$ intermediate states have to be taken into account. As the scalar product $\langle m|\hat{D}|n\rangle$ for each m,n is proportional to the electric field amplitude E_L, the multiphoton ionization rate for a n-photon ionization process scales with

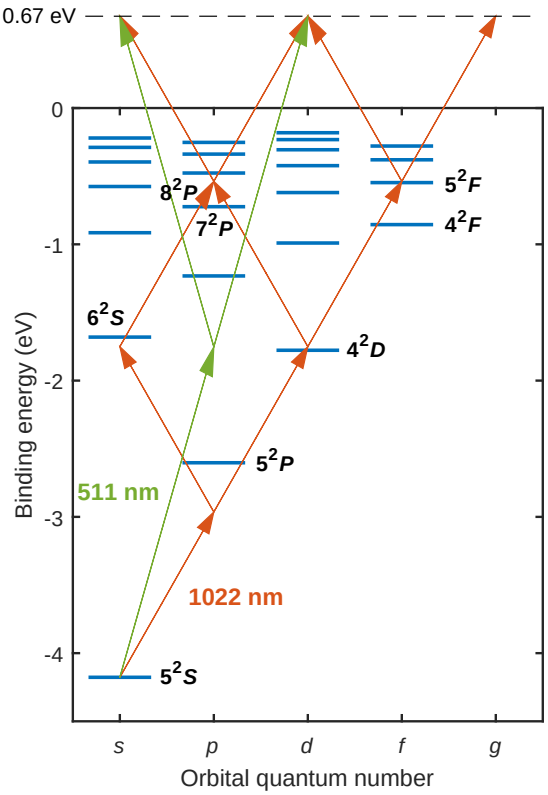

Figure 3.2: Multiphoton transitions and ^{87}Rb electronic energy levels. The dipole transition pathways are illustrated for the two-photon ionization process at 511 nm (green arrows) and the four-photon ionization at 1022 nm (red arrows). The dashed black line indicates the excess energy of 0.67 eV, which is almost entirely transferred to the photoelectron. The two-photon process avoids atomic resonances, while for the four-photon process, the 4^2D and 5^2F excited states are energetically close enough for resonance-enhanced photoionization. Figure taken from [1] and licensed under CC BY 4.0.

the laser intensity I_L to the power of n [35]

$$\Gamma_n = \sigma_n \times I_\mathrm{L}^n \tag{3.4}$$

with the generalized multiphoton cross section σ_n. This intensity scaling has been verified for the first time for atomic helium [135]. For the measurements presented in this chapter, the second harmonic of the femtosecond laser (see Chap 2.3.1) at a central wavelength of 511.4 nm was used for two-photon ionization as well as the fundamental wavelength of 1022 nm to investigate four-photon ionization. The corresponding generalized cross sections are taken from the literature and are given by $\sigma_2 = 1.5 \times 10^{-49}$ cm^{4}s [133] and $\sigma_4 = 1.32 \times 10^{-107}$ cm^{8}s^3 [136].

Figure 3.2 shows the unperturbed electronic energy levels of ^{87}Rb extracted from experimental values in the NIST database [137]. Furthermore, it contains the dipolar transition pathways for ionization wavelengths of 511 nm and 1022 nm. Whereas the two-photon process clearly avoids atomic resonances, the four-photon process approaches the 4^2D and 5^2F states, which are in reach for resonant ionization. The fundamental wavelength λ_F and FWHM bandwidth $\Delta\lambda_\mathrm{F} = 4.36$ nm correspond to a photon energy of $\Delta E_\mathrm{F} = 1.21$ eV and a spectral bandwidth

of $\Delta E_{\mathrm{F}} = (hc/\lambda_{\mathrm{F}}^2)\Delta\lambda_{\mathrm{F}} = 5.18$ meV. Accordingly, the 5^2F state, which is separated from the 5^2S state by 3.63 eV, is accessible for resonant three-photon excitation within the bandwidth of $3(E_{\mathrm{F}} \pm \Delta E_{\mathrm{F}}) = (3.64 \pm 0.02)$ eV. The excess energy E_{ex} of 0.67 eV given by

$$E_{\mathrm{ex}} = n\hbar\omega - E_{\mathrm{I}} \tag{3.5}$$

is almost entirely transferred to the released electron due to the large electron-ion mass ratio, e.g. $1/(1.59 \times 10^5)$ for ^{87}Rb.

At elevated intensities additional photons can be absorbed in the ionization process. This process is dubbed above-threshold ionization (ATI) [138–140]. The excited electron of the s-th ATI ends up with a kinetic energy given by the excess energy of $E_{\mathrm{ex}} = (n+s)\hbar\omega - E_{\mathrm{I}}$. The first ATI for the photoionization of ^{87}Rb at a wavelength of 511.4 nm corresponds to an excess energy of 3.1 eV.

The discrete spectrum of photoelectron energies predicted by the MPI model is significantly modified for increasing laser intensities as the continuum states experience a ponderomotive shift towards higher energies in the presence of the pulse. This shift is evoked by the intensity-dependent ponderomotive potential, which has to be additionally provided by the ionizing photons. As the ponderomotive potential is not a conservative potential, the electrons do not regain the required potential energy for sufficiently short laser pulses [128, 141]. Accordingly, the created photoelectrons end up with the excess energy given by the relation $E_{\mathrm{ex}} = (n+s)\hbar\omega - E_{\mathrm{I}} - U_{\mathrm{P}}$ with the ponderomotive potential U_{P} in the moment of ionization. For sufficiently high intensities, the ponderomotive shift can even close n-photon ionization channels, when the effective ionization potential in the presence of the laser pulse exceeds the n-photon energy.

Besides shifting the continuum states relative to the bound electron states, the strong laser fields also cause relative energy shifts between the bound states due to the AC-Stark effect which depends on the polarizability of each orbital state. Accordingly, the intensity-dependent shifts enable dynamical resonances in the presence of the pulse leading to a splitting of the observed photoelectron lines [128]. As the weakly bound valence electron in alkali atoms provides comparably high polarizabilities even for the electronic ground state, the influence of the AC Stark shift is expected to become dominant for sufficiently high laser intensity [142–144]. The substantial shifts allow to implement coherent control methods to selectively tune transient population transfer between different bound states during the pulse [145].

Tunnel and over-the barrier ionization

As the laser pulse peak intensity is further increased, atomic states involved in the ionization process are significantly perturbed by the increasing electric field. Thus, the resulting time-dependent-deformation of the ionic Coulomb potential has to be taken into account and a de-

scription of electronic trajectories in a driving laser field becomes relevant [146]. For high laser intensities ($\gamma \ll 1$), the superposition of the ionic Coulomb potential and the potential gradient evoked by the laser field leads to the formation of a potential barrier [147–149] (see Fig. 3.1b). Photoionization can be described as the tunneling of the valence electron trapped in the effective potential though this barrier.

At a Keldysh parameter much smaller than unity, the tunneling time

$$\omega_{\mathrm{tun}}^{-1} = \sqrt{\frac{2c\varepsilon_0 m_{\mathrm{e}} E_{\mathrm{I}}}{e^2 I}} \tag{3.6}$$

is much shorter than the period of the light field $\omega_{\mathrm{tun}}^{-1} \ll \omega^{-1}$ and the electric field can be treated by a quasi-stationary approximation [35]. The ionization probability in this regime is determined by the tunneling rate of the valence electron within the Ammosov-Delone-Krainov (ADK) model [148]. The time-averaged rate is given by

$$w_{\mathrm{ADK}} = |C_{n^*0}|^2 \sqrt{\frac{6}{\pi R(I)}} \frac{E_{\mathrm{I}}}{\hbar} \times R^{2n^*-1}(I) \exp\left(-\frac{R(I)}{3}\right) \tag{3.7}$$

where

$$R(I) = \frac{4E_{\mathrm{I}}^{\frac{3}{2}}}{\hbar e} \sqrt{\frac{\varepsilon_0 c m_{\mathrm{e}}}{I}} \tag{3.8}$$

and

$$|C_{n^*0}|^2 = \frac{2^{2n^*}}{n^* \Gamma(n^*+1)\Gamma(n^*)}. \tag{3.9}$$

Here, Γ denotes the Gamma function and n^* indicates the effective principal quantum number

$$n^* = Z\sqrt{\frac{E_{\mathrm{I,H}}}{E_{\mathrm{I}}}}. \tag{3.10}$$

using the ionic charge state Z and the ration between the ionization potential E_{I} and the ionization potential of hydrogen $E_{\mathrm{I,H}} = 13.6$ eV.

Beyond a critical laser intensity I_{OBI}, the tunnel barrier is suppressed to the point where the barrier maximum undercuts the ground state energy and the valence electron can classically escape the Coulomb potential within over-the-barrier ionization. In this intensity regime, the ionization probability is assumed to equal unity. The corresponding intensity

$$I_{\mathrm{OBI}} = \frac{\pi^2 c \varepsilon_0^3 E_{\mathrm{I}}^4}{2Z^2 e^6} = 1.22 \times 10^{12}\ \mathrm{W/cm^2} \tag{3.11}$$

non-linearly depends on the ionization potential and thus strongly on the regarded atomic species.

Time-dependent Schrödinger equation

At a Keldysh parameter close to unity the intuitive models of photoionization can not be applied a priori to describe strong-field ionization and a numerical treatment of the ionization process becomes inevitable. This was also disclosed experimentally in former investigations accessing this regime for alkali atoms [150–152]. As a consequence, *ab-initio* calculations are required, which numerically solve the time-dependent Schrödinger equation (TDSE). The corresponding simulated data shown here were obtained in calculations performed by Andrey K. Kazansky and Nikolay M. Kabachnik.

For this purpose, the ^{87}Rb atom is described within the single active electron approximation by a model interaction potential of the valence electron with the positive rubidium ion, which is adapted to recreate the experimentally well-known energy levels of the electronic ground state and the lower lying excited states. Before exposure to the light field, the atom is constituted in the 5^2S ground state. Subsequently, the time-dependent population of the regarded excited states is calculated by solving the TDSE for the coupled system according to the pulse parameters used in this experiment. This allows to extract both, ionization probabilities and excited state fractions during and after pulse exposure. A more detailed description can be found in [1].

Model ionization probabilities

For a quantitative analysis of the photoionization processes occurring in the experiment, the predicted ionization rates of each ionization model are calculated, which determine the number of ionized atoms per time-interval. In general, these ionization rates $w(t)$ depend on the instantaneous intensity $I(t)$ of the laser given by the temporal intensity envelope of the pulses. When combinations of ionization models are used, the total ionization rate is calculated as the maximum of both rates.

$$w(t) = \max\{w_1(t), w_2(t)\} \tag{3.12}$$

For a given ionization rate $w(t)$, the time-dependent ionization probability $P(t)$ can be inferred by solving the resulting differential equation

$$\frac{\mathrm{d}P(t)}{\mathrm{d}t} = [1 - P(t)]\, w(t). \tag{3.13}$$

The solution is given by

$$P(t) = 1 - \exp\left(-\int_{-\infty}^{t} w\left(t'\right) \mathrm{d}t'\right). \tag{3.14}$$

The experimental method only allows to access the ionization probabilities P after illumination

with the laser pulse. The corresponding modeled probability is then given in the limit $t \to \infty$ by

$$P = \lim_{t\to\infty} P(t). \tag{3.15}$$

3.1.2. Preparation of ultracold atomic targets

The measurements presented in this chapter have been performed at the former quantum gas setup, which was rebuilt and updated within this work to the stage as described in Chap. 2. This setup has been consisting of the 2D-MOT glass cell and the pumping chamber (see Chap. 2.1.1) with a second glass cell attached, where the 3D-MOT and hybrid trap has been located. A more detailed description can be found in the PhD thesis of Bernhard Ruff [95] and Alexander Grote [153].

Even though both setups differ, a similar experimental cycle was used. After evaporation into the vacuum from a dispenser, the atoms are trapped in a 2D-MOT and subsequently moved to the 3D-MOT by a near-resonant pushing beam. After a MOT loading time of 12 s, the atoms are further cooled down by a bright optical molasses for 4 ms and transferred into a hybrid trap. Here, the hybrid trap is formed by the combination of a magnetic quadrupole field and a crossed non-resonant optical dipole trap at 1064 nm. The atoms are cooled by forced radio-frequency evaporation in the hybrid trap and after switching off the magnetic field, a second stage of evaporative cooling is employed by successively reducing the laser power in the crossed dipole trap. Whereas condensed targets are utilized for the dipole force measurements in the second part of this chapter, the strong-field ionization measurements are exerted by the use of a purposely dilute and thermal atomic sample, which facilitates the *in-situ* determination of atom numbers. The different atomic targets are achieved by tuning the evaporation efficiency and the final intensity values of the two dipole trap beams after evaporation. For the measurements reported here at 511 nm ionizing wavelength, the atomic clouds with $1.43(5) \times 10^4$ atoms are prepared at 109(5) nK temperature and for 1022 nm the atomic clouds with $1.53(11) \times 10^4$ atoms are prepared at 90(8) nK temperature.[35]

3.1.3. Measuring absolute local losses

Figure 3.3 gives a schematic overview on the methodology. A single femtosecond laser pulse is focused down into the ultracold sample, locally ionizes atoms within the atomic target and resulting in a volume of reduced density within the cloud. The remaining atomic density distribution is subsequently recorded by resonant absorption imaging onto a CCD camera with a spatial resolution of 3.0(5) µm. The detection scheme employs an imaging pulse of 50 µs duration at a wavelength of 780 nm, resonant to the D_2 transition in ^{87}Rb. In contrast to MOT

[35] For the measurements at 511 nm wavelength the atomic samples are held in an optical DT with radial/axial trap frequencies of $\nu_a = 26(3)$ Hz and $\nu_r = 129(9)$ Hz leading to an in-situ radial/axial rms cloud size of $\sigma_a = 23.9(4)$ µm and $\sigma_r = 6.94(9)$ µm. For the measurements at 1022 nm wavelength the atomic samples are held in an optical DT with radial/axial trap frequencies of $\nu_a = 29(3)$ Hz and $\nu_r = 211(2)$ Hz leading to a radial/axial rms cloud size of $\sigma_a = 26.3(9)$ µm and $\sigma_r = 10.1(2)$ µm after 2 ms time-of-flight.

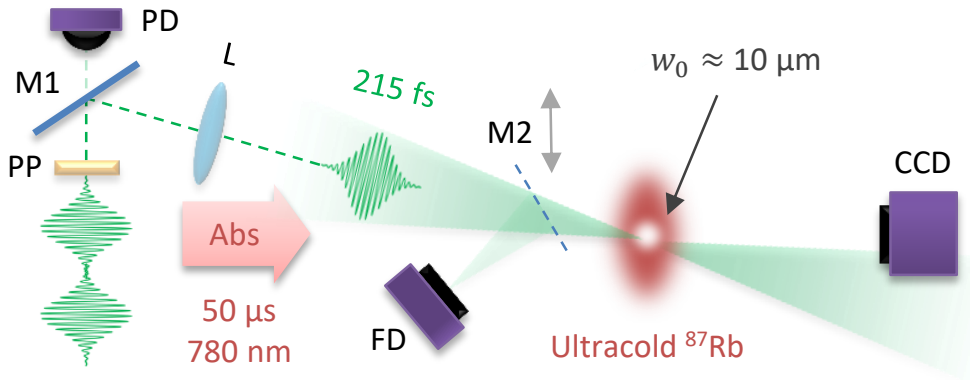

Figure 3.3: Quantitative measurement of strong-field ionization probabilities in ultracold ^{87}Rb. A pulse-picker (PP) selects a single femtosecond laser pulse, which is focused down by a $f = 200$ mm lens (L) to a waist of $w_0 = 10$ µm into a cloud of ultracold ^{87}Rb held in an optical dipole trap. Local photoionization results in a volume of reduced density within the atomic cloud. The remaining atomic density distribution is imaged onto a CCD camera (CCD) by use of resonant absorption imaging. The leakage through a mirror (M1) is exploited to simultaneously measure the applied pulse energy with a photodiode (PD). A moveable mirror (M2) enables imaging the focus intensity profile onto a diagnostics camera (FD). Figure taken from [1] and licensed under CC BY 4.0.

atomic targets, the nanokelvin temperatures of the ultracold atomic target provide negligible atomic motion of a few hundred nanometers during the absorption pulse, which is well below the imaging resolution. Thus, the imprinted density reduction can be imaged in real space and the measured local atomic density losses directly provide access to the absolute ionization probabilities. The dilute thermal atomic sample is utilized to ensure accurate determination of the optical densities, which is limited by the dynamic range and the noise level of the 12-bit CCD camera to a maximum value of $OD_{\max} = 3.7$ before saturation correction.

For the measurements at 511 nm, the femtosecond laser pulse is applied in-situ, while the atoms are optically trapped, whereas the pulses at 1022 nm were applied after a time-of-flight duration of 2 ms. This is required to circumvent ionization losses caused by the pulse leakage from the oscillator cavity through the pulse picker. Due to their intensity below the conversion threshold of the SHG, these pulses do not affect the measurements at 511 nm. Within each measurement, the applied pulse energy E_p is recorded by a calibrated measurement of the leakage through a mirror (see Fig. 3.3) by use of a silicon photodiode. In addition, the spatial intensity distribution of the laser pulses in the focal plane is measured for both wavelengths. For this purpose, the pulses are reflected onto the focal diagnostics camera by a moveable mirror between the focusing lens and the atoms.

3.1.4. Calculation of photoionized fraction

The measured focal intensity profiles for both wavelengths are depicted in figure 3.4a,b. Here, z denotes the pulse propagation direction and x/y correspond to the two radial directions. The spatial intensity distributions in the focal plane in combination with the measured pulse duration give rise to the 3D spatio-temporal intensity profile $I(x,y,z,t)$, which can be calculated as

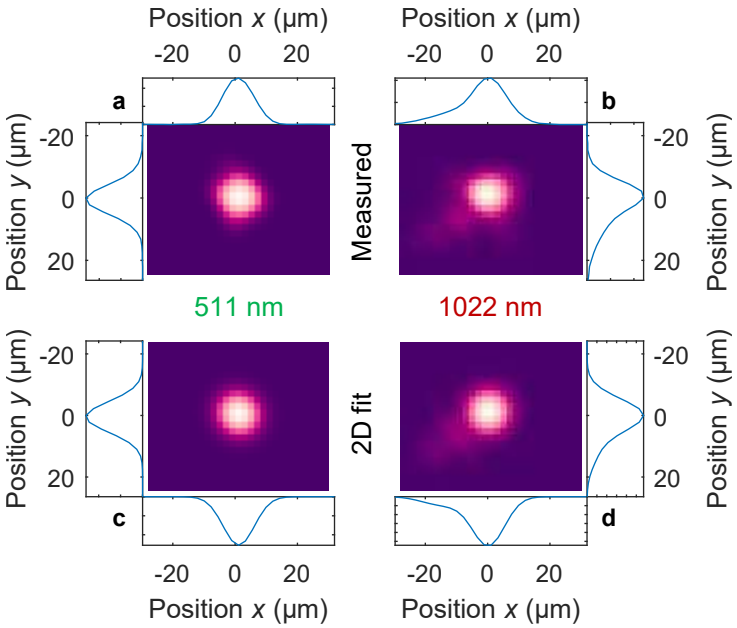

Figure 3.4: Femtosecond laser intensity distributions in the focal plane. a.-b. Measured intensity profile for 511 nm and 1022 nm. **c.-d.** Intensity profiles obtained by the 2D-fit to the measured data according to Eq.3.18. For both the measured and reconstructed intensity profiles the row and column sums are depicted for a camera/grid pixel size of 2.2 x 2.2 μm^2. Figure taken from [1] and licensed under CC BY 4.0.

$$I(x,y,z,t) = I_{\text{peak}}(x,y,z) \times \exp\left(-\frac{t^2}{2\tau}\right), \tag{3.16}$$

with

$$I_{\text{peak}}(x,y,z) = I_0 \times \sum_{k=1}^{3} A^k \frac{w_{0x}^k w_{0y}^k}{w_x^k(z) w_y^k(z)} \exp\left(-\left[\frac{2x^2}{w_x^k(z)^2} + \frac{2\left(y-y_0^k\right)^2}{w_y^k(z)^2}\right]\right) \tag{3.17}$$

the peak intensity with respect to time for each point in space. Here, I_0 denotes the global peak intensity of the spatio-temporal profile

$$I_0 = \frac{2P_0}{\pi \sum_{k=1}^{3} A^k w_{0x}^k w_{0y}^k}, \tag{3.18}$$

which is determined by the peak power $P_0 = E_{\text{p}}/\left(\sqrt{2\pi}\tau\right)$ including the pulse energy E_{p} as well as the rms pulse duration $\tau = \tau_{\text{FWHM}}/\left(2\sqrt{2\ln(2)}\right)$. The sum accounts for the different elliptical Gaussian features $k \in \{1, 2, 3\}$ contributing to the overall intensity profile including the offset along the y direction y_0^k. For each of these profiles the waist in the direction $i \in \{x, y\}$ is given by $w_i^k(z) = w_{0i}^k \sqrt{1 + \left(z/z_{\text{R}i}^k\right)^2}$, where $z_{\text{R}i}^k = \pi {w_{0i}^k}^2/\lambda$ denotes the Rayleigh length. In addition, A^k stands for the amplitude of each profile, with $\sum_{k=1}^{3} A^k = 1$. The relative amplitudes as well as the widths are obtained by 2D Gaussian fits at $z = 0$ to the measured focal intensity profiles according to Eq. 3.18. The fit results are displayed in (see Fig. 3.4c,d). In the case of 511 nm contributions apart the main Gaussian profiles are negligible, whereas for the 1022 nm

case two additional focal features have to be taken into account, since they contain a fourth of the pulse energy. The fit results are given in Tab. 1.3 (see Appendix).

In order to compare the measured experimental results to the ionization probabilities according to different ionization models, the expected loss fraction has to be determined in a 3D simulation including the cloud and beam properties given by the experiment. As a reference, the unperturbed atomic density profile is recorded after time-of-flight measurements without ionization pulse, which allows reconstructing the 3D atomic density distribution ρ_a during pulse application for a known dipole trap configuration. Determined by the measured focal intensity distributions and pulse durations of the femtosecond laser pulses, each point in space experiences a Gaussian temporal intensity profile with a peak intensity $I_\mathrm{peak}(x,y,z)$ according to Eq. 3.18. Thus, for a given global peak intensity I_0, the spatial distribution of ionization probabilities $P(x,y,z)$ can be inferred for each ionization process. The theoretically expected distribution of ionized atoms $\rho_i(x,y,z)$ for the different models is then calculated by superimposing the atomic density map $\rho_a(x,y,z)$ with the obtained distributions of ionization probabilities.

$$\rho_i(x,y,z) = \rho_a(x,y,z) \times P(x,y,z) \tag{3.19}$$

Consequently, the remaining atomic density distribution after photoionization $\rho_f(x,y,z)$ is given by

$$\rho_f(x,y,z) = \rho_a(x,y,z) \times [1 - P(x,y,z)]\,. \tag{3.20}$$

Figure 3.5a depicts the absorption image of the remaining density profile of the atomic cloud after exposure to a single femtosecond laser pulse with a peak intensity $I_0 = 6.9^{+0.7}_{-0.8} \times 10^{12}$ W/cm^2 at a wavelength of 511 nm. By photoionization, the laser pulse locally reduces the density of the atomic cloud, which remains unchanged over the imaging timescales. This gives direct access to the local atomic losses due to photoionization in different intensity regimes. For comparison, the computed remaining density distribution applying the ionization probabilities according to numerical TDSE calculations is shown in Fig. 3.5b.

For a quantitative analysis, the row sum profiles of both the experimental data (gray crosses) and the theoretical predictions (dashed red line) are displayed in Fig. 3.5b. The two profiles show notable agreement without any free parameters. In order to access the integrated fraction of atoms lost by ionization, two Gaussian profiles

$$\Sigma_\mathrm{OD} = A_0 + A_\mathrm{c} \exp\left(-\frac{(x-x_\mathrm{c})}{2\sigma_\mathrm{c}^2}\right) - A_\mathrm{v} \exp\left(-\frac{(x-x_\mathrm{v})}{2\sigma_\mathrm{v}^2}\right) \tag{3.21}$$

are fitted to the experimentally obtained profiles. Here, A_0 denotes an offset, $A_\mathrm{c}/A_\mathrm{v}$, $x_\mathrm{c}/x_\mathrm{v}$ and $\sigma_\mathrm{c}/\sigma_\mathrm{v}$ correspond to the amplitude, central position and width of either the atomic cloud (c) or the imprinted vacancy due to density reduction (v). The fraction of lost atoms f_l is then derived as the ratio between the number of ionized N_i and the initial atom number N_0.

$$f_\mathrm{l} = \frac{N_\mathrm{i}}{N_0} = \frac{A_\mathrm{c}\sigma_\mathrm{c}}{A_\mathrm{v}\sigma_\mathrm{v}} \tag{3.22}$$

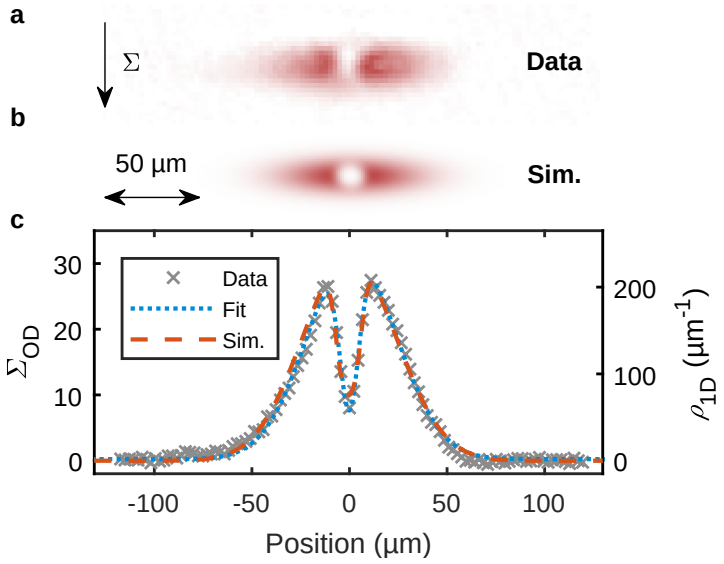

Figure 3.5: Quantification of the photoionization loss fraction in an ultracold atomic target. Measured (**a.**) and calculated (**b.**) 2D projection of the atomic density distribution after photoionization with a pulse at 511 nm wavelength and a peak intensity of $I_0 = 6.9^{+0.7}_{-0.8} \times 10^{12}$ W/cm^2. **c.** 1D density profiles determined by the row sum of the measured (gray crosses) and calculated (dashed red line) density distributions. The loss fraction is extracted by a double Gaussian fit to the obtained 1D profiles (dashed blue line, fit to the measured profile). Figure taken from [1] and licensed under CC BY 4.0.

The simulated loss fraction $f_\mathrm{l}^\mathrm{sim}$ is derived analogously from the modeled 1D profile with the computed ionization probabilities. Comparison of both the experimentally and theoretically obtained fraction for different pulse peak intensities gives a reliable measure for the validity of different ionization models.

3.1.5. Non-resonant two-photon ionization at 511 nm

Figure 3.6a displays the computed ionization probabilities for an atom being exposed to a single laser pulse at a wavelength of 511 nm as a function of the applied peak intensity. The resulting loss fractions $f_\mathrm{l}^\mathrm{sim}$ as well as the measured fractions f_l are presented in Figure 3.6b in double-logarithmic scaling for the same peak intensity range. The vertical axis on the right contains the absolute number of ionized atoms N_i given by the product of loss fraction and initial atom number. The measured atomic loss fraction (blue data points) increases monotonously with increasing peak intensity of the laser pulse, which is attributed to the rising ionization probabilities in Fig. 3.6a. Whereas the measured fraction scales asymptotically with I_0^2 as expected for a two-photon ionization process at low intensities (dotted red line), the slope decreases due to saturation for peak intensities higher than $I_0 = 5 \times 10^{12}$ W/cm^2. Here, the ionization probability reaches unity within the center of the focal region and the increase of the fraction of ionized atoms is caused by increasing ionization probabilities in the wings of the intensity profile.

The atomic losses predicted by numerically solving the TDSE (dashed red line) show remarkable agreement to the data points over the covered intensity range, which is even more conspicuous for the linearly scaled zoom into the graph illustrated in Fig. 3.6c. Due to the

precise knowledge of target size and density as well as the pulse intensity distribution, the theoretical curve is obtained without free parameters and thus can be compared on the level of absolute values to the experimental data.

Even though the TDSE method noticeably reproduces the measured data while solely relying on the single active electron approximation, it is useful to compare the measured loss fractions to the intuitive traditional ionization models as a test of validity for different peak intensities. Within the model of multiphoton ionization the ^{87}Rb atom needs to absorb at least two photons for ionization at a wavelength of 511 nm. The corresponding ionization probabilities are determined by use of the dedicated multiphoton ionization cross section $\sigma_2 = 1.5 \times 10^{-49}\text{cm}^4\text{s}$ at 511 nm [133]. The result is depicted in Fig. 3.6a as solid green line. Even though the perturbative description is strictly valid only for $\gamma \gg 1$, the computed MPI probabilities are almost equivalent to those obtained by ab-initio calculations even for the Keldysh parameter approaching unity.

A key difference in the photoionization of rare gas and alkali atoms is given by their disparity of valence electron binding energy. Thus, the ionic Coulomb field is exceeded by the electric field of the laser for much lower laser intensities in alkali atoms. Whereas the over-the barrier ionization intensity in rare gases is typically reached beyond 1×10^{14} W/cm^2 for 511 nm, in ^{87}Rb it is already attained at $I_{\text{OBI}} = 1.2 \times 10^{12}$ W/cm^2 (vertical dashed black line) at a Keldysh parameter of $\gamma = 8.4$. The fact that the OBI intensity is reached within the multiphoton intensity regime has been discussed in previous experimental [150, 152] and theoretical [154, 155] work. As a simple approach for the combined ionization process of MPI and OBI, the ionization probability is assumed to equal the MPI probabilities and is set to one for intensities exceeding the OBI intensity (purple line in Fig. 3.6a). The resulting expected loss fraction is given by the dashed purple line in Fig. 3.6b-c. Due to the vast increase of the ionization probabilities above I_{OBI}, the combined model including the contribution of OBI significantly overestimates the experimentally obtained loss fraction.

Despite the Keldysh parameter reaching values below unity within the experimentally accessible peak laser intensities, the predicted ionization losses of the ADK model of tunnel ionization [148] are as well compared to the measured data. Such a comparison is motivated by a significant contribution of tunnel-ionization in rare gas atoms at values of the Keldysh parameter still exceeding unity. For this purpose, a combined ionization probability for MPI and tunnel ionization (see Chapter 3.1.1) is employed, the obtained loss fractions are depicted as dashed yellow lines in Fig. 3.6b-c. Even though the tunnel ionization probabilities only exceed the MPI probabilities for the small intensity range above 1.2×10^{12} W/cm^2, the contribution of the tunnel ionization causes a predicted loss fraction that significantly deviates from the error bars of the experimentally obtained data. This disregards contributions from tunnel-ionization at Keldysh parameters close to unity and, furthermore, discloses the sensitivity of the applied method, which allows to resolve subtle modifications of the ionization probability curve.

The conventional adiabatic models of OBI and TI lead to significant deviations between the predicted loss fractions and the experimental data. This hints at a breakdown of the quasi-static

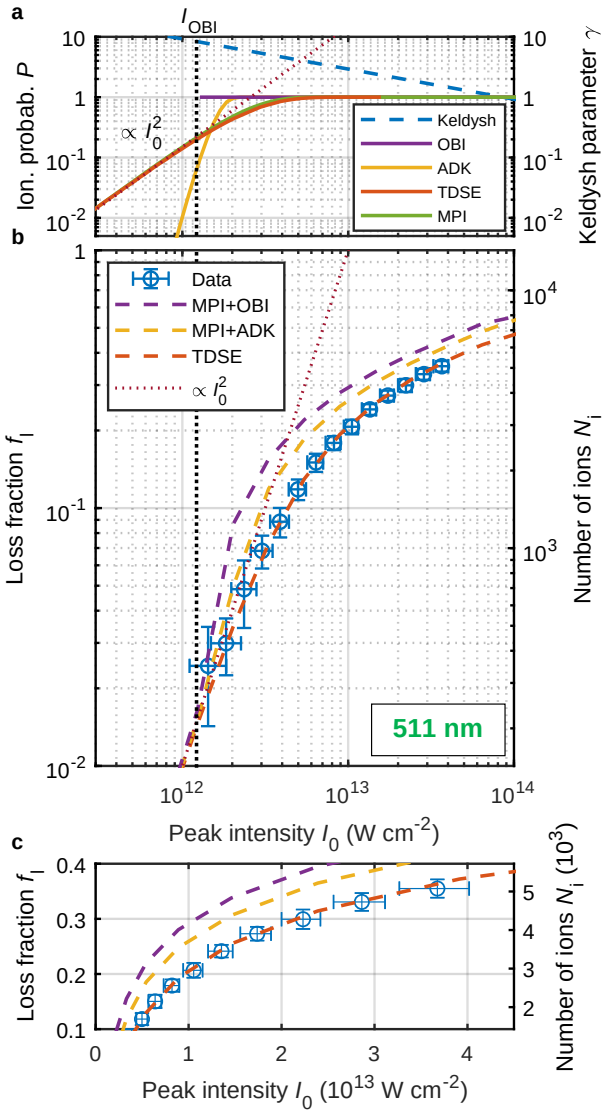

Figure 3.6: Non-resonant strong-field ionization yield of ^{87}Rb at 511 nm. a. Keldysh parameter (dashed blue line) and ionization probabilities for different ionization models after a single femtosecond laser pulse with respect to the applied peak intensity I_0. **b.** Measured fraction of atoms lost by ionization f_l (blue data points) after exposure to one pulse. The dashed lines indicate the simulated loss fractions f_l^{sim} predicted by numerical time-dependent Schrödinger equation (TDSE) calculations (red) and combined models using multiphoton ionization (MPI) for low intensities and Ammosov-Delone-Krainov (ADK) theory (yellow) as well as over-the-barrier ionization (purple). Both combined models overestimate the measured ionized fraction. The over-the-barrier intensity according to Eq. 3.11 is given by the vertical dotted black line. The dotted red line indicates the I_0^2 scaling expected for a two-photon process. **c.** Same data set plotted in a linear scaling. Vertical error bars are given by the standard deviation of the individual loss measurements, horizontal error bars are given by the standard deviation of the binned intensity including systematic errors of the intensity measurement. Figure taken from [1] and licensed under CC BY 4.0.

approximation within the model of an adiabatic deformation of the Coulomb binding potential, which is expected due to the Keldysh parameter being bigger than unity. As a consequence, one has to determine ionization probabilities by numerical TDSE calculations, which reproduce the measured data perfectly. Furthermore, the measurements reveal a dominant contribution of multiphoton ionization in agreement with previous experiments [150–152] and theory [154,

155] for alkali atoms.

3.1.6. Resonant multiphoton ionization at 1022 nm

Analogous to the measurements at 511 nm wavelength, ionization measurements were conducted at the fundamental wavelength of 1022 nm of the femtosecond laser. Here, due to the halved photonic energy, at least four photons are required to ionize the ^{87}Rb atom (see Fig. 3.2). Figure 3.7a depicts the calculated ionization probabilities obtained by numerically solving the TDSE. In comparison with the predictions for 511 nm, ionization probabilities of a few percent are reached within considerably lower intensities. In addition, even though the ionization probability for a non-resonant four-photon process is expected to scale with I_0^4, a slope corresponding to a I_0^2 scaling (dashed red line) is observed for small intensities. Both, the enhanced ionization probabilities as well as the scaling are result from an ionization process involving resonant atomic levels.

Figure 3.7b displays the measured loss fraction and the corresponding number of created ions in dependency of the applied pulse peak intensity (blue data points). In addition, the predicted ionization losses obtained by numerically solving the TDSE are depicted (red dashed line). Considering the absence of any scaling parameters, the TDSE calculations show remarkable agreement with the measured data over the full intensity range. The minor discrepancy is attributed to the complex femtosecond laser intensity distribution in the focal plane compared to the 511 nm case (see Fig. 3.4b) and eventually might be resolved by a more sophisticated intensity model accounting for additional subtle features. In addition, the intensity profile can be cleaned up experimentally by use of a spatial filter.

In the unperturbed limit, the 4^2D excitation from the electronic ground state requires an photonic energy of 2.40 eV, lying outside the spectral bandwidth of the two-photon energy of 2.43 eV. In the presence of the strong-light field of the femtosecond laser pulse, the energy levels experience a time-dependent AC Stark shift. Consequently, energy levels are shifted in and out of resonance within the temporal intensity profile of the pulse. Beyond excellent reproduction of the measured ionization fractions, the TDSE method grants access to the population of bound states after and even during the ionizing pulse shedding light on the excitation dynamics. Thus, it allows to distinguish between a 2 + 1 + 1 photon process including the 4^2D and 5^2F state and a 3 + 1 photon process solely involving the 5^2F resonance.

For this purpose, the electron wave packet after pulse exposure is projected onto the 5^2S ground state and the 5^2F intermediate state. The contribution of both states to the final electronic state is depicted in Fig.3.8a in dependency of the applied peak intensity. In addition, the population sum over all bound states is shown, which is generally used to derive the ionization probability. Evidently, the depopulation of the electronic ground state with increasing intensity is caused by population of both the 5^2F excited state and non-bound, i.e. ionized states, whereas the 4^2D intermediate state shows negligible population after the pulse.

In order to illustrate the complex excitation dynamics during one pulse, Fig. 3.8b depicts

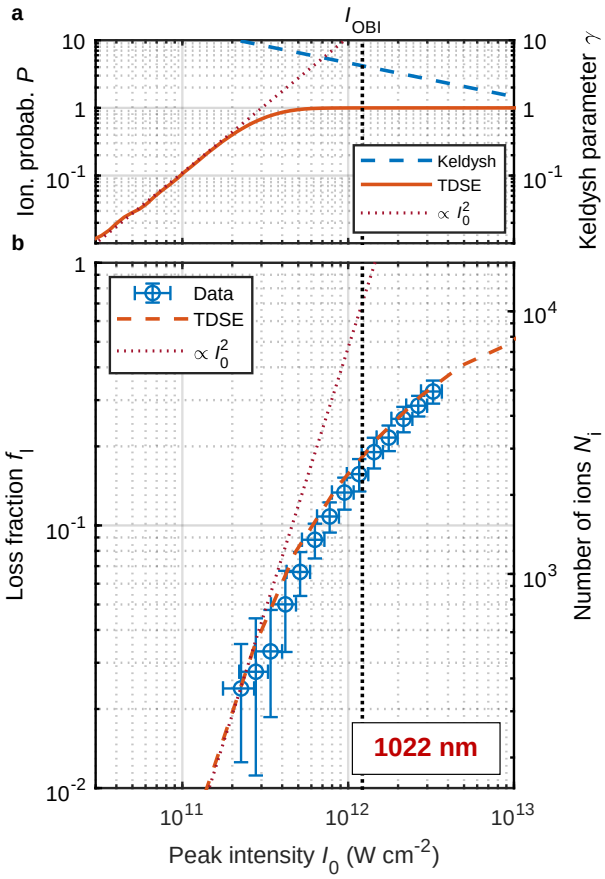

Figure 3.7: Resonant strong-field ionization yield of ^{87}Rb at 1022 nm. a. Keldysh parameter (dashed blue line) and ionization probabilities obtained by numerically solving the time-dependent Schrödinger equation (solid red line) after a single femtosecond laser pulse with respect to the applied peak intensity I_0. **b.** Measured fraction of atoms lost by f_l (blue data points) and loss fraction f_l^{sim} predicted by the TDSE calculations (dashed red line). The over-the-barrier intensity according to Eq. 3.11 is given by the vertical dotted black line. The dotted red line indicates a I_0^2 scaling for the ionization probabilities. Vertical error bars are given by the standard deviation of the individual loss measurements, horizontal error bars are given by the standard deviation of the binned intensity including systematic errors of the intensity measurement. Figure taken from [1] and licensed under CC BY 4.0.

the dynamics of the bound-state populations for a pulse with a Gaussian envelope at a pulse duration of 300 fs (FWHM) and a peak intensity of $I_0 = 7 \times 10^{10}$ W/cm^2. Even though the final electron wave function after pulse exposure shows negligible population of the 4^2D state, a significant transient population is evident in the presence of the pulse that contributes to the enhanced ionization rates. Apparently, the three considered bound states exhibit a Rabi-type population transfer with an oscillation frequency around 7 THz. In addition, for the 5^2S and 5^2F state population this oscillation is superimposed with a second oscillation at approximately twice the laser frequency, which is barely resolved in Fig. 3.8b. This clearly suggests a two-photon population transfer process in agreement with the obtained asymptotic I_0^2 scaling of the ionization probabilities. The observation of intensity- and time-dependent oscillations in the final state population is in accordance to related theoretical investigations for alkali atoms [154–156].

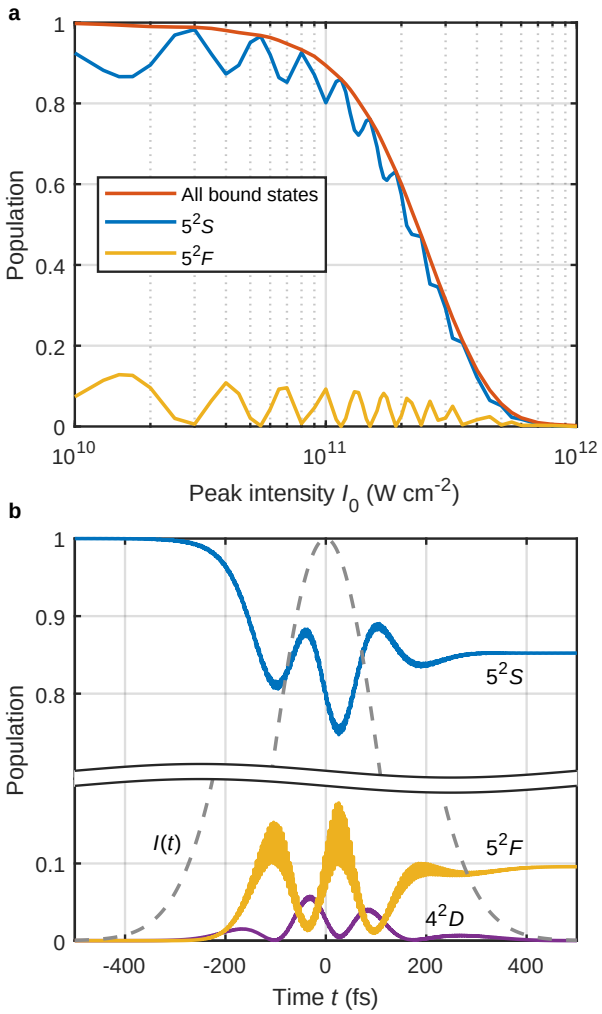

Figure 3.8: Simulated bound-state populations. a. The final bound-state population after exposure to a Gaussian laser pulse of 300 fs duration (FWHM) is shown with respect to the applied peak intensity I_0 for the 5^2S electronic ground state (blue line), the 5^2F excited state (yellow line) and for the sum over all ^{87}Rb bound states (red line). **b.** Time-dependent populations of the 5^2S (blue line), 4^2D (purple line) and 5^2F (yellow line) state in the course of a Gaussian pulse intensity envelope with a peak intensity of $I_0 = 7 \times 10^{10}$ W/cm^2 (dashed gray line). Figure taken from [1] and licensed under CC BY 4.0.

The presented experimental method determining absolute ionization probabilities relies on absorption imaging utilizing resonant excitation of the remaining atoms from the 5^2S electronic ground state. Thus, one may wonder if this method is suitable to accurately attain the bound and thus not ionized fraction of atoms, when a significant fraction of the remaining atoms populates the 5^2F state. Fortunately, the absorption of a single imaging photon at 780 nm is sufficient to transfer the valence electron from the 5^2F excited state to the continuum. Thus, our method is sensitive on ionization and correctly attributes the excited state fraction to non-ionized atoms. As a result, the ionization probabilities can be derived as the difference of the bound state population from unity.

3.1.7. Conclusion

As a summary, absolute ionization probabilities have been measured for non-resonant two-photon and resonance-enhanced four-photon ionization of ultracold ^{87}Rb atoms with femtosecond laser pulses. The measurements access the transitional regime, where both the ionization probability and the Keldysh parameter are around unity. In contrast to the widely used rare gas atoms, alkali atoms have a single valence electron in combination with a high polarizability and low ionization potential. This makes them an ideal, simple model system to study strong-field physics.

The presented experimental method employs an ultracold atomic target at a temperature of approximately 100 nK captured in an optical dipole trap. By absorption imaging of both the atomic target with and without pulse application, the ratio of ionized atoms can be extracted. The measured data is compared to the predicted losses for different ionization models without any free parameter and shows a good agreement with ionization probabilities calculated by ab-initio TDSE calculations.

Whereas atoms trapped in a MOT rely on a confining magnetic field and inherently show a significant excited state fraction, photoionization of an ultracold atomic ensemble in a far-detuned optical dipole trap simplifies subsequent momentum-resolved electron and ion spectroscopy [157]. Additionally, the access to absolute ionization probabilities can be used to calibrate absolute detector efficiencies for ultracold atoms experiments using charged particle detectors.

As a focused laser beam exhibits a variety of acting laser intensities, the accuracy of strong-field photoionization measurements typically suffers from focal-averaging. The presented method allows to break this obstacle as it enables a pixel-wise evaluation of the photoionization probabilities. As a result, this allows for simultaneous measurement of the ionization yield at several peak intensities given by the intensity distribution of the beam and thus facilitates measurements with laser pulse sources with fluctuating pulse parameters. In addition, pixel-wise analysis of the ionization yield enables direct comparison to theoretical calculations, which are typically performed for single peak intensities. Furthermore, absorption imaging allows for a spatially resolved selective detection of populated intermediate bound states by tuning the imaging pulse wavelength.

Moreover, interesting future experiments will examine the influence of Bose-Einstein condensation onto strong-field ionization with femtosecond laser pulses. Previous investigations have targeted this topic, but conclude with differing statements, whether ionization rates in- or decrease for a condensed sample [158, 159].

3.2. Strong-field acceleration of ultracold atoms

Alongside photoionization, the strong light field of ultrashort laser pulses allows for manipulation of ultracold quantum gases by strong forces in the intensity gradient of the focused pulses [158, 160]. Former experimental realizations report on deflection of an effusive beam of noble gas atoms exerted by a single femtosecond laser pulse yielding accelerations of 10^{14} times the Earth's gravitational acceleration [161]. The controlled deflection of cold atomic samples enables the creation of atomic beams with narrow velocity spread of a few m/s [162] required for cold collision [163, 164] and cold chemistry experiments [165, 166]. Furthermore, using ultrashort laser pulses for trapping and cooling of ultracold atomic targets has been proposed theoretically [167–170] and examined experimentally [171–175].

Here, the creation of matter wave halos created by radial acceleration of a BEC using blue detuned femtosecond laser pulses is reported. These halos constitute ultracold atom sources with beam temperatures in the nanokelvin range. Additionally, the compression of a BEC by red-detuned pulses and their feasibility for crossed pulsed dipole traps is examined and discussed.

3.2.1. Gradient forces in strong light fields

The high intensity gradients of focused ultrashort laser pulses allow exerting significant time-dependent forces onto neutral atoms. Analogously to strong-field photoionization, an accurate description of gradient forces in inhomogeneous strong light fields depends on the acting laser intensity and frequency of the pulses as well as the electronic structure of the exposed atom. For alkali atoms in the low intensity limit, where a perturbative treatment of the AC Stark shift exerted by the alternating laser field is accurate, the forces are given by the interaction of the induced atomic dipole with the electric field of the laser [119]. For increasing intensities approaching the tunnel regime, the force on the neutral atom can be described by the ponderomotive force on a quasi-free electron [160, 161], which recombines with the remaining ion after pulse exposure in a process called frustrated tunnel ionization [176].

Time-dependent transient optical dipole forces

This experiment tests the validity of the dipolar model for different pulse energies by measuring the momentum transfer after a train of ultrashort laser pulses. According to Eq. 2.4, for each time t, the ultrashort laser pulse evokes a potential energy proportional to its instantaneous intensity $I(\vec{r},t)$. Figure 3.9a shows the dipole potential in the focal plane for different times during pulse application for a pulse at a central wavelength of 511 nm and 75 µJ pulse energy. Accordingly, an atom at point $\vec{r}$ experiences a force $\vec{F}_{\mathrm{dip}}(\vec{r},t) \propto -\vec{\nabla} I(\vec{r},t)/\delta$, which accelerates the atoms according to the Gaussian intensity profile of the pulses. Here, δ denotes the detuning of the laser with respect to the D_2 transition in ^{87}Rb. In one dimension, the transferred momentum per pulse is given by the integrated force with respect to time

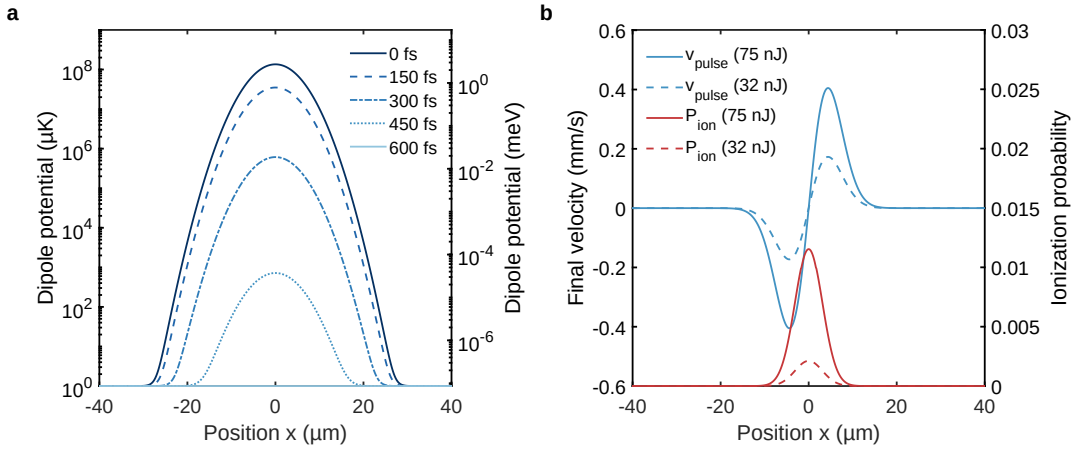

Figure 3.9: Dipole potential of the femtosecond laser pulse. a. Dipole potential of the repulsive femtosecond laser field on a single ^{87}Rb atom in the focal plane calculated for a pulse energy of 75 nJ, a mean waist size of $w_{\mathrm{mean}} = 8.8$ µm and a central wavelength of 511 nm according to Eq. 2.4. The different potentials reflect linear time-steps during the pulse after the peak intensity is reached. **b.** Final velocities after pulse exposure calculated from the spatially dependent momentum transfer according to Eq. 3.23 for pulse energies of 75 nJ and 32 nJ (solid/dashed blue line). In addition, the corresponding calculated TDSE ionization probabilities for a single pulse are given (red lines).

$$p_{\mathrm{pulse}}(x) = \int_{-\infty}^{\infty} F_{\mathrm{dip}}(x,t)\,\mathrm{d}t. \tag{3.23}$$

Figure 3.9b shows the final velocities $v_{\mathrm{pulse}}(x) = p_{\mathrm{pulse}}(x)/m_{\mathrm{a}}$ of the atoms after pulse exposure in relation to the position x in the focal plane for pulse energies of 75 nJ and 32 nJ (solid/dashed blue line), which correspond to peak intensities of $I_0 = 2.7 \times 10^{11}$ W/cm^2 and $I_0 = 1.2 \times 10^{11}$ W/cm^2. At 511 nm wavelength, the femtosecond laser pulses are blue detuned with respect to the D_2 transition in ^{87}Rb and thus the focal intensity gradient provides a repulsive dipole potential for the atomic cloud. As a consequence, the atoms are radially accelerated perpendicular to the beam propagation direction. The spatial intensity gradient of a Gaussian beam is proportional to the applied peak intensity, which allows controlling the momentum transfer by tuning the pulse energy. For both pulse energies, the ionization probability distribution of a single pulse (red lines) does not surpass 1.2% and thus can be neglected in this regime.

Measuring ultrafast momentum transfer

The momentum transfer onto the illuminated atoms is investigated within the same experimental setup as described in Sec. 3.1.2. Figure 3.10 schematically depicts the procedure of the measurement. A BEC held in the crossed optical dipole trap is illuminated by a train of femtosecond laser pulses at a central wavelength of 511 nm, a pulse length of 215^{+20}_{-15} fs and a repetition rate of $f_{\mathrm{rep}} = 100$ kHz. The pulses are focused onto the BEC with a waist of $w_{\mathrm{x}} = 8.3$ µm and $w_{\mathrm{y}} = 9.3$ µm enabling peak intensities up to of $I_0 = 10^{13}$ W/cm^2. The pulses arrive at an angle of 13.7° relative to the imaging axis (z) in the yz plane. After a variable time-of-flight, the

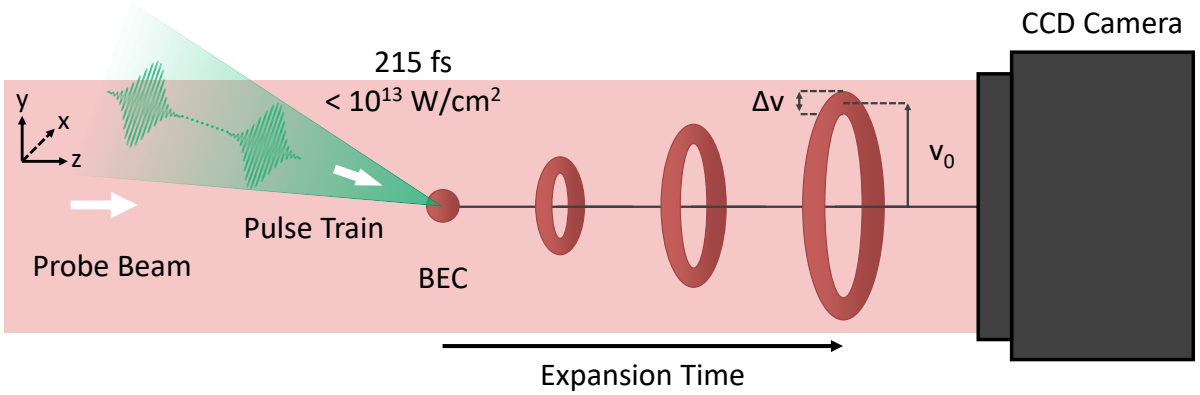

Figure 3.10: Measuring ultrafast momentum transfer. A BEC is held in a crossed optical dipole trap and is illuminated by a train of femtosecond laser pulses focused onto a waist of 10 µm. Due to transient optical dipole forces, the pulses accelerate the atoms perpendicular to the pulse propagation direction. After a variable expansion time, the atoms are recorded by absorption imaging with a resonant probe pulse. The absorption images give rise to the mean expansion velocity v_0 as well as the velocity spread Δv of the expanding density rings.

density distribution of the atomic ensemble is recorded by absorption imaging (see Sec. 2.1.6).

In addition, the momentum transfer onto the BEC can be described in terms of phase-imprinting onto the matter wave function. Here, the space- and time-dependent dipole potential $U_{\mathrm{dip}}(\vec{r},t)$ during one pulse imprints a space-dependent phase onto the BEC wave function $\psi \mapsto \psi e^{i\varphi(\vec{r})}$, where $\varphi(\vec{r}) = -\hbar^{-1}\int_{-\infty}^{\infty} U_{\mathrm{dip}}(\vec{r},t)\,\mathrm{d}t$. The resulting matter wave velocity $v(\vec{r})$ after application of a single pulse is then determined by the phase gradient as

$$\vec{v}(\vec{r}) = \frac{\hbar}{m_{\mathrm{a}}}\vec{\nabla}\varphi(\vec{r}) = \int_{-\infty}^{\infty} -\vec{\nabla}\frac{U_{\mathrm{dip}}(\vec{r},t)}{m_{\mathrm{a}}}\mathrm{d}t. \tag{3.24}$$

Through the relation $\vec{F}_{\mathrm{dip}}(\vec{r},t) = -\vec{\nabla}U_{\mathrm{dip}}(\vec{r},t)$ this corresponds to the momentum transfer due to optical dipole forces on single atoms in one dimension as described by Eq. 3.23.

3.2.2. Femtosecond acceleration of a BEC

As a reference, Fig. 3.11a shows the measured expansion of the unperturbed BEC density distribution after time-of-flight before the application of femtosecond laser pulses. First, the radius of the BEC is determined by a 2D Thomas-Fermi fit to the absorption images for different time-of-flights and then the expansion velocity is obtained by a linear fit to the evolution of the radius. This yields expansion velocities of the unperturbed BEC of $v_{\mathrm{x}} = 2.39(3)$ mm/s and $v_{\mathrm{x}} = 2.05(4)$ mm/s.

In Fig. 3.11b-d the time-evolution of the BEC density is depicted after illumination with 11 (b), 31 (c) and 51 (d) femtosecond laser pulses. The pulse trains are applied in-situ, while the dipole trap is switched on, and the atomic cloud is imaged after a variable subsequent time-of-flight. Evidently, one obtains a halo-like structure of a radially expanding matter wave, with an expansion velocity monotonously increasing with the number of applied pulses. In the center of the halo, a fraction of mainly thermal atoms expands with a velocity increasing with the number

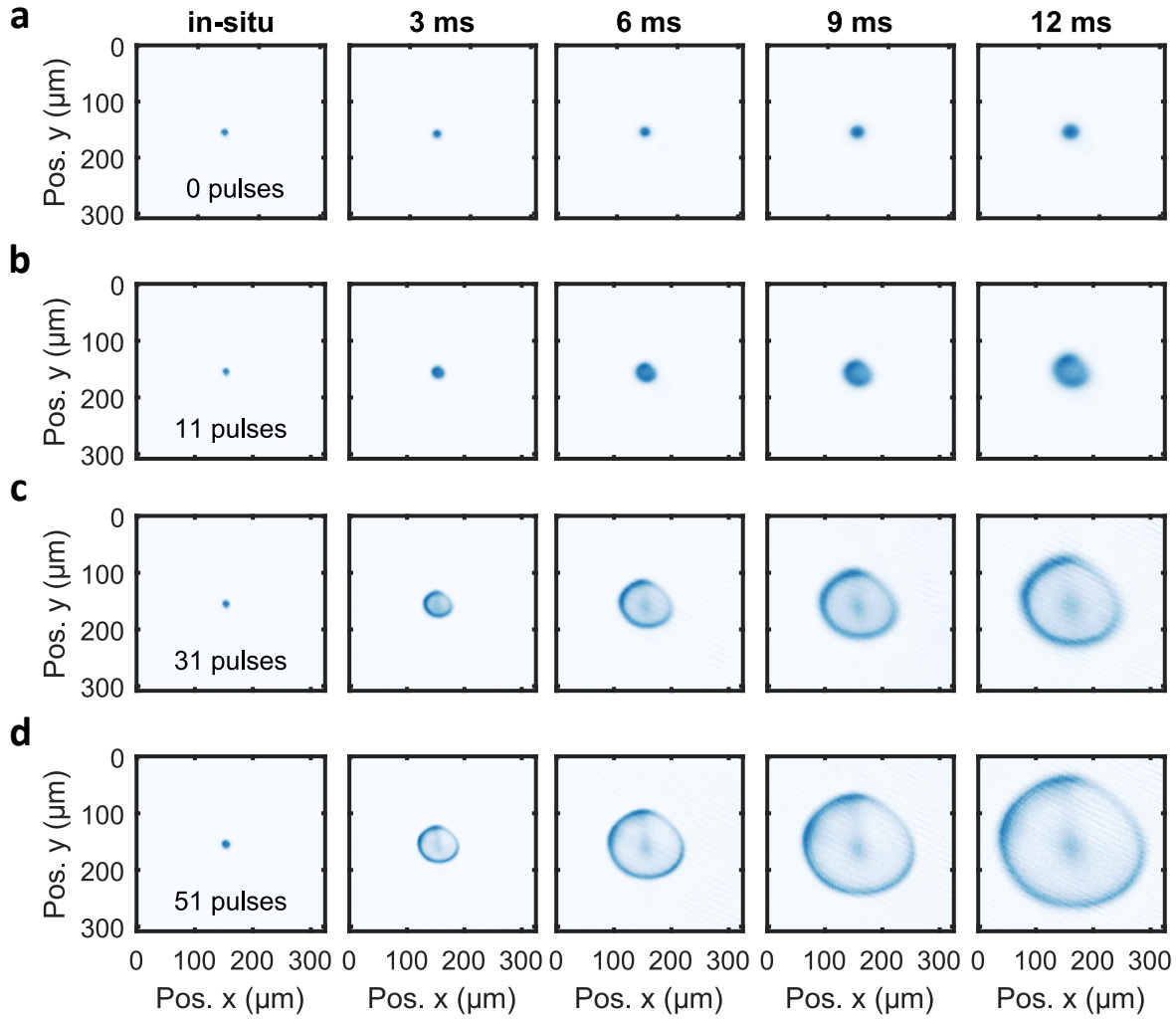

Figure 3.11: Matter wave halo expansion. Absorption images of the expanding BEC during time-of-flight without pulse exposure (a) and after application of 11 (b), 31 (c) and 51 (d) pulses at a pulse energy of 75 nJ. The images are averaged over more than eight realizations.

of applied pulses.

For a quantitative analysis of the expansion velocities, the density profile is determined by the row sum of a cut through the optical density distribution. Figure 3.12a shows the optical density for a BEC illuminated with 31 pulses of 75 nJ pulse energy. The row sum is calculated for the central area marked by the vertical black lines, which spans over 9 pixels around the maximum of the column sum profile of the optical density distribution. This width is chosen small enough to avoid an underestimation of the radius due to the halo curvature and large enough to gain a sufficient signal to noise ratio. The obtained profile is shown in Fig. 3.12b (data points). One clearly identifies three peaks in the density profile, two on the edges corresponding to the expanding ring and a broad central one given by the thermal background of the initial atomic distribution. In order to attain the halo radius for each time step and pulse number, a threefold Gaussian function

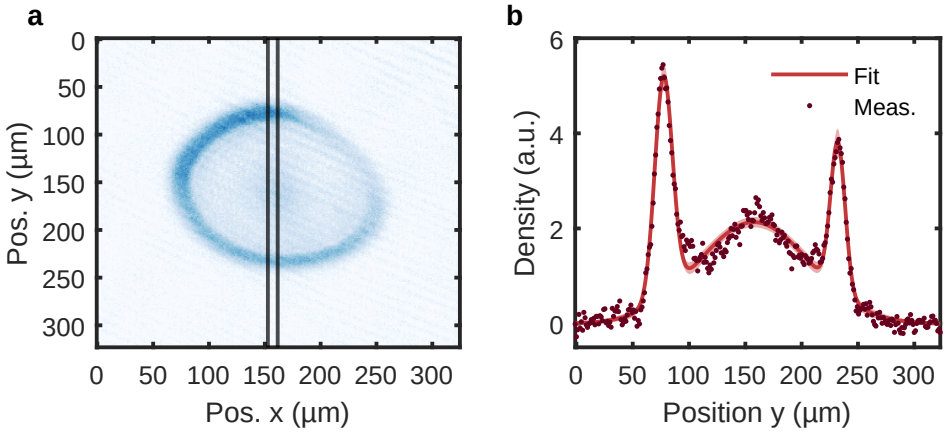

Figure 3.12: Expansion velocity extraction. a. Absorption image of a BEC after illumination with 31 pulses at 75 nJ pulse energy and 12 ms time-of-flight. The image is averaged over eight realizations. The black lines mark the area used for the row sum profile in (b). **b.** Row sum profile of the optical density distribution given in (a) (data points) and the threefold Gaussian function fitted to the data points according to Eq. 3.25 (solid red line). The light red area depicts the 95% confidence interval of the fit.

$$f(y) = d + \sum_{i=1}^{3} a_i \times e^{-\left(\frac{y-b_i}{c_i}\right)^2} \tag{3.25}$$

is fitted to the data points (solid red line). Here, a_i, b_i and c_i denote the amplitude, center position and width of each Gaussian profile and d accounts for a global offset. The indices assign the three peaks from top to bottom. For each applied pulse number the expansion velocity is determined by a linear fit to the evolution of the halo radius $(a_1 - a_3)/2$ in relation to the time-of-flight.

Figure 3.13a depicts the measured expansion velocities in dependency of the number of applied pulses for pulse energies of 75 nJ (dark data points) and 32 nJ (light data points). In addition, for both pulse energies the expected expansion velocity given by the momentum transfer of each pulse according to Eq. 3.23 is depicted (dashed lines). In this simple model, the transferred momentum of n pulses is given by $n \times p_{\text{pulse}}$, where $p_{\text{pulse}} = m_{\text{a}} \times 0.43$ mm/s and $p_{\text{pulse}} = m_{\text{a}} \times 0.19$ mm/s for a pulse energy of 75 nJ and 32 nJ, respectively. For few pulses the predicted momentum transfer according to the time-integrated optical dipole forces reasonably agrees with the measured expansion velocities. In contrast, for an increasing number of applied pulses, the measured velocities clearly deviate from the linear model due to the expansion of the atomic target during illumination with the pulse train. An illumination with 60 pulses corresponds to a pulse train duration of 600 µs. At a pulse energy of 75 nJ, atoms located around $x = 5$ µm, which experience the maximum terminal velocity of 0.43 mm/s per pulse (see Fig. 3.9), travel at least a distance 0.43 mm/s $\times 600$ µs ≈ 2.5 µm during the pulse train. As a result, these atoms end up beyond a position of $x \approx 7.5$ µm, where only a fraction of the maximum velocity is given by the last pulses. Thus, the transferred momentum saturates. For the lower energy pulses, this saturation occurs for an accordingly higher pulse number.

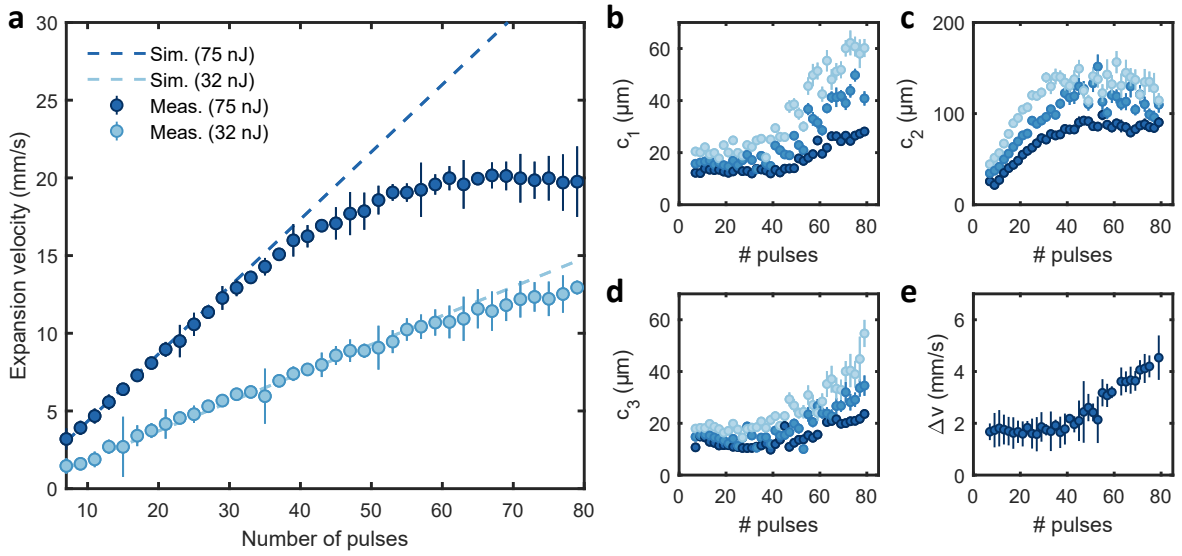

Figure 3.13: Halo expansion velocities and velocity spread. **a.** Expansion velocities of the matter wave halos in dependency of the applied number of pulses at a pulse energy of 75 nJ (dark data points) and 32 nJ (light data points). The expected expansion velocities determined by the sum of the transferred momentum per pulse for each pulse energy are given by the dashed lines. **b.-d.** Fit results of the widths c_1, c_2 and c_3 according to Eq. 3.25 after a time-of-flight of 6 ms (dark) , 9 ms (medium) and 12 ms (light data points) in relation to the number of applied pulses at 75 nJ pulse energy. **e.** Velocity spread Δv obtained by a linear fit to the time-evolution of the rms width of the rings $(c_1 + c_3)/2$. For 61 and 77 pulses reliable linear fitting of the expansion is impossible. Accordingly, the data points are excluded. All vertical error bars are given by the 95% confidence interval of each fit.

Ultracold Matter Wave Sources

Absorption imaging of the expanding matter wave halos during expansion allows for an accurate determination of the momentum transfer onto the atoms and reveals the precise tunability of the mean velocity of the atomic beams by the number of applied pulses. In addition to the mean expansion velocity, the quality of cold atom sources depends on the longitudinal temperature T_{beam} of the beam, which is determined by the rms width of the radial velocity spectrum through the relation $T_{\mathrm{beam}} = m_{\mathrm{a}}\Delta v^2/(3k_{\mathrm{B}})$. Besides measuring the halo expansion velocity, the Gaussian profiles fitted to the row sum profiles according to Eq. 3.25 provide access to the radial velocity spectrum by the time-evolution of the width of the rings $c_{1,3}$. Hence, this analysis allows to evaluate the created matter-wave halos with respect to their properties as cold atom sources.

Figure 3.13b-d shows the fit results for the rms widths c_i in relation to the number of pulses and time-of-flight duration. The width c_2 of the thermal background linearly expands with the number of pulses and saturates analogously to the halo expansion, when atomic motion during the pulse train becomes relevant. In contrast, the halo width, given by c_1 and c_2, is constant over low pulse numbers and increases approximately, where the halo expansion saturates. The corresponding velocity spreads Δv for each pulse number are determined by a linear fit to the time-of-flight evolution of the mean rms width of the rings $(c_1 + c_3)/2$ and are depicted in

Fig. 3.13e. In accordance to the halo widths, the velocity spread is constantly small around 2 mm/s as long as the imprinted velocity distribution is negligibly influenced by atomic motion and significantly increases for higher pulse numbers. For exposure with 51 pulses at 75 nJ pulse energy, one obtains an expansion velocity of $v_0 = 18.6(9)$ mm/s with an rms velocity spread of $\Delta v = 2.4(3)$ mm/s . This yields a ratio of $\Delta v/v_0 = 0.13(2)$, which surpasses atom lasers created by coupling out a magnetically trapped BEC by rf-radiation pulses [177] and is on the same order of magnitude as reported for the acceleration of magneto-optically trapped argon with in a chirped optical lattice of $\Delta v/v_0 < 0.05$ [162]. Moreover, this corresponds to a longitudinal beam temperature of $T_{\mathrm{beam}} = 20(5)$ nK, which undercuts the coldest thermal atom beam so far reported by one order of magnitude [177]. As a result, the high control over the transferred momentum per pulse and the applied pulse number allows for atomic beam creation with tunable mean velocities up to 20 mm/s with ultralow longitudinal beam temperatures.

Finally, the expanding ring-structure constitutes a radial matter wave source. Although coherence properties are not experimentally accessible as the imaging system can not resolve the expected interference patterns, for numerical simulations solving the Gross-Pitaevskii equation a coherent matter wave evolution is expected even for phase imprinting on infinitely short timescales. BECs on the surfaces of a sphere are typically only available under microgravity [178]. Atom sources employing radial acceleration of a BEC with ultrashort laser pulses can provide an alternative to bubble-shaped atom traps relying on rf-induced adiabatic potentials [179–181] for the creation of hollow BECs. Such BECs allow addressing topological issues by projecting the bulk wave function onto (parts of) the surface of a sphere [182–184].

Strong-field acceleration of a BEC

In order to minimize the ratio between the velocity spread and the expansion velocity and hence improve the source quality, the matter wave halo expansion is studied for the application of single pulses with peak intensities up to 10^{13} W/cm^2. This enables tuning the transferred momentum while avoiding atomic motion during the pulse train. Figure. 3.14 shows the free expansion of a BEC (a) and the expansion of a BEC illuminated with a single laser pulse with increasing pulse energy (b-d). Here, the pulse is applied after 8 ms time-of-flight. One clearly identifies a ring-like atomic density distribution as observed in the previous measurement with an expansion velocity correlated with the pulse energy. The less symmetric structure is attributable to beam artifacts in the focal plane, which were erased for the multi-pulse measurements. The quantitative analysis is performed analogously to the pulse number scan. Fig. 3.15a shows the row sum profile of the atomic density distribution after applying a pulse with 1.24 µJ pulse energy, which corresponds to a peak intensity of $I_0 = 4.5 \times 10^{12}$ W/cm^2, and 5 ms time-of-flight. In addition, the double Gaussian function fitted to the data is shown.

Figure. 3.15c illustrates the measured expansion velocity (data points) in relation to the pulse energy as well as the predicted expansion velocities according to Eq. 3.23 (dashed line). Ap-

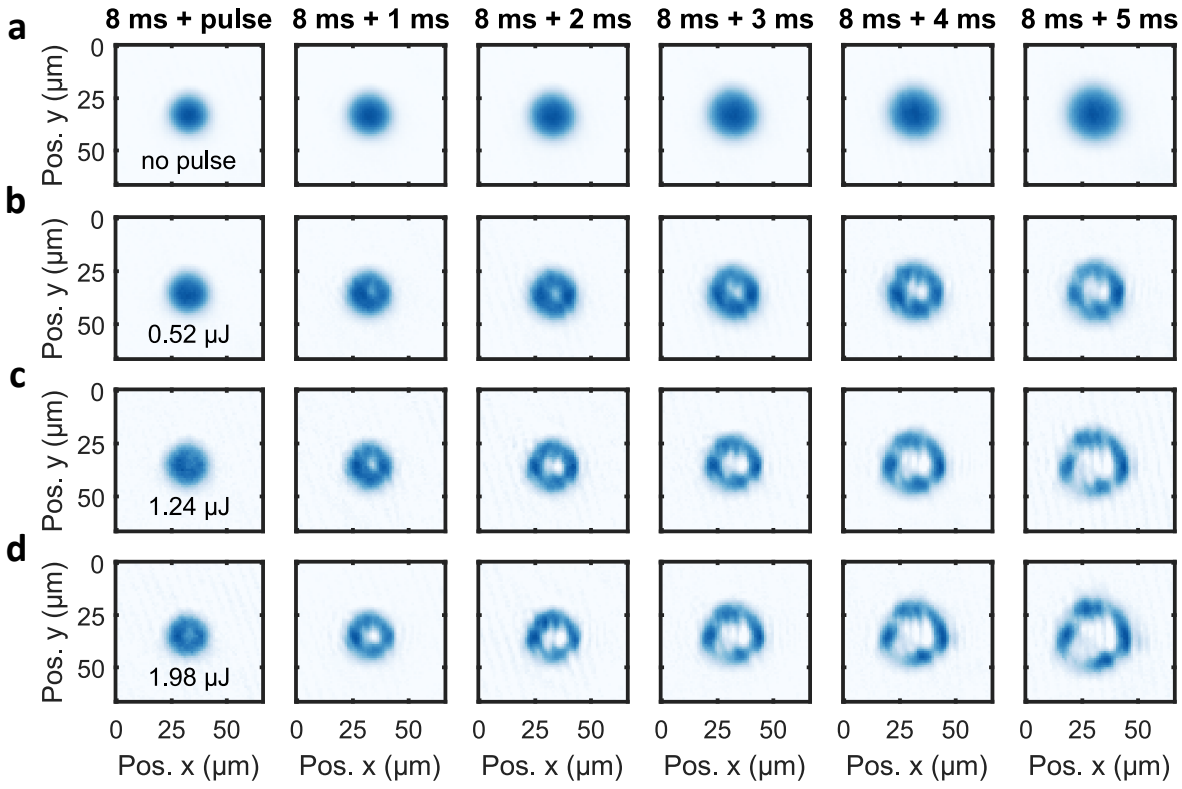

Figure 3.14: Strong-field acceleration of a BEC. Absorption images of the expanding BEC during time-of-flight without pulse exposure (a) and after illumination with a single pulse of 0.52 µJ (b), 1.24 µJ (c) and 1.98 µJ (d) pulse energy. The pulses are applied after a time-of-flight of 8 ms. The images are averaged over more than eight realizations.

parently, the calculated expansion velocities clearly overestimate the actual velocities, which saturate for peak intensities in the 10^{13} W/cm^2 range. This saturation is a result of significant atom losses due to the non-linearly increasing ionization probabilities for increasing peak intensities. Figure 3.15b depicts the ionization probability $P_{\mathrm{ion}}(y)$ in dependence on the position in the focus after a pulse with 1.98 µJ pulse energy, which corresponds to a peak intensity of $I_0 = 7.3 \times 10^{12}$ W/cm^2 (dashed red line). In addition, the terminal velocities neglecting ionization are given (dashed blue line). As the ionization probability reaches unity beyond $I_0 = 5 \times 10^{12}$ W/cm^2, the center region of the focus is fully ionized. Accordingly, even atoms on the wings of the Gaussian beam profile, which would experience the highest acceleration during the pulse, are ionized and do not contribute to the measured velocity distribution. In order to account for photoionization, the terminal velocities are weighted with the ionization probability as $v_{\mathrm{pulse,i}}(y) = [1 - P_{\mathrm{ion}}(y)] \times v_{\mathrm{pulse}}(y)$. The expected expansion velocities considering ionization are given in (c) for different pulse energies (solid blue line) and reasonably agree with the measured data. In conclusion, photoionization limits the attainable momentum transfer per pulse to $p_{\mathrm{pulse}} \leq m_{\mathrm{a}} \times 5$ mm/s for the chosen waist size and pulse parameters. However, this momentum transfer corresponds to an average acceleration of 2×10^{10} g over the fwhm pulse duration.

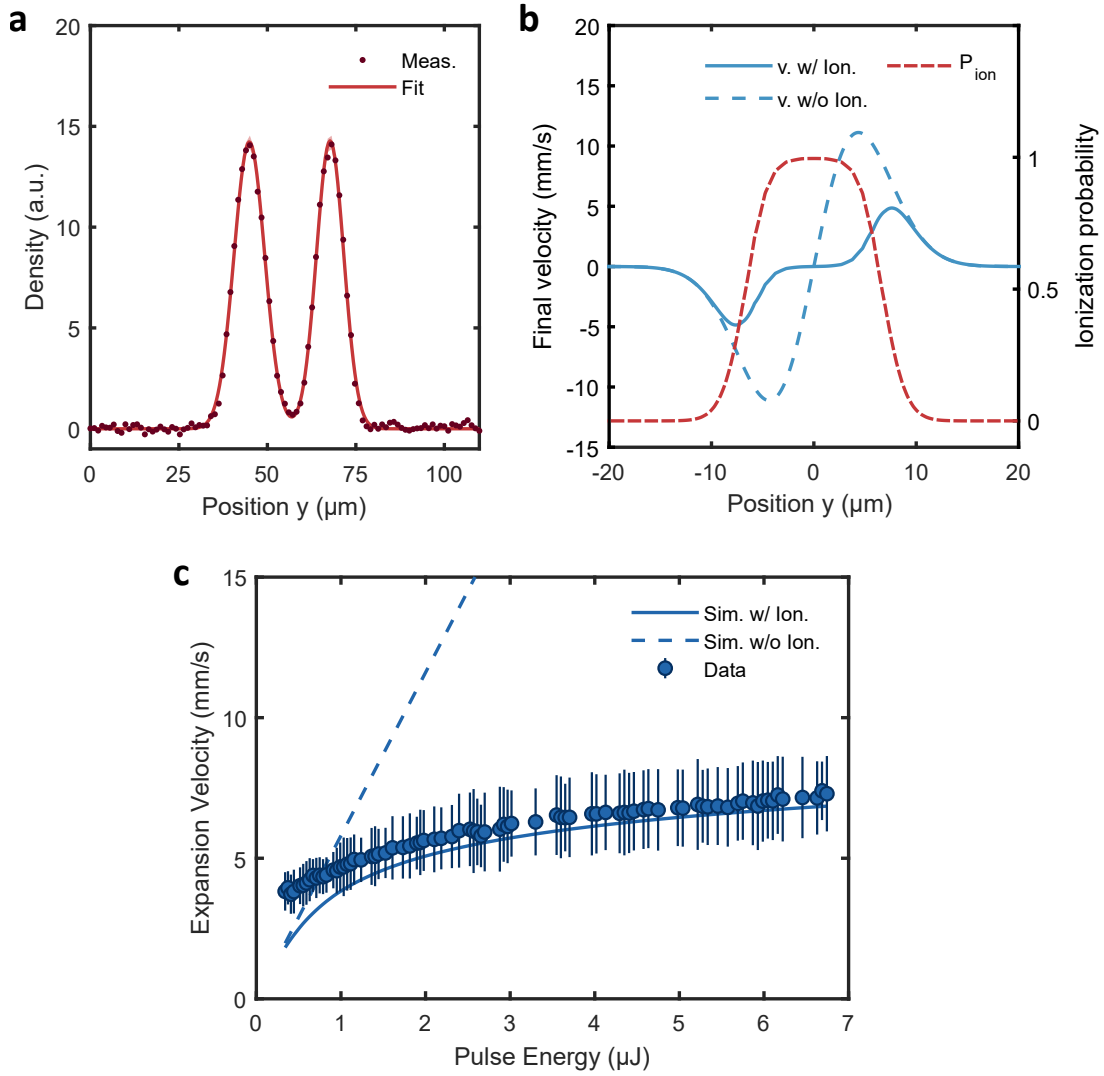

Figure 3.15: Strong-field acceleration of a BEC. a. Row sum profile of the optical density distribution given in Fig. 3.14c at a pulse energy of 1.24 μJ (data points) after 5 ms time-of-flight. The solid line illustrates the double Gaussian function fitted to the data points and the light red area depicts the 95% confidence interval of the fit. **b.** Final velocities after pulse exposure calculated from the spatially dependent momentum transfer according to Eq. 3.23 for pulse energy of 1.98 μJ (dashed blue line). The solid blue line shows the terminal velocities weighted with the ionization probability distribution (dashed red line). **c.** Halo expansion velocities in dependency of the applied pulse energy (data points). The vertical error bars are given by the 95% confidence interval of the linear fit to the expanding ring radius. The simulated expansion velocities are determined by the maximum velocities according to Eq. 3.23 neglecting ionization (dashed line) and weighted with the ionization probability (solid line).

3.2.3. Femtosecond compression of a BEC

The impact of high-intensity laser pulses at a central wavelength of 1022 nm on the BEC is investigated. As the fundamental wavelength of the pulses in this case is red-detuned with respect to the D_2 transition, they introduce an attractive potential. Analogously to the strong-field acceleration measurements, the femtosecond laser pulses are applied after 8 ms time-of-flight. Figure 3.16a,b shows the time-evolution of the atomic density distribution without pulse and after illumination with a single femtosecond laser pulse at 104 nJ pulse energy, which yields

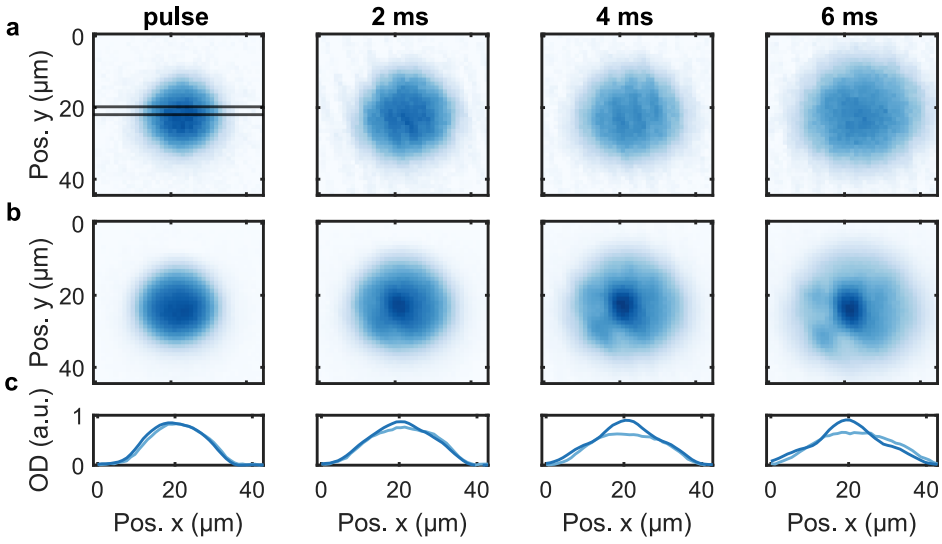

Figure 3.16: Femtosecond compression of a BEC. a. Absorption images of the expanding BEC during time-of-flight without pulse application. The black lines mark the area used for the row sum profiles in (c). **b.** Corresponding images after application of a single pulse at 1022 nm wavelength and 104 nJ pulse energy. **c.** Column sum profile of the optical density distributions in (a) (light line) and (b) (dark line).

a peak intensity of $I_0 = 1.9 \times 10^{11}$ W/cm^2 and corresponds to an imprinted peak phase of about 4π. While the BEC outside of the focus expands unperturbed by the pulse, the illuminated central part is compressed by dipolar forces on a millisecond timescale leading to an increased central density. The time evolution of the corresponding line cut profiles is shown in Fig. 3.16c after pulse application (dark line) and without pulse application (bright line). Apparently, the imposed dipolar potential partly reverses the BEC expansion and effects a density enhancement in the cloud center. In order to further investigate the many-body dynamics of the BEC after momentum transfer, numerical simulations of the 3D Gross-Pitaevskii equation are required, which also account for the repulsive interparticle interactions. These calculations are beyond the scope of this work.

By using a pulse train of red-detuned laser pulses with a repetition rate much higher than the trap frequencies of 0.1-1 kHz, the periodic momentum transfer during each single pulse can create a time-averaged, attractive effective potential, which allows to trap cold atomic gases. Such pulsed optical dipole traps for neutral atoms have been experimentally realized with picosecond laser pulses [173] and femtosecond laser pulses [175]. With the possibility of frequency conversion for ultrashort laser pulses into the blue and UV spectrum with high efficiency, such pulsed optical dipole traps might enable efficient trapping of atomic species not accessible for laser-cooling and dipole trapping so far. In addition, the duty cycle of a pulsed beam provides an interaction free time frame for spectroscopic measurements.

In this experiment, a crossed pulsed dipole trap (CPDT) scheme is used as shown in Fig. 3.17, where the femtosecond laser beams is divided into two perpendicular beams. By adapting the length of the separate beam paths, a time delay between the pulses is ensured to reduce ionization losses compared to simultaneous arrival of the pulses resulting in higher peak inten-

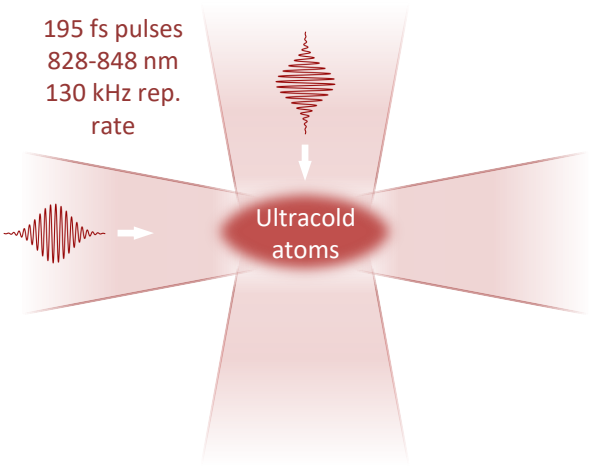

Figure 3.17: Crossed pulsed dipole trap. Two perpendicular red-detuned pulsed laser beams are focused onto the ultracold cloud and provide a time-averaged trapping potential. The wavelength is tuned by the OPA module.

sities. Before being transferred to the CPDT, an ultracold thermal cloud with 1.5×10^4 to 2.0×10^4 atoms is prepared at a temperature of $T_a = 122(4)$ nK in the crossed dipole trap at trap frequencies of $\omega_x = 96(7)$ Hz and $\omega_y = 89(1)$ Hz. After switching off the dipole trap, the atoms are illuminated with pulse trains at a repetition rate of 130 kHz and a peak intensity of $I_0 = 5 \times 10^{10}$ W/cm^2 in both arms. The central wavelength is tuned in the range of 828 nm to 848 nm using the OPA module in the femtosecond laser system (see Sec. 2.3.1).

Figure 3.18a shows the measured number of atoms in the CPDT for different hold times after transfer (data points). The BEC lifetime is determined by the halflife period of an exponential decay function fitted to the data (solid blue line)[36]. In order to analyze the role of dissipation due to photoionization in this setup, the expected ionization losses over time are calculated for the utilized cloud and pulse train parameters by use of TDSE ionization probabilities calculated by Andrey K. Kazansky and Nikolay M. Kabachnik. The dashed orange line illustrates the expected progression of the atom number due to the recurring photoionization by the trapping pulses.

The resulting lifetimes for different wavelengths of the femtosecond laser are depicted in Fig. 3.18b (data points). In addition, the expected lifetime limit due to photoionization according to TDSE calculations is given (red data points). At the pulse train parameters utilized here, there are two main mechanisms limiting the achievable lifetimes: For an decreasing detuning of the laser pulses the ionization probabilities per pulse increase, which results in a reduced lifetime of the cloud. For the lower two wavelengths, the measured lifetime reasonably agrees with the expected lifetimes according to the TDSE calculations (red data points) and thus is limited by photoionization. For increasing detuning, the trapping potential vanishes and the lifetime is limited by the trapping power of the effective potential. As a result, only lifetimes below 10 ms

[36] As the high optical densities for the lowest two hold times inhibit reliable determination of the atom number, the exponential decay function is only fitted to the data points with hold times $t \geq 4$ ms.

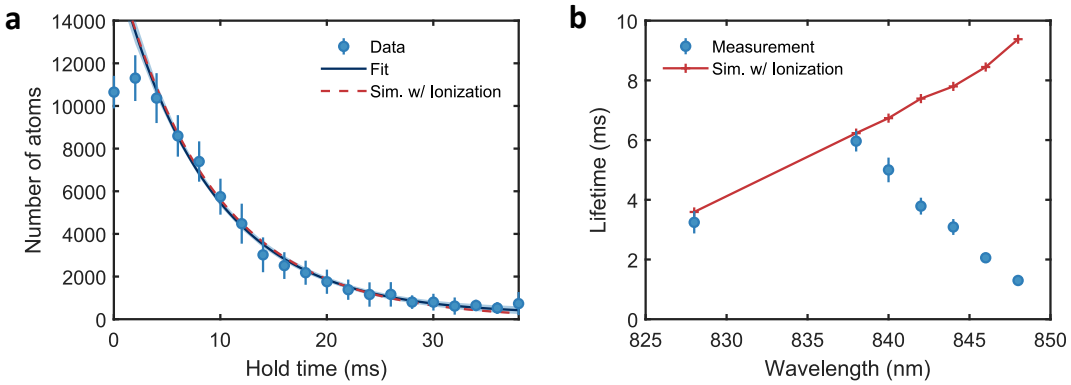

Figure 3.18: Crossed pulsed dipole trap. a. Number of atoms for different hold times after transfer to the CPDT at 838 nm central wavelength (data points) measured after 2 ms time-of-flight. The error bars denote the standard deviation over more than 10 realizations. The solid line corresponds to the exponential decay function fitted to the data points and the shaded area shows the 95 % confidence interval of the fit. The dashed orange line depicts the expected decay of the atom number due to photoionization according to TDSE calculations. **b.** Measured lifetime in the CPDT (blue data points) and expected lifetime limit due to photoionization (red data points) for different central wavelengths. The lifetimes are obtained by the half-life period of the exponential decay fitted to the measured and expected atom number evolution in (a) and the error bars correspond the 95% confidence interval for each fit.

are achieved in this configuration, which remains significantly lower than typical lifetimes in dipole traps using continuous wave laser beams on the order of ten seconds and than achieved in femtosecond pulsed DT of a few hundred milliseconds [175]. In order to increase the trapping potential without non-linearly increasing the ionization probabilities, the repetition rate of the femtosecond laser or the pulse duration needs to be increased significantly. The experimental realization in [175] with ^{87}Rb employs pulses with 70 fs and 150 fs pulse duration at repetition rate of 80 MHz and a central wavelength of 825 nm. In this regime, peak intensities of $I_0 = 10^4$ W/cm^2 are sufficient to achieve trap depths of tens of microkelvin and loading the DT directly from a MOT. Thus, in contrast to the regime presented here, photoionization is negligible and the lifetime is rather limited by momentum diffusion due to dipole force fluctuations, which become relevant at high intensities [175, 185].

3.2.4. Conclusion

In this section, the strong-field acceleration of a BEC in the intensity gradient of femtosecond laser pulses has been examined quantitatively in different regimes. First, a repulsive potential created by blue-detuned light at 511 nm wavelength has been utilized to radially accelerate the atoms producing matter wave halos with a longitudinal beam temperature of $T_{\mathrm{beam}} = 20(5)$ nK at a tunable beam velocity up to $v_0 = 20$ mm/s. Even for high intensities, a description of the acceleration by transient optical dipolar forces is found to be accurate. Dissipation by photoionization as well as the dynamics of the wavefunction during exposure to the pulse train limit the achievable momentum transfer.

Additionally, the compression of the BEC by attractive red-detuned pulses at 1022 nm is

studied where a density enhancement of the wavefunction results from the interplay of the attractive forces of the femtosecond laser pulses and the repulsive atomic interactions. Finally, the feasibility of a crossed optical dipole trap with femtosecond pulses close to the D_2 resonance of ^{87}Rb in the range of 828 - 848 nm is investigated. For the pulse parameters provided by the femtosecond laser system which allow sufficient CPDT depths, the BEC lifetime in the trap is inherently limited by photoionization losses to less than 8 ms.

In conclusion, ultrashort laser pulses arise as a versatile tool for precise manipulation of ultracold gases regardless of the specific atomic level structure. The experimental findings demonstrate a general scheme for shaping matter waves and engineering monoenergetic beams of atoms.

4. Ultracold plasma triggered by femtosecond laser pulses in a BEC

Ultrashort laser pulses open up new pathways for manipulating and controlling atomic quantum gases on femtosecond timescales. As discussed in Chapter 3.1 the strong light-field of a femtosecond laser pulse is able to instantaneously ionize a controlled number of atoms in a Bose-Einstein condensate (BEC). If the number of ionized atoms exceeds a critical threshold, the space charge potential produced by the ions is large enough to trap a fraction of the photoelectrons, thus forming an ultracold plasma [75]. Whereas such plasmas created from laser-cooled targets in a magneto-optical trap have been intensively studied recently [76–78], here the creation within a BEC is reported. The high initial charge carrier densities inherited from the BEC give rise on an unexplored density regime of ultracold plasmas which are governed by dynamics on ultrashort timescales.

This chapter presents detailed studies of the creation of ultracold microplasma and the dynamics emerging in this novel regime. Starting from introducing the defining plasma parameters, the creation of ultracold plasma in a BEC by femtosecond laser pulses is described (Section 4.1). As plasma formation at BEC densities requires only a few thousand charged particles, ultracold microplasmas allow for a charged particle tracing (CPT) simulation giving access to the plasma dynamics at a single particle level (Section 4.2). As the central part of the chapter, experimental and simulation results are presented revealing an ultrafast electron cooling during the plasma expansion (Section 4.3). The chapter concludes with the analysis of the ultracold microplasma as a potential source for ultracold electrons (Section 4.4).

Parts of this chapter including experimental data and simulation results are already presented in [2]. Data acquisition and analysis has been done by the author with support from Mario Großmann, Juliette Simonet and Philipp Wessels-Staarmann.

4.1. Ultracold plasma

4.1.1. Plasma regimes and coupling parameter

The majority of visible matter in the universe consists of ionized gases forming plasma. These plasmas, which typically consist of ionized atoms or molecules as well as free electrons, span several orders of magnitude in size, temperature and number density. Astrophysical plasma occurs at densities between $10^5 - 10^6$ m^{-3} in the interstellar medium and 10^{36} m^{-3} in the core of white dwarfs [78] and typical temperatures vary between 200 K in the ionosphere of the earth to approximately 10^7 K in the solar core. Figure 4.1 gives an excerpt of the different plasmas occurring in nature together with various examples for laboratory based plasma systems.

The properties of plasma are predominantly determined by the density and temperature of the charged particles forming the plasma state. Two regimes can be distinguished by means of the electron/ion Coulomb coupling parameter

$$\Gamma_{\mathrm{e,i}} = \frac{e^2}{4\pi\varepsilon_0 a_{\mathrm{e,i}} k_{\mathrm{B}} T_{\mathrm{e,i}}}. \tag{4.1}$$

Here, $T_{\mathrm{e,i}}$ describes the electron/ion temperature determined by the mean kinetic energy per particle and $a_{\mathrm{e,i}} = \left(\frac{3}{4\pi\rho_{\mathrm{e,i}}}\right)^{1/3}$ denotes the Wigner-Seitz radius at the electron/ion density $\rho_{\mathrm{e,i}}$. The coupling parameter relates the Coulomb potential energy to the kinetic energy per particle for the ions and the electrons, respectively. Whereas for weakly coupled plasmas ($\Gamma_{\mathrm{e,i}} < 1$) the thermal motions of each particle prevail, the dynamics in strongly coupled plasmas ($\Gamma_{\mathrm{e,i}} > 1$) is dominated by Coulomb forces between charged particles, which leads to the development of spatial density correlations [186] and the formation of liquid-like and crystalline, self-assembled structures. Accessing the interesting regime of strongly coupled plasma in well-controlled experiments paves the way towards benchmark systems for multi-scale theories and sheds light on the extreme conditions present in inertial confinement fusion [79], the core of Jovian planets and white dwarfs [80].

Tailored plasmas created in a laboratory framework to approach the strongly coupled regime are typically created by photoionization of a neutral atomic target. For a given excess energy of the ionization process, assuming a Gaussian ionic density distribution, a minimum number of ions N^* is required for plasma formation

$$N^* = \frac{E_{\mathrm{kin,e}}}{U_0} \quad \text{and} \quad U_0 = \sqrt{\frac{2}{\pi}}\left(\frac{e^2}{4\pi\varepsilon_0\sigma}\right), \tag{4.2}$$

where σ denotes the rms radius of the ionic distribution and $E_{\mathrm{kin,e}}$ denotes the initial electron kinetic energy [75]. This condition for plasma formation can equivalently be defined as a comparison of length scales. The characteristic length scale for plasma is given by the Debye length

$$\lambda_{\mathrm{D}} = \sqrt{\frac{\varepsilon_0 k_{\mathrm{B}} T_{\mathrm{e}}}{\rho_{\mathrm{e}} e^2}}, \tag{4.3}$$

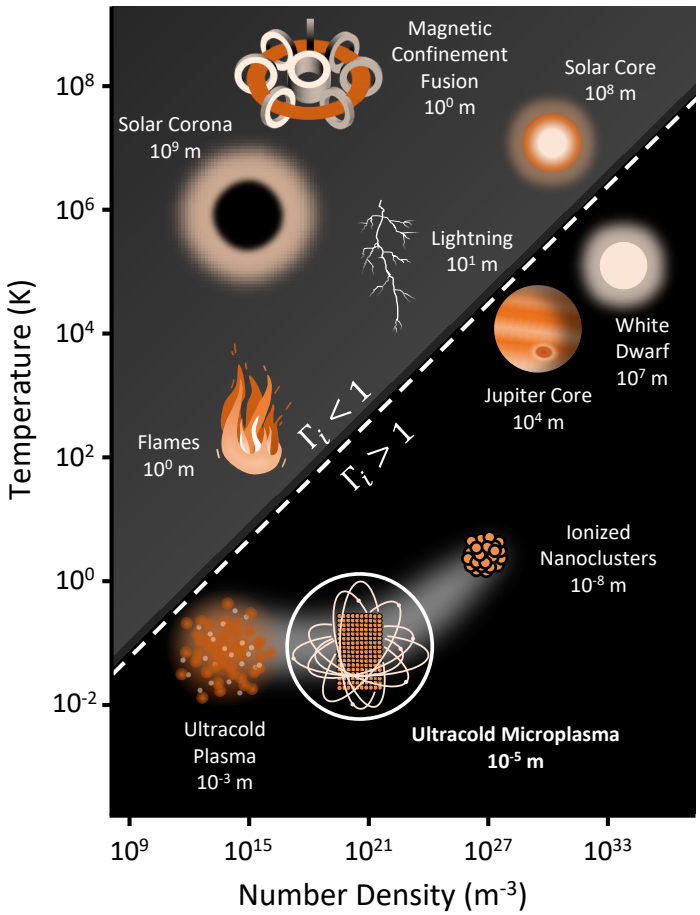

Figure 4.1: Number density and temperature diagram of plasmas. Plasmas occurring in nature or prepared in the laboratory span several orders of magnitude in size, temperature and number density. The majority of naturally occurring plasmas are weakly coupled ($\Gamma_i < 1$), however, the regime of strongly coupled plasma ($\Gamma_i > 1$) is realized in astronomical objects like Jupiter's core or white dwarfs. The dynamics in this challenging region can experimentally be approached by ultracold neutral plasma, ionized nanoclusters and ultracold microplasma. Figure adapted from [2] and licensed under CC BY 4.0.

where ρ_e and T_e denote the electron density and temperature. The Debye length refers to the length the electronic plasma component requires to screen external electric fields by restructuring the density distribution. An interacting ensemble of charged particles exhibits collective dynamics and forms a plasma, if the Debye length is small in comparison to the overall system size given by σ, i.e. if $\lambda_D/\sigma \ll 1$. As a result, for a given excess energy the minimum system size as well as the minimum particle number scale with the inverse root of the density $\rho_{e,i}^{-1/2}$. Figure 4.2 shows the minimum plasma size and ion number in dependency of the atomic target density for excess energies of $E_{kin,e} = 1$ meV, 0.1, 10 eV (dashed lines) as well as for the excess energy of 0.68 eV (solid line), which is used in this experiment. Accessing higher plasma densities allows for decreasing the particle number and thus the complexity of the system.

One approach to create strongly coupled plasmas is to access condensed matter densities. This can be achieved by photoionizing nanoclusters with ultrashort laser pulses. In such systems, the interplay between interparticle Coulomb energies and molecular bonds is essential to

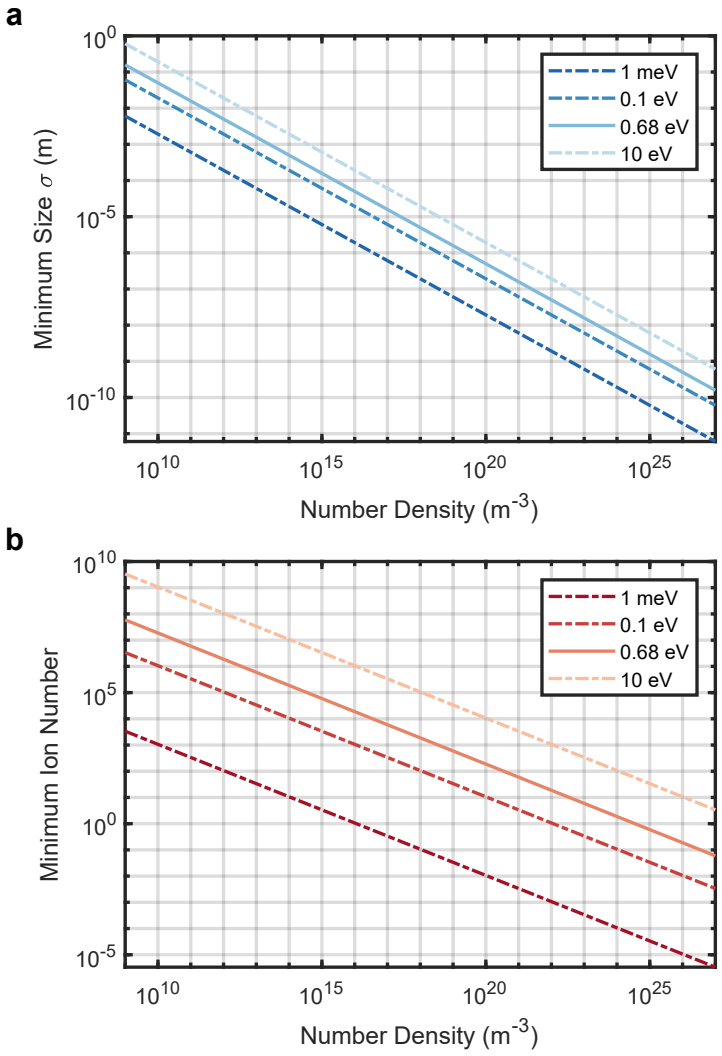

Figure 4.2: Minimum Plasma size and particle number for different density regimes. a. Minimum rms radius σ for plasma formation in dependency of the charged particle number density $\rho_{e,i}$. **b.** Minimum ion number required for plasma formation at each charged particle number density. The ion numbers are calculated from the minimum plasma size according to Eq. 4.2.

understand energy transfer between electrons and ions [83–85] (see Fig. 4.1). Recent experiments have studied charged particle dynamics at solid-state densities in finite-size nanoclusters [86–88] and observed the emergence of low-energy electrons [187].

A second approach relies on the photoionization of laser-cooled atomic targets, which exhibit negligible atomic thermal motion in combination with high degree of experimental target control. This enables plasma formation with initial ionic kinetic energies in the millikelvin range at MOT densities yielding interaction energies many times higher than the average kinetic energies [77, 78]. As these plasmas typically exhibit macroscopic quasi-neutrality, they are often referred to as ultracold neutral plasma (UNP). The first experimental realization was conducted by T.C. Killian et al. in 1999 with laser-cooled Xenon atoms [75]. Ensuing, UNP have been created in numerous laser cooled earth-alkaline and alkaline atomic systems as well as in supersonic expansion of molecular NO [188]. A comprehensive review of the progress in this field

can be found in [77, 78]. Recent work approaches the strong coupling regime by laser cooling the ions after plasma creation in order to reduce the thermal energy per particle [81].

The plasma realized in this experiment belongs to a still unexplored plasma regime given by the charge carrier density above 10^{20} m^{-3} inherited from the BEC. The negligible temperatures below 100 nK allow realizing micrometer-sized plasma (see Fig. 4.2), where the initial Coulomb energies exceed the thermal energies by three orders of magnitude. Such a microplasma with a few hundred to thousands of particles bridges the gap between the dynamics of energy transfer studied in photoionized nanoclusters and ultracold neutral plasma. Moreover, as the density in quantum gases is still much lower than in atomic clusters, interatomic binding energies can be neglected, which considerably simplifies the theoretical description of the dynamics.

4.1.2. Ultracold microplasma in a BEC

In contrast to former realizations of photoionizing laser-cooled atoms in a MOT, here the dynamics of an ultracold microplasma is experimentally investigated by interfacing ultracold quantum gases with the ultrashort timescales of femtosecond laser pulses. As shown in Fig. 4.3a, a ^{87}Rb BEC is locally ionized by a single laser pulse at 511 nm wavelength with a full width at half maximum (FWHM) duration of 215^{+20}_{-15} fs. Whereas earlier photoionization studies in ^{87}Rb BECs used nanosecond laser pulses [158], here, the pulse duration is significantly shorter than the picosecond timescale for the electron dynamics given by the inverse electron plasma frequency (see Chapter 4.1.3). As a result, the initial plasma dynamics is not perturbed by the laser pulse and the creation of the charged particles can be considered as instantaneous.

A high-resolution objective with a numerical aperture of 0.5 (see Chapter 2.3.3) focuses the femtosecond laser pulse down to a waist of $w_1 = 0.99(3)$ µm and $w_2 = 1.00(5)$ µm leading to peak intensities up to 2×10^{13} W/cm^2. The number of ionized atoms can be tuned from a few hundred to $N_{\mathrm{e,i}} \approx 4000$ in a controlled manner via the pulse intensity. At the highest intensity, the ionization probability reaches unity within the center region of a cylindrical volume depicted in Fig. 4.3b [1], resulting in charge carrier densities of up to $\rho_{\mathrm{e/i}} = 2 \times 10^{20}$ m^{-3}. The radius of this volume of 1.35 µm is determined by the laser focus, while the height of 5 µm is limited by the atomic target (see chapter 4.2.1). In contrast to previous realizations of ultracold neutral plasma, this provides a locally confined ionized volume with tunable charge density within the atomic cloud.

As shown in Fig. 4.3c, the photoionization of ^{87}Rb at 511 nm can be described as a non-resonant two-photon-process (see chapter 3.1), with an excess energy of 0.68 eV. The initial electron kinetic energy resulting from the two-photon ionization corresponds to an initial temperature of $T_{\mathrm{e}} = 5250$ K. Since the plasma is created from an ultracold atomic target with negligible atomic kinetic energy, the initial ionic kinetic energies are dominated by the photoionization recoil yielding a low initial ionic temperature of $T_{\mathrm{i}} \approx 33$ mK. In combination with the enhanced initial charge carrier densities, a remarkably high initial ionic coupling parameter of $\Gamma_{\mathrm{i}} = 4800$ is reached, whereas the initial electron coupling parameter of $\Gamma_{\mathrm{e}} = 0.03$ predicts

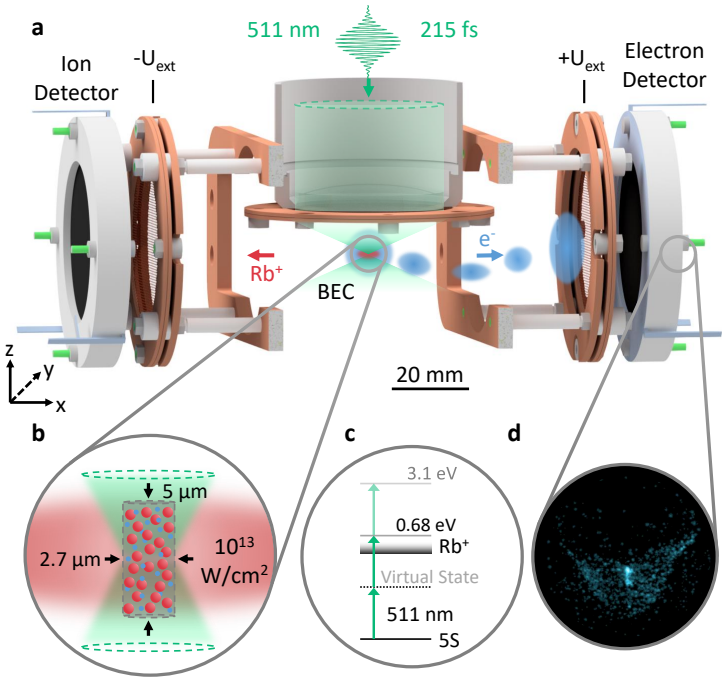

Figure 4.3: Detection of ionization fragments after ultrafast ionization of a BEC. a. A single femtosecond laser pulse is focused to a waist of $w_0 \approx 1$ µm and locally photoionizes a ^{87}Rb BEC. The created photoelectrons and ions are separated by an electrical field produced by the two extraction meshes at tunable opposite voltages $\pm U_{\text{ext}}$. Their kinetic energy distribution is converted into a spatial information during the expansion towards the detectors consisting of a microchannel plate assembly and a phosphor screen, which is imaged by a highspeed camera. **b**. At laser peak intensities of 10^{13} W/cm^2, the femtosecond laser pulse ionizes the majority of atoms within a micrometer-sized cylindrical volume creating a charged particle ensemble immersed in the BEC. **c**. At a central wavelength of 511 nm, ^{87}Rb is ionized from the 5*S* ground state via non-resonant two- and three-photon processes that correspond to electron excess energies of 0.68 eV and 3.1 eV respectively. **d**. Measured averaged electron distribution at $U_{\text{ext}} = 300$ V and $I_0 = 1.7 \times 10^{12}$ W/cm^2. The spatial extent on the detector reflects the kinetic energy distribution of the electrons. Figure adapted from [2] and licensed under CC BY 4.0.

weak coupling.

As a key feature, this experimental setup grants access to the atomic density via absorption imaging as well as the energy distribution of the photoionization products (Fig. 4.3d, see also chapter 2.2). A tunable electric field separates electrons and ions and directs them onto opposite position sensitive detectors. The extraction field sets the expansion time towards the detectors and, thus, the velocity resolution, which can be tuned from 10 meV at $\pm U_{\text{ext}} = 300$ V to the 1 meV level at $\pm U_{\text{ext}} = 5$ V (corresponding to static electric fields of 162 V/m and 4.6 V/m in the center, respectively).

4.1.3. Dynamical timescales

For ultracold plasma created by photoionization of a cold atomic ensemble, the plasma evolution typically starts from a state of strong disequilibrium, where a hot electron gas carrying the entire excess energy of the ionization process is combined with a quasi static ionic component. As a result, unconfined ultracold plasma commonly exhibits similar stages of dynamics as it

expands.

The plasma evolution can be divided into three different temporal phases with characteristic timescales [77, 189]. The first two stages correspond to the separate thermalization of the electronic and the ionic plasma component and the third one is given by the subsequent hydrodynamic expansion of the plasma. The durations for these processes are set by the electron/ion plasma frequency

$$\omega_{\mathrm{p,e/i}} = \sqrt{\frac{\rho_{\mathrm{e/i}} e^2}{m_{\mathrm{e/i}} \varepsilon_0}}, \tag{4.4}$$

which is determined by the electron/ion density $\rho_{\mathrm{e/i}}$. Electron-electron thermalization occurs on a timescale of the inverse electron plasma frequency $\omega_{\mathrm{p,e}}^{-1}$, whereas the much slower ion-ion equilibration is reached on the timescale of $\omega_{\mathrm{p,i}}^{-1}$. For typical plasma densities attained in MOT experiments, the comparably light electrons reach thermal equilibrium after a duration of $\omega_{\mathrm{p,e}}^{-1} \approx 10$ ns [77]. On this timescale the electronic component expands, a small local charge imbalance is established and the electrons are captured in the resulting attractive potential. For the much heavier ions, the equilibration process takes place on a duration of $\omega_{\mathrm{p,i}}^{-1} \approx 1$ µs, tractable for time-resolved experimental studies utilizing fluorescence [190] and absorption imaging of the ions [191, 192].

As the initial ionic spatial distributions are inherited from spatially uncorrelated atomic systems, the ions have larger Coulomb potential energy due to the disorder. Within the timescale of the inverse ion plasma frequency the disorder-induced potential energy translates in kinetic energy. This process is referred to as disorder-induced heating (DIH) [89, 193] and typically limits the attainable ion coupling parameters in UNPs [78]. The ion equilibrium temperature associated to this process is given by

$$T_{\mathrm{DIH,i}} = \frac{e^2}{12\pi\varepsilon_0 a_{\mathrm{i}} k_{\mathrm{B}}} \tag{4.5}$$

and thus scales with the ion density as $T_{\mathrm{DIH,i}} \propto \rho \mathrm{i}^{-1/3}$ [81] yielding $T_{\mathrm{DIH,i}} \approx 1$ K for MOT densities.

Assuming quasi-neutrality, the plasma expansion beyond the inverse plasma frequencies can be described as an hydrodynamic expansion on a timescale $\tau_{\mathrm{exp}} = \sqrt{m_{\mathrm{i}} {\sigma_0}^2 / \left(k_B \left[T_{\mathrm{e}} + T_{\mathrm{i}}\right]\right)}$ of typically $\tau_{\mathrm{exp}} \approx 10 - 100$ µs [77]. On this timescale, the rms ion radius expands uniformly with the hydrodynamic expansion velocity

$$v_{\mathrm{hyd}} = \sqrt{\frac{k_{\mathrm{B}} \left(T_{\mathrm{e},0} + T_{\mathrm{i},0}\right)}{m_{\mathrm{i}}}}. \tag{4.6}$$

At the same time the electron kinetic energy decreases by adiabatic cooling according to [77]

$$E_{\mathrm{kin,e}}(t) = E_{\mathrm{kin,e}}(0) \left[1 + \frac{t^2}{\tau_{\mathrm{exp}}^2}\right]. \tag{4.7}$$

Since the enhanced charge carrier density of ultracold microplasma created from a BEC surpasses realizations at MOT densities by orders of magnitude, it is associated with a strongly differing regime of timescales. At densities of $\rho_{e/i} = 2 \times 10^{20}$ m^{-3} an initial inverse electron plasma frequency of $\omega_{p,e}^{-1} = 1.3$ ps is attained as well as an inverse ion plasma frequency of $\omega_{p,i}^{-1} = 0.5$ ns. For the measurements reported here, a comparably high initial electron energy of 0.68 eV is used, corresponding to an initial electron temperature of 5250 K. With an approximate plasma size of $\sigma_0 = 2$ µm, a hydrodynamic expansion timescale of $\tau_{exp} \approx 2.8$ ns is expected. As the high excess energy of the ionization process combined with the small ionization volume evokes a significant macroscopic charge imbalance for the ultracold plasma, the validity of the self-similar expansion model is questionable. An accurate description has to additionally account for Coulomb-driven contributions, which could prevent reaching global thermal equilibrium for the ions at all [194].

4.2. Charged particle tracing simulations

For a deeper understanding how the velocity distributions of the created photoelectrons (Chap. 4.2.1) convert into spatial information measured on the detector, the electron trajectories are tackled by charged particle tracing (CPT) simulations within the commercial simulation environment of the COMSOL Multiphysics® software [195]. In order to have a full simulation of the conducted experiments, the external electromagnetic fields induced by the experimental setup are computed with the finite element method (Chap. 4.2.2). Afterwards the trajectories of individual electrons/ions in these fields are calculated by CPT trajectory simulations (Chap. 4.2.3).

In addition, the collective dynamics of the electrons and ions after creation is simulated within CPT plasma simulations (Chap. 4.2.3). These simulations account for mutual Coulomb interactions between the charged particles and allow to accurately describe the dynamics in ultracold microplasma.

4.2.1. Initial charge distributions

The initial electron/ion distributions $\rho_{\mathrm{e,i}}(x,y,z)$ that arise from the photoionization are calculated according to Eq. 3.19 by superimposing the 3D atomic density distribution with the ionization probability distribution. The ionization probabilities are calculated by use of the TDSE results presented in chapter 3.1. Here, z denotes the pulse propagation direction, x and y the two transverse directions aligned in direction of the beam waists reported in chapter 2.3.3. Figure 4.4a displays the 2D-projection onto the $x-z$ plane of the calculated electron/ion density distribution at a pulse peak intensity of $I_0 = 1.9 \times 10^{13}$ W/cm^2. As a result of the quasi circular focus, the created 3D distribution is cylindrically symmetric. The bounds of the cylindrical volume used for both CPT trajectory and CPT plasma simulations to approximate the charge carrier distributions are depicted by the white dashed lines. The corresponding ionization probability profiles are given in Fig. 4.4b in x-direction at $(y,z) = (0,0)$ (solid blue line) and in z-direction at $(x,y) = (0,0)$ (dotted dark blue line). In addition, the normalized atomic density distribution in x-direction at $(y,z) = (0,0)$ (dashed red line) is shown. As the trapping frequencies are similar in all directions, the atomic density profile is almost spherical. Thus, the photoionization can be regarded as local in x- and y-direction, whereas the atomic ensemble is fully ionized in the pulse propagation direction (z).

At the starting point ($t = 0$) of the CPT trajectory and plasma simulations (see Chap. 4.2.3 and Chap. 4.2.4), a number $N_{\mathrm{e,i}}$ of electrons and ions is randomly distributed in the cylindrical ionization region (see 4.4) of 1.35 µm radius and 5 µm height. The particles of both species are created monoenergetically with their initial velocities determined by the excess energy of 0.68 eV of the two-photon ionization process. The initial velocity directions are randomly distributed in an isotropic manner. Thus, the simulations neglect strong-field ionization effects on the photoelectron spectra [150, 152].

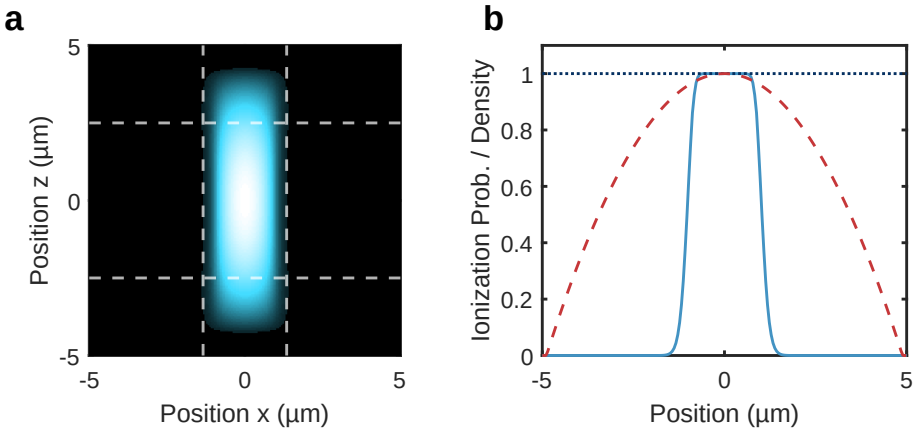

Figure 4.4: Ionization volume. **a**. 2D projection of the simulated 3D electron/ion density distribution $\rho_{e/i}(x,y,z)$ after strong-field ionization by a single pulse with $I_0 = 1.9 \times 10^{13}$ W/cm^2. The dashed white lines mark the cylindrical volume, which is used for the CPT plasma simulations. **b**. Ionization probability in x-direction (solid blue line), in z-direction (dotted dark blue line) and normalized atomic density distribution in x-direction (dashed red line). Figure adapted from [2] and licensed under CC BY 4.0.

4.2.2. FEM simulation of experimental environment

In order to compute the trajectories of the individual particles, which are initialized as explained above, precise knowledge of the present electromagnetic fields is required. Here the calculation of the 3D electrostatic field configuration is discussed, which is induced by the mesh electrodes and MCPs in the Science chamber. For this purpose, the 3D computer-aided design (CAD) geometry of the Science chamber is included into the CPT simulations. By use of the Electrostatics Module within the COMSOL Multiphysics® software [195], the stationary electric field configuration is calculated for different extraction voltages. Here, the physics-controlled mesh option 'finer' was used to approximate the electrodes, with a minimum/maximum element size of 0.88 mm/12 mm. Fig. 4.5 shows a sectional view onto the Science chamber as well as the equipotential lines calculated for an extraction voltage of $U_{\text{ext}} = 300$ V and a MCP front potential of $U_{\text{front,e}} = 268$ V.

In order to realize a micrometer-sized laser focus, the high-resolution objective has to be close to the ultracold atomic cloud. A grounded copper mesh with high transparency is used to shield the reentrant vacuum window and to avoid static charge accumulation. The grounded electrode distorts the homogenous field created by the parallel-plate capacitor configuration of the extraction meshes. This leads to a reduced potential gradient around the ionization region and it introduces a top-down asymmetry.

The calculated magnitudes of the electric field E_{IV} at the position of the ionization volume are given in Tab. 4.1. The extraction field in the interaction region can be precisely controlled by the voltages U_{ext}. However its amplitude is not perfectly proportional to the applied voltage for low extraction fields. This is due to the voltages of the electron MCP, which give rise to an electric field on the order of 2 V/m in the center. In addition, accurately including the shielding by the spherical cube vacuum chamber influences the CPT simulation results. The FEM simulation

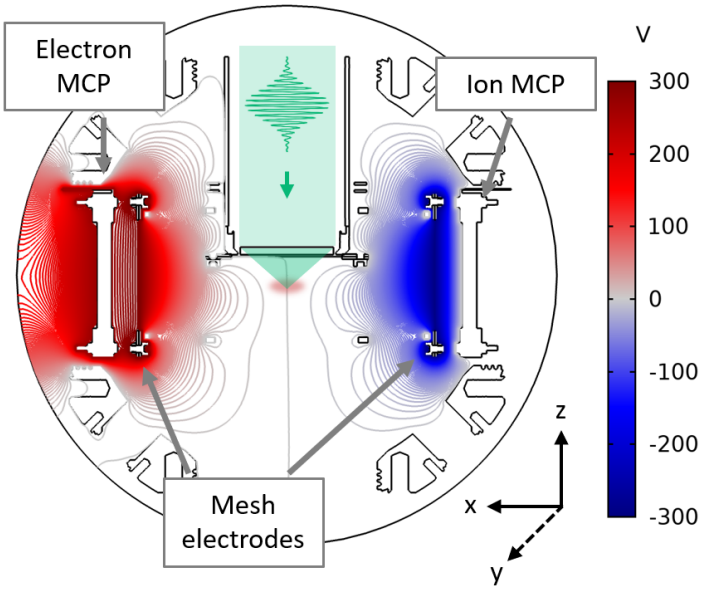

Figure 4.5: Electric extraction field. Sectional view into the 3D-CAD model of the vacuum chamber (black lines). The electric potential obtained for $\pm U_{\mathrm{ext}} = 300$ V is depicted as equipotential lines (from blue to red). As the ion MCP and the vacuum chamber are grounded, the electric potential is dominated by the mesh electrodes and the electron MCP. Figure taken from [2] and licensed under CC BY 4.0.

does not account for a finite transparency of the extraction meshes for electrostatic fields and thus neglects the electric field feedthrough of the electron MCP. However, the measurements (see Chapter 4.3) reveal a clear dominance of the extraction field at $U_{\mathrm{ext}} = 5$ V over electric stray fields. Hence, a stray field control to the V/m level is assumed.

U_{ext} (V)	5	25	100	300
E_{IV} (V/m)	4.6	14.4	55	162

Table 4.1: Electric fields in the ionization volume for different extraction voltages.

4.2.3. CPT trajectory simulations

The inhomogeneous electric field configuration complicates simple analytic predictions for the points of impact of the photoelectrons. Thus, the simulation of the electron trajectories in the extraction fields is needed to access the mapping between the electron velocity distribution and the recorded spatial distributions on the detector. For this purpose, charged particle tracing trajectory simulations are conducted using the previously discussed Electrostatics results as well as the Particle Tracing Module within the COMSOL Multiphysics® software [195]. In addition, a global magnetic field of 370 mG perpendicular to the detection axis and the femtosecond beam propagation direction is included, which centers the electron signal onto the detectors.

The software allows separating the simulations into two steps, first the static electric field configurations are calculated by use of a stationary solver and then the electron trajectories are simulated within the electric potential landscape by a time-dependent solver. The trajectories

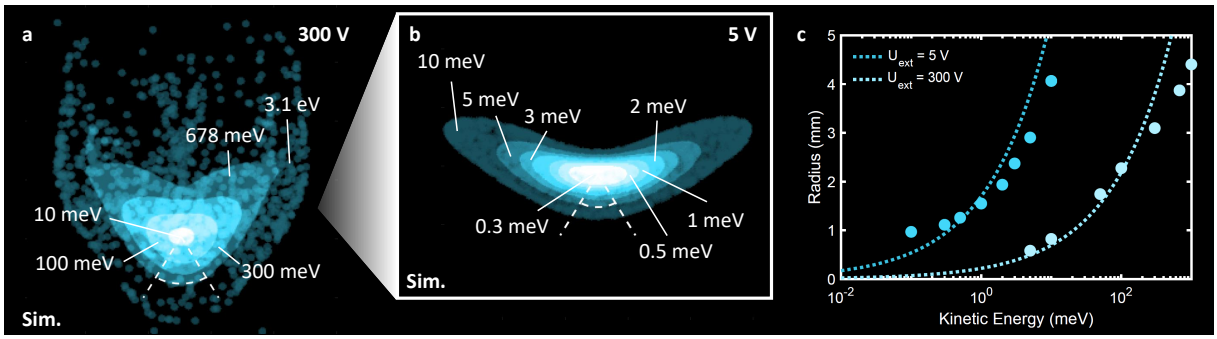

Figure 4.7: Electron CPT trajectory simulation results. a.-b. Electron signals on the detector obtained by CPT trajectory simulations at $U_{\text{ext}} = 300$ V (a) and $U_{\text{ext}} = 5$ V (b) for different initial kinetic energies. **c.** Radius of the electron signals in the circular sectors marked as dashed white lines in (a) and (b). CPT simulation results (blue data points) and expected radii in an ideal parallel-plate capacitor at $\pm U_{\text{ext}}$ with the plate distance of the extraction meshes.

are obtained by numerically solving Newton's equation of motion of each particle in three dimensions including the Lorentz forces exerted by the external electromagnetic fields. The CPT trajectory simulations do not include mutual Coulomb interactions between the charged particles as well as a bidirectional coupling between the charged particles and the external fields.

After creation, the electronic cloud expands isotropically according to the velocity distribution and is directed onto the electron detection unit by the extraction field. Fig. 4.7a displays the simulated electron distributions on the detector obtained at an extraction voltage of $U_{\text{ext}} = 300$ V and initial kinetic energies of $E_{\text{kin,e}} = 10,\ 100,\ 300$ meV as well as the two- and three-photon excess energies of 678 meV and 3.1 eV. The calculated electron signals form closed structures with increasing spatial extent for increasing initial kinetic energy. The sharp edges allow distinguishing the different energy classes of electrons.

By decreasing the extraction field, the extraction time and accordingly the expansion time of the electronic cloud on the way to the detector is increased. Thus, controlling the extraction voltages gives a handle to zoom into the velocity distribution providing an enhanced energy resolution up to the meV level. Figure 4.7b depicts the simulated electron signals at an extraction potential of $U_{\text{ext}} = 5$ V for initial electron kinetic energies of $E_{\text{kin,e}} = 0.1,\ 0.5,\ 1,\ 3,\ 5$ and 10 meV. Even though the structures apparently deviate from a 2D projection of an ideal spherical density distribution expected in a homogenous electric field, the signal size approximately increases radially within the marked sector (dashed white line) in Fig. 4.7a,b. Figure 4.7c depicts the radii of the different electron signals obtained for the different initial kinetic energies (blue data points). In addition, the expected radius in an parallel-plate capacitor at $\pm U_{\text{ext}}$ with a plate distance according to the extraction mesh distance is displayed. Despite the fact, that the obtained radii are overestimated by the simple model, they exhibit a $E_{\text{kin}}^{1/2}$ dependency as well.

4.2.4. CPT plasma simulations

The aim of accurately describing the dynamics of plasmas covering orders of magnitudes in density and temperature has brought up a multitude of theoretical methods. A comprehensive

overview on the different methods for ultracold neutral plasma is given by Killian et al. [77]. In general, one can distinguish two approaches: macroscopic methods applying kinetic and hydrodynamic models to describe the time evolution of the charged particle phase space density and microscopic methods, describing the dynamics of N particle positions determined by their coupled differential equations of motion.

Whereas macroscopic approaches efficiently describe plasma dynamics mainly in the weakly coupled regime even for high particle numbers and system sizes, they typically do not account for strong ionic coupling as well as the non-equilibrium dynamics driven by the individual inter-particle Coulomb interactions, both occurring on ultrashort timescales in ultracold plasma [76]. For a more accurate description of the ultracold plasma dynamics microscopic models utilizing molecular dynamics (MD) simulations are applied, which calculate charged particle trajectories considering interparticle Coulomb or Coulomb-type interactions and can serve as a validation for macroscopic kinetic models [76]. Regardless of the simplicity of the coupled equations of motion for the charged particles, a full MD description of the ultracold plasma suffers from two main problems.

Given by the long-range character of the Coulomb interaction, for each time step of the simulation, the force on each of the N particles has to be calculated by comparing its position relative to the position of all $N-1$ other particles. Thus, the required computations for a full MD simulation scale with $N(N-1) \approx N^2$ limiting the accessible particle numbers in the plasma [76]. Sophisticated methods [196, 197], which prioritize force contributions of adjacent particles over distant particles are required to diminish this scaling law. As plasma expansion and finite-size effects play a decisive role in ultracold plasma dynamics, simulations confined to a small region assuming periodic boundary conditions are not an option.

A second difficulty arises from the large ion-electron mass ratios (e.g. ≈ 160.000 for ^{87}Rb) causing widely differing timescales of electronic and ionic motion from the femtosecond range to the nano- and microsecond range. In order to circumvent this obstacle, former works have employed drastically reduced mass ratios [198, 199] or imposed different calculation time-steps for different plasma particles [76, 199, 200]. In addition, hybrid approaches combine a hydrodynamic treatment of the fast electronic component and MD simulations of the slow ionic motion [201–203].

The most accurate way to model ultracold plasma is given by a full-scale molecular dynamics simulation at realistic particle mass ratios. Such simulations are limited to a few tens of thousands of particles [204]. By experimentally decreasing the number of particles required for plasma formation to $N \approx 10^2 - 10^3$, ultracold microplasma arising from BEC atomic densities allows to meet the requirements for a full MD treatment over all timescales of the plasma expansion. Thus, it provides a well-controlled experimental benchmark for multi-scale theories. Accessing a density regime, that enables plasma creation with few hundreds to a few thousands of charged particles provides the opportunity to calculate the plasma dynamics within a full MD simulation on the level of individual charged particles.

Here, charged particle tracing plasma simulations are exerted by use of the Particle Tracing

Module COMSOL Multiphysics® software [195]. In contrast to the previously described CPT trajectory simulations, the CPT plasma simulations do account for mutual Coulomb interactions between the charge carriers. For $t > 0$, the emerging dynamics of the plasma is simulated by numerically solving the 3D differential equation of motion for each particle including mutual Coulomb interaction as well as the external electric extraction fields used for the CPT trajectory simulations. In order to avoid the divergence of the interparticle Coulomb potential $U_{\mathrm{C}}(r)$, a bounded interaction potential

$$\tilde{U}_{\mathrm{C}}(r) = \begin{cases} U_{\mathrm{C}}(r), & r > r_0 \\ U_{\mathrm{C}}(r_0), & r \leq r_0 \end{cases} \tag{4.8}$$

is introduced. Here, r indicates the interparticle distance and $r_0 = 20$ nm denotes the potential cut-off radius. Even though this cut-off radius is chosen well below the initial mean particle distance, which is further increasing over time, this model potential limits the validity for the prediction of short-range collisional effects as for example three-body recombination. The simulations furthermore neglect interactions with the remaining neutral atoms as well as radiative energy losses of the charge carriers.

The CPT plasma simulations are carried out paralleled on 35 processing units (2.2 GHz). For $N_{\mathrm{e,i}} = 4000$ particles and a time-evolution of a few microseconds a calculation lasts between 5-22 days, depending on the applied extraction field, which corresponds to a CPU time of a few hundred days.

4.3. Ultrafast electron cooling in an expanding ultracold plasma

4.3.1. Direct observation of electron temperatures

Directly accessing electron temperatures in an ultracold neutral plasma requires dedicated momentum-resolved charged particle detection even for low kinetic energies of the electrons extracted from the plasma. So far, experiments have determined the electron temperatures by measuring the fraction of electrons spilled from the plasma in presence of an extraction field [205], the free plasma expansion [206] driven by the electron temperature or detecting the three-body recombination rate [207], which depends non-linearly on the electron temperatures. Thus, experiments have been inferring electron temperatures only indirectly by deriving them from other observables and consequently rely on accurate theoretical models. In contrast, the experimental setup used in this work provides direct access to the final electron temperature after extraction from the expanded plasma (see Chapter 4.2.3).

Figure 4.8a-c shows the averaged electron signals measured after ionizing a BEC with a single pulse at laser pulse peak intensities I_0 of 1.7×10^{12} W/cm^2 (a), 3.8×10^{12} W/cm^2 (b) and 1.9×10^{13} W/cm^2 (c). Here an extraction voltage of $U_{\mathrm{ext}} = 300$ V is applied (corresponding to an extraction field of 162 V/m at the center). For low intensities (a) the dominant structure on the detector is given by the spatial distribution of the electrons emerging from the non-resonant two-photon ionization process with a kinetic energy of 0.68 eV, corresponding to an initial electron temperature of $T_{\mathrm{e}} \approx 5250$ K. The measured structure is in excellent agreement with the trajectory simulation results (Fig. 4.7a). For the highest intensity shown (c), a second class of electrons appears around the first structure. These electrons stem from the three-photon ATI process with an excess energy of 3.1 eV (compare to Fig. 4.7a).

As a central result, in (b) and (c) an extremely narrow peak appears, corresponding to electrons exhibiting very small kinetic energies. At these intensities, the number of photoionized atoms exceeds the critical number of ions required for plasma formation at the two-photon excess energies. For the non-Gaussian ionic distribution created in this experiment, the plasma condition (see Eq. 4.2) is approximated by a Gaussian distribution with the arithmetic mean radius of $\sigma = (2 \times 1.35\ \mu\mathrm{m} + 5\ \mu\mathrm{m})/3$ leading to a critical ion number of $N^* = 960$. As a result of the plasma creation, a fraction of the photoelectrons is trapped and cooled in the resulting space charge potential of the emerging plasma state.

For a quantitative analysis, Fig. 4.8d shows the radially averaged electron distributions in the depicted circular sector in Fig. 4.8a for $I_0 = 1.7 \times 10^{12}$ W/cm^2 and 3.8×10^{12} W/cm^2. The vertical lines mark the limit of the distributions obtained from the trajectory simulations for 10 meV and 678 meV, previously shown in Fig. 4.7a. At the lowest laser intensity, the kinetic energy distribution is homogeneous up to the energy corresponding to two-photon ionization. At the intermediate intensity, a large fraction of cold electrons is concentrated below the 10 meV line, which corresponds to a temperature lower than 77 K. These slow electrons arise from the cooling dynamics occurring in the ultracold microplasma (see Chap. 4.3.3).

For an increasing number of generated ions the space charge potential further deepens. The

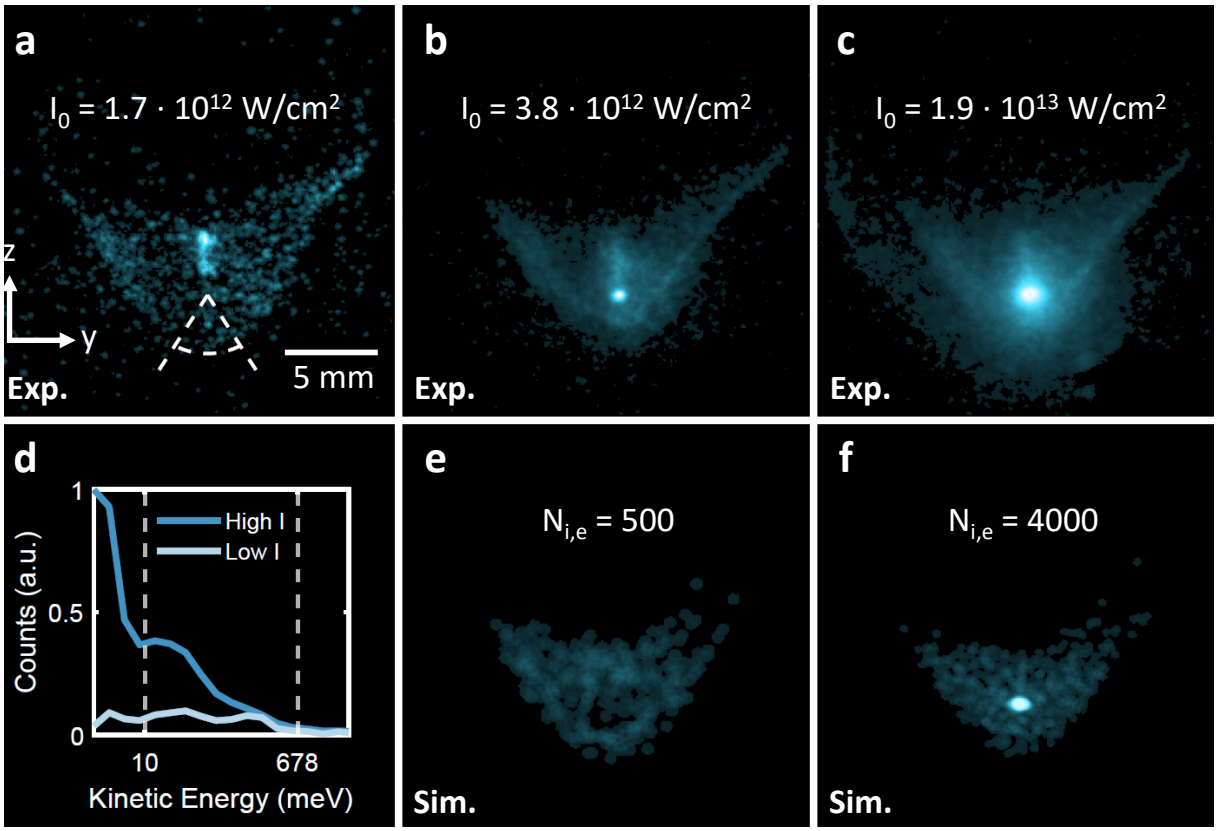

Figure 4.8: Direct measurements of the electron kinetic energy. a-c. Measured time-integrated electron distributions at $\pm U_{\text{ext}} = 300$ V and peak intensity of $I_0 = 0.17, 0.38$ and 1.9×10^{13} W/cm^2 (mean detector image over 18, 23 and 22 realizations). A clear signature for the electrons at the two-photon excess energy is obtained (compare Fig. 4.3d). As the number of ionized atoms exceeds a critical value, an ultracold plasma is formed signalized here by low kinetic energy electrons (b). At highest intensity, the fraction of slow electron grows and the signature for three-photon ATI electrons is visible (c). **d**. Radially averaged spectrum of the recorded electrons at $I_0 = 0.17$ and 0.38×10^{13} W/cm^2 within the circular sector depicted in (a). At high intensities, a bright narrow peak appears, corresponding to electrons with kinetic energy below 10 meV. A clear shift of the photoelectrons towards lower energies resulting from the deceleration imposed by the ionic core can be observed. The vertical dashed white lines depict the radii of the electron distributions obtained by trajectory simulations (see Fig. 4.7a) for $E_{\text{kin,e}}$ = 10 and 678 meV. **e-f**. Plasma simulation results for different electron/ion numbers and an initial kinetic energy of 0.68 eV. For $N_{\text{i,e}} = 500$ (e) we solely observe the two-photon signature while for $N_{\text{i,e}} = 4000$ (f) slow electrons are produced as consequence of ultracold plasma dynamics. Figure adapted from [2] and licensed under CC BY 4.0.

increasing potential depth enables trapping more electrons in the plasma as can be seen in the transition from (b) to (c). In addition, increasing ion numbers also significantly increase the deceleration of the escaping electrons. This deceleration is evident in the averaged spectrum (Fig. 4.8d) as a shift of the electron distribution to the lower energy limit but can also be observed qualitatively as a decrease of the area covered by the kinetic energy distribution in Fig. 4.8a-c.

The dynamics is reproduced by plasma simulations including the mutual Coulomb-interactions between all charged particles. As the calculated electrostatic fields are included, these simulations allow extracting the resulting electron distributions given by the electron points of inci-

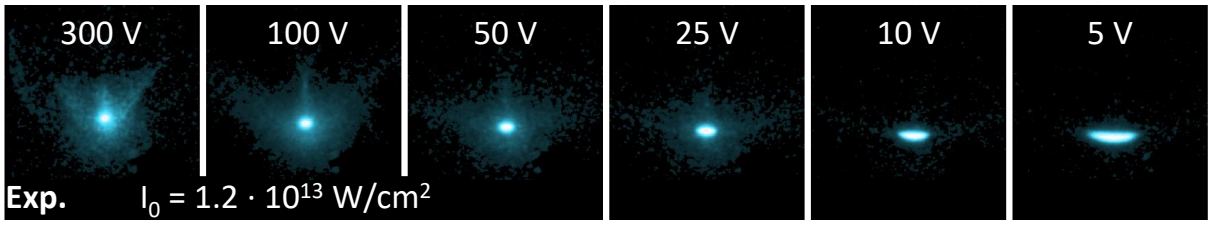

Figure 4.9: Extraction Voltage Scan. Measured electron distributions at a peak intensity of I_0 = 1.2×10^{13} W/cm^2 for different extraction fields (same space scaling). The extraction voltage is reduced from 300 V to 5 V.

dence on the detector surface. Figure 4.8e-f shows the simulated results calculated with initial electron/ion numbers of $N_{\mathrm{i,e}} = 500$ (e) and 4000 (f) as well as an initial electron kinetic energy of 0.68 eV. The simulated kinetic energy distributions are in perfect agreement with the measured ones in Fig. 4.8a-b. In accordance to the measurements, slow plasma electrons emerge only above the critical charge carrier density required for plasma formation.

Whereas applying an extraction voltage of $U_{\mathrm{ext}} = 300$ V allows for detection of electron kinetic energies up to the kinetic energy corresponding to the first ATI process, reducing the extraction field enables measuring low electron kinetic energies with increasing accuracy. Figure 4.9 illustrates the evolution of the measured electron distributions at a peak intensity of I_0 = 1.2×10^{13} W/cm^2, for extraction voltages gradually decreased from 300 V to 5 V. Reducing the extraction field increases the expansion time of the electrons on their way to the detectors and thus enhances the detected spatial extent of the electron distributions. As a result, it enables zooming into the kinetic energy distribution. The highest accuracy is attained at the lowest applicable extraction voltage of $U_{\mathrm{ext}} = 5$ V (corresponding to an extraction field of 4.6 V/m at the center). As CPT trajectory simulations reveal (see Fig. 4.7b), this working point allows for determination of the electrons final kinetic energy down to the meV level.

Figure 4.10a illustrates the measured electron signals obtained for a peak intensity of I_0 = 1.2×10^{13} W/cm^2 and an extraction voltage of $U_{\mathrm{ext}} = 5$ V. The electrons detected within the predominant elliptical structure are low-energy electrons stemming from the ultracold plasma. The higher energy electrons, which escape the ionic core form a dilute uniform background signal, as the low extraction field is not sufficient to draw them to the detector. The corresponding plasma simulation result for $N_{\mathrm{i,e}} = 4000$ is depicted in Fig. 4.10b. Even in this experimentally challenging regime, the measurements and the plasma simulation almost perfectly agree.

Analogously to the measurement at high extraction field, Fig. 4.10c shows the radially averaged electron distributions in the circular sector given by the dashed white lines in Fig. 4.10a. The vertical lines mark the extent of the distributions obtained from the CPT trajectory simulations for 1, 2 and 10 meV (see Fig. 4.7b). As a key result, an upper bound for the final electron kinetic energy of approximately 1 meV is determined experimentally corresponding to an electron temperature of $T_{\mathrm{e}} \approx 8$ K. Consequently, the measured electron cooling within the evolution of the ultracold microplasma covers almost three orders of magnitude from an initial electron temperature of 5250 K to below 10 K.

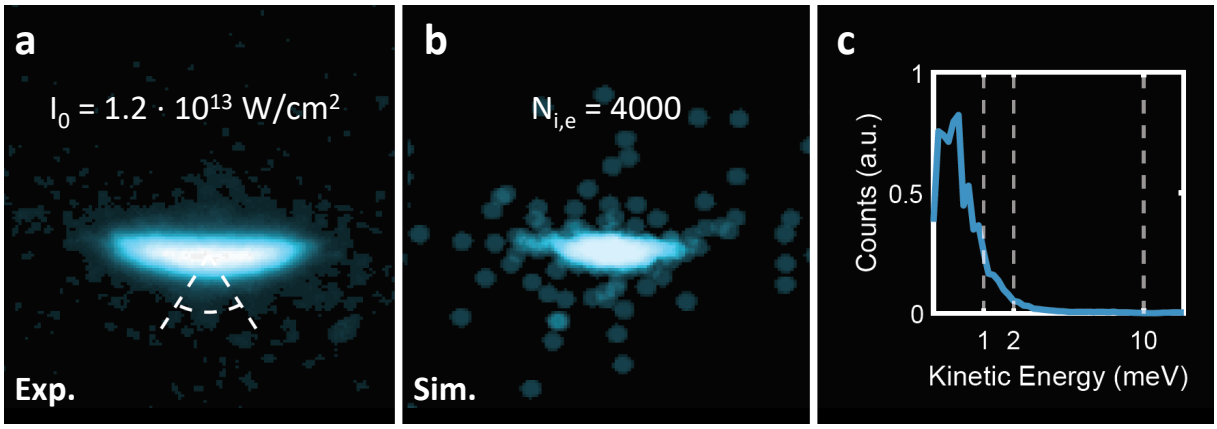

Figure 4.10: Direct measurements of the electron kinetic energy. a. Measured electron distribution for a peak intensity of $I_0 = 1.2 \times 10^{13}$ W/cm^2 at a lower extraction field of $\pm U_{\text{ext}} = 5$ V (mean detector image over 14 realizations). **b**. Electron distribution obtained for $\pm U_{\text{ext}} = 5$ V extraction field after plasma simulation with $N_{\text{i,e}} = 4000$ for an initial electron kinetic energy of $E_{\text{kin,e}} = 0.68$ eV. **c**. Radially averaged spectrum of the recorded electrons within the circular sector depicted in (a). The vertical dashed white lines depict the radii of the electron distributions obtained by trajectory simulations (see Fig. 4.7b) for $E_{\text{kin,e}} = 1$, 2 and 10 meV. Figure adapted from [2] and licensed under CC BY 4.0.

4.3.2. Formation of ultracold plasma

The CPT plasma simulation results presented in Chap. 4.3.1 show, that the occurrence of slow electrons originates from the creation of ultracold plasma, when a critical number N* of electron ion pairs is created. By ionizing different atomic densities at constant laser intensity, the setup allows validating this finding experimentally and distinguishing it from possible strong-field ionization effects contributing to the measured electron spectra .

For this purpose, the initially created charge carrier densities are tuned either by varying the laser intensity and thus the ionization probabilities or by varying the atomic density itself. For this purpose, the intermediate power used in the evaporative cooling during the crossed dipole trap is varied from 2 W providing optimal evaporation to 1 W, where almost all atoms are lost within the evaporation (see Chap. 2.1.5). Thus the target density can be gradually tuned by orders of magnitude from a Bose-Einstein condensed sample with an atomic density of $\rho = 1.3 \times 10^{20}$ m^{-3} to an ultracold thermal cloud at $\rho = 6 \times 10^{17}$ m^{-3}. The corresponding atomic densities are determined by the analysis of the optical density distributions in a time-of-flight measurement where the densities are recorded by absorption imaging for different time steps after switching off the optical dipole trap. Whereas the calculation of in-situ atomic densities is reliable for the limiting case of a fully condensed or thermal atomic sample, it is notoriously difficult for partly condensed samples. In order to account for both the thermal and condensed contribution, the determination requires a bimodal fit using a Gaussian as well as the Thomas-Fermi density model.

Figure 4.11a shows the electron distributions recorded for an extraction field of $U_{\text{ext}} = 300$ V and a peak intensity range from 0.1×10^{13} W/cm^2 to 1.7×10^{13} W/cm^2. The absolute number of detected electrons increases monotonously with both the increasing target density and the

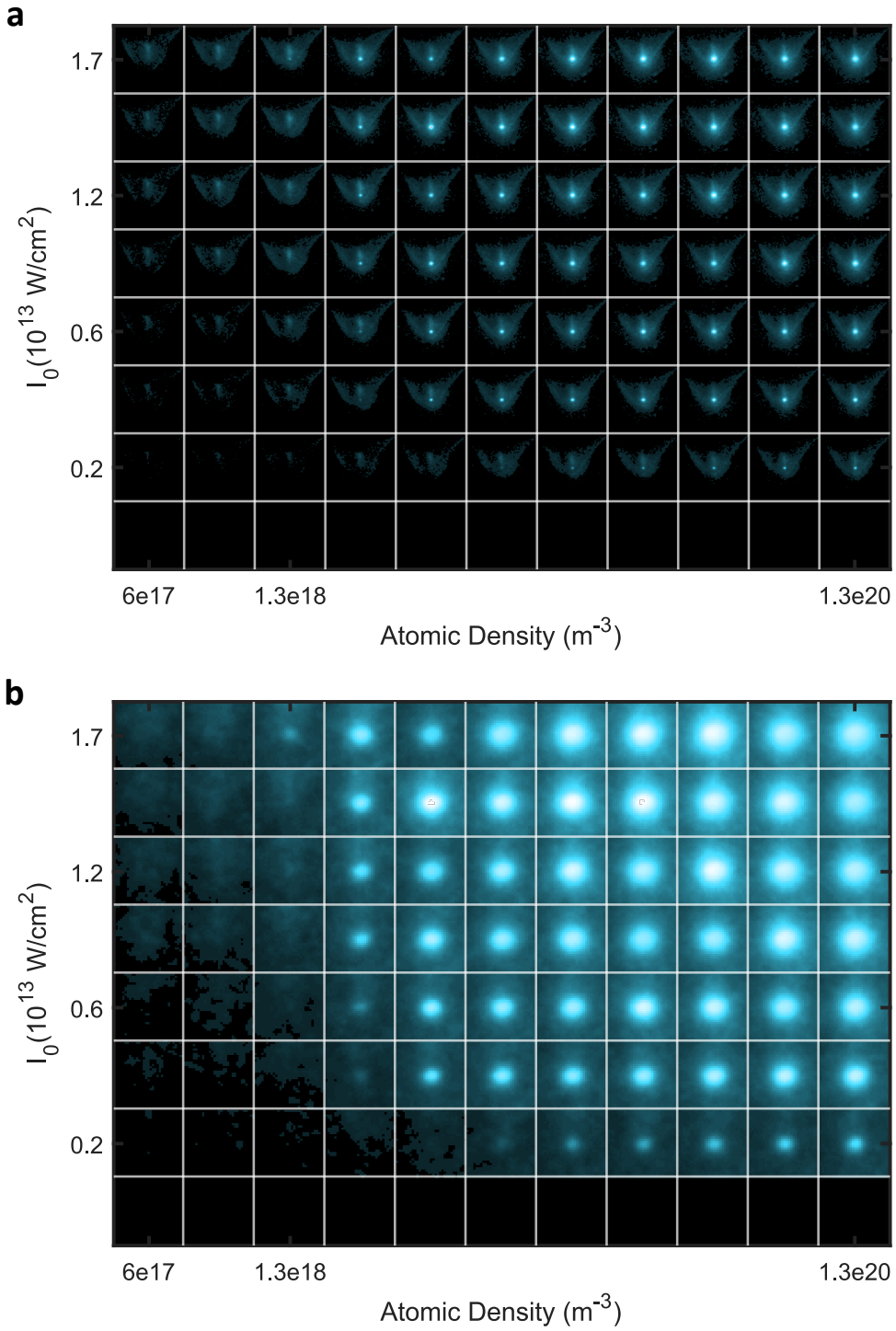

Figure 4.11: Density Dependence of Plasma Formation. a. Measured electron distributions at an extraction voltage of $U_{\text{ext}} = 300$ V. The atomic target density is varied over 3 orders of magnitude and the pulse peak intensity from 0.1×10^{13} W/cm^2 to 1.7×10^{13} W/cm^2. **b.** Zoom into the distributions in (a) around the center of the plasma electron peak.

increasing applied laser intensity. According to Eq. 4.2 for a given density, plasma creation and thus the occurrence of plasma-cooled electrons is expected, if a critical pulse peak intensity is reached. Indeed, the critical intensity for plasma creation decreases with increasing target density. This density-dependence becomes even more evident for a zoom into the electron dis-

tributions around the incidence points of the plasma electrons, which is depicted in Fig. 4.11b.

As a result, the threshold intensity depends on the density of the atomic target, evidencing a collective effect depending on the number of ionized atoms. Consequently, this rules out low energetic electrons directly created in the strong-field ionization process as reported at high Keldysh parameters [208] or speculated in alkali atoms at high intensities [150, 209]. The critical ion number can be deduced from the number of detected electrons for each intensity-density point. As the ionization volume slightly increases with increasing peak intensity, the critical number of ions increases as well. While at $I_0 = 0.2 \times 10^{13}$ W/cm^2 around 500 ions are required, at $I_0 = 1.7 \times 10^{13}$ W/cm^2 around 1000 ions need to be created, which is in good agreement with the calculated value of $N^* = 960$.

4.3.3. Ultrafast plasma dynamics

Substantiated by the excellent agreement with the measured kinetic energy distributions, the CPT plasma simulations grant access to the dynamics of each particle in the plasma evolution. Thus, they enable detailed studies of the energy transfer revealing two electron cooling mechanisms occurring on distinct timescales: an ultrafast cooling process in the course of the plasma formation on picosecond timescales and a subsequent process driven by the Coulomb expansion of the ionic cloud on nanosecond timescales. In order to illustrate the underlying dynamics, Fig. 4.12a-e shows snapshots of the CPT plasma simulations of an ultracold microplasma consisting of a few thousand charged particles.

Initial ultrafast electron cooling

The initial ultrafast cooling process arises from the unique starting conditions of the ultracold microplasma. In contrast to ultracold neutral plasmas (UNP) created at MOT densities and comparably low excess energies (typically below 0.13 eV) [75], the enhanced charge carrier densities in ultracold microplasma allows for plasma creation with high excess energies (0.68 eV), enabling initial electron temperatures of $T_e \approx 5250$ K in a micrometer-sized region. As a result, the majority of photoelectrons leaves the ionization volume within a few picoseconds. On this timescale the ions can be regarded as static (Fig. 4.12a).

The radial expansion of the electron ensemble spatially separates the electronic component from a positively charged ionic core remaining in the plasma center. The decrease of electronic density in the plasma core reduces the shielding between the ions, which thus gain potential energy. In addition, this charge separation process gives rise to a space charge potential that strongly decelerates the escaping electrons (Fig. 4.12b). As a result, the electron kinetic energy is partly converted into ionic potential energy. Whereas half of the electrons entirely escape the ionic core (escaping electrons), the other half is trapped within the evoked space charge potential (plasma electrons[37]). Figure 4.12f depicts the time-evolution of the mean total electron (light

[37]Escaping and plasma electrons in the CPT plasma simulations are distinguished by the maximum ion radius

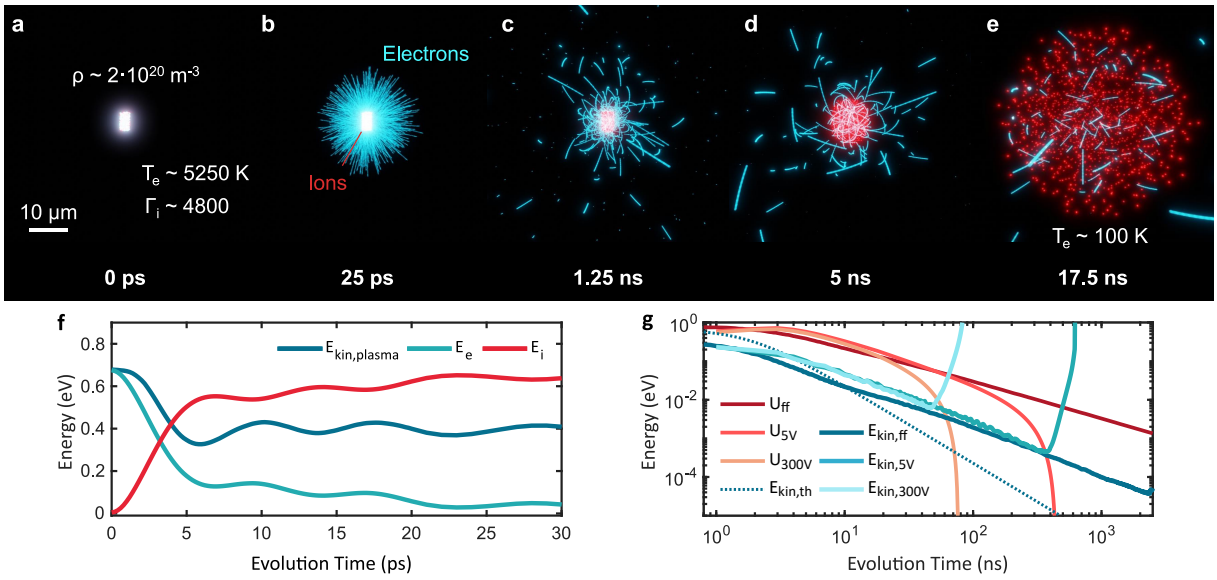

Figure 4.12: Ultrafast dynamics of a highly charged ultracold microplasma. a-e. Snapshots from a CPT simulation tracing the photoelectrons (blue) and ions (red) right after strong-field ionization of an ultracold atomic cloud. An initial homogeneous distribution of ions at a density of $\rho = 2 \times 10^{14}$ cm^{-3} and electrons at a temperature of $T_e \approx 5250$ K is created in a micrometer-sized volume (a). The initial kinetic energy of the ions corresponds to a coupling parameter of $\Gamma_i = 4800$ according to Eq. (4.1). The electrons leave the ionization volume on a picosecond timescale and are subsequently decelerated by the positively charged core of remaining ultracold ions (b). While the outer electrons escape, the inner electrons are bound onto orbital trajectories in the ions' attractive Coulomb potential forming an ultracold plasma (c). On a nanosecond timescale the ionic component expands driven by Coulomb-repulsion and further cools the electrons to temperature below 100 K (d-e). **f**. Picosecond time-evolution of the field-free plasma simulation with the total energy per particle for the electrons (light blue) and the ions (red) and the mean kinetic energy of the electrons captured within the plasma (dark blue). **g**. Evolution of the kinetic energy of the trapped plasma electrons and the effective depth of the space charge potential on the nano- to microsecond timescale for field-free expansion (dark blue/red), $\pm U_{ext} = 5$ V (blue/red) and $\pm U_{ext} = 300$ V (light blue/red) as well as the theoretically predicted kinetic energy evolution for adiabatic electron cooling (dotted blue line). Figure taken from [2] and licensed under CC BY 4.0.

blue line) and ion energy (red line) per particle determined by the sum of kinetic and potential energy of each component. Additionally, the kinetic energy of the plasma electrons (dark blue line) is shown. Quantitative analysis reveals an energy transfer of 50% of the initial electron kinetic energy onto ionic potential energy within the first 7 ps of plasma evolution. On this timescale, the trapped electrons are cooled down from 5250 K to about 2500 K. As a key result, this yields an unprecedented electron cooling rate of 400 K/ps. Disorder-induced heating of the electrons is negligible, as the associated temperature according to Eq. 4.5 of $T_{DIH} \approx 70$ K in this density regime is exceeded by orders of magnitude by the initial electron temperature.

The large charge imbalance of the microplasma strongly influences the many-body dynamics.

given by the smallest sphere around the ionization center containing all ions. For the field-free simulations, electrons are regarded as plasma electrons, if their distance from the ionization center at $t = 2500$ ns is less than twice the maximum ion radius. For the simulations at $U_{ext} = 300$ V and $U_{ext} = 5$ V, electrons are regarded as plasma electrons, if their distance from the ionization center after 40 / 300 ns is less than twice the maximum ion radius.

As depicted in Fig. 4.12c, the electrons are trapped in orbital trajectories within the Coulomb potential of a quasi-static ionic core. This leads to an oscillatory exchange of energy between the captured electrons and the ions (see Fig. 4.12f). The timescale of these oscillations is determined by the inverse of the initial electron plasma frequency $2\pi/\omega_{\mathrm{p,e}} \approx 8$ ps. Whereas the energy transfer between the individual electrons and the ions is predominantly in phase during the initial electron expansion, it dephases over time leading to a damping behavior of the oscillation amplitude.

Coulomb-driven plasma expansion

On a nanosecond timescale, the potential energy stored in the ions gradually translates into kinetic energy leading to a Coulomb explosion of the plasma (Fig. 4.12d,e). Whereas UNP typically exhibit hydrodynamic expansion after equilibration due to the electrons' thermal pressure [189], here, the positively charged plasma expansion is dominated by the Coulomb pressure of the charge imbalance, yielding an asymptotic expansion velocity of the rms ion radius of 418 m/s. However, this is in reasonable agreement with the expected hydrodynamic expansion velocity $v_{\mathrm{hyd}} = 710$ m/s according to Eq. 4.6.

The ionic expansion leads to a further reduction of the electronic temperature down to $T_{\mathrm{e}} \approx 100$ K within tens of nanoseconds. The evolution of the mean kinetic energy of the plasma electrons during the plasma expansion are shown in Fig. 4.12g for CPT simulations without extraction field (dark blue line), with $\pm U_{\mathrm{ext}} = 5$ V (blue line) and $\pm U_{\mathrm{ext}} = 300$ V (light blue line). In addition, the expected electron kinetic energy progression given by adiabatic cooling during the plasma expansion according to Eq. 4.7 is shown (dotted blue line). The observed electron cooling rates largely follow the prediction by the hydrodynamic model. However, the initial ultrafast electron cooling is not captured by this model, which only predicts a maximum cooling rate of 1.9 K/ps.

The decrease of the ionic density over time lowers the depth of the binding space charge potential. As a result, for the simulations including an extraction field the number of plasma electrons is reduced by about 80% over time, since electrons escape from the plasma, when they enter large orbits where the non-linearly increasing extraction field becomes dominant. When the gradient of the space charge potential is exceeded by the extraction field, the plasma electrons are escaping the space charge potential and are drawn to the detector. Hence, the final electron temperatures can be controlled by the extraction field, which determines the plasma lifetime and thus the duration of the electron cooling process. Without extraction field, electrons can be cooled down to sub meV energies in less than 1 µs.

The CPT Plasma simulations provide access to the potential well created by the unpaired ions during the plasma expansion. The extraction field E_{ext} adds up to the 1D space charge potential $U(r)$ along the detection axis lowering the effective trapping potential

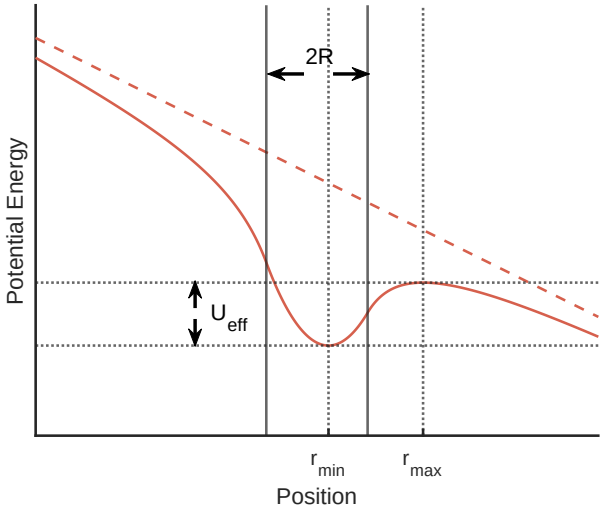

Figure 4.13: Space charge potential. The potential energy gradient induced by the extraction field (dashed orange line) lowers the Coulomb potential evoked by the ionic core with radius R (solid orange line). The effective potential well depth U_{eff} is given by the potential difference between r_{max} and r_{min}.

$$U_{\text{eff}}(r) = U(r) - E_{\text{ext}} \cdot r, \tag{4.9}$$

where r denotes the distance to the ionization center. Fig. 4.12g shows the evolution of the effective space charge potential depth for the plasma simulations without extraction field (dark red line) as well as at extraction voltages of $\pm U_{\text{ext}} = 5$ V (red line) and $\pm U_{\text{ext}} = 300$ V (light red line) (corresponding to E_{ext} = 4.6 V/m and E_{ext} = 162 V/m). Here, for each time-step $U(r)$ is approximated by the Coulomb potential of a homogeneously charged sphere

$$U(r) = \begin{cases} \frac{Q}{8\pi\varepsilon_0 R}\left(3 - \frac{r^2}{R^2}\right), & r \leq R \\ \frac{Q}{4\pi\varepsilon_0 r}, & r > R \end{cases} \tag{4.10}$$

where the radius R is given by the maximal ion radius and the charge $Q = e \cdot N_{\text{diff}}$ is given by the difference N_{diff} of number of ions and electrons within the maximum ion radius. The potential depth is determined by the difference of the local maximum $U_{\text{eff}}(r_{\text{max}})$ and the local minimum $U_{\text{eff}}(r_{\text{min}})$ of the effective potential at

$$r_{\text{min}} = \frac{4\pi\varepsilon_0 E_{\text{ext}} R^3}{Q} \text{ and } r_{\text{max}} = \sqrt{\frac{Q}{4\pi\varepsilon_0 E_{\text{ext}}}}. \tag{4.11}$$

Single-particle plasma dynamics

The CPT plasma simulations allow accessing information for each charged particle during the plasma evolution providing insight to the individual contribution of each particle to the over-

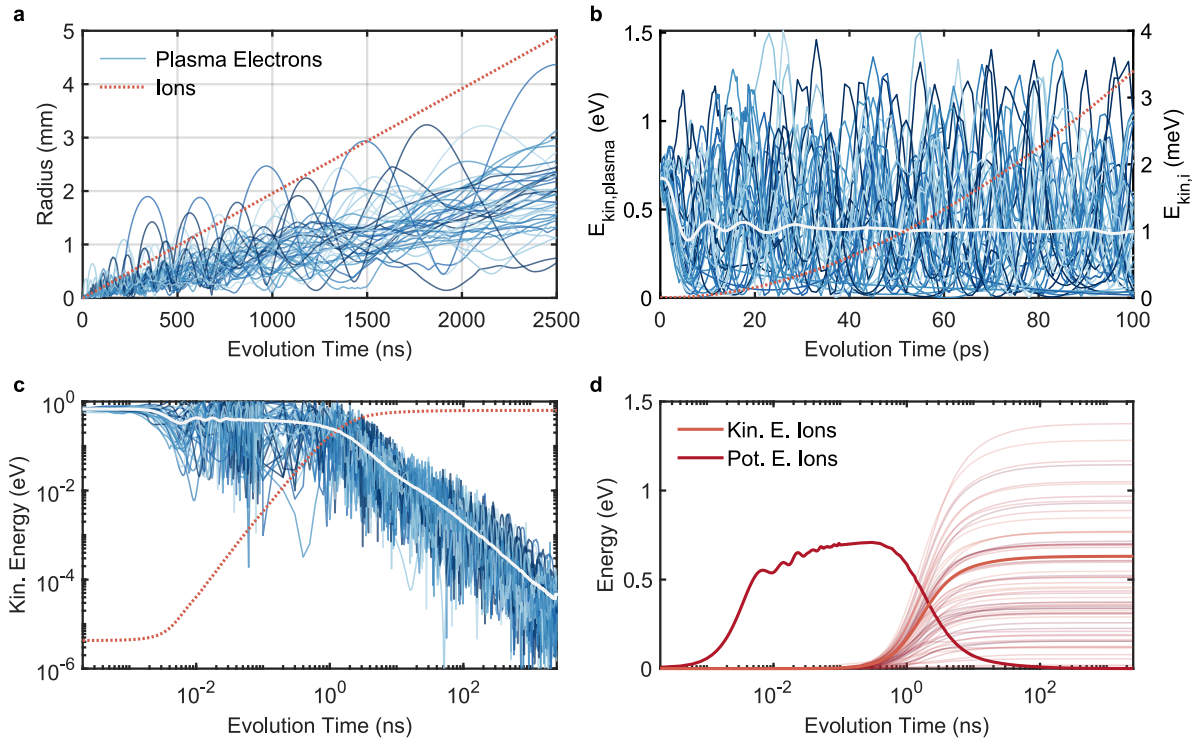

Figure 4.14: Plasma dynamics at the single particle level. The dynamics is shown for a generic selection of 41 plasma electrons out of $N_{e/i} = 4000$ simulated particles. **a.** Time-evolution of the distance to the ionization center for the plasma electrons (blue lines) in the field-free plasma simulation (see Fig. 4f-g) together with the maximal ion radius (dotted orange line). **b.** Time-evolution of the single electron kinetic energies (blue lines). In addition, the mean kinetic energy of all plasma electrons (bold white line) and all ions (dotted orange line) is given for the first 100 ps of plasma evolution. **c.** Same data as depicted in (b) displayed in log/log scaling up to an evolution time of 2500 ns. **d.** Time-evolution of the single ion kinetic energies (light red lines, generic selection of 60 ions), the mean kinetic energy per ion (orange line) and the mean potential energy per ion (red line). Subfigures (a-b) are taken from [2] and licensed under CC BY 4.0.

all dynamics. In Fig. 4.14a the time-evolution of distance from the plasma center is depicted for single plasma electrons (blue lines), which are obtained by a field-free plasma simulation with $N_{e/i} = 4000$. For clarity, the graph only depicts a generic selection of 41 plasma electrons to illustrate the dynamics. One identifies different oscillatory motions exhibiting a variety of frequencies ranging from hundreds of gigahertz to a few megahertz. The frequency is decreasing with increasing amplitude of the oscillations, since the driving ionic Coulomb potential is shielded by the more closely bound electrons. Accordingly, the oscillation frequencies also decrease over time, as the attractive potential flattens within the expansion of the ionic core. Furthermore, the maximum ion radius (dashed orange line) is shown, which gives the spatial extent of the ionic core during evolution.

In Fig. 4.14b the corresponding kinetic energies of the plasma electrons (blue lines) as well as the mean kinetic energy of all 1961 plasma electrons (bold white line) for the first 100 ps of plasma evolution. The observed oscillations in the mean kinetic energy (also compare Fig. 4.12f) are caused by the oscillatory motion of the individual electrons with similar fre-

quencies and the apparent damping is evoked by their dephasing. On the picosecond timescale, the ions start to accelerate driven by their mutual Coulomb repulsion (dotted orange line). Figure 4.14c shows the same data for the entire plasma evolution plotted on a logarithmic scale. The electrons exhibit oscillatory in- and decrease of kinetic energy on their motion on orbital trajectories within the plasma expansion. As the electrons for each oscillation leave a deeper potential as the return into, they experience a net energy loss and thus further cooling.

In order to understand the plasma expansion on the nanosecond timescale, which is given by the expansion of the ionic core, Fig. 4.14d displays the time-evolution of the mean potential energy (red line) and the mean kinetic energy per ion (orange line). As the initially confined electrons expand and the charge imbalance is established, the ions gain potential energy energy. The initial oscillations observed for the mean kinetic energy of the plasma electrons given by the in-phase oscillations of the electronic component into and out of the ionic core translates in an oscillation of the exerted electron shielding and thus an oscillation of the ionic potential energy in the first picoseconds. After a few hundreds of picoseconds, the ionic potential energy reaches its maximum and is subsequently radially accelerating the ions. The experienced acceleration of each ion is determined by its radial position in the ionic core. Whereas ions in the center of the ionic core are barely accelerated since force contributions of the surrounding ions cancel out, the ions at the edges of the ionization volume are repelled by the entire ionic core. The single ion kinetic energy evolutions (light red lines, generic selection of 60 ions) indicate strong acceleration within the first 10 ns, which is gradually decreasing with decreasing ionic density. After 100 ns of plasma evolution, each ion approximately reaches its asymptotic expansion velocity and the plasma expands uniformly.

Thermalization

Another perspective on the plasma dynamics is given by the time-evolution of the velocity distributions of both components. Figure 4.15a-c show histograms of the distributions of the magnitude of the velocities of the plasma electrons and ions. After creation, the monoenergetic electronic component broadens in the velocity space within the first picoseconds and as the electrons expand, the distribution further spreads towards the low velocity limit. In the subsequent cooling, the distribution narrows again approaching zero velocity.

The ionic velocity distribution broadens as well, albeit on the order of nanoseconds. The velocity profile reflects the radial density profile of the ionic cloud with increasing particle number for higher radii and a relative sharp edge underlining the translation of radial position in radial velocity given by the Coulomb explosion. After a few nanoseconds, most potential energy is transformed to kinetic energy and the velocity distribution stays almost unchanged for the subsquent expansion.

In order to compare the microplasma to UNPs, where electron and ion thermalization occur, the equilibration for both components is investigated. As a quantitative measure for the equili-

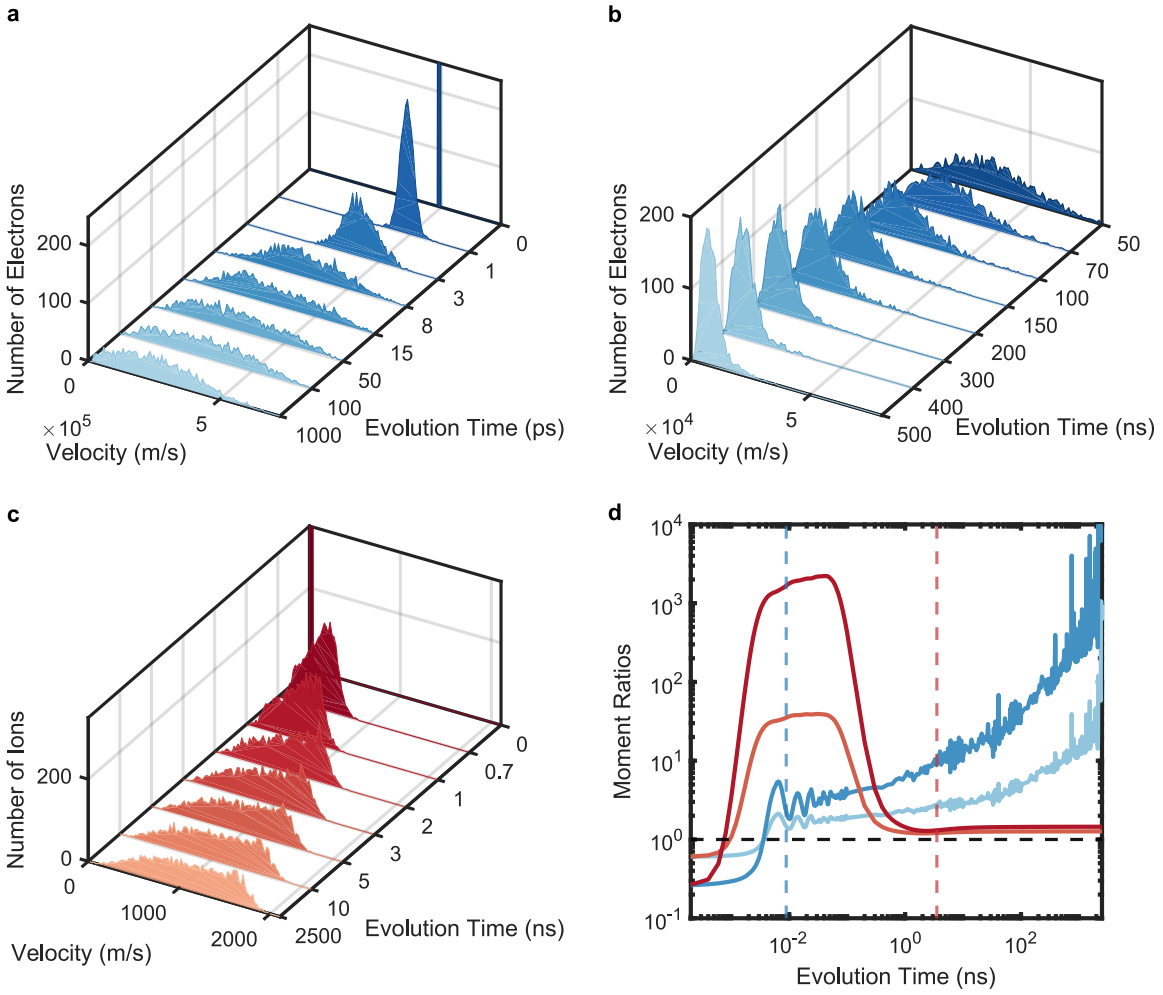

Figure 4.15: Time-Evolution of electron/ion kinetic energy distributions. a.-b. Histogram of the kinetic energy distribution of the plasma electrons for different evolution times. **c.** Histogram of the kinetic energy distribution of the ions for different evolution times. **d.** Moment ratios $\frac{3}{5}\langle v^4\rangle / \langle v^2\rangle^2$ (solid dark blue/red line) and $\frac{9}{35}\langle v^6\rangle / \langle v^2\rangle^3$ (solid light blue/red line). The blue/red vertical dashed lines denote electron/ion plasma period $\tau_{\mathrm{p,e/i}}$.

bration of the electronic and ionic plasma components, Fig. 4.15d displays the moment ratios $\frac{3}{5}\langle v^4\rangle / \langle v^2\rangle 2$ as well as $\frac{9}{35}\langle v^6\rangle / \langle v^2\rangle^3$ for the plasma electrons (a) and the ions (b), where v denotes the electron/ion velocity and $\langle ...\rangle$ denotes the averaged value over all electrons/ions for each time-step. In the global thermal equilibrium, where the components exhibit Maxwell-Boltzmann velocity distribution, these moment ratios equal unity [210]. For the electrons, one obtains a quasi-equilibrium state approaching a Maxwell-Boltzmann velocity distribution after an evolution time of $\tau_{\mathrm{p,e}}$ with subsequently diverging moment ratios yielding a non-thermalized electron ensemble. For the ionic component at evolution times $t < \tau_{\mathrm{p,i}}$, as the ionic core explodes due to the mutual Coulomb repulsion, the ion velocity distributions widely differs from a Maxwell-Boltzmann distribution. Beyond the ion plasma period, the moment ratios approach unity.

Plasma parameters

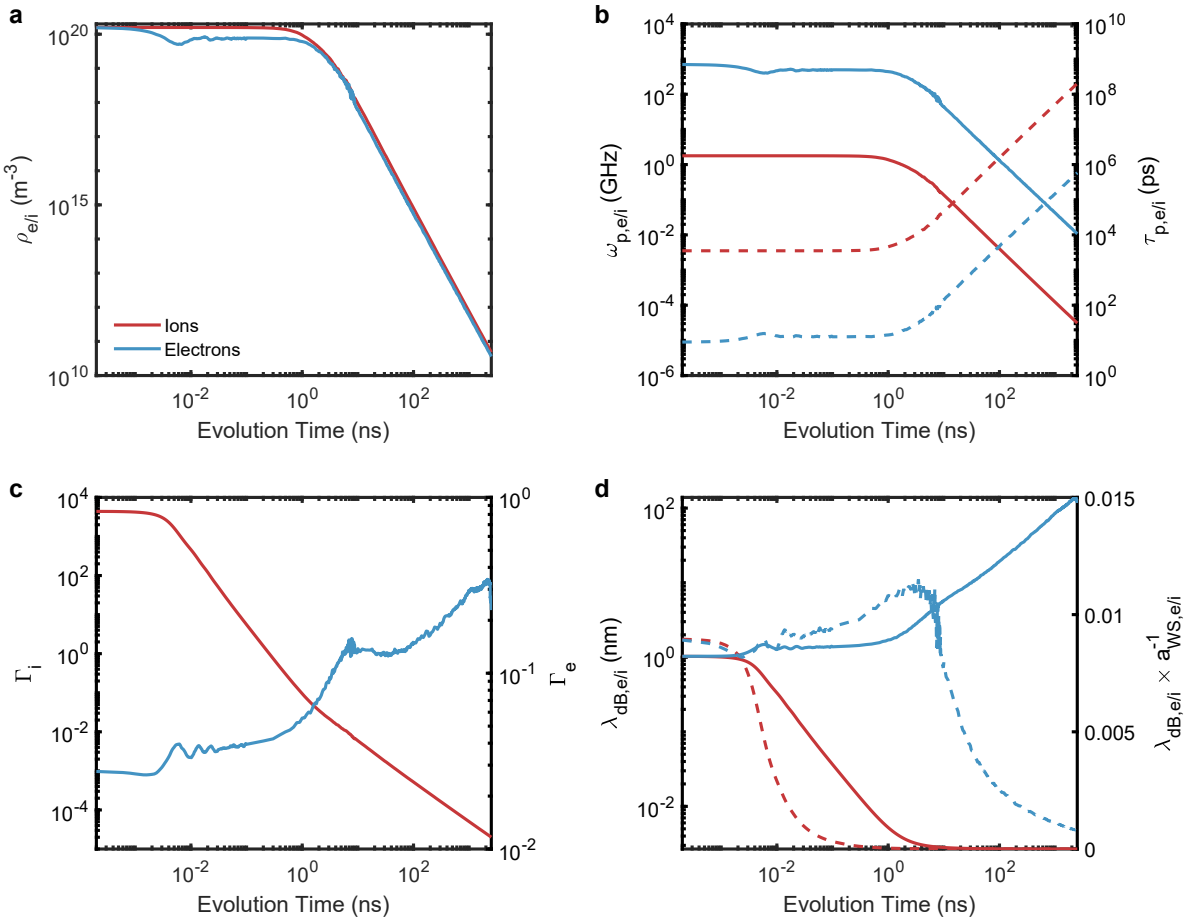

Figure 4.16: Time-Evolution of plasma parameters. **a.** Density evolution of electrons (blue line) and ions (red line) in a spherical volume around the ionization center. **b.** The resulting electron/ion plasma period $\tau_{p,e/i} = 2\pi\omega_{p,e/i}^{-1}$ (dashed blue/red line) and plasma frequencies $\omega_{p,e/i}$ (solid blue/red lines). **c.** Coulomb coupling parameter of the electron/ion component (blue/red line) determined by the particle densities (a) and the plasma electron/ion mean kinetic energy (see Fig. 4.14). **d.** Electron/ion de Broglie wavelength $\lambda_{dB,e/i}$ (dashed blue/red line) and ratio between de Broglie wavelength and Wigner-Seitz radius $a_{WS,e/i}$. Figure adapted from [2] and licensed under CC BY 4.0.

Since the ultracold microplasma passes orders of magnitude in size and charged particle kinetic energy in the course of the expansion, it is essential to take a closer look on the time-evolution of the plasma parameters. Figure 4.16a shows the electron and ion density evolution in the center of the plasma. The electron density drops within the first expansion and stays constant for the first nanosecond. As the ionic component expands, the electron and ion density equally decreases and even fall below typical initial UNP densities. The density evolution determines the plasma frequency as well as the plasma period given in Fig. 4.16b slowing down the electronic orbital oscillations during the plasma expansion. In addition, the ionic plasma frequency significantly decreases within the first plasma period (given by the initial ionic density). In contrast to UNP, where plasma expansion can be regarded as slow compared to the inverse

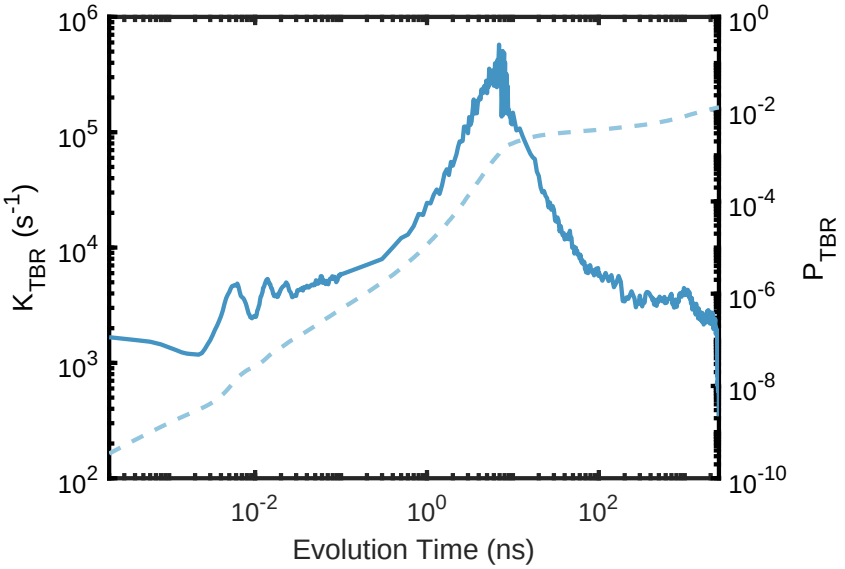

Figure 4.17: Three-body recombination in the ultracold microplasma. Time-evolution of the TBR rate K_{TBR} per ion during the plasma expansion (solid blue line) as well as the resulting time-integrated recombination probability P_{TBR} per ion (dashed blue line). Figure taken from [2] and licensed under CC BY 4.0.

ionic plasma frequency, here, during the plasma expansion, the evolution time exceeds the ionic plasma period, preventing ionic thermalization. The ions only accumulate an integrated phase $\theta_{\mathrm{p,i}} = \int \omega_{\mathrm{p,i}}\, dt = 2.6\,\pi$ corresponding to roughly one oscillation within the expansion.

In Fig. 4.16c the ion and electron plasma coupling parameters are depicted. The ionic coupling parameter decreases after the first electron plasma period when charge imbalance is established due to ionic acceleration and increasing interparticle distance. On the contrary, the electronic coupling parameter increases during the plasma expansion since the electron temperature decreases over orders of magnitude. The simulations reveal a maximum electron coupling parameter of $\Gamma_{\mathrm{e}} = 0.3$ approaching significant electron coupling.

Electron temperatures in the Kelvin domain raise the question of quantum degeneracy for the electronic ensemble. Fig. 4.16d illustrates the electron/ion de Broglie wavelengths $\lambda_{\mathrm{dB,e/i}}$ at different expansion times. Whereas the ionic wavelength quickly decreases due to acceleration, the electrons attain a maximum de Broglie wavelength on the order of $\lambda_{\mathrm{dB,e/i}} \approx 100$ nm at the end of the plasma expansion. However, the ratio of the mean interparticle distance given by the Wigner-Seitz radius $a_{\mathrm{WS,e/i}}$ and the matter wavelength (dashed blue/red line) never exceeds 1.3%, which yields $E_{\mathrm{kin,e}}/E_{\mathrm{F}} > 6000$, where $E_{\mathrm{F}} = \frac{\hbar^2}{2m_{\mathrm{e}}}\left(3\pi^2\rho_{\mathrm{e}}\right)^{2/3}$. Thus, a quantum mechanical description required for a fermionic ensemble close to degeneracy can be safely disregarded.

4.3.4. Plasma lifetime

For ultracold plasma in the density and temperature regime described in this manuscript, three-body recombination (TBR) is expected to be the dominant process of electron-ion recombination. The TBR rate K_{TBR} per ion according to classical TBR theory is given by $K_{\mathrm{TBR}} \approx$

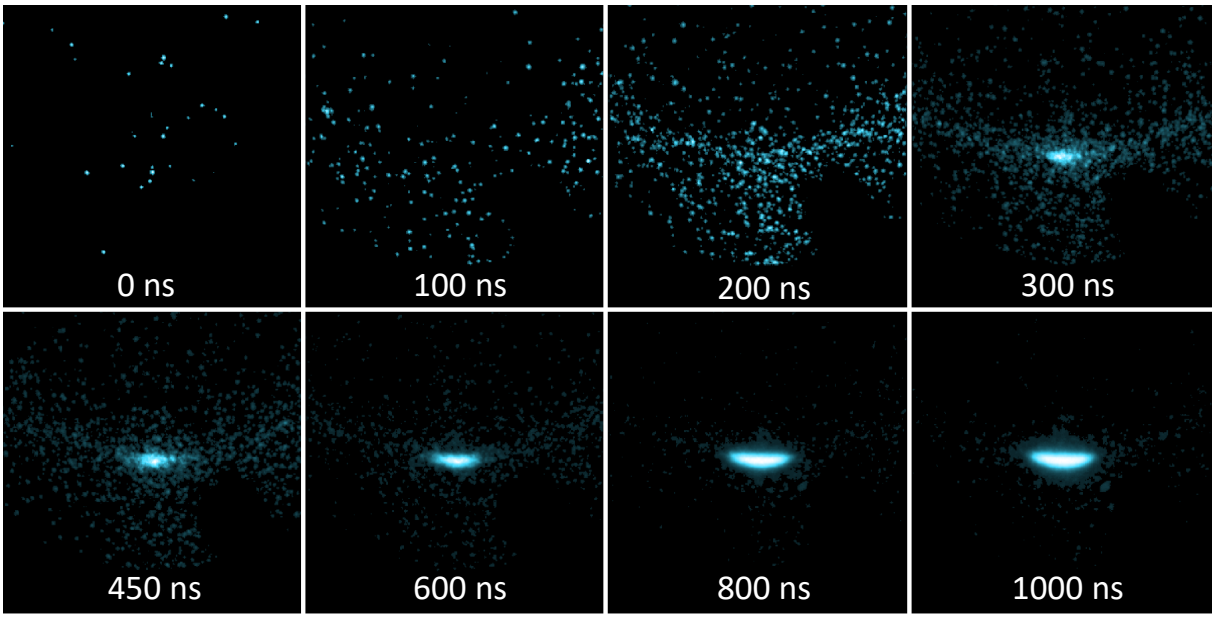

Figure 4.18: Time-resolved electron detection. Cumulated electron signal detected up to time delays of 0, 100, 200, 300, 450, 600, 800 and 1000 ns between femtosecond laser pulse with a peak intensity of 1.2×10^{13} W/cm^2 and the repulsive voltage pulse. The signals are averaged over more than 10 realizations and normalized to each maximum value to improve contrast. Figure adapted from [2] and licensed under CC BY 4.0.

$3.8 \times 10^{-9} T_e^{-9/2} \rho_e$ s^{-1}, where T_e is the electron temperature in K and the electron density ρ_e is given in cm^{-3} [77]. Figure 4.17 shows the calculated TBR rate per ion (solid line) as well as the time-integrated TBR probability per ion (dashed line). After 2.5 µs of plasma expansion, a cumulated TBR probability of approximately 1% is reached. As a result, the plasma is expected to last on the order of 100 µs before a significant fraction of Rydberg atoms is created by recombination. However, on the ten microsecond timescale, when the plasma is dilute and collisions barely occur, radiative and dielectronic recombination might further limit the plasma lifetime.

Besides detecting the accumulated electron signal giving access to the underlying kinetic energy distribution, a gated detection scheme allows for time-resolved electron detection (see Chapter 2.2.2). A short repulsive voltage pulse reverses the polarity of the electron extraction mesh and repels electrons that have not already passed the mesh. Thus, it enables to access cumulated electron signals up to a variable arriving time, while preserving the spatial resolution. Figure 4.18 shows the cumulated electron signals obtained at an extraction voltage of $U_{ext} = 5$ V for different delay times of the repulsive voltage pulse to the femtosecond laser pulse. Here, the BEC is ionized with a peak intensity of 1.2×10^{13} W/cm^2. Within first 200 ns electrons are detected at almost randomly distributed positions on the detector, displaying a homogeneous signal as expected for the escaping photoelectrons at 0.68 eV kinetic energy, since the low extraction voltage is not sufficient to direct all of their trajectories onto the detector. In the subsequent timesteps between 300 ns and 600 ns only a small fraction of cold plasma electrons

is detected. These electrons can be associated to the electrons leaking out of the plasma as a consequence of the extraction field during the expansion. In the last 200 ns the fraction of plasma electrons significantly increases. This strong increase is evoked by the electrons which are captured within the plasma up to the point, when the ionic Coulomb potential is exceeded by the extraction potential and the plasma is torn apart. After an arrival time of 1000 ns, all electrons are detected and the signal remains unchanged.

Figure 4.19a-d displays the measured cumulated electron counts integrated over the whole detection area for different electron arrival times. The temporal profiles are recorded at extraction voltages of $U_{\text{ext}} = 5$ V (a), $U_{\text{ext}} = 25$ V (b), $U_{\text{ext}} = 50$ V (c) and $U_{\text{ext}} = 100$ V (d) and ionizing laser peak intensities of $I_0 = 4,\ 6,\ 9,\ 12 \times 10^{12}$ W/cm^2 (blue data points, from dark to light). In accordance to the qualitative observations in Fig. 4.18, at an extraction voltage $U_{\text{ext}} = 5$ V (a) one clearly distinguishes two plateaus in the electron signal being attributed to the escaping electrons arriving first and the plasma electrons arriving with a delay of several hundreds of nanoseconds. Observing two distinct classes of electrons constitutes an additional signature for ultracold plasma formation [75]. As expected, for an increasing extraction field (b-f), the arrival time of both the escaping as well as the plasma electrons is reduced.

In order to quantitatively analyze the temporal distributions, a double sigmoid function

$$f(t) = \frac{a_1}{1 + e^{-b_1 \cdot (t - c_1)}} + \frac{a_2}{1 + e^{-b_2 \cdot (t - c_2)}} \tag{4.12}$$

is fitted to the data in Fig. 4.20a, where the parameters a_1/a_2, b_1/b_2 and c_1/c_2 correspond to the amplitude, the slope of the increasing signal and the point of inflection of the first/second plateau. The solid lines in Fig. 4.19a-d show the obtained fit results as well as the 95 % confidence interval of the fit (shaded areas). At $U_{\text{ext}} = 100$ V the temporal resolution of the detection scheme only supports distinguishing a few data points and thus prevents reliable fitting for the lower two intensities.

Figure 4.19e-f shows the obtained amplitudes a_1 of the escaping electrons (e) and a_2 of the plasma electrons (f). As expected, with increasing intensity, as the total number of created electrons is increased, the amplitude of both the escaping as well as the plasma electrons increases monotonously. In principle, the fit enables extracting the fraction of plasma electrons from the relative height of both plateaus, but this deduction is challenging as the detection efficiency depends on both the velocity class of electrons and the applied extraction field. As previously discussed in Chap. 2.2.1, on the one hand low extraction fields increase the detection efficiency for low kinetic energy electrons by increasing the area of incidence and thus preventing electron depletion in the MCP material and on the other hand the detection of high kinetic energy electrons benefits from the increased capture range of high extraction fields as clearly seen for the escaping electrons in Fig. 4.19e. The electron counts corresponding to the plasma electrons do not increase for reduction of the extraction field within the error bars.

Figure 4.20a depicts the electron arrival rates given by the time derivative of $f(t)$ for a peak intensity of $I_0 = 1.2 \times 10^{13}$ W/cm^2. The plasma lifetime is determined by the time delay be-

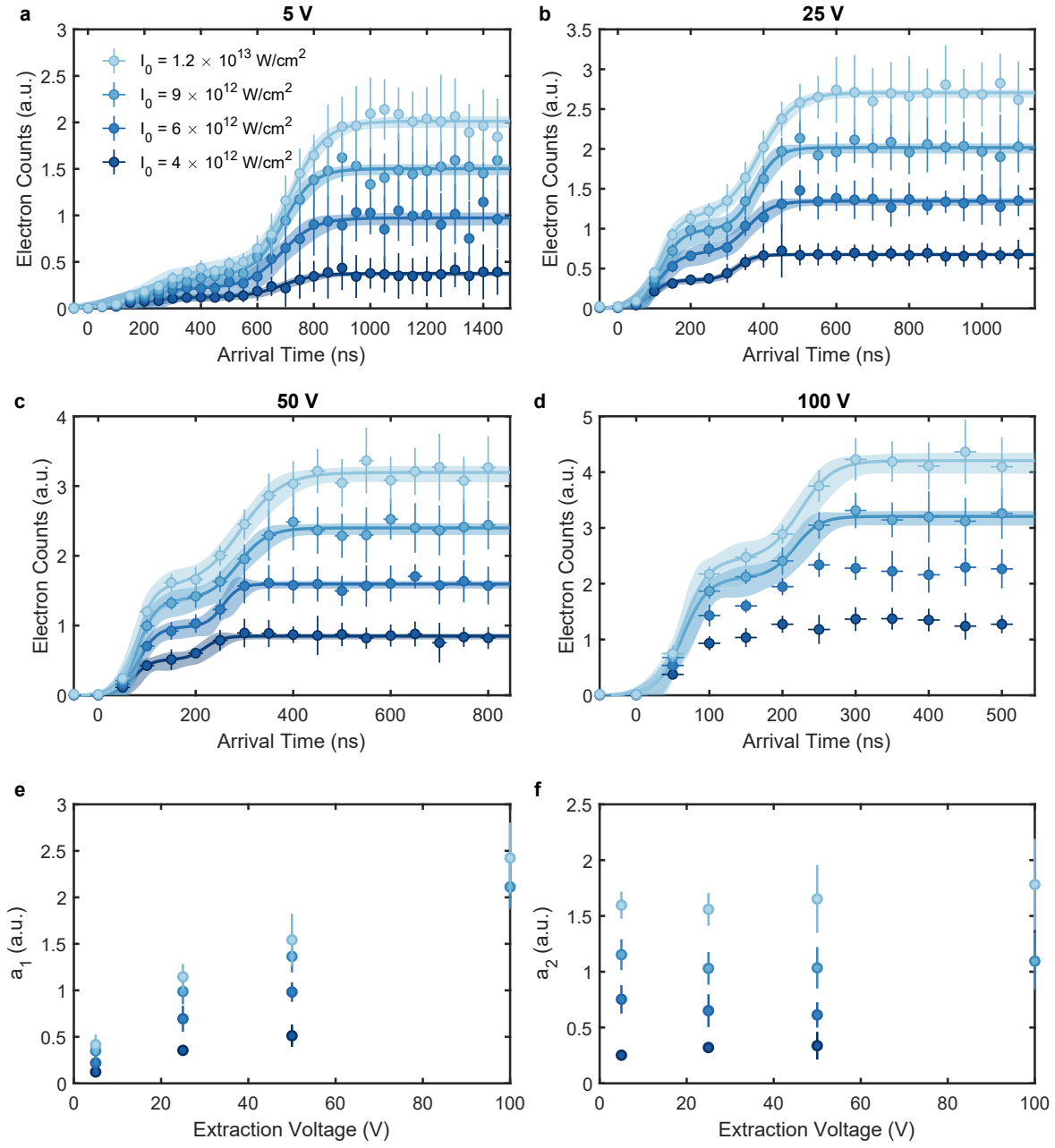

Figure 4.19: Time-Resolved Measurement of Plasma Electrons. a.-d. Measured arrival time distributions obtained for peak intensities of $I_0 = 4,\ 6,\ 9,\ 12 \times 10^{12}$ W/cm^2 (data points from darkest to lightest blue) at extraction voltages of $U_{\text{ext}} = 5$ V (a), $U_{\text{ext}} = 25$ V (b), $U_{\text{ext}} = 50$ V (c), $U_{\text{ext}} = 100$ V (d). The counts are spatially integrated over the whole detector area. The vertical error bars are given by the standard deviation over all realizations, while the horizontal ones indicate the time uncertainty of the repulsive voltage pulse. The solid lines correspond to the double-sigmoid function fitted to the data points according to Eq. 4.12 and the shaded areas show the 95 % confidence interval of the fit. **e.-f.** Escaping/captured electron numbers given by the amplitudes a_1/a_2 of the double-sigmoid fit. The error bars are given by the 95 % confidence interval of the fit.

tween the photoelectrons and plasma electrons given by the arrival time difference $c_1 - c_2$. The calculated plasma lifetimes are reported in Fig. 4.20b, the error bars are given by the 95 % confidence interval for the fitted inflection points. As the extraction field is increased, the effective Coulomb potential (see Eq. 4.9) vanishes at earlier stages of the plasma expansion. Hence, the

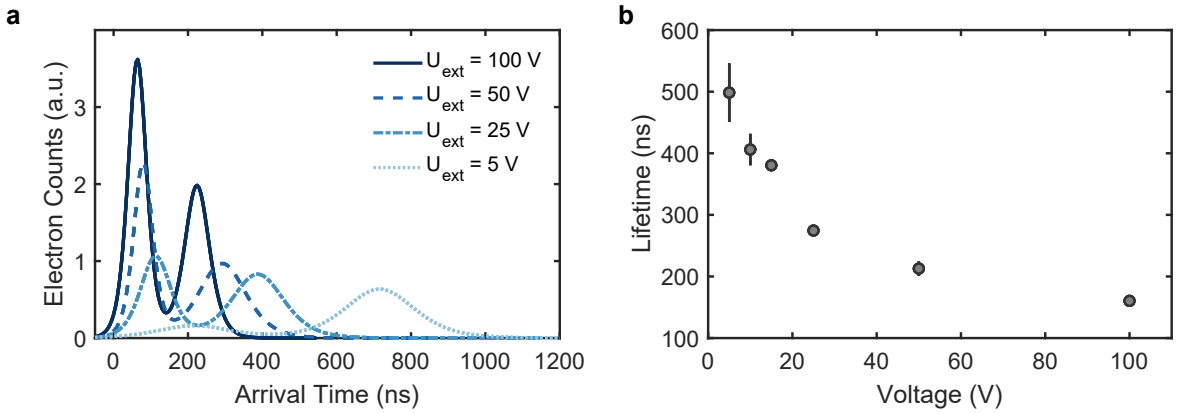

Figure 4.20: Plasma Lifetime. a. Electron time-of-flight distributions obtained by the derivative of double-sigmoid fits to the data in Fig. 4.19a-d at a peak intensity of $I_0 = 1.2 \times 10^{13}$ W/cm^2. The two peaks correspond to the escaping arriving first and the delayed plasma electrons. **b.** Plasma lifetime for different extraction fields calculated by the arrival time difference $c_1 - c_2$ (see Eq. 4.12). The error bars are determined by the 95 % confidence interval for c_1 and c_2. Figure adapted from [2] and licensed under CC BY 4.0.

extraction field terminates the plasma evolution and can be utilized to control the plasma evolution time on a nanosecond timescale. The measured plasma lifetimes for $U_{\text{ext}} = 5$ and 100 V are in good agreement with the times for the vanishing effective Coulomb potential extracted from the CPT plasma simulations (compare Fig. 4.12g). The longest plasma lifetime of 499(48) ns is attained at the minimum extraction voltage of $U_{\text{ext}} = 5$ V and sets the temporal limit for the electron cooling process from 5250 to below 10 K.

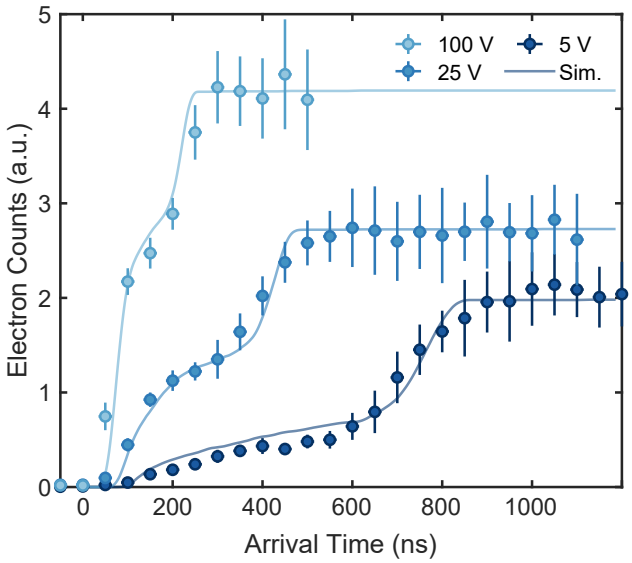

Figure 4.21: Time-resolved photoelectron detection. Accumulated electron counts measured at peak intensities of 1.2×10^{13} W/cm^2 for different extraction fields. The vertical error bars are given by the standard deviation over all realizations, while the horizontal ones indicate the time uncertainty of the repulsive voltage pulse. The solid lines show the vertically scaled results of the corresponding CPT plasma simulations started with $N_{\text{e,i}} = 4000$ electrons/ions. Figure adapted from [2] and licensed under CC BY 4.0.

For the extraction fields of $U_{\mathrm{ext}} = 5,\ 25$ and 100 V, CPT plasma calculations have been conducted as well. The corresponding, simulated arrival time distributions for $N_{\mathrm{e,i}} = 4000$ electrons/ions are depicted in Fig. 4.20 (solid lines, vertically scaled with one free parameter) together with the measured data for $I_0 = 1.2 \times 10^{13}$ W/cm^2. The obtained simulated results for all three extraction voltages show excellent agreement with respect to their temporal profile. In addition, the relative height of the distinct plateaus is in good agreement with the measurements.

4.4. Ultracold electron sources

Besides the fundamental interest in the plasma dynamics of ultracold microplasma, such ultracold microplasmas are also interesting as ultracold electron or ion sources.

Microplasma-based ultracold electron sources

Providing low electron temperatures and enormous cooling rates, ultracold plasma may be used in plasma-based ultracold electron sources [211]. The generated low-emittance electron bunches can be utilized for seeding high-brilliance particle accelerators [212] and coherent imaging of biological systems [213]. The ultracold microplasma system links contemporary source designs utilizing MOTs [214, 215] where the electron-cathode interactions are negligible and traditional state-of-the-art electron sources [216–218] where the emittance is fundamentally limited by such interactions. The BEC density regime indeed promotes an electron cooling mechanism based on their interaction with the ionic core acting as photoemission cathode.

For the use of ultracold electron bunches for electron diffraction imaging of crystal structures, the transverse coherence length [214, 215]

$$L_\perp = \frac{\hbar}{m_\mathrm{e} c} \frac{\sigma_\mathrm{r}}{\varepsilon_\mathrm{r}} \tag{4.13}$$

has to cover a few unit-cell spacings of the target, in order to obtain interference. Here, σ_r is the rms bunch radius and ε_r denotes the normalized transverse rms emittance

$$\varepsilon_\mathrm{r} = \sigma_\mathrm{r} \cdot \sqrt{\frac{k_\mathrm{B} T_\mathrm{e}}{m_\mathrm{e} c^2}}. \tag{4.14}$$

The rms emittance gives a measure for the volume covered in the position-and-momentum phase space by the electron ensemble and reflects the focusability of the resulting beam. Thus, the normalized emittance is traditionally used to quantify the beam quality. As the emittance stays conserved over typical beam shaping methods, the transverse coherence length can be arbitrarily adapted onto different target sizes. For this purpose, the relative transverse coherence

$$C_\perp = \frac{L_\perp}{\sigma_\mathrm{r}} = \frac{\hbar}{m_\mathrm{e} c \varepsilon_\mathrm{r}}, \tag{4.15}$$

which is solely determined by ε_r is preferably used as a second measure for the beam quality.

Fig. 4.22 shows the time-evolution of the velocities and the displacement of all plasma electrons in one spatial direction obtained for the field-free simulation with $N_\mathrm{i,e} = 4000$. For comparison, the initial area covered by the electrons within this 1D phase space and corresponds to the normalized emittance in this direction is highlighted by the dashed black line. In the course of the first picoseconds of plasma evolution, the electrons expand corresponding to the initial velocity components yielding a rotation of the rectangular distribution in the phase space representation. As the electrons start thermalizing, the distribution extends further in space, while

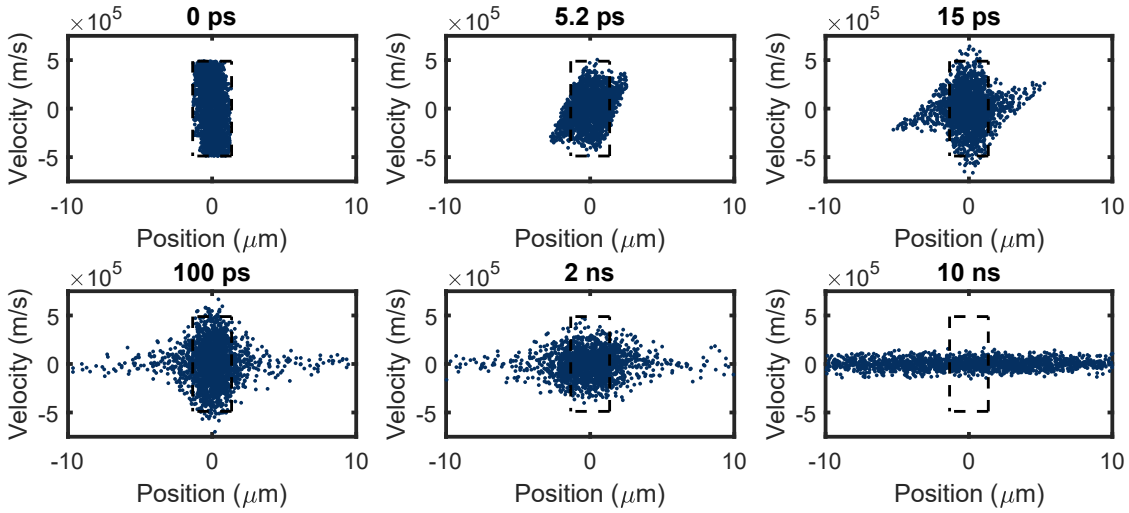

Figure 4.22: Phase-space evolution of plasma electrons. Electron position x and velocity v_x projection in the course of the plasma expansion obtained by CPT simulation of a field-free plasma expansion with $N_{\mathrm{i,e}} = 4000$. The dashed black line marks the area covered by the initial electron distribution.

the electron temperature is constantly decreasing. This evolution continues on the nanosecond timescale, as the ionic component expands.

In order to quantify the source properties of the electronic component, the time-evolution of the normalized transverse rms emittance according to Eq. 4.14 is shown in Fig. 4.23 during the plasma expansion. Here, the radial rms bunch size σ_{r} is given by the standard deviation of the electron positions in all three dimensions and the electron temperature is given by the mean kinetic energy of the plasma electrons. As a central result, the normalized emittance only varies within one order of magnitude for a plasma expansion of 2.5 s. As the electronic component expands from a micrometer-sized sample at sub-electronvolt kinetic energies to millimeter-sized sample at sub-millielectronvolt energies, ε_{r} increases by a factor of ten. The maximal emittance of $\varepsilon_{\mathrm{r}} = 1$ nm rad is comparable to values achieved in contemporary source designs utilizing MOTs [214, 215, 219] and results in a transverse relative coherence of $C_{\perp} = 4 \times 10^{-4}$. In this experimental setup, the electron excess energy can be reduced further by working closer to the ionization threshold, which shall allow reaching the value of $C_{\perp} = 10^{-3}$ required for single-shot electron diffraction imaging of microcrystals [214].

It should be noted, that the initial electron bunch right after photoionization already exhibits optimal source properties, whereas the plasma evolution leads to an increase of the emittance over time. Thus, utilizing the electron bunch right after photoionization provides a reasonable alternative to the bunch after plasma evolution. In addition, this paves the way to the creation of sub-picosecond electron bunches. Extraction of a picosecond electron bunch from the expanding plasma would require high voltage switching times in the picosecond range, which are typically not realizable. In contrast, photoionizing the atoms in the presence of an extraction field, which is strong enough to prevent plasma formation, gives access to electron bunch durations inherited from the ionizing pulse. For an ion number of $N_{\mathrm{i,e}} = 4000$ within the micrometer-

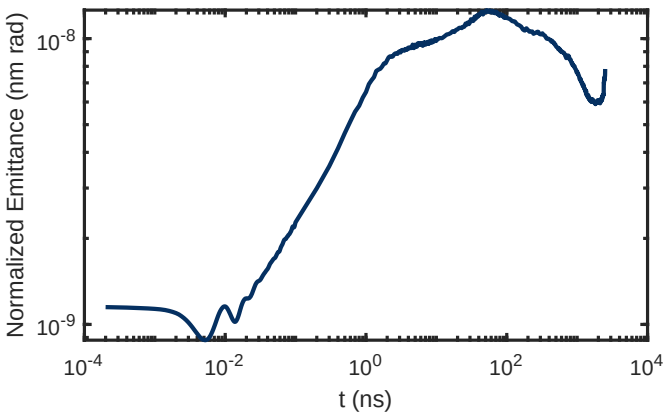

Figure 4.23: Electron bunch emittance. Time-evolution of the transverse normalized rms emittance according to Eq. 4.14 within the plasma expansion.

sized ionization volume, an extraction field of $E_{\mathrm{IV}} \approx 50$ kV/m is required. By implementing a dedicated scheme of extraction electrodes providing sufficient electric field strength, the combination of a BEC being ionized locally by a femtosecond laser pulse does enable creation of sub-picosecond electron bunches with a normalized rms emittance of $\varepsilon_{\mathrm{r}} = 1$ nm rad and a tunable bunch charge of 0.1-0.6 fC. With these properties, the bunches should be suited for the usage in ultrafast electron diffraction experiments. These experiments study structural dynamics of molecules with nanometer spatial resolution on picosecond and sub-picosecond timescales [220–222].

High repetition rate electron source

Besides the source parameters regarding emittance, coherence and bunch duration being sufficient for single-shot imaging of molecular structures on ultrafast time-scales, using a Bose-Einstein condensate as electron source limits achievable repetition rates. Whereas the comparably high temperature and atom number in MOTs enables recycling the atomic target after photoionization, the condensed atomic target is irreversibly disturbed by one photoionizing pulse due to significant photoionization losses and dynamics induced by the dipolar forces of the femtosecond laser pulses.

As depicted in Fig. 4.24, a different scheme is proposed, where the ultracold thermal cloud held in the optical tweezer (see Chap. 2.1.4) during optical transport is used as atomic target. Here, instead of having the final position of the optical transport at the position of the ionization region, the focus of the optical tweezer is moved through the ionization region with constant velocity v while being ionized by a pulse train of the femtosecond laser. In order to overcome the ionization losses, the atoms have to travel a distance d exceeding twice the radius of the cylindrical ionization volume within the time frame between two ionizing pulses. As the femtosecond laser features a pulse repetition rate of 100 kHz, a transport velocity of $v = 0.3$ m/s is required, which is well within the range of the transport system.

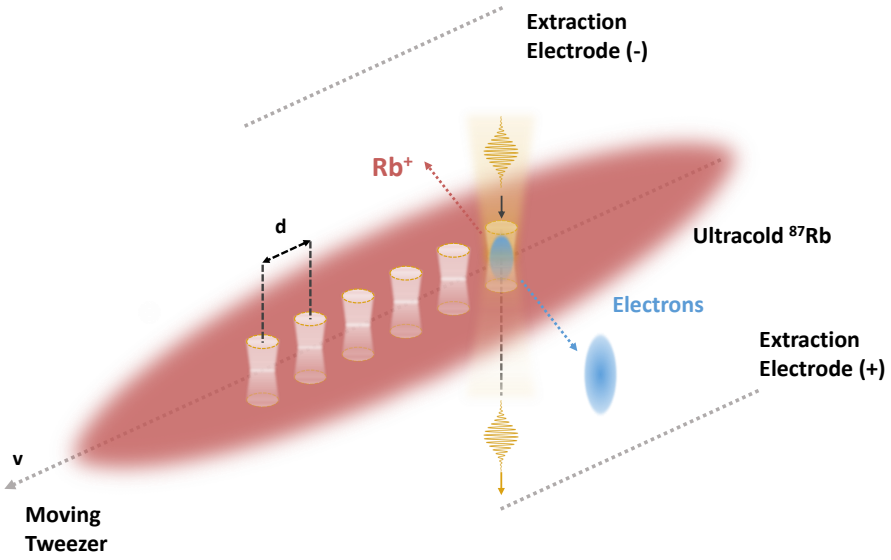

Figure 4.24: Moving optical tweezer as ultracold electron source. The ultracold atomic cloud is held in the dipole trap beam of the optical transport and is moved through the pulse train of femtosecond laser pulses with a velocity of v, which determines the distance d of two adjacent ionization centers. The created ultracold electron bunches are extracted by two opposing high voltage electrodes.

Since the thermal clouds in the optical tweezer contain more than 10^6 atoms, the proposed configuration allows for electron bunch trains of a few hundred electron bunches within few milliseconds yielding an averaged beam current of up to 0.1 nA. Due to the lower atomic density of $\rho_a \approx 10^{18}$ m^{-3} the ionizing laser power and thus the ionization volume has to be increased at the cost of beam quality, leading to an achievable normalized emittance of approximately $\varepsilon_r = 10$ nm rad.

4.5. Conclusion

In this chapter, the creation of ultracold plasma by local photoionization of a ^{87}Rb BEC has been reported. In section 4.1 the experimental realization was described and the main plasma parameters arising from the unexplored charge carrier density regime are presented. The large density combined with the extremely low temperature of the BEC support an initial ionic coupling parameter of $\Gamma_i = 4800$.

Section 4.2 introduces the charged particle tracing simulations, which serve as virtual twin for the conducted experiments. As the creation ultracold microplasma only requires a few thousand charged particles, such CPT plasma simulations enable a full-scale MD treatment over all timescales of the plasma expansion. In addition, these simulations include the geometries of the experimental environment allowing for a full simulation of the experiment.

In section 4.3 the central experimental results are presented. Electron cooling from 5250 K to below 10 K within 500 ns of plasma evolution has been directly measured by kinetic energy resolved charged particle detection. The corresponding CPT simulation results perfectly agree with the measured data and additionally reveal an ultrafast energy transfer of 50% of the initial electron energy onto the ionic component within the first plasma period of $\tau_e \approx 8$ ps. This yields an ultrafast initial electron cooling rate of 400 K/ps. The combination of high experimental control over the initial plasma state and accurate theoretical description by the CPT plasma combination provides an unique model system for testing the validity of statistical plasma models.

The chapter concludes with an evaluation of the ultracold microplasma as a source for ultracold electrons in section 4.4. The attainable normalized rms emittance of $\varepsilon_r = 1$ nm rad is comparable to contemporary source designs utilizing MOTs. By applying an extraction field of approximately 50 kV/m, the a dedicated electron source should provide tunable bunch charges of 0.1-0.6 fC with bunch durations inherited from the femtosecond laser pulse and thus suitable for ultrafast electron diffraction (UED) experiments.

5. Outlook

5.1. Strongly-coupled ultracold plasma

Photoionizing ultracold quantum gases in the strong light field of ultrashort laser pulses paves the way towards even more elaborate ultracold plasma system than the ultracold microplasma. By further exploiting the toolbox of ultrafast dynamics, our experimental setup allows investigating more advanced dynamical schemes. The impact of the plasma geometry can be studied by taking advantage of the non-linearity of the strong-field ionization process in order to shape the ionization volume beyond Gaussian distributions, which allows to significantly influence the expansion dynamics [223]. The interaction between several microplasmas, launched simultaneously within a BEC, can also be explored. This allows to target open questions as the interaction and thermalization of multiple ionic components with mass ratios around unity, which were recently studied in dual species plasma [224]. Moreover, pump-probe schemes utilizing a second synchronized terahertz pulse for controlling the plasma evolution can offer direct experimental access to the ultrafast dynamics of the microplasma.

As discussed in the previous chapter, attaining strong coupling in both the ionic and electronic component constitutes a major motivation for studying ultracold plasma. In this regime, particle motion is predominantly determined by interparticle Coulomb interaction and random thermal motion is negligible. By tuning the laser wavelength close to the ionization threshold, the initial kinetic energy of both, the electrons and ions can be minimized. The minimum kinetic energy for the two-photon ionization process is given by twice the spectral bandwidth of the femtosecond laser pulse. The time-bandwidth product of a Fourier-transform-limited Gaussian pulse yields $\Delta\tau\Delta f = 0.441$, with the FWHM duration $\Delta\tau = 215^{+20}_{-15}$ fs and bandwidth Δf of the pulse. The resulting minimum excess energy of the electrons is given by

$$E_{\mathrm{kin,e}} = 2h\Delta f = 2h\frac{0.441}{\Delta\tau} = 17 \text{ meV}, \tag{5.1}$$

where h denotes Planck's constant. At BEC densities of 2×10^{20} m^{-3}, this corresponds to an initial electron/ion coupling parameter of $\Gamma_{\mathrm{e}} = 1.2$ and $\Gamma_{\mathrm{i}} = 1.9 \times 10^5$. The coupling can be further increased by decreasing the spectral bandwidth using a grating monochromator [225]. First measurements with these plasma systems have been conducted in the time of this thesis, but are beyond the scope of this work.

However, for plasma creation from spatially uncorrelated atomic targets disorder-induced heating, also called correlation heating, limits the achievable ionic coupling parameter and prevents the development of ionic correlations. Several approaches have been proposed to circumvent this limitation. Small initial ionic distances can be avoided by ionizing a degenerate fermionic atomic target, which obtains spatial correlation from the Pauli hole [193], or a beforehand Rydberg-excited atomic target [76, 89]. In addition, reducing the heating by additional laser cooling of the ions in an UNP has been examined theoretically [201] and recently realized experimentally [81].

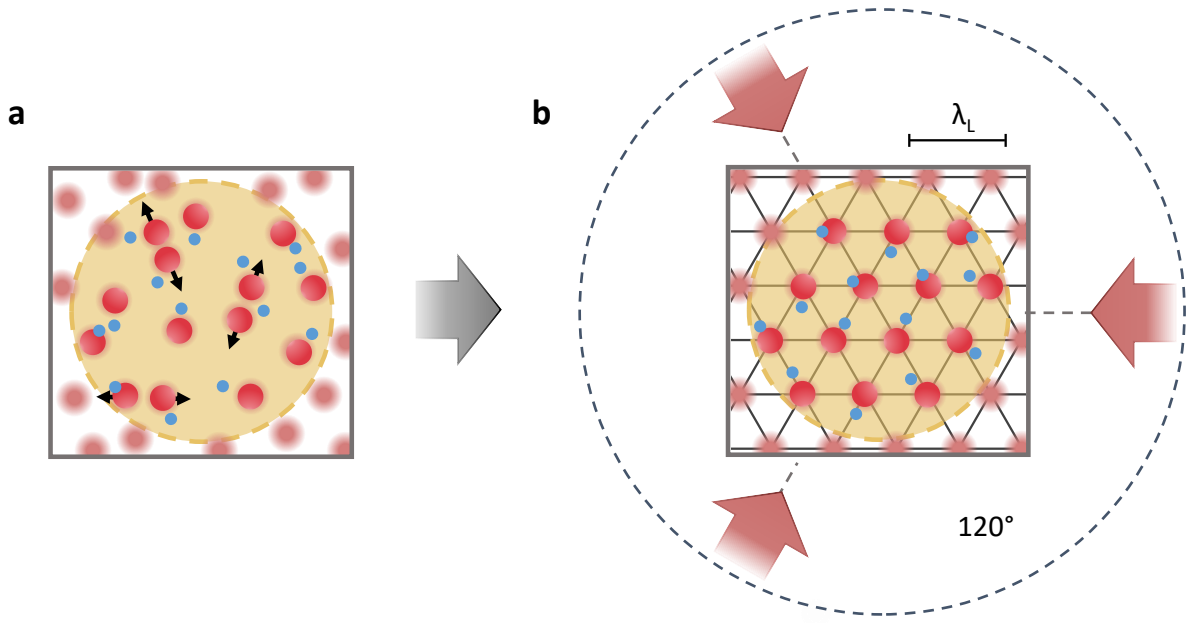

Figure 5.1: Creation of a crystalline ultracold plasma. a. Plasma creation by photoionization of a disordered atomic sample in the focal plane of an ultrashort pulse (yellow area). Ion pairs with short mutual distances experience a repulsive acceleration which leads to disorder-induced heating of the ionic ensemble. **b.** Plasma creation from a BEC trapped in a triangular lattice created by three laser beams (red arrows) which intersect under an angle of 120° and two counterpropagating beams perpendicular to the drawing plane. As the ions are created in the equilibrium distances forming a crystalline structure, the forces of the nearest neighbor ions cancel out.

Utilizing ultracold atoms at sub-microkelvin temperatures instead of a magneto-optically trapped gas as atomic targets allows loading the BEC into an optical lattice as depicted in Fig. 5.1b- This imposes a spatial correlation to the atomic target, which is inherited by the ionic component after photoionization [226]. Thus, the level of control established in the manipulation of quantum gases can be transferred to the initial state of ultracold plasma. By controlling the lattice depth, the initial spatial correlation of the atomic target can be gradually tuned from a superfluid phase with randomized atomic positions to a Mott insulating phase, where each lattice site is populated by one atom [227]. This technique grants access to the role of correlation in ultracold plasma and enables creation of ultracold plasma with an initially crystalline distribution of charged particles. Moreover, plasma dynamics could be studied for different lattice geometries by variation of the intersection angles and beam polarizations.

The achievable electron/ion densities in such correlated systems is given by the density of lattice sites, which is determined by the lattice geometry and the applied laser wavelength. The use of a typical triangular lattice created with an Nd:YAG laser at $\lambda_L = 1064$ nm wavelength allows preparing a Mott insulating phase with single particle filling at an atomic density of $\rho_a = 7.7 \times 10^{18}$ m^{-3}. Together with the minimum excess energy according to Eq. 5.1 this enables initial electron/ion coupling parameters of $\Gamma_e = 0.81$ and $\Gamma_i = 1.3 \times 10^5$. The reduced density compared to the BEC significantly reduces the initial electron plasma period to $\tau_{p,e} = 40$ ps. As a result, picosecond laser pulses are sufficient for plasma creation, which allow for sub meV

initial kinetic energies enabling even strongly coupled electron components with $\Gamma_e > 10$ while avoiding disorder-induced heating.

In addition, a second route to strong electron coupling is proposed by the additional creation of Rydberg atoms in the ultracold plasma [228]. Whereas three-body recombination to Rydberg atoms constitutes an electron heating mechanism in ultracold plasma, the collisional ionization of Rydberg atoms can remove kinetic energy from the electrons and thus providing significant electron cooling process [229]. The experimental setup allows to study such systems by further reducing the laser frequency to or below the ionization threshold starting with a mixture of ionized and Rydberg-excited atoms. In addition, the large spectral bandwidth of the femtosecond laser pulses shall prevent Rydberg blockade effects and enable an efficient excitation of a dense ultracold Rydberg gas, which can form strongly-coupled plasma by avalanche ionization [91, 93, 188].

Finally, the novel experimental setup allows to utilize ion detection with spatial and temporal resolution as well to access the microplasma dynamics. The analysis of the corresponding ion signals is beyond the scope of this thesis, but could enable further studies on the energy transfer between the electronic and ionic component as well as the Coulomb driven expansion during plasma evolution. Moreover, this could provide insight to the evolution of spatial correlations for the ionic component [186] in the regime of strong coupling.

5.2. Hybrid atom-ion systems

Besides exploring the many-body physics of hundreds of charged particles in an ultracold plasma, the experimental setup paves the way for another approach towards a hybrid atom-ion quantum system. A single femtosecond laser pulse allows for instantaneous creation of single ions immersed in a Bose-Einstein condensate of neutral atoms. The lowest achievable ion kinetic energy is given by the minimum excess energy according to Eq. 5.1. For our pulse parameters this corresponds to an initial ion temperature of $T_i = 0.4$ mK, which can be further reduced by employing a grating monochromator to $T_i = 0.18(3)$ mK [225]. Such ion temperatures are on the same order as achievable temperatures in conventional Paul traps, typically limited by the ionic micro-motion in the time-dependent electric fields [67]. Whereas the RF ion traps thus inherently involve a continuous energy input to the hybrid system, here, the ion is immersed in the quantum gas without any external electromagnetic fields.

The Coulomb field of the positively charged ion induces an electric dipole moment in the ground state atoms. The polarization causes an attractive potential well for the atoms enabling trapping and the formation of mesoscopic molecular ions [58, 59, 230]. For large atom-ion distances R, the interaction potential is given by $V(R) \approx -\frac{C_4}{R^4}$, where $C_4 = \frac{1}{2}q^2\alpha_a$ denotes the induction coefficient determined by the static dipole polarizability of the atom in the ground state with zero orbital angular momentum [53]. Accordingly, the interaction strength can be controlled by tuning the polarizability of the atomic ensemble. Experimentally, this can be realized by optically coupling the atoms to Rydberg states [231, 232]. As the polarizability

non-linearly scales with the principal quantum number as $\alpha_a \propto n^7$ [233], the atom-ion interaction strength can be tuned over orders of magnitude. This allows to vastly increase the atom-ion collision rate [234], which is beneficial for sympathetic cooling of the ion. A dedicated laser setup has been built within two master thesis and allows for Rydberg-dressing as well as resonantly exciting a controlled number of Rydberg excitations within the BEC [235, 236]. This opens the way for studying the sympathetic cooling and eventual trapping of an ionic impurity in a Rydberg-dressed BEC.

5.3. Further experimental outlook

The novel setup provides the experimental infrastructure to investigate strong-field ionization of ^{87}Rb using the electron/ion detection for momentum-resolved spectroscopy. The electron spectroscopy measurements can be carried out analogously to the operation mode used for the detection of ultracold plasma creation with tunable momentum resolution and capture range. Hence, it can shed further light on the underlying ionization processes and transient population transfer, when using a dilute thermal atomic samples, where the interparticle Coulomb interactions are negligible. Here, the main interest lays on dynamical resonances introduced by the enhanced AC-Stark shift in alkali atoms [142]. By combining the predicted electron wavepacket creation from TDSE calculations with the trajectory simulations presented in this work, this method should resolve even subtle deviations between measurements and theoretically predicted kinetic energy distributions.

As the diminished spatial resolution for the ion spectroscopy will not be sufficient for accurate measurements, a time-resolved mode is proposed, which applies a low extraction field and measures the ionic arrival times for different rotation angles between the linear laser polarization and the detector axis.

Besides studying the individual strong field response of ^{87}Rb atoms exposed to femtosecond laser pulses, the effect on the matter wave function of the BEC can be studied as well. Local optical dipole forces enabled by the micrometer focus of the new setup can be used to induce matter-wave dynamics in the BEC, which can be theoretically described by numerical solutions of the 3D GPE. In addition, continuous photoionization with a train of femtosecond laser pulses can provide local dissipation in a BEC, which could act as a spatial projection of the quantum system [237]. As observed for local dissipation with electron beams [238], the resulting position measurement of the density distribution is expected to affect the BEC dynamics due to the quantum Zeno effect.

Finally, the novel setup enables to investigate the coherence transfer from the macroscopic wave function of the bosonic atoms onto the microscopic fermionic constituents. Here, spatial coherence should be probed by interference measurements of two photoelectrons created by local ionization in two adjacent focii within the BEC [95]. In addition, temporal coherence can be probed by introducing a variable time delay between both pulses, which furthermore addresses the more general question on the speed of information transfer in quantum systems.

References

[1] P. Wessels, B. Ruff, T. Kroker, A. K. Kazansky, N. M. Kabachnik, K. Sengstock, M. Drescher and J. Simonet: "Absolute strong-field ionization probabilities of ultracold rubidium atoms", Commun. Phys. **1**, 32 (2018).

[2] T. Kroker, M. Großmann, K. Sengstock, M. Drescher, P. Wessels-Staarmann and J. Simonet: "Ultrafast electron cooling in an expanding ultracold plasma", Nat. Commun. **12**, 596 (2021).

[3] Bose: "Plancks Gesetz und Lichtquantenhypothese", Z. Phys. **26**, 178–181 (1924).

[4] A. Einstein: "Quantentheorie des einatomigen idealen Gases", S. B. Preuss. Akad. Wiss. phys.-math. Klasse (1924).

[5] M. H. Anderson, J. R. Ensher, M. R. Matthews, C. E. Wieman and E. A. Cornell: "Observation of Bose-Einstein Condensation in a Dilute Atomic Vapor", Science **269**, 198–201 (1995).

[6] C. C. Bradley, C. A. Sackett, J. J. Tollett and R. G. Hulet: "Evidence of Bose-Einstein Condensation in an Atomic Gas with Attractive Interactions", Phys. Rev. Lett. **75**, 1687–1690 (1995).

[7] K. B. Davis, M. O. Mewes, M. R. Andrews, N. J. van Druten, D. S. Durfee, D. M. Kurn and W. Ketterle: "Bose-Einstein Condensation in a Gas of Sodium Atoms", Phys. Rev. Lett. **75**, 3969–3973 (1995).

[8] T. Hänsch and A. Schawlow: "Cooling of gases by laser radiation", Opt. Commun. **13**, 68–69 (1975).

[9] A. L. Migdall, J. V. Prodan, W. D. Phillips, T. H. Bergeman and H. J. Metcalf: "First Observation of Magnetically Trapped Neutral Atoms", Phys. Rev. Lett. **54**, 2596–2599 (1985).

[10] S. Chu, L. Hollberg, J. E. Bjorkholm, A. Cable and A. Ashkin: "Three-dimensional viscous confinement and cooling of atoms by resonance radiation pressure", Phys. Rev. Lett. **55**, 48–51 (1985).

[11] P. D. Lett, R. N. Watts, C. I. Westbrook, W. D. Phillips, P. L. Gould and H. J. Metcalf: "Observation of Atoms Laser Cooled below the Doppler Limit", Phys. Rev. Lett. **61**, 169–172 (1988).

[12] J. Dalibard and C. Cohen-Tannoudji: "Laser cooling below the Doppler limit by polarization gradients: simple theoretical models", J. Opt. Soc. Am. B **6**, 2023 (1989).

[13] D. E. Pritchard: "Cooling Neutral Atoms in a Magnetic Trap for Precision Spectroscopy", Phys. Rev. Lett. **51**, 1336–1339 (1983).

[14] H. F. Hess: "Evaporative cooling of magnetically trapped and compressed spin-polarized hydrogen", Phys. Rev. B **34**, 3476–3479 (1986).

[15] W. Petrich, M. H. Anderson, J. R. Ensher and E. A. Cornell: "Stable, Tightly Confining Magnetic Trap for Evaporative Cooling of Neutral Atoms", Phys. Rev. Lett. **74**, 3352–3355 (1995).

[16] O. J. Luiten, M. W. Reynolds and J. T. M. Walraven: "Kinetic theory of the evaporative cooling of a trapped gas", Phys. Rev. A **53**, 381–389 (1996).

[17] C. Chin, R. Grimm, P. Julienne and E. Tiesinga: "Feshbach resonances in ultracold gases", Rev. Mod. Phys. **82**, 1225–1286 (2010).

[18] M. Saffman, T. G. Walker and K. Mølmer: "Quantum information with Rydberg atoms", Rev. Mod. Phys. **82**, 2313–2363 (2010).

[19] I. Bloch: "Ultracold quantum gases in optical lattices", Nat. Phys. **1**, 23–30 (2005).

[20] M. Lewenstein, A. Sanpera, V. Ahufinger, B. Damski, A. Sen(De) and U. Sen: "Ultracold atomic gases in optical lattices: mimicking condensed matter physics and beyond", Adv. Phys. **56**, 243–379 (2007).

[21] H. Labuhn, D. Barredo, S. Ravets, S. de Léséleuc, T. Macrì, T. Lahaye and A. Browaeys: "Tunable two-dimensional arrays of single Rydberg atoms for realizing quantum Ising models", Nature **534**, 667–670 (2016).

[22] D. Barredo, S. de Léséleuc, V. Lienhard, T. Lahaye and A. Browaeys: "An atom-by-atom assembler of defect-free arbitrary two-dimensional atomic arrays", Science **354**, 1021–1023 (2016).

[23] I. M. Georgescu, S. Ashhab and F. Nori: "Quantum simulation", Rev. Mod. Phys. **86**, 153–185 (2014).

[24] I. Bloch, J. Dalibard and W. Zwerger: "Many-body physics with ultracold gases", Rev. Mod. Phys. **80**, 885–964 (2008).

[25] I. Bloch, J. Dalibard and S. Nascimbène: "Quantum simulations with ultracold quantum gases", Nat. Phys. **8**, 267–276 (2012).

[26] H. Bernien, S. Schwartz, A. Keesling, H. Levine, A. Omran, H. Pichler, S. Choi, A. S. Zibrov, M. Endres, M. Greiner, V. Vuletić and M. D. Lukin: "Probing many-body dynamics on a 51-atom quantum simulator", Nature **551**, 579–584 (2017).

[27] T. Brabec and F. Krausz: "Intense few-cycle laser fields: Frontiers of nonlinear optics", Rev. Mod. Phys. **72**, 545–591 (2000).

[28] F. J. McClung and R. W. Hellwarth: "Giant Optical Pulsations from Ruby", J. Appl. Phys. **33**, 828–829 (1962).

[29] A. H. Zewail: "Laser Femtochemistry", Science **242**, 1645–1653 (1988).

[30] A. H. Zewail: "Femtochemistry: Atomic-Scale Dynamics of the Chemical Bond", J. Phys. Chem. A **104**, 5660–5694 (2000).

[31] R. Kienberger, E. Goulielmakis, M. Uiberacker, A. Baltuska, V. Yakovlev, F. Bammer, A. Scrinzi, T. Westerwalbesloh, U. Kleineberg, U. Heinzmann, M. Drescher and F. Krausz: "Atomic transient recorder", Nature **427**, 817–821 (2004).

[32] M. Drescher, M. Hentschel, R. Kienberger, M. Uiberacker, V. Yakovlev, A. Scrinzi, T. Westerwalbesloh, U. Kleineberg, U. Heinzmann and F. Krausz: "Time-resolved atomic inner-shell spectroscopy", Nature **419**, 803–807 (2002).

[33] M. Y. Ivanov, R. Kienberger, A. Scrinzi and D. M. Villeneuve: "Attosecond physics", J. Phys. B: At., Mol. Opt. Phys. **39**, R1–R37 (2006).

[34] D. Strickland and G. Mourou: "Compression of amplified chirped optical pulses", Opt. Commun. **55**, 447–449 (1985).

[35] M. Protopapas, C. H. Keitel and P. L. Knight: "Atomic physics with super-high intensity lasers", Rep. Prog. Phys. **60**, 389–486 (1997).

[36] P. Lambropoulos, P. Maragakis and J. Zhang: "Two-electron atoms in strong fields", Phys. Rep. **305**, 203–293 (1998).

[37] P. Agostini and L. F. DiMauro: "Atomic and Molecular Ionization Dynamics in Strong Laser Fields: From Optical to X-rays", pages 117–158 (2012).

[38] W. Neuhauser, M. Hohenstatt, P. E. Toschek and H. Dehmelt: "Localized visible Ba^+ mono-ion oscillator", Phys. Rev. A **22**, 1137–1140 (1980).

[39] D. Wineland and W. M. Itano: "Spectroscopy of a single Mg+ ion", Phys. Lett. A **82**, 75–78 (1981).

[40] F. Penning: "Die glimmentladung bei niedrigem druck zwischen koaxialen zylindern in einem axialen magnetfeld", Physica **3**, 873–894 (1936).

[41] W. Paul: "Electromagnetic traps for charged and neutral particles", Rev. Mod. Phys. **62**, 531–540 (1990).

[42] D. J. Wineland, R. E. Drullinger and F. L. Walls: "Radiation-Pressure Cooling of Bound Resonant Absorbers", Phys. Rev. Lett. **40**, 1639–1642 (1978).

[43] W. Neuhauser, M. Hohenstatt, P. Toschek and H. Dehmelt: "Optical-Sideband Cooling of Visible Atom Cloud Confined in Parabolic Well", Phys. Rev. Lett. **41**, 233–236 (1978).

[44] D. Leibfried, R. Blatt, C. Monroe and D. Wineland: "Quantum dynamics of single trapped ions", Rev. Mod. Phys. **75**, 281–324 (2003).

[45] A. D. Ludlow, M. M. Boyd, J. Ye, E. Peik and P. O. Schmidt: "Optical atomic clocks", Rev. Mod. Phys. **87**, 637–701 (2015).

[46] R. Blatt and C. F. Roos: "Quantum simulations with trapped ions", Nat. Phys. **8**, 277–284 (2012).

[47] J. Zhang, G. Pagano, P. W. Hess, A. Kyprianidis, P. Becker, H. Kaplan, A. V. Gorshkov, Z.-X. Gong and C. Monroe: "Observation of a many-body dynamical phase transition with a 53-qubit quantum simulator", Nature **551**, 601–604 (2017).

[48] J. I. Cirac and P. Zoller: "Quantum Computations with Cold Trapped Ions", Phys. Rev. Lett. **74**, 4091–4094 (1995).

[49] H. Haffner, C. Roos and R. Blatt: "Quantum computing with trapped ions", Phys. Rep. **469**, 155–203 (2008).

[50] C. Monroe and J. Kim: "Scaling the Ion Trap Quantum Processor", Science **339**, 1164–1169 (2013).

[51] A. Härter and J. Hecker Denschlag: "Cold atom–ion experiments in hybrid traps", Contemp. Phys. **55**, 33–45 (2014).

[52] R. Côté: "Ultracold Hybrid Atom-Ion Systems", pages 67–126 (2016).

[53] M. Tomza, K. Jachymski, R. Gerritsma, A. Negretti, T. Calarco, Z. Idziaszek and P. S. Julienne: "Cold hybrid ion-atom systems", Rev. Mod. Phys. **91**, 035001 (2019).

[54] Z. Idziaszek, T. Calarco, P. S. Julienne and A. Simoni: "Quantum theory of ultracold atom-ion collisions", Phys. Rev. A **79**, 010702 (2009).

[55] T. Schmid, C. Veit, N. Zuber, R. Löw, T. Pfau, M. Tarana and M. Tomza: "Rydberg Molecules for Ion-Atom Scattering in the Ultracold Regime", Phys. Rev. Lett. **120**, 153401 (2018).

[56] T. Dieterle, M. Berngruber, C. Hölzl, R. Löw, K. Jachymski, T. Pfau and F. Meinert: "Inelastic collision dynamics of a single cold ion immersed in a Bose-Einstein condensate", Phys. Rev. A **102**, 041301 (2020).

[57] R. Côté, V. Kharchenko and M. D. Lukin: "Mesoscopic Molecular Ions in Bose-Einstein Condensates", Phys. Rev. Lett. **89**, 093001 (2002).

[58] J. M. Schurer, A. Negretti and P. Schmelcher: "Capture dynamics of ultracold atoms in the presence of an impurity ion", New J. Phys. **17**, 083024 (2015).

[59] J. M. Schurer, A. Negretti and P. Schmelcher: "Unraveling the Structure of Ultracold Mesoscopic Collinear Molecular Ions", Phys. Rev. Lett. **119**, 063001 (2017).

[60] T. Dieterle, M. Berngruber, C. Hölzl, R. Löw, K. Jachymski, T. Pfau and F. Meinert: "Transport of a Single Cold Ion Immersed in a Bose-Einstein Condensate", Phys. Rev. Lett. **126**, 033401 (2021).

[61] G. E. Astrakharchik, L. A. P. Ardila, R. Schmidt, K. Jachymski and A. Negretti: "Ionic polaron in a Bose-Einstein condensate", Commun. Phys. **4**, 94 (2021).

[62] K. Jachymski, M. Krych, P. S. Julienne and Z. Idziaszek: "Quantum Theory of Reactive Collisions for $1/r^n$ Potentials", Phys. Rev. Lett. **110**, 213202 (2013).

[63] Z. Idziaszek, T. Calarco and P. Zoller: "Controlled collisions of a single atom and an ion guided by movable trapping potentials", Phys. Rev. A **76**, 033409 (2007).

[64] H. Doerk, Z. Idziaszek and T. Calarco: "Atom-ion quantum gate", Phys. Rev. A **81**, 012708 (2010).

[65] S. Schmid, A. Härter and J. H. Denschlag: "Dynamics of a Cold Trapped Ion in a Bose-Einstein Condensate", Phys. Rev. Lett. **105**, 133202 (2010).

[66] C. Zipkes, S. Palzer, C. Sias and M. Köhl: "A trapped single ion inside a Bose–Einstein condensate", Nature **464**, 388–391 (2010).

[67] M. Cetina, A. T. Grier and V. Vuletić: "Micromotion-Induced Limit to Atom-Ion Sympathetic Cooling in Paul Traps", Phys. Rev. Lett. **109**, 253201 (2012).

[68] T. Feldker, H. Fürst, H. Hirzler, N. V. Ewald, M. Mazzanti, D. Wiater, M. Tomza and R. Gerritsma: "Buffer gas cooling of a trapped ion to the quantum regime", Nat. Phys. (2020).

[69] P. Weckesser, F. Thielemann, D. Wiater, A. Wojciechowska, L. Karpa, K. Jachymski, M. Tomza, T. Walker and T. Schaetz: "Observation of Feshbach resonances between a single ion and ultracold atoms", (2021).

[70] C. Schneider, M. Enderlein, T. Huber and T. Schaetz: "Optical trapping of an ion", Nat. Photonics **4**, 772–775 (2010).

[71] T. Huber, A. Lambrecht, J. Schmidt, L. Karpa and T. Schaetz: "A far-off-resonance optical trap for a Ba+ ion", Nat. Commun. **5**, 5587 (2014).

[72] A. Lambrecht, J. Schmidt, P. Weckesser, M. Debatin, L. Karpa and T. Schaetz: "Long lifetimes and effective isolation of ions in optical and electrostatic traps", Nat. Photonics **11**, 704–707 (2017).

[73] K. S. Kleinbach, F. Engel, T. Dieterle, R. Löw, T. Pfau and F. Meinert: "Ionic Impurity in a Bose-Einstein Condensate at Submicrokelvin Temperatures", Phys. Rev. Lett. **120**, 193401 (2018).

[74] F. Engel, T. Dieterle, T. Schmid, C. Tomschitz, C. Veit, N. Zuber, R. Löw, T. Pfau and F. Meinert: "Observation of Rydberg Blockade Induced by a Single Ion", Phys. Rev. Lett. **121**, 193401 (2018).

[75] T. C. Killian, S. Kulin, S. D. Bergeson, L. A. Orozco, C. Orzel and S. L. Rolston: "Creation of an Ultracold Neutral Plasma", Phys. Rev. Lett. **83**, 4776–4779 (1999).

[76] T. C. Killian: "Ultracold Neutral Plasmas", Science **316**, 705 – 708 (2007).

[77] T. Killian, T. Pattard, T. Pohl and J. Rost: "Ultracold neutral plasmas", Phys. Rep. **449**, 77–130 (2007).

[78] M. Lyon and S. L. Rolston: "Ultracold neutral plasmas", Rep. Prog. Phys. **80**, 017001 (2017).

[79] M. S. Murillo: "Strongly coupled plasma physics and high energy-density matter", Phys. Plasmas **11**, 2964–2971 (2004).

[80] S. Ichimaru: "Strongly coupled plasmas: high-density classical plasmas and degenerate electron liquids", Rev. Mod. Phys. **54**, 1017–1059 (1982).

[81] T. K. Langin, G. M. Gorman and T. C. Killian: "Laser cooling of ions in a neutral plasma", Science **363**, 61 – 64 (2019).

[82] G. M. Gorman, M. K. Warrens, S. J. Bradshaw and T. C. Killian: "Magnetic Confinement of an Ultracold Neutral Plasma", Phys. Rev. Lett. **126**, 085002 (2021).

[83] T. Ditmire, E. Springate, J. W. G. Tisch, Y. L. Shao, M. B. Mason, N. Hay, J. P. Marangos and M. H. R. Hutchinson: "Explosion of atomic clusters heated by high-intensity femtosecond laser pulses", Phys. Rev. A **57**, 369–382 (1998).

[84] U. Saalmann, C. Siedschlag and J. M. Rost: "Mechanisms of cluster ionization in strong laser pulses", J. Phys. B: At., Mol. Opt. Phys. **39**, R39–R77 (2006).

[85] T. Fennel, K.-H. Meiwes-Broer, J. Tiggesbäumker, P.-G. Reinhard, P. M. Dinh and E. Suraud: "Laser-driven nonlinear cluster dynamics", Rev. Mod. Phys. **82**, 1793–1842 (2010).

[86] C. Bostedt, M. Adolph, E. Eremina, M. Hoener, D. Rupp, S. Schorb, H. Thomas, A. R. B. de Castro and T. Möller: "Clusters in intense FLASH pulses: ultrafast ionization dynamics and electron emission studied with spectroscopic and scattering techniques", J. Phys. B: At., Mol. Opt. Phys. **43**, 194011 (2010).

[87] T. Gorkhover, M. Adolph, D. Rupp, S. Schorb, S. W. Epp, B. Erk, L. Foucar, R. Hartmann, N. Kimmel, K.-U. Kühnel, D. Rolles, B. Rudek, A. Rudenko, R. Andritschke, A. Aquila, J. D. Bozek, N. Coppola, T. Erke, F. Filsinger, H. Gorke, H. Graafsma, L. Gumprecht, G. Hauser, S. Herrmann, H. Hirsemann, A. Hömke, P. Holl, C. Kaiser, F. Krasniqi, J.-H. Meyer, M. Matysek, M. Messerschmidt, D. Miessner, B. Nilsson, D. Pietschner, G. Potdevin, C. Reich, G. Schaller, C. Schmidt, F. Schopper, C. D. Schröter, J. Schulz, H. Soltau, G. Weidenspointner, I. Schlichting, L. Strüder, J. Ullrich, T. Möller and C. Bostedt: "Nanoplasma Dynamics of Single Large Xenon Clusters Irradiated with Superintense X-Ray Pulses from the Linac Coherent Light Source Free-Electron Laser", Phys. Rev. Lett. **108**, 245005 (2012).

[88] Y. Kumagai, H. Fukuzawa, K. Motomura, D. Iablonskyi, K. Nagaya, S.-i. Wada, Y. Ito, T. Takanashi, Y. Sakakibara, D. You, T. Nishiyama, K. Asa, Y. Sato, T. Umemoto, K. Kariyazono, E. Kukk, K. Kooser, C. Nicolas, C. Miron, T. Asavei, L. Neagu, M. S. Schöffler, G. Kastirke, X.-j. Liu, S. Owada, T. Katayama, T. Togashi, K. Tono, M. Yabashi, N. V. Golubev, K. Gokhberg, L. S. Cederbaum, A. I. Kuleff and K. Ueda: "Following the Birth of a Nanoplasma Produced by an Ultrashort Hard-X-Ray Laser in Xenon Clusters", Phys. Rev. X **8**, 031034 (2018).

[89] D. Gericke and M. Murillo: "Disorder-induced heating of ultracold plasmas", Contrib. Plasma Phys. **43**, 298–301 (2003).

[90] N. Takei, C. Sommer, C. Genes, G. Pupillo, H. Goto, K. Koyasu, H. Chiba, M. Weidemüller and K. Ohmori: "Direct observation of ultrafast many-body electron dynamics in an ultracold Rydberg gas", Nat. Commun. **7**, 13449 (2016).

[91] M. P. Robinson, B. L. Tolra, M. W. Noel, T. F. Gallagher and P. Pillet: "Spontaneous Evolution of Rydberg Atoms into an Ultracold Plasma", Phys. Rev. Lett. **85**, 4466–4469 (2000).

[92] M. Robert-de Saint-Vincent, C. S. Hofmann, H. Schempp, G. Günter, S. Whitlock and M. Weidemüller: "Spontaneous Avalanche Ionization of a Strongly Blockaded Rydberg Gas", Phys. Rev. Lett. **110**, 045004 (2013).

[93] M. Mizoguchi, Y. Zhang, M. Kunimi, A. Tanaka, S. Takeda, N. Takei, V. Bharti, K. Koyasu, T. Kishimoto, D. Jaksch, A. Glaetzle, M. Kiffner, G. Masella, G. Pupillo, M. Weidemüller and K. Ohmori: "Ultrafast Creation of Overlapping Rydberg Electrons in an Atomic BEC and Mott-Insulator Lattice", Phys. Rev. Lett. **124**, 253201 (2020).

[94] M. Wollenhaupt, A. Assion, D. Liese, C. Sarpe-Tudoran, T. Baumert, S. Zamith, M. A. Bouchene, B. Girard, A. Flettner, U. Weichmann and G. Gerber: "Interferences of Ultrashort Free Electron Wave Packets", Phys. Rev. Lett. **89**, 173001 (2002).

[95] B. Ruff: "Ultracold Gases in Strong Light Fields of Femtosecond Laser Pulses, PhD thesis", (2017).

[96] J. Butlewski: "A quantum gas machine for local photoionization of ultracold ^{87}Rb on ultrafast time-scales, Master's thesis", (2018).

[97] M. Fricke: "Aufbau eines Bose-Fermi-Quantengassystems für Forschung und Lehre (in German), Diploma thesis", (2010).

[98] A. Grote: "Aufbau eines Ultrahochvakuumsystems und einer 2D-3D-Fallenkombination eines Quantengasmessplatzes für Forschung und Lehre (in German), Diploma thesis", (2011).

[99] M. Pfau: "Aufbau einer Dipolfalle zur Untersuchung von Solitonen in einem Rubidium Bose-Einstein Kondensat (in German), Diploma thesis", (2013).

[100] H. Krüger: "Aufbau und Charakterisierung einer Hybridfalle für ultrakalte Quantengase (in German), Master's thesis", (2015).

[101] T. Kroker: "Photoionisation ultrakalter ^{87}Rb-Atome in starken Laserfeldern (in German), Master's thesis", (2016).

[102] S. Pehmöller: "Aufbau eines abgeschirmten Elektronen und Ionendetektionssystems zur Materiewelleninterferometrie (in German), Master's thesis", (2017).

[103] M. Schröder: "Entwicklung und Aufbau einer optischen Pinzettefür ultrakalte Atome (in German), Bachelor's thesis", (2015).

[104] S. Pehmöller: "Aufbau und Test eines bildgebenden Elektronendetektors für Ionisationsexperimente im Laser-Doppelfokus (in German), Bachelor's thesis", (2015).

[105] M. Neundorf: "Aufbau und Charakterisierung einer 2D-Strahllagenstabilisierung (in German), Bachelor's thesis", (2016).

[106] T. Anlauf: "Aktive Magnetfeldkompensation für Photoionisation am ultrakalten Quantengas (in German), Bachelor's thesis", (2016).

[107] J. Fiedler: "Aufbau einer Detektoreinheit zum Nachweis von Materiewelleninterferenz langsamer Elektronen (in German), Bachelor's thesis", (2017).

[108] J. Heyer: "Abbildungssysteme für Ultrakalte Quantengase (in German), Bachelor's thesis", (2018).

[109] D. Imeri: “Eine Detektionseinheit für geladene Teilchen als Schnittstelle zwischen ultrakalten Atomen und Femtosekundenlaserpulsen (in German), Bachelor’s thesis”, (2019).

[110] H. J. Metcalf and P. van der Straten: “Laser Cooling and Trapping of Neutral Atoms”, in “The Optics Encyclopedia”, Wiley-VCH Verlag GmbH & Co. KGaA, Weinheim, Germany (2007).

[111] D. Steck: “Rubidium 87 D line Data”, available online at http://steck.us/alkalidata (revision 2.2.1,21 November 2019), accessed 9 November 2020 .

[112] P. D. Lett, W. D. Phillips, S. L. Rolston, C. E. Tanner, R. N. Watts and C. I. Westbrook: “Optical molasses”, J. Opt. Soc. Am. B **6**, 2084 (1989).

[113] P. J. Ungar, D. S. Weiss, E. Riis and S. Chu: “Optical molasses and multilevel atoms: theory”, J. Opt. Soc. Am. B **6**, 2058 (1989).

[114] K. Dieckmann, R. J. C. Spreeuw, M. Weidemüller and J. T. M. Walraven: “Two-dimensional magneto-optical trap as a source of slow atoms”, Phys. Rev. A **58**, 3891–3895 (1998).

[115] L. H. Hamester: “Graue Melasse zum Sub-Dopplerkühlen von Rubidium-87 (in German), Bachelor’s thesis”, (2020).

[116] W. Ketterle, D. S. Durfee and D. M. Stamper-Kurn: “Making, probing and understanding Bose-Einstein condensates”, (1999).

[117] E. Majorana: “Atomi orientati in campo magnetico variabile”, Il Nuovo Cimento **9**, 43–50 (1932).

[118] Y.-J. Lin, A. R. Perry, R. L. Compton, I. B. Spielman and J. V. Porto: “Rapid production of ^{87}Rb Bose-Einstein condensates in a combined magnetic and optical potential”, Phys. Rev. A **79**, 063631 (2009).

[119] R. Grimm, M. Weidemüller and Y. B. Ovchinnikov: “Optical Dipole Traps for Neutral Atoms”, Adv. At. Mol. Opt. Phys. **42**, 95–170 (2000).

[120] M. Greiner, I. Bloch, T. W. Hänsch and T. Esslinger: “Magnetic transport of trapped cold atoms over a large distance”, Phys. Rev. A **63**, 031401 (2001).

[121] T. L. Gustavson, A. P. Chikkatur, A. E. Leanhardt, A. Görlitz, S. Gupta, D. E. Pritchard and W. Ketterle: “Transport of Bose-Einstein Condensates with Optical Tweezers”, Phys. Rev. Lett. **88**, 020401 (2001).

[122] A. Couvert, T. Kawalec, G. Reinaudi and D. Guéry-Odelin: “Optimal transport of ultracold atoms in the non-adiabatic regime”, Europhys. Lett. (Europhys. Lett.) **83**, 13001 (2008).

[123] ProxiVision GmbH: “Scintillation Detectors (Scintillating Screens)”, available online at https://www.proxivision.de/product/scintillating-screens/, accessed 20 May 2020 .

[124] Dr. Sjuts Optotechnik GmbH: “Quantenausbeuten / Nachweiswahrscheinlichkeiten (in German)”, available online at http://www.sjuts.com/Quality_efficiencies_deutsch.html, accessed 20 May 2020 .

[125] M. Krems, J. Zirbel, M. Thomason and R. D. DuBois: “Channel electron multiplier and channelplate efficiencies for detecting positive ions”, Rev. Sci. Instrum. **76**, 093305 (2005).

[126] P. Wessels: “Time-resolved imaging of magnetic nanostructures in the visible and soft X-ray spectral range, PhD thesis”, (2014).

[127] E. Mevel, P. Breger, R. Trainham, G. Petite, P. Agostini, A. Migus, J.-P. Chambaret and A. Antonetti: “Atoms in strong optical fields: Evolution from multiphoton to tunnel ionization”, Phys. Rev. Lett. **70**, 406–409 (1993).

[128] R. R. Freeman, P. H. Bucksbaum, H. Milchberg, S. Darack, D. Schumacher and M. E. Geusic: “Above-threshold ionization with subpicosecond laser pulses”, Phys. Rev. Lett. **59**, 1092–1095 (1987).

[129] T. P. Dinneen, C. D. Wallace, K.-Y. N. Tan and P. L. Gould: “Use of trapped atoms to measure absolute photoionization cross sections”, Opt. Lett. **17**, 1706–1708 (1992).

[130] D. N. Madsen and J. W. Thomsen: “Measurement of absolute photo-ionization cross sections using magnesium magneto-optical traps”, J. Phys. B: At., Mol. Opt. Phys. **35**, 2173–2181 (2002).

[131] M. Anderlini, E. Courtade, D. Ciampini, J. H. Müller, O. Morsch and E. Arimondo: “Two-photon ionization of cold rubidium atoms”, J. Opt. Soc. Am. B **21**, 480–485 (2004).

[132] J. R. Lowell, T. Northup, B. M. Patterson, T. Takekoshi and R. J. Knize: “Measurement of the photoionization cross section of the $5S_{1/2}$ state of rubidium”, Phys. Rev. A **66**, 062704 (2002).

[133] T. Takekoshi, G. M. Brooke, B. M. Patterson and R. J. Knize: “Absolute Rb one-color two-photon ionization cross-section measurement near a quantum interference”, Phys. Rev. A **69**, 053411 (2004).

[134] L. Keldysh: “Ionization in the Field of a Strong Electromagnetic Wave”, Sov. Phys. JETP **20**, 1307–1314 (1965).

[135] L. A. Lompre, G. Mainfray, C. Manus and J. Thebault: "Multiphoton ionization of rare gases by a tunable-wavelength 30-psec laser pulse at 1.06 μm", Phys. Rev. A **15**, 1604–1612 (1977).

[136] M. Edwards, X. Tang, P. Lambropoulos and R. Shakeshaft: "Multiphoton absorption by alkali-metal atoms above the ionization threshold", Phys. Rev. A **33**, 4444–4445 (1986).

[137] M. S. Safronova and U. I. Safronova: "Critically evaluated theoretical energies, lifetimes, hyperfine constants, and multipole polarizabilities in ^{87}Rb", Phys. Rev. A **83**, 052508 (2011).

[138] P. Agostini, F. Fabre, G. Mainfray, G. Petite and N. K. Rahman: "Free-Free Transitions Following Six-Photon Ionization of Xenon Atoms", Phys. Rev. Lett. **42**, 1127–1130 (1979).

[139] Y. Gontier and M. Trahin: "Energetic electron generation by multiphoton absorption", J. Phys. B: At., Mol. Opt. Phys. **13**, 4383–4390 (1980).

[140] P. Kruit, J. Kimman, H. G. Muller and M. J. van der Wiel: "Electron spectra from multiphoton ionization of xenon at 1064, 532, and 355 nm", Phys. Rev. A **28**, 248–255 (1983).

[141] J. Steinmann: "Multiphoton Ionization of Laser Cooled Lithium, PhD thesis", (2007).

[142] M. Z. Milošević and N. S. Simonović: "Calculations of rates for strong-field ionization of alkali-metal atoms in the quasistatic regime", Phys. Rev. A **91**, 023424 (2015).

[143] A. Bunjac, D. B. Popović and N. S. Simonović: "Resonant dynamic Stark shift as a tool in strong-field quantum control: calculation and application for selective multiphoton ionization of sodium", Phys. Chem. Chem. Phys. **19**, 19829–19836 (2017).

[144] T. B. Miladinović and V. M. Petrović: "Laser Field Ionization Rates in the Barrier-Suppression Regime", J. Russ. Laser Res. **36**, 312–319 (2015).

[145] M. Krug, T. Bayer, M. Wollenhaupt, C. Sarpe-Tudoran, T. Baumert, S. S. Ivanov and N. V. Vitanov: "Coherent strong-field control of multiple states by a single chirped femtosecond laser pulse", New J. Phys. **11**, 105051 (2009).

[146] P. B. Corkum: "Plasma perspective on strong field multiphoton ionization", Phys. Rev. Lett. **71**, 1994–1997 (1993).

[147] A. M. Perelomov, V. S. Popov and M. V. Terent'ev: "Ionization of Atoms in an Alternating Electric Field", Sov. Phys. JETP **23**, 924–934 (1966).

[148] M. Ammosov, N. Delone and V. Krainov: "Tunnel ionization of complex atoms and of atomic ions in an alternating electromagnetic field", Sov. Phys. JETP **64**, 1191–1194 (1986).

[149] S. Augst, D. Strickland, D. D. Meyerhofer, S. L. Chin and J. H. Eberly: "Tunneling ionization of noble gases in a high-intensity laser field", Phys. Rev. Lett. **63**, 2212–2215 (1989).

[150] M. Schuricke, G. Zhu, J. Steinmann, K. Simeonidis, I. Ivanov, A. Kheifets, A. N. Grum-Grzhimailo, K. Bartschat, A. Dorn and J. Ullrich: "Strong-field ionization of lithium", Phys. Rev. A **83**, 023413 (2011).

[151] M. Schuricke, K. Bartschat, A. N. Grum-Grzhimailo, G. Zhu, J. Steinmann, R. Moshammer, J. Ullrich and A. Dorn: "Coherence in multistate resonance-enhanced four-photon ionization of lithium atoms", Phys. Rev. A **88**, 023427 (2013).

[152] N. A. Hart, J. Strohaber, A. A. Kolomenskii, G. G. Paulus, D. Bauer and H. A. Schuessler: "Selective strong-field enhancement and suppression of ionization with short laser pulses", Phys. Rev. A **93**, 063426 (2016).

[153] A. Grote: "Ultracold ^{87}Rb: from quantum metrology to two-photon ionisation, PhD thesis", (2016).

[154] T. Morishita and C. D. Lin: "Photoelectron spectra and high Rydberg states of lithium generated by intense lasers in the over-the-barrier ionization regime", Phys. Rev. A **87**, 063405 (2013).

[155] S.-D. Jheng and T. F. Jiang: "A theoretical study on the strong-field ionization of the lithium atom", J. Phys. B: At., Mol. Opt. Phys. **46**, 115601 (2013).

[156] S.-D. Jheng and T. F. Jiang: "Effect of bound electron wave packet displacement on the multiphoton ionization of a lithium atom", J. Phys. B: At., Mol. Opt. Phys. **50**, 195001 (2017).

[157] S. Sharma, B. P. Acharya, A. H. N. C. De Silva, N. W. Parris, B. J. Ramsey, K. L. Romans, A. Dorn, V. L. B. de Jesus and D. Fischer: "All-optical atom trap as a target for MOTRIMS-like collision experiments", Phys. Rev. A **97**, 043427 (2018).

[158] D. Ciampini, M. Anderlini, J. H. Müller, F. Fuso, O. Morsch, J. W. Thomsen and E. Arimondo: "Photoionization of ultracold and Bose-Einstein-condensed Rb atoms", Phys. Rev. A **66**, 043409 (2002).

[159] I. E. Mazets: "Photoionization of neutral atoms in a Bose-Einstein condensate", Quantum Semiclass. Opt. **10**, 675–681 (1998).

[160] H. Zimmermann and U. Eichmann: "Atomic excitation and acceleration in strong laser fields", Phys. Scr. (2016).

[161] U. Eichmann, T. Nubbemeyer, H. Rottke and W. Sandner: "Acceleration of neutral atoms in strong short-pulse laser fields", Nature **461**, 1261–1264 (2009).

[162] C. Maher-McWilliams, P. Douglas and P. F. Barker: "Laser-driven acceleration of neutral particles", Nat. Photonics **6**, 386–390 (2012).

[163] J. J. Gilijamse, S. Hoekstra, S. Y. T. van de Meerakker, G. C. Groenenboom and G. Meijer: "Near-Threshold Inelastic Collisions Using Molecular Beams with a Tunable Velocity", Science **313**, 1617–1620 (2006).

[164] L. Scharfenberg, S. Y. T. van de Meerakker and G. Meijer: "Crossed beam scattering experiments with optimized energy resolution", Phys. Chem. Chem. Phys. **13**, 8448 (2011).

[165] M. Qiu: "Observation of Feshbach Resonances in the F + H2 -> HF + H Reaction", Science **311**, 1440–1443 (2006).

[166] R. V. Krems: "Cold controlled chemistry", Phys. Chem. Chem. Phys. **10**, 4079 (2008).

[167] T. G. Freegarde, J. Walz and T. W. Hänsch: "Confinement and manipulation of atoms using short laser pulses", Opt. Commun. (1995).

[168] V. I. Balykin: "Motion of an atom under the effect of femtosecond laser pulses: From chaos to spatial localization", Journal of Experimental and Theoretical Physics Letters **81**, 209–213 (2005).

[169] V. I. Romanenko and L. P. Yatsenko: "Theory of one-dimensional trapping of atoms by counterpropagating short pulse trains", J. Phys. B: At., Mol. Opt. Phys. **44**, 115305 (2011).

[170] D. N. Yanyshev, V. I. Balykin, Y. V. Vladimirova and V. N. Zadkov: "Dynamics of atoms in a femtosecond optical dipole trap", Phys. Rev. A - Atomic, Molecular, and Optical Physics (2013).

[171] H. Metcalf: "Colloquium : Strong optical forces on atoms in multifrequency light", Rev. Mod. Phys. **89**, 041001 (2017).

[172] A. Goepfert, I. Bloch, D. Haubrich, F. Lison, R. Schütze, R. Wynands and D. Meschede: "Stimulated focusing and deflection of an atomic beam using picosecond laser pulses", Phys. Rev. A **56**, R3354–R3357 (1997).

[173] R. Clarke, T. Graf and E. Riis: "Dipole traps with mode-locked lasers", Appl. Phys. B **70**, 695–700 (2000).

[174] L. C. Karssen: "Trapping cold atoms with ultrashort laser pulses, PhD thesis", (2008).

[175] A. E. Afanasiev, A. A. Meysterson, A. M. Mashko, P. N. Melentiev and V. I. Balykin: "Atom femto trap: experimental realization", Appl. Phys. B **126**, 26 (2020).

[176] T. Nubbemeyer, K. Gorling, A. Saenz, U. Eichmann and W. Sandner: "Strong-field tunneling without ionization", Phys. Rev. Lett. **101** (2008).

[177] V. Bolpasi, N. K. Efremidis, M. J. Morrissey, P. C. Condylis, D. Sahagun, M. Baker and W. von Klitzing: "An ultra-bright atom laser", New J. Phys. **16**, 033036 (2014).

[178] M. Meister, A. Roura, E. M. Rasel and W. P. Schleich: "The space atom laser: An isotropic source for ultra-cold atoms in microgravity", New J. Phys. (2019).

[179] O. Zobay and B. M. Garraway: "Atom trapping and two-dimensional Bose-Einstein condensates in field-induced adiabatic potentials", Phys. Rev. A **69**, 023605 (2004).

[180] Y. Colombe, E. Knyazchyan, O. Morizot, B. Mercier, V. Lorent and H. Perrin: "Ultracold atoms confined in rf-induced two-dimensional trapping potentials", Europhys. Lett. **67**, 593–599 (2004).

[181] I. Lesanovsky and W. von Klitzing: "Time-Averaged Adiabatic Potentials: Versatile Matter-Wave Guides and Atom Traps", Phys. Rev. Lett. **99**, 083001 (2007).

[182] K. Padavić, K. Sun, C. Lannert and S. Vishveshwara: "Physics of hollow Bose-Einstein condensates", Europhys. Lett. **120**, 20004 (2017).

[183] K. Sun, K. Padavić, F. Yang, S. Vishveshwara and C. Lannert: "Static and dynamic properties of shell-shaped condensates", Phys. Rev. A (2018).

[184] A. Tononi and L. Salasnich: "Bose-Einstein Condensation on the Surface of a Sphere", Phys. Rev. Lett. **123**, 160403 (2019).

[185] J. P. Gordon and A. Ashkin: "Motion of atoms in a radiation trap", Phys. Rev. A **21**, 1606–1617 (1980).

[186] M. A. Viray, S. A. Miller and G. Raithel: "Expansion Dynamics of Cold Non-Neutral Plasma", (2019).

[187] B. Schütte, C. Peltz, D. R. Austin, C. Strüber, P. Ye, A. Rouzée, M. J. J. Vrakking, N. Golubev, A. I. Kuleff, T. Fennel and J. P. Marangos: "Low-Energy Electron Emission in the Strong-Field Ionization of Rare Gas Clusters", Phys. Rev. Lett. **121**, 063202 (2018).

[188] J. P. Morrison, C. J. Rennick, J. S. Keller and E. R. Grant: "Evolution from a Molecular Rydberg Gas to an Ultracold Plasma in a Seeded Supersonic Expansion of NO", Phys. Rev. Lett. **101**, 205005 (2008).

[189] P. McQuillen, T. Strickler, T. Langin and T. C. Killian: "Ion temperature evolution in an ultracold neutral plasma", Phys. Plasmas **22**, 033513 (2015).

[190] E. A. Cummings, J. E. Daily, D. S. Durfee and S. D. Bergeson: "Fluorescence Measurements Of Expanding Strongly Coupled Neutral Plasmas", Phys. Rev. Lett. **95**, 235001 (2005).

[191] C. E. Simien, Y. C. Chen, P. Gupta, S. Laha, Y. N. Martinez, P. G. Mickelson, S. B. Nagel and T. C. Killian: "Using Absorption Imaging to Study Ion Dynamics in an Ultracold Neutral Plasma", Phys. Rev. Lett. **92**, 143001 (2004).

[192] Y. C. Chen, C. E. Simien, S. Laha, P. Gupta, Y. N. Martinez, P. G. Mickelson, S. B. Nagel and T. C. Killian: "Electron Screening and Kinetic-Energy Oscillations in a Strongly Coupled Plasma", Phys. Rev. Lett. **93**, 265003 (2004).

[193] M. S. Murillo: "Using Fermi Statistics to Create Strongly Coupled Ion Plasmas in Atom Traps", Phys. Rev. Lett. **87**, 115003 (2001).

[194] T. Chen, R. Lu, L. Guo and S. Han: "The charge imbalance in ultracold plasmas", Phys. Plasmas **23**, 092102 (2016).

[195] COMSOL AB, Stockholm, Sweden: "COMSOL Multiphysics® v. 5.4.", www.comsol.com .

[196] J. Barnes and P. Hut: "A hierarchical O(N log N) force-calculation algorithm", Nature **324**, 446–449 (1986).

[197] L. Greengard and V. Rokhlin: "A fast algorithm for particle simulations", J. Comput. Phys. **73**, 325–348 (1987).

[198] S. Mazevet, L. A. Collins and J. D. Kress: "Evolution of Ultracold Neutral Plasmas", Phys. Rev. Lett. **88**, 055001 (2002).

[199] S. G. Kuzmin and T. M. O'Neil: "Numerical Simulation of Ultracold Plasmas: How Rapid Intrinsic Heating Limits the Development of Correlation", Phys. Rev. Lett. **88**, 065003 (2002).

[200] S. G. Kuzmin and T. M. O'Neil: "Numerical simulation of ultracold plasmas", Phys. Plasmas **9**, 3743–3751 (2002).

[201] T. Pohl, T. Pattard and J. M. Rost: "Coulomb Crystallization in Expanding Laser-Cooled Neutral Plasmas", Phys. Rev. Lett. **92**, 155003 (2004).

[202] T. Pohl, T. Pattard and J. M. Rost: "Kinetic modeling and molecular dynamics simulation of ultracold neutral plasmas including ionic correlations", Phys. Rev. A **70**, 033416 (2004).

[203] T. Pohl, T. Pattard and J. M. Rost: "Relaxation to Nonequilibrium in Expanding Ultracold Neutral Plasmas", Phys. Rev. Lett. **94**, 205003 (2005).

[204] R. Ayllon, H. Terças and J. T. Mendonça: "Electron trapping in freely expanding ultracold neutral plasmas", Phys. Plasmas **26**, 033501 (2019).

[205] J. L. Roberts, C. D. Fertig, M. J. Lim and S. L. Rolston: "Electron Temperature of Ultracold Plasmas", Phys. Rev. Lett. **92**, 253003 (2004).

[206] P. Gupta, S. Laha, C. E. Simien, H. Gao, J. Castro, T. C. Killian and T. Pohl: "Electron-Temperature Evolution in Expanding Ultracold Neutral Plasmas", Phys. Rev. Lett. **99**, 075005 (2007).

[207] R. S. Fletcher, X. L. Zhang and S. L. Rolston: "Using Three-Body Recombination to Extract Electron Temperatures of Ultracold Plasmas", Phys. Rev. Lett. **99**, 145001 (2007).

[208] C. I. Blaga, F. Catoire, P. Colosimo, G. G. Paulus, H. G. Muller, P. Agostini and L. F. DiMauro: "Strong-field photoionization revisited", Nat. Phys. **5**, 335–338 (2009).

[209] M. A. Pocsai, I. F. Barna and K. Tökési: "Photoionisation of rubidium in strong laser fields", Eur. Phys. J. D **73**, 74 (2019).

[210] M. S. Murillo: "Ultrafast Dynamics of Strongly Coupled Plasmas", Phys. Rev. Lett. **96**, 165001 (2006).

[211] B. J. Claessens, S. B. van der Geer, G. Taban, E. J. D. Vredenbregt and O. J. Luiten: "Ultracold Electron Source", Phys. Rev. Lett. **95**, 164801 (2005).

[212] A. J. McCulloch, D. V. Sheludko, S. D. Saliba, S. C. Bell, M. Junker, K. A. Nugent and R. E. Scholten: "Arbitrarily shaped high-coherence electron bunches from cold atoms", Nat. Phys. **7**, 785–788 (2011).

[213] R. W. Speirs, C. T. Putkunz, A. J. McCulloch, K. A. Nugent, B. M. Sparkes and R. E. Scholten: "Single-shot electron diffraction using a cold atom electron source", J. Phys. B: At., Mol. Opt. Phys. **48**, 214002 (2015).

[214] W. J. Engelen, M. A. van der Heijden, D. J. Bakker, E. J. D. Vredenbregt and O. J. Luiten: "High-coherence electron bunches produced by femtosecond photoionization", Nat. Commun. **4**, 1693 (2013).

[215] A. J. McCulloch, D. V. Sheludko, M. Junker and R. E. Scholten: "High-coherence picosecond electron bunches from cold atoms", Nat. Commun. **4**, 1692 (2013).

[216] H. Zhang, J. Tang, Q. Zhang, G. Zhao, G. Yang, J. Zhang, O. Zhou and L.-C. Qin: "Field Emission of Electrons from Single LaB6 Nanowires", Adv. Mater. **18**, 87–91 (2006).

[217] D. Ehberger, J. Hammer, M. Eisele, M. Krüger, J. Noe, A. Högele and P. Hommelhoff: "Highly Coherent Electron Beam from a Laser-Triggered Tungsten Needle Tip", Phys. Rev. Lett. **114**, 227601 (2015).

[218] H. Zhang, J. Tang, J. Yuan, Y. Yamauchi, T. T. Suzuki, N. Shinya, K. Nakajima and L.-C. Qin: "An ultrabright and monochromatic electron point source made of a LaB6 nanowire", Nat. Nanotechnol. **11**, 273–279 (2016).

[219] J. G. H. Franssen, T. C. H. de Raadt, M. A. W. van Ninhuijs and O. J. Luiten: "Compact ultracold electron source based on a grating magneto-optical trap", Phys. Rev. Accel. Beams **22**, 023401 (2019).

[220] B. J. Siwick, J. R. Dwyer, R. E. Jordan and R. J. D. Miller: "An Atomic-Level View of Melting Using Femtosecond Electron Diffraction", Science **302**, 1382–1385 (2003).

[221] R. Srinivasan, V. A. Lobastov, C.-Y. Ruan and A. H. Zewail: "Ultrafast Electron Diffraction (UED)", Helv. Chim. Acta **86**, 1761–1799 (2003).

[222] J. R. Dwyer, C. T. Hebeisen, R. Ernstorfer, M. Harb, V. B. Deyirmenjian, R. E. Jordan and R. Dwayne Miller: "Femtosecond electron diffraction: 'making the molecular movie'", Philos. Trans. R. Soc. A **364**, 741–778 (2006).

[223] M. K. Warrens, G. M. Gorman, S. J. Bradshaw and T. C. Killian: "Expansion of ultracold neutral plasmas with exponentially decaying density distributions", Phys. Plasmas **28**, 022110 (2021).

[224] L. G. Silvestri, R. T. Sprenkle, S. D. Bergeson and M. M. Murillo: "Relaxation of strongly coupled binary ionic mixtures in the coupled mode regime", Phys. Plasmas **28**, 062302 (2021).

[225] V. L. A. Dietz: "A grating monochromator for stretching ultrashort light pulses (in German), Bachelor's thesis", (2021).

[226] T. Pohl, T. Pattard and J. M. Rost: "On the possibility of correlation cooling of ultracold neutral plasmas", J. Phys. B: At., Mol. Opt. Phys. **37**, L183–L191 (2004).

[227] M. Greiner, O. Mandel, T. Esslinger, T. W. Hänsch and I. Bloch: "Quantum phase transition from a superfluid to a Mott insulator in a gas of ultracold atoms", Nature **415**, 39–44 (2002).

[228] N. Vanhaecke, D. Comparat, D. A. Tate and P. Pillet: "Ionization of Rydberg atoms embedded in an ultracold plasma", Phys. Rev. A **71**, 013416 (2005).

[229] T. Pohl, D. Comparat, N. Zahzam, T. Vogt, P. Pillet and T. Pattard: "Use of Rydberg atoms to control electron temperatures in ultracold plasmas", Eur. Phys. J. D **40**, 45–50 (2006).

[230] J. M. Schurer, P. Schmelcher and A. Negretti: "Ground-state properties of ultracold trapped bosons with an immersed ionic impurity", Phys. Rev. A **90**, 033601 (2014).

[231] T. Secker, R. Gerritsma, A. W. Glaetzle and A. Negretti: "Controlled long-range interactions between Rydberg atoms and ions", Phys. Rev. A **94**, 013420 (2016).

[232] T. Secker, N. Ewald, J. Joger, H. Fürst, T. Feldker and R. Gerritsma: "Trapped Ions in Rydberg-Dressed Atomic Gases", Phys. Rev. Lett. **118**, 263201 (2017).

[233] T. F. Gallagher: *Rydberg Atoms*, Cambridge University Press (1994).

[234] N. V. Ewald, T. Feldker, H. Hirzler, H. A. Fürst and R. Gerritsma: "Observation of Interactions between Trapped Ions and Ultracold Rydberg Atoms", Phys. Rev. Lett. **122**, 253401 (2019).

[235] J. Fiedler: "Lasersystem zum Rydberg-Dressing eines Bose-Einstein-Kondensats (in German), Master's thesis", (2020).

[236] J. Bergmann: "Rydberg dressing of a Bose-Einstein condensate for the trapping of a single ion, Master's thesis", (2020).

[237] J. Franz: "The Quantum Zeno Effect in the Local Photoionisation of a Bose Einstein Condensate, Master's thesis", (2016).

[238] G. Barontini, R. Labouvie, F. Stubenrauch, A. Vogler, V. Guarrera and H. Ott: "Controlling the Dynamics of an Open Many-Body Quantum System with Localized Dissipation", Phys. Rev. Lett. **110**, 035302 (2013).

A. Appendix

A.1. Further contributions to the experimental setup

The vacuum system was designed by Bernhard Ruff and built up, baked-out and evacuated by the author, Bernhard Ruff and Jakob Butlewski. The cooling laser system was set up by Marlene Fricke [97] and re-built by the author [101]. The magnetic coils, which are used for the MOT and magnetic trap were designed by Harry Krüger [100] and build by Reinhard Mielck and Dieter Barlösius. The dipole trap laser system was set up by Markus Pfau [99]. The configuration of the MOT, the hybrid trap as well and the RF forced evaporation where set up by the author with help from Jakob Butlewski and Bernhard Ruff. The imaging objective in the Preparation chamber was designed by Jette Heyer [108]. The optical transport as well as the Science chamber optics were set up by the author with help of Philipp Wessels-Staarmann. The charged particle detection scheme was designed by Bernhard Ruff, adapted by the author and set up by Bernhard Ruff, Jakob Butlewski and the author with help from Julian Fiedler [107]. The gated detection scheme was designed and set up by the author and Mario Großmann. The compensation coils were designed by the author and set up together with Jakob Butlewski, Bernhard Ruff, Steffen Pehmöller, Julian Fiedler, Juliette Simonet, Reinhard Mielck and Dieter Barlösius. The beam transport setup for the femtosecond laser was designed by the author and set up by Donika Imeri, Philipp Wessels-Staarmann and the author.

A.2. Bake-out of the vacuum chambers

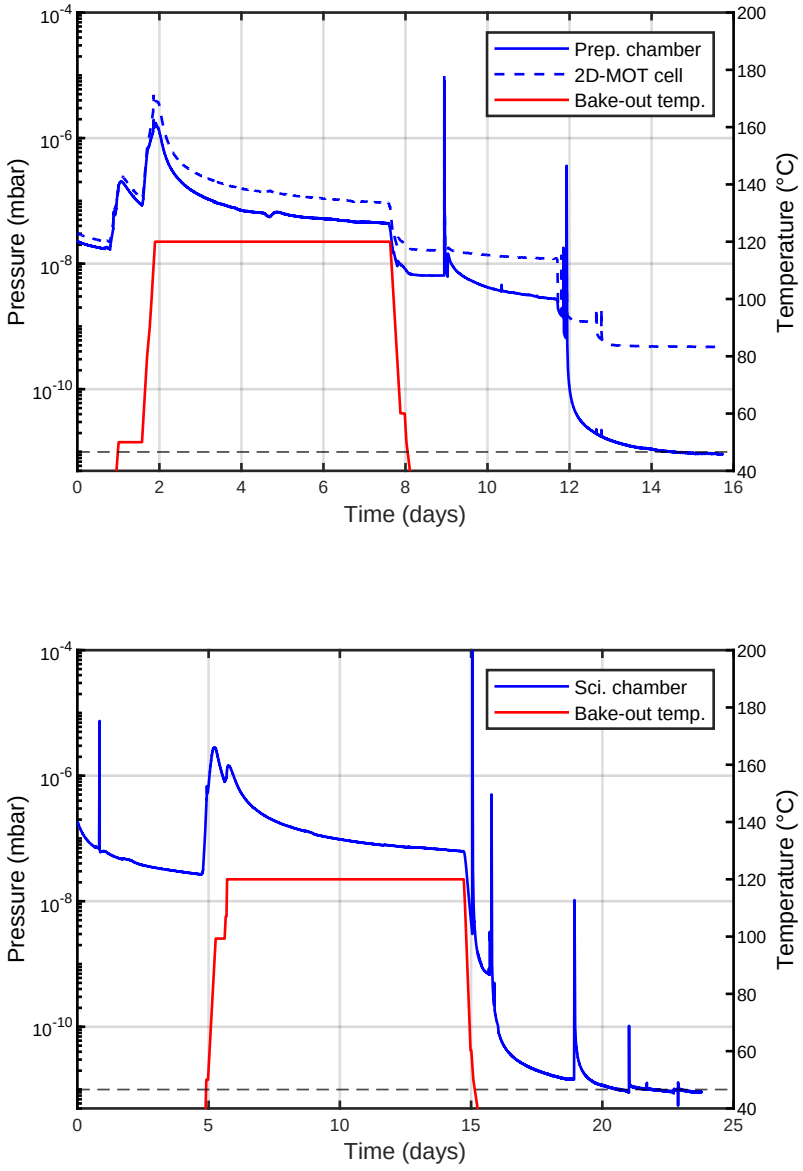

Figure 1.1: Bake-out of the vacuum chambers. a. Temperature and base pressure during the bake-out of the preparation chamber and 2D-MOT-cell. **b.** Temperature and pressure during the bake-out of the Science chamber. After the pressure in both chambers surpasses the 1×10^{-11} mbar range (dashed gray line), they are merged by opening the gate valve.

Figure 1.1 shows the progression of bake-out temperature and pressure over time for both chambers. By keeping the system for days at a peak temperature of 120 °C, the adsorbed water is evaporated from the inner surfaces of the chambers. During the bake-out, both chambers were continuously pumped by a TMP. After reaching a base pressure below 10^{-8} mbar, the TMP is supported by the IGPs. Below 5×10^{-9} mbar, when the actual pressure starts to be limited by

the compression ratio of the TMP, the valves are closed and the chambers are solely pumped by the IGPs. As IGPs exhibit reduced pump efficiency for rare gases and hydrogen, the attainable base pressure is typically limited by the hydrogen partial pressure. For this purpose, the titanium sublimation cartridges are required to reach the final base pressure below 1×10^{-11} mbar. The whole procedure takes around two to three weeks for each chamber. After the successful evacuation of both chambers the valve gate was opened.

A.3. Pin configuration of alkali metal dispensers

Figure 1.2 shows a scheme of the alkali metal dispenser setup in the current experiment. Each dispenser (Rb1-4, K1-2) is connected to two feedthrough pins (a-h). The pin assignment as well as the corresponding measured electric resistance is given in Tab. 1.1. The same data is shown in [96].

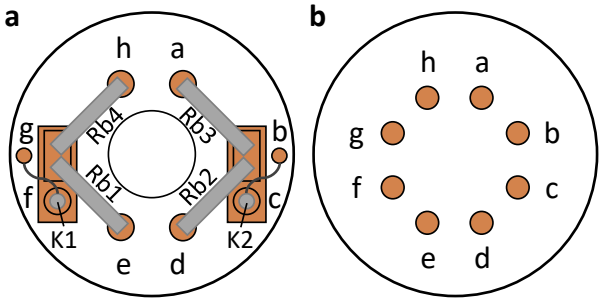

Figure 1.2: Pin connection scheme alkali metal dispensers. a. Schematic drawing of the dispenser configuration with 6 alkali metal dispensers (Rb1-4, K1-2). The potassium dispensers are connected **b.** Pins (a-h), which are connected to the dispensers in (a) by vacuum feedthroughs.

	ground	pos.	R_{AMD} (Ω)
Rb1	f	e	0.3
Rb2	c	d	0.3
Rb3	c	a	0.3
Rb4	f	h	0.4
K1	f	g	0.3
K2	c	b	0.2

Table 1.1: Pin assignment alkali metal dispensers. Pin assignment and corresponding electric resistance R_{AMD} of each alkali metal dispenser in this setup. The resistance has been measured between the corresponding pins for the positive pole (pos.) and ground.

A.4. Radio-Frequency Antenna

In order to optimize the output properties of the RF antenna for efficient evaporation in the hybrid trap, different numbers of windings were tested. As coil diameter, 50 mm was chosen, which is below the outer diameter of the vacuum window and enables propagation of the expanded MOT beam through the coil. For the characterization measurement, a second coil with same diameter and 5 windings is used to pick up the induced RF power. Figure 1.3 shows the RF output power for different number of windings used for the RF coil measured by the induced voltage in a second coil. Whereas the output power for low frequencies increases with the number of windings, the cutoff frequency shifts to lower frequencies for increasing inductance of the RF coil. As a result, the coil with three windings provides the highest output power over the frequency range from 2.8 MHz to 30 MHz (marked by the dashed black lines) required for forced RF evaporation.

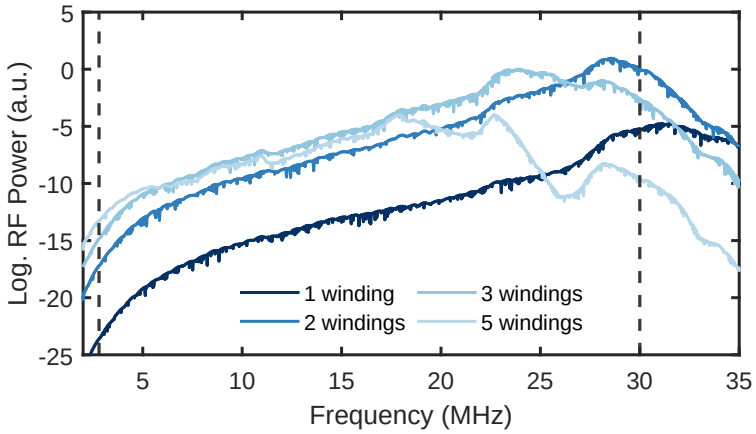

Figure 1.3: RF Antenna Characterization. Measured induced RF power at different output frequencies for RF antennas with 1, 2, 3 and 5 windings.

A.5. Magnetic field compensation currents

The compensation cage is used to compensate magnetic stray fields in the Preparation chamber, during optical transport and for the charged particle detection in the Science chamber. The compensation currents are given in Tab. 1.2 and are switched after the transport.

axis	I_{Prep} (A)	I_{Sci} (A)
x	0.15	0
y	1.5	0
z	0.1	3.5

Table 1.2: Compensation currents used for static magnetic field compensation in the Preparation chamber and during optical transport (I_{Prep}) and the charged particle detection in the Science chamber (I_{Sci}).

A.6. Fit results focus measurements

The two-dimensional focal intensity distributions shown in Fig. 3.4 are fitted according to Eq. 3.18 including a global rotation by an angle α_z around the z axis. The fit results are given in the following tabular.

	511 nm	1022 nm
w^1_{0x} (µm)	10.22(7)	10.3(1)
w^1_{0y} (µm)	9.67(7)	10.5(1)
A^2	0	0.14(4)
w^2_{0x} (µm)	-	15(2)
w^2_{0y} (µm)	-	5.0(9)
y^2_0 (µm)	-	-13.5(4)
A^3	0	0.12(1)
w^3_{0x} (µm)	-	9(1)
w^3_{0y} (µm)	-	11(3)
y^3_0 (µm)	-	-22(2)
α_z (°)	37(5)	-126(1)

Table 1.3: Fit parameter results for two-dimensional fits according to Eq. 3.18 to the measured intensity distributions shown in Fig. 3.4.

Danksagung

Diese Arbeit ist durch die Mithilfe und Unterstützung vieler Menschen möglich gemacht worden, denen ich hier einmal danken möchte.

Zuerst möchte ich meinen beiden Betreuern Markus Drescher und Klaus Sengstock für die Möglichkeit und das Vertrauen danken, dass ich diese Arbeit im Kooperationsprojekt *Femto-BEC* durchführen durfte. Ihr habt in diesem Projekt für hervorragende Forschungsbedingungen gesorgt und in den gemeinsamen Diskussionen habe ich enorm von eurer Erfahrung und Expertise profitiert.

Mein besonderer Dank gilt den beiden Projektleitenden Juliette Simonet und Philipp Wessels-Staarmann für viel Vertrauen, Support, ein immer offenes Ohr und ein Begegnen auf Augenhöhe. Auch von euch habe ich Woche für Woche gelernt und durch eure herausragende Betreuung von Bachelor- und Masterstudierenden legt ihr den Grundstein für eine erfolgreiche Zukunft des Experiments. Zudem habt ihr es geschafft, eine außergewöhnlich kollegiale Atmosphäre zu etablieren, in der gemeinsames Arbeiten Spaß macht.

Darüberhinaus danke ich den Mitpromovierenden in meinen Jahren am Experiment. Besonders herauszustellen ist zum einen Bernhard Ruff, der einen großen Teil des beschriebenen Experiments geplant und entworfen hat und der mir den Start der Promotion enorm erleichtert hat. Zum anderen danke ich besonders Mario Großmann, mit dem ich viele Stunden unterhaltsam und doch effektiv im Labor verbracht habe. Zudem danke ich Julian Fiedler und Jette Heyer, den Masterstudierenden Jakob Butlewski und Steffen Pehmöller sowie den zahlreichen Bachelorstudierenden, die alle zum Erfolg des Projekts beigetragen haben. Außerdem danke ich den weiteren Mitgliedern der Arbeitsgruppen Drescher und Sengstock, die mich immer hilfsbereit und kollegial unterstützt haben, sowie Andrey Kazansky und Nikolay Kabachnik für die spannende und fruchtbare Zusammenarbeit, bei der ich extrem viel lernen durfte.

Weiterer Dank gilt Reinhard Mielck und Dieter Barlösius sowie den Mitarbeitenden der Feinmechanikwerkstatt auf dem Forschungscampus Bahrenfeld, die beim Aufbau des Experiments immer mit Rat und Tat zur Seite standen. Zusätzlich danke ich Ellen Gloy, Janina Neubert und dem CUI-Office für die Hilfe in verschiedenen administrativen Fragen.

Zu guter Letzt danke ich meinen Freund:innen und meiner Familie, die mich fortwährend unterstützt haben.

Eidesstattliche Versicherung / Declaration on oath

Hiermit versichere ich an Eides statt, die vorliegende Dissertationsschrift selbst verfasst und keine anderen als die angegebenen Hilfsmittel und Quellen benutzt zu haben.

Hamburg, den 07.09.2021

Tobias Kroker